Development of MEMS-based Piezoresistive Three Dimensional Stress/Strain Sensor with Temperature Compensation

by

Mohammed Omar Haridy Kayed

A thesis submitted in partial fulfillment of the requirements for the degree of

Doctor of Philosophy

Department of Mechanical Engineering
University of Alberta

Abstract

In this research, a developed n-type piezoresistive three dimensional (3D) stress sensor with full temperature compensation is presented. The proposed sensing rosette benefits from the stress insensitivity of the full-circular n-type piezoresistor, oriented over (111) silicon plane, to detect only temperature changes for compensation. Moreover, the unique behavior of shear piezoresistive coefficient (π_{44}) of n-Si is utilized to construct a piezoresistive stress sensing rosette over (111) silicon plane that is capable of extracting 3D stress components. Prototype stress sensing chip was microfabricated to test the capability of the developed sensing rosette to accurately extract stress applied on structures at different thermal environments. The fabricated sensing chip was subjected to different mechanical loads using a loading rig with a four-point bending fixture. The testing was carried out over a temperature range of -20 to 60 °C. The results showed that the proposed sensing chip has the capability of capturing the stress applied at different temperatures. Also, the developed sensing rosette showed less sensitivity to the uncertainty in piezoresistive coefficients' values compared to the other developed 3D piezoresistive stress sensors. Further improvements of the proposed sensor were achieved by developing a hybrid smart temperature compensation system to reduce the temperature effect on both resistivity and sensitivity of the sensing rosette. The developed compensation system integrates a temperature sensor, placed in close proximity to the stress sensing rosettes, with the artificial neural networks (ANNs). The results showed an improvement in

stress measurement accuracy compared to the other developed compensation systems for such 3D stress sensors. The proposed compensation system has merit since the employed temperature sensor shares the same thermal environment with the stress sensing rosette. Moreover, the developed system has the capability to compensate for both resistance and sensitivity, for 3D stress sensor, with no need for additional circuitry on the sensing device itself.

Preface

The research work related to developing new temperature sensor, to detect the temperature changes within the piezoresistive 3D stress sensors for compensation, has been published in M. O. Kayed, A. A. Balbola, and W. A. Moussa, "A New Temperature Transducer for Local Temperature Compensation for Piezoresistive 3-D Stress Sensors," *IEEE/ASME Transactions on Mechatronics*, vol. 24, no. 2, pp. 832-840, 2019. This publication includes an analytical study, microfabrication, and experimental evaluation, of the proposed temperature sensor, which are presented in part of Chapter 3, Chapter 4, Chapter 5 and Chapter 6. M. O. Kayed was responsible for modeling, design, fabrication, and testing of the temperature sensor along with the manuscript composition. A. A. Balbola contributed in part of the fabrication, data collection and manuscript revision. Dr. W. A. Moussa was the supervising author for this work.

The research work related to developing a new piezoresistive 3D stress sensing rosette with temperature compensation and less sensitivity to process noise, due to the fabrication non-uniformity, has been published in M. O. Kayed, A. A. Balbola, E. Lou, and W. A. Moussa, “Development of Doped Silicon Multi-element Stress Sensor Rosette with Temperature Compensation,” *IEEE Sens. J.*, vol. 20, no. 3, pp. 1176–1183, Oct. 2019. This publication includes the theory of operation, sensitivity analysis, microfabrication, and testing, of the developed stress sensing rosette, which are presented in part of Chapter 3, Chapter 4, Chapter 5 and Chapter 6. M. O. Kayed was responsible for simulation, design, fabrication, characterization and calibration and testing of the prototype sensor along with the manuscript composition. A. A. Balbola contributed in part of the fabrication, characterization and calibration and manuscript revision as well. Dr. E. Lou contributed with the circuitry needed for testing the prototype sensing chip in addition to his partial contribution to manuscript composition. Dr. W. A. Moussa was the supervising author for this work.

The research work related to proposing a smart calibration technique, using Artificial Neural Networks (ANNs), to solve for the uncertainty in piezoresistive coefficients' values, due to the fabrication non-uniformity, has been published in M. O. Kayed, A. A. Balbola, and W. A. Moussa, "A Smart High Accuracy Calibration Algorithm for 3D Piezoresistive Stress Sensor," *IEEE Sens. J.*, vol. 17, no. 5, pp. 1255–1263, 2017. This publication includes finite element modeling (FEM), numerical and experimental sensitivity analysis, and experimental evaluation of the proposed ANNs calibration algorithm, which are presented in part of Chapter 3 and Chapter 6. M. O. Kayed was responsible for FEM, numerical and experimental analysis, ANNs function generation along with the manuscript composition. A. A. Balbola contributed in part of the data collection and testing for ANNs and manuscript revision as well. Dr. W. A. Moussa was the supervising author for this work.

The research work related to developing a hybrid smart temperature compensation system for piezoresistive 3D stress sensor to reduce the temperature effect on both the sensitivity and the resistance of the piezoresistor, which is included in part of Chapter 5 and Chapter 6, has been submitted in a manuscript for publication, M. O. Kayed, A. A. Balbola, E. Lou, and W. A. Moussa, “Hybrid Smart Temperature Compensation for Piezoresistive 3D Stress Sensors,” *IEEE Sensors Journal*, 2020 (submitted). The manuscript is currently under review. M. O. Kayed was responsible for data collection, ANNs training, and testing along with the manuscript composition. A. A. Balbola contributed in part of the data collection and testing for ANNs and manuscript revision as well. Dr. E. Lou contributed with the circuitry needed for collecting data for the ANNs algorithm. Dr. W. A. Moussa was the supervising author for this work.

The research work related to integrating the strain engineering with the proposed the stress sensing rosette during fabrication to enhance the sensitivity of the out-of-plane stress measurement, which is included in part of Chapter 6, has been submitted in a manuscript for publication, M. O. Kayed, A. A. Balbola, E. Lou, and W. A. Moussa, “Development of MEMS-based Piezoresistive 3D Stress/Strain Sensor Using Strain Technology and Smart Compensation System Part A: Microfabrication and Testing,” *Journal of Microengineering and Micromechanics*, 2020 (submitted). The manuscript is currently under review. M. O. Kayed was responsible for Design, microfabrication, and testing along with manuscript composition. A. A. Balbola contributed in part to the fabrication and testing of the developed sensor in addition to his partial contribution to the manuscript. Dr. E. Lou contributed with the circuitry needed for testing of the prototype sensor. Dr. W. A. Moussa was the supervising author for this work.

Dedicated

To

My Beloved Mother

For being my first and life-long teacher and for supporting and encouraging me to believe in myself. May Allah have mercy on her soul and grant her the paradise.

My Kind Father

For earning honest living for our family and for his persistent support, encourage and prays that made me the man I am today

My Lovely Wife

Who provided me with unconditional love and support and whom I owe everything to

Acknowledgement

First and foremost , I give thanks to Allah for his countless bounties, blessings and favours upon me. Also, I would like to thank all my siblings: Amany, Hazem, Ayman and Hatem, for the great support and encouragement they provided me to reach to this important milestone in my life.

I sincerely thank my supervisor Dr. Walied Moussa for the ongoing support and ecourgement he showed me since the first day of joining the program. I would also like to express my gratitude to him for providing all the resources needed to successfully complete this work.

In addition, I would like to thank my supervisory committee members, Dr. Edmond Lou and Dr. Samer Adeeb for their valuable insights and help for the completion of this work. I would also like to thank my colleagues at the MEMS/NEMS Advanced Design Lab for their continuous encouragement, support and insights. Special thanks to my dear friend and teammate Amr Balbola for the amazing and effective collaboration and the great support he showed me that allowed me to successfully complete this research work. I would also like to thank my dear friend Dr. Hossam Gharib for his support and encouragement and help during the entire program. I would also like to thank my dear friend Ahmed Badr for his encouragement during this research. I would also like to thank Dr. Mohamed EL Gowini, Dr. Shichao Yue, Dr. Yang Qui, Dr. Else Gallagher, Aliaa Nabih, Mostafa Hassan for their very useful feedbacks especially during the group meetings.

I would also like to thank all the staff members of the nanoFab facility at the University of Alberta for their support, specially to the Director Dr. Eric Flaim, and other staff members such as Glenn Elaschuk, Melissa Hawrelenchko, Scott Munro, Les Schowalter, and Stephanie Bozic.

Finally, I would like to thank the Canadian National Science and Engineering Research Council (NSERC) and CMC Microsystems Inc. for their financial supports.

Table of Contents

List of Tables

List of Figures

List of Nomenclature and Acronyms

SHM	: Structural Health Monitoring
AER	: Alberta Energy Regulator
NEB	: National Energy Borad
MEMS	: Micro-electro-mechanical Systems
3D	: Three dimensional
ΔR/R	: Change in electrical resistance for piezoresistor
NEMS	: Nano-electro-mechanical Systems
PRCs	: Piezoresistive coefficients
R	: Initial electrical resistance of piezoresistor
ε	: Mechanical Strain
Δρ/ρ	: Change in electrical resistivity
GF	: Gauge factor
PDMS	: Polydimethylsiloxane
PP	: Polypropylene
PC	: Polycarbonate
PMMA	: Polymethyl methacry-late
PE	: Polyelectrolytes
PVA	: Flexible epoxy and polyvinylalcohol
π_{11}, π_{12}, and π_{44}	: Principal crystallographic piezoresistive coefficients
IC	: Integrated Circuits
TCR	: Temperature coefficient of resistance
Ge	: Germanium
Si	: Silicon
ε	: Mechanical Strain
a, b	: The two groups of piezoresistors of eight-element rosette representing two doping concentration
ACA	: Anisotropic conductive adhesive

ADL	: Advanced Design Laboratory
α	: First order temperature coefficient of resistance
t_i^p and T_i^p	:Time and temperature for the pre-deposition process i if more than one pre-deposition steps are implemented
B_i	: Coefficients representing functions of the crystallographic piezoresistive coefficients, i=1,2,3
BOE	: Buffered oxide etch
ρ	: Resistivity
TCS	: Temperture coefficient of sensitivity
$P(N,T)$	: Piezoresistance factor
CMOS	: Complementary Metal Oxide Semiconductor
ADC	: Analog-to-digital converter
DAC	: Digital-to-analog converter
ANNs	: Artificial Neural Network
σ'_{ij}	: Stresses in the primed coordinate system with, i, j = 1,2,3
σ'_{β}	: Stresses in the primed coordinate system with reduced notation, β = 1,2,..,6
σ_{ij}	: Stresses in the unprimed coordinate system with, i, j = 1,2,3
$\pi'_{\gamma\beta}$	: off-axis piezoresistive coefficients with γ, β equals 1,2,…6
l, m, n	: Direction cosines with respect to the on-axis coordinate system, i.e. x_1, x_2, and x_3
l', m', n'	: Direction cosines with respect to the off-axis coordinate system, i.e. x'_1, x'_2, and x'_3
C(x,t)	: Impurity concentration
C_0	: Impurity concentration at the wafer surface
C_B	: Background concentration
D	: Diffusion coefficient
erfc	: Complementary error function

$\left(Dt\right)_{tot}^{p}$	: Product of diffusion coefficient and time for the pre-deposition step
$\left(Dt\right)_{tot}^{d}$	: Product of diffusion coefficient and time for the drive-in step
D_0	: Diffusion constant
HMDS	: Hexamethyldisilazane
E	: Young's Modulus
F	: Force applied during for four-point bending
F_d	: Force of the dead weight applied in the four-point bending
FEA	: Finite element analysis
FEM	: Finite element model
h	: Thickness of the four-point bending beam
L	: Distance between the applied forces in 4PB
L_d	: Distance between the dead weights in the 4PB
ν	: Poisson's ratio
PCB	: Printed circuit board
PECVD	: Plasma Enhanced Chemical Vapor Deposition
π_{p}	: Piezoresistive pressure coefficient
PSG	: Phosphosilicate Glass
Q	: Total number of dopants per unit area
q	: charge of an electron
R	: Electrical resistance
RIE	: Reactive Ion Etching
R_s	: Sheet resistance
t_i^p	: Time for the pre-deposition process i if more than one pre-deposition steps are implemented in seconds
T_i^p	: Temperature for the pre-deposition process i if more than one pre-deposition steps are implemented in Kelvin
t^d	: Time for the drive-in step in seconds
T^d	: Temperature for the drive-in step in Kelvin

ΔT	: Change in Temperature
TLM	: Transfer line method
w	: Width of the four-point bending beam
V_s	: Voltage source to the Wheatstone bridge
X_j^p	: Junction depth after the pre-deposition steps or ion implantation step
X_j^d	: Junction depth after the drive-in step
ZIF	: Zero Insertion Force

CHAPTER 1: INTRODUCTION

Structural Health Monitoring (SHM) system is a process of identifying the structural integrity and defining the failure threshold of the engineering components using non-destructive evaluation techniques. To this end, the capability of measuring stress and strain fields within structure is considered key parameter for SHM, as failure of such structures is often due to stress application. The engineering structures can vary in scale from small (e.g. electronic components) to large structures (e.g. pipelines, aircraft and bridges).

The evaluation of the stress and strain distributions within a structure can be carried out either theoretically using analytical and numerical approaches (e.g. finite element method), or experimentally using stress/strain sensors (e.g. strain gauges). In the theoretical evaluation, the geometry, material and loads have to be assumed since the real structure does not exist, thus an approximate solution is obtained. On the other hand, the experimental stress analysis can provide actual and real-time information in regards to the structural behavior of an engineering component with no need for knowing the applied loads, which is not possible with analytical or numerical methods. Therefore, the problems can be detected and fixed during the service cycles of such engineering components.

1.1 Motivation

Alberta Energy Regulator (AER), the provincial regulator of oil pipelines, published an analysis of pipeline performance from 1990 to 2012. According to AER's analysis, there were 6,488 pipeline incidents involving a release of hazardous materials into the environment with an average of 282 spills per year over the period from 1990 to 2012 [1]. The leading cause of pipelines rupture was determined by National Energy Board (NEB) to be the corrosion, including cracking and metal loss. The simplest and direct approach to overcome the propagation of minor cracks through the pipeline is to replace the cracked part. However, for large structures, the replacement decision can be costly. An alternative approach is to use an adhesively bonded patch repairs which are fixed over the crack. The main advantage of using the bonded patch repairs is their reduced installation cost, but they are prone to adhesive degradation that leads to patch debonding. Therefore, there is a need for monitoring the out-of-plane stresses, along with the in-plane stress components, to be able to predict the debonding initiation of the patches. To reduce the maintenance cost and time of the patch repairs, *in-situ* monitoring of debonding initiation of the patches is required. Most of the available systems, for real-time monitoring, rely on conventional macro-sized sensors that require large installation areas and measurement equipment and complicated signal processing. However, Micro-electro-mechanical (MEMS) based stress sensors can provide a simpler and smaller SHM system, formed of an array of sensing chips connected through a wireless RF transmission to communicate with the outside world.

For biomedical and implantable applications, a 3D stress sensor, specifically, MEMS-based devices can be used to monitor the implant loosening, stresses induced during intra-cortical recording, and forces induced in dental brackets. For example, to early detect non-painful implant loosening and avoid unnecessary implant-revision surgery, a diagnosis protocol that is capable of monitoring and quantifying the anchorage of the prosthesis is needed. Such a diagnosis protocol needs a full evaluation of the three-dimensional (3D) stress and strain fields at the bone/implant interference. MEMS-based sensors are typically attractive for such applications due to their scale that allows them to be used in a variety of locations in the body where the macro-scale devices are not accessible. However, the biomedical application of the 3D stress sensor requires more attention in terms of its design, integration and material selection, compared to industrial applications, to guarantee appropriate bio-compatibility.

In electronic packaging, i.e. IC chip packaging, a 3D state of stress is induced by thermal loads during the packaging process which may lead to potential delamination and failure of the packaged chip [2]. These thermally-induced stresses can be monitored using a 3D stress sensor integrated with the semiconductor die used in electronic packaging. In the next chapter, the previous state of the art piezoresistive 3D stress sensors, developed for electronic packaging applications, are discussed.

1.2 Problem Statement

Doped silicon-based piezoresistive stress sensors are sensitive to temperature changes, which changes the mobility and number of carriers of piezoresistors, resulting in a change in resistivity [3]. Small temperature variations may result in serious deviations in experimental results when compared to stresses obtained from non-temperature compensated stress formulae [4]. As temperature changes may lead to a change in electrical resistance by as much as 0.2 % per ◦C, while the maximum value of mechanical stress effects in piezoresistive elements is on the order of 1% $\Delta R/R$ [5].

The majority of the developed temperature compensation techniques are only for pressure sensors or strain gauges [6]–[10]. However, less effort was spent towards developing temperature compensation systems for piezoresistive 3D stress sensors. A number of researchers have used silicon diodes on their piezoresistive 3D stress sensors for temperature compensation [11]. These stress sensors use p and n-type piezoresistors as sensing elements, thus a p-n junction diode becomes the most logical and simplest choice for temperature sensing. However, the p-n junction diode temperature sensors have a poor accuracy (absolute error as large as ±3 °C may be obtained), according to Huynh [12]. Other researchers developed stress sensing rosettes with extra sensing elements to solve for the six stress components with full temperature compensations [13], [14]. But these rosettes showed a large process noise while extracting stresses due to the fabrication non-uniformity [15].

To this end, a new 3D stress sensing rosette with a robust temperature compensation system is required to reduce the thermal impact on stress measurement accuracy for doped silicon-based 3D piezoresistive stress sensors.

1.3 Research Objectives

The current research adopts the piezoresistive sensing rosette approach to develop a single-polarity (n-type doped silicon) 3D stress sensor to extract all 6 stress components with full temperature-compensation. A single-polarity rosette is found to be more appealing than a dual-polarity, because of the simplicity of the microfabrication process since there is no need for the p-type doping equipment. Moreover, a smaller footprint can be obtained, compared to the dual-polarity, due to the absence of the n-well. The following are the overall objectives of the current research study:

1. Design a new MEMS-based piezoresistive 3D stress sensing rosette with full temperature compensation: A primary objective is to find an alternative sensing rosette to the available eight-element dual polarity and ten-element single polarity stress sensing rosettes that are capable of monitoring all the six stress components within a material with more accurate temperature compensation system, simpler fabrication process, and less process noise due to the fabrication non-uniformity.
2. Fabricate a sensing-chip with the newly developed rosette: For experimental verification, a prototype sensing-chip with the developed rosette needs to be fabricated using the semiconductors fabrication processes and the available resources on the nanofab and the MEMS/NEMS advanced design laboratory (ADL) at the University of Alberta.

3. Calibrate the developed sensing rosette: This calibration process is an early experimental assessment of the behavior of the sensing rosette against known loads (structural and thermal loads).
4. Test the prototype sensing-chip: The prototype sensing-chip needs to be tested under different loads at different thermal environments to evaluate the stress measurement and temperature compensation capabilities of the new sensing rosette.
5. Develop a smart calibration and compensation system: For more accurate stress measurements, a smart and accurate calibration and compensation system, using artificial intelligence, is required to consider the nonlinearity and temperature dependence of the piezoresistive coefficients (PRCs) that may exist.

The methodology involves multi-discipline sciences and technologies to achieve the objectives of the research study. As shown in Figure 1-1, the methodology is divided into three main milestones: sensor design, microfabrication and characterization, and evaluation of prototype sensors. The following chapters describe the phases of the methodology in detail.

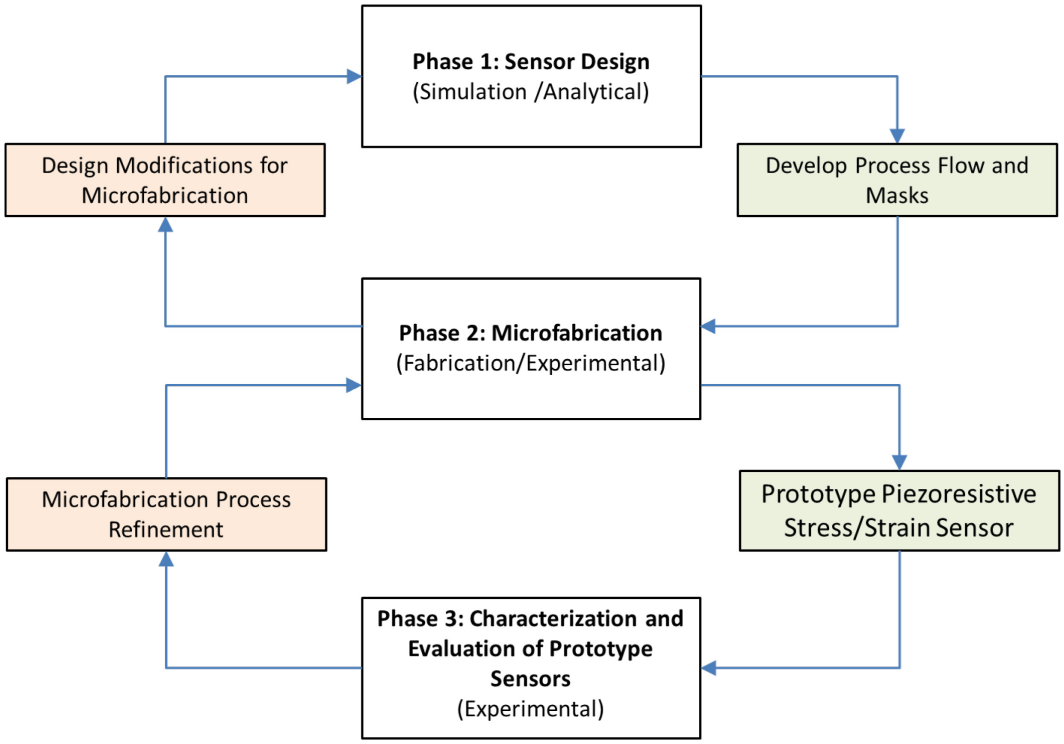

Figure 1-1 Research Methodology Flow Chart

1.4 Thesis Organization

This thesis provides a detailed description of the new 8-element piezoresistive 3D stress sensing rosette with temperature compensation in terms of theory of operation, microfabrication, calibration, and experimental testing. The thesis is divided into 7 chapters as follows:

Chapter 1 provides an introduction and overview of the presented research and highlights the motivation, the problem statement, research objectives, and the approached methodology during this study.

Chapter 2 provides a literature review related to the core aspects of the thesis objectives, including the different types of stress sensors with more focus on the previous efforts to develop piezoresistive sensors, especially the 3D stress sensors. Moreover, it discusses the conducted efforts with the calibration and the temperature compensation for doped silicon piezoresistive sensors.

Chapter 3 presents the theoretical background of the multi-element piezoresistive stress sensors, including the previous state of the art 3D stress sensors. Also, the theory of operation of the novel temperature transducer, along with a numerical assessment, is provided to investigate the feasibility of the new approach.

Chapter 4 discusses the fabrication procedures followed to prototype the proposed n-type 8-element stress sensing rosette and temperature sensor to conduct an experimental evaluation of the new sensing rosette. The chapter presents the basic mathematical modeling of the diffusion doping and the full process flow and characterization of the prototype sensor.

Chapter 5 presents the calibration and testing of the prototype sensing chip. For calibration, the three calibration setups including uni-axial, thermal, and hydrostatic loading are presented and the resulting coefficients are given to prove the feasibility of the approach. The experimental testing conducted to evaluate the capability of the developed sensor to capture the stresses applied at different thermal environments. The test setup using four-point-bending of a chip-on-beam assembly is also discussed.

Chapter 6 presents the sources of error for multi-element sensing rosettes, including the fabrication non-uniformity and temperature dependency of PRCs. Also, a smart and more accurate calibration technique is proposed using artificial intelligence, i.e. artificial neural networks (ANNs), to overcome the fabrication non-uniformity issue. Moreover, a hybrid temperature compensation system is provided, which integrates both the ANNs and the developed temperature sensor, to eliminate the nonlinearity and the temperature dependence of the PRCs that may exist. In addition, the integration of strain engineering into the developed rosette to improve the sensitivity of the proposed 3D stress sensor to extract the out-of-plane stress components is provided.

Chapter 7 provides an overview and concluding remarks of this research and offers directions for future work.

CHAPTER 2: LITERATURE REVIEW

2.1 Overview

In this chapter, the history of the piezoresistivity, is presented along with its application in stress and strain sensors. Moreover, the temperature dependency of the PRCs is presented for both n-type and p-type piezoresistors. Finally, the available temperature compensation techniques, for piezoresistive stress sensors, are discussed.

2.2 Piezoresistance

The piezoresistive effect was first discovered by Lord Kelvin in 1856. He reported that a metal conductor (i.e. iron or copper) may change in its electrical resistance when it experiences elongation [16]. In the 1950s, the piezoresistivity in silicon (Si) and germanium (Ge) was first observed experimentally by Talyor [17], Bridgman [18], Smith [19] and Paul *et al.* [20]. This was a step forward since this effect provides a direct relation between the mechanical load and electrical resistance, it is commonly used for stress/strain sensing applications. The piezoresistive stress/strain sensors can generally be divided into geometrical-based effect and resistivity-based effect sensors. As given in equation (2-1), the change in resistance due to applied stress is a function of geometry and resistivity changes [21]. The change in resistance ($\Delta R/R$) from an initial unstrained state (R) is given by:

$$\frac{\Delta R}{R} = (1+2\nu)\varepsilon + \frac{\Delta\rho}{\rho} \tag{2-1}$$

Where ν is Poisson's ratio of the material, ρ is the resistivity of the conductor and ε is the mechanical strain in the conductor. In geometrical based-effect piezoresistors, like metals, their resistance change in response to the applied load due to the shape deformation, thus the first term in equation (2-1) is dominant, while the change in resistivity ($\Delta\rho / \rho$) is negligible. However, in resistivity based-effect sensors, like semiconductors, the applied stress results in a transfer of electrons between energy levels, which improves the electrons' mobility and consequently leads to a significant change in resistivity.

2.3 Geometrical Effect–based Piezoresistive Sensors

2.3.1 Metal Foil Strain Gauges

Metal foil strain gauges are the most affordable and reliable gauges among the available metal piezoresistive strain gauges. The strain gauge was first devised by Edward Simmons and Aurthur Ruge in 1938, while they were in two different places and have no contact with each other [22]. Simmons invented the strain gauge principle, as part of research project, to be used for the measurement of the shock loads on metal specimens. While Arthur with support of his assistant J. Hanna Maier was successfully able to measure the strain, induced by the earthquake, within the mechanical structures using the resistance change of thin wire from a potentiometer [23], [24].

Today the metal foil strain gauges are commercially available in the form of metallic foil pattern supported by a plastic carrier, as shown in Figure 2-3. The metal foil gauge is attached to the structure using adhesive. The strain limit of such gauges is about $40x10^3$ με, while the temperature of operation of such devices can reach about 130 °C [25]. However, these gauges have a small gauge factor (GF) of about 2-5.

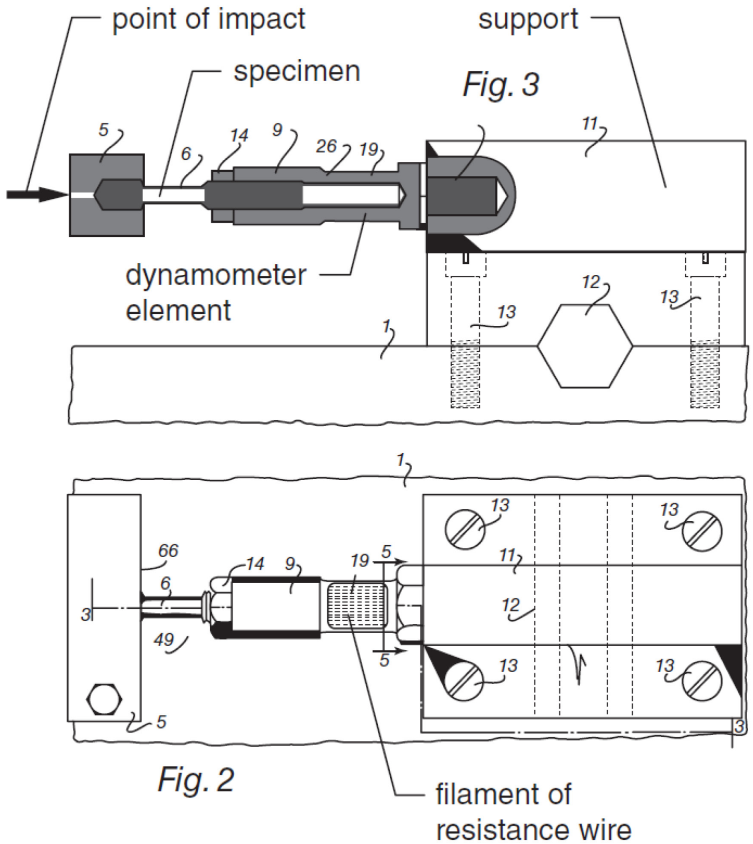

Figure 2-1 Simmons's strain gauge for the measurement of the shock loads [26]

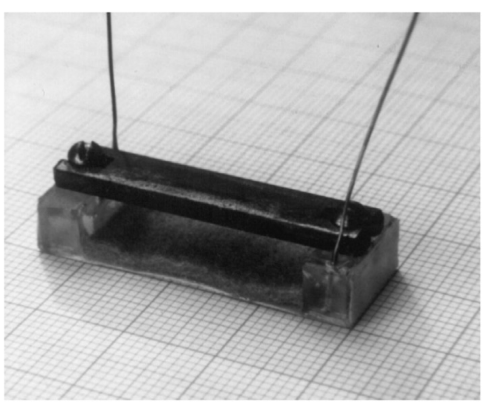
a)

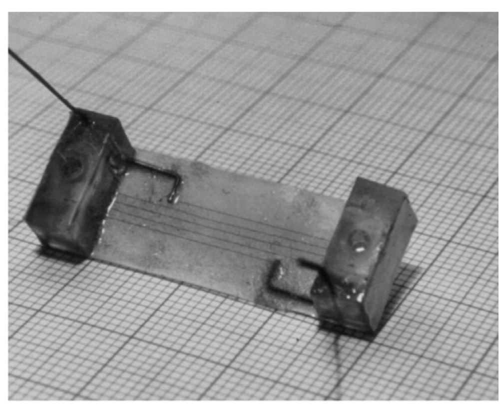
b)

Figure 2-2 Ruge's strain gauge from 1938 [27]

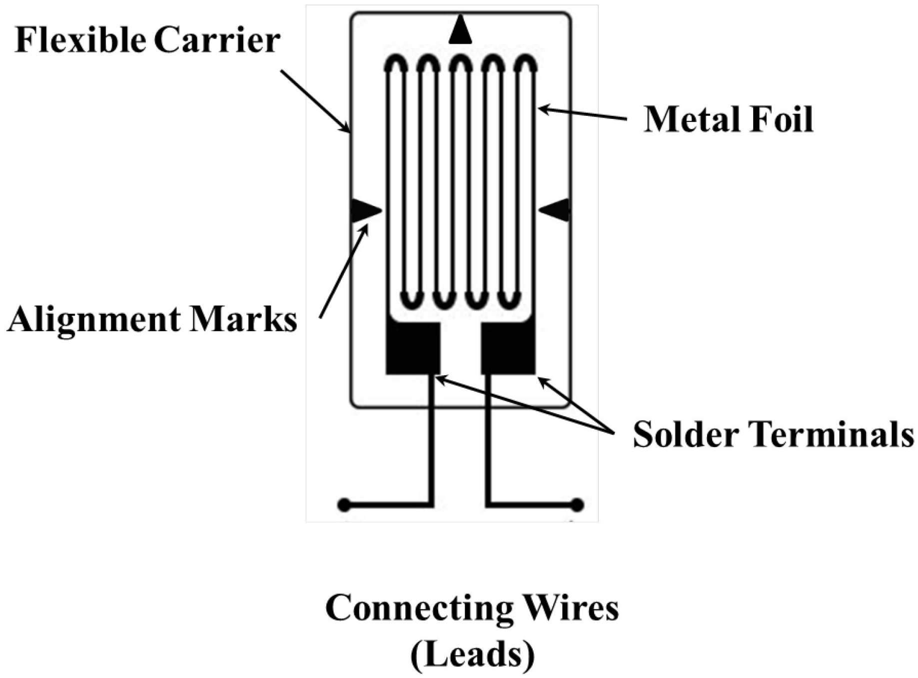

Figure 2-3 Layout of the metal foil strain gauge

2.3.2 Metallic Nanowires for Piezoresistive Stress/Strain sensors

Nanowires fabricated from different materials, i.e. silver, gold, and copper, have also been employed for new designs of piezoresistive stress/strain sensors, especially for electronic skin applications [28]–[30]. Since silver and gold nanowires have high conductivity, they offer sensing devices with low power consumption [31]. The main drawback is the costly fabrication process of these nanowires. On the other hand, copper nanowires are much cheaper to fabricate, compared to silver and gold nanowires. Although the good conductivity of the copper-based nanowires [32], they experience degradation in conductivity over time due to the thermal oxidation and chemical corrosion that occur in harsh conditions [33].

2.3.3 Non-metal Piezoresistive Sensors

Non-metal materials, i.e. Conductive rubber and carbon–fiber, have been widely used in developing strain gauges, particularly in the field of robotics because of their compliance, lightness, sturdiness, and low-cost production [34]–[36]. High GF of up to 134 at a maximum tensile strain of 40% was achieved, and the potential applications of these gauges could be the dynamic detection of human joint motion [37]–[39]. Conductive polymer composites are commonly engineered by mixing carbon fillers and polymer materials using low–frequency ultrasound with or without the addition of detergents [40], [41]. For such sensors, variety of polymers have been adopted, for instance, polydimethylsiloxane (PDMS), polypropylene (PP), polycarbonate (PC), polymethyl methacrylate (PMMA), polyelectrolytes (PE), flexible epoxy and polyvinylalcohol (PVA) [42]–[49]. The fabrication process of these materials is quick and simple, overcoming limitations of metal and semiconductor systems. However, one of the main challenges is that it is usually difficult to homogenously distribute the carbon fillers within the polymer matrix [50]. Moreover, both conductive rubber and carbon–fiber strain gauges suffer non–linearity and a high degree of hysteresis [25].

2.4 Resistivity Effect-based Piezoresistive Sensors

The doped silicon stress/strain sensors exhibit exceptional piezoresistive behavior, compared to the metal foil strain gauges, because of their low cost, small size, good linearity, low power consumption, batch fabrication capability and absence of hysteresis [3]. For silicon-based piezoresistor, the change in its resistivity is related to the applied stress through the fourth-order piezoresistive tensor. Due to the cubic symmetry of silicon, the piezoresistive tensor is defined by only three distinct principal coefficients (π_{11}, π_{12}, and π_{44}). Kanda provided analytical modeling of piezoresistive coefficients and their dependency on doping concentration and temperature at different crystal orientations [51]. Also, the principal piezoresistive coefficients of silicon and germanium were studied experimentally by Tufte *et al.* [52], [53], Morin *et al.* [54], and Richter *et al.* [55].

The first silicon strain gauges, to measure forces and displacements, was developed by Mason and Thurston in 1958 [56]. Thanks to the developments in fabrication techniques of semiconductors which evolved the piezoresistive sensors from single strain gauges to multi-element sensing rosettes with smaller footprint and capability of integration with chip electronics [57]. Doped crystalline silicon piezoresistive sensors have a privilege, compared to the conventional strain gauges, of sensing all six stress components from a single rosette oriented over the (111) plane [13], [58]. Extraction of these stress components is necessary for electronic packaging and composite structures, where three dimensional (3D) state of stress may exist [15], [59]. Table 2-1 shows a qualitative and quantitative comparison between some of the representative piezoresistive sensors, i.e. metal gauges, non-metal gauges and doped silicon sensors that have been reviewed.

Besides the direct stress/strain measurement, the piezoresistivity in semiconductors has been utilized in developing sensors for a variety of applications, for example, force sensors [60]–[63], pressure sensors [64]–[66], and flow sensors [67], [68], in which the change in electrical resistance resulted from the induced stress is captured to measure the phenomenon of interest

Table 2-1: Comparison between different piezoresistive stress/strain sensors

	Metal gauges [69]–[71]	**Non Metal gauges** [25], [37], [38], [72], [73],	**Doped Silicon gauges** [11], [13], [15], [74]–[76]
Sensitivity	Low GF: 2-5	High GF:134	High GF: 200
Temperature Sensitivity	Low	High	High
Operating Temperature	About 130 °C	Up to 200 °C	Up to 300 °C (SOI)
Non-Linearity	Average	High	Low <0.2%
Hysteresis	Average	High	Low
Circuitry	Simple	Complex	Complex
Assembly	Complex	Complex	Simple
Ease of Installation	Easy	Easy	Easy
Application	2D strain/stress sensors	2D and 3D strain/stress sensor	2D and 3D strain/stress sensor

2.5 MEMS-based Piezoresistive 3D Stress Sensors

MEMS-based piezoresistive sensors benefited massively from developments in silicon processing and modeling for the integrated circuits (IC) industry. The continuous enhancement in the fabrication processes of ICs including doping, etching, and thin-film deposition methods, has allowed significant improvements in piezoresistive device sensitivity, resolution, bandwidth, and miniaturization [77].

Cordes et al. [78] reported that (111) silicon plane is the optimal silicon plane to orient the piezoresistors over to develop a 3D stress sensing rosette. The development of a piezoresistive 3D stress sensor was early carried out by a group of researchers at Auburn University [2], [79]–[81]. They employed dual polarity (p-type and n-type) eight piezoresistive elements to form a set of independent linear equations to solve for the 3D stress components. Only three components, in-plane, and out-of-plane shear stress components, were temperature-compensated. Figure 2-4 shows a microscopic image of their developed dual polarity eight-element 3D stress rosette on (111) silicon. To compensate for the effect of temperature on the remaining stress components, the legitimate choice was using a p-n junction temperature transducer for such dual polarity sensors. Also, the research group at Auburn University dealt with a number of development areas in regards to the stress sensing rosettes. Jaeger et al. [79], [82] investigated the errors associated with the design and calibration of the piezoresistive stress sensing rosettes over (100) silicon plane. Cho et al. [83] studied the temperature dependency of the PRCs and the temperature coefficient of resistance (TCR) in the stress sensors. Hussain et al. conducted a sensitivity analysis to study the impact of measurement and calibration errors on the output of the stress sensing rosettes over (111) silicon plane [84].

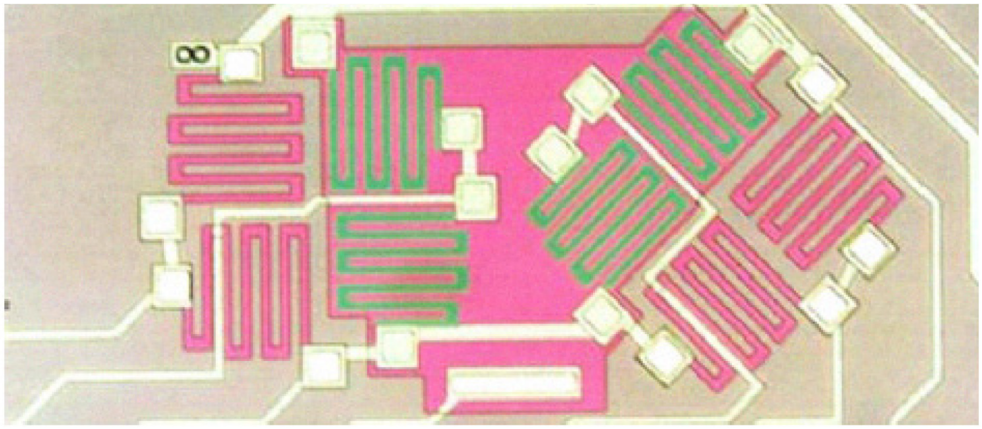

Figure 2-4 Dual polarity eight-element piezoresistive 3D stress sensing rosette developed by a group of researchers at Auburn University [85], Copyright © 2009 IEEE

Gharib [13], [14] utilized the fact that the shear piezoresistive coefficient π_{44}, for n-type silicon, is independent of impurity concentration unlike the other PRCs, π_{11} and π_{12}, to develop a single polarity piezoresistive 3D stress sensor. The developed rosette was made up of ten n-type sensing elements of three different doping concentrations to have linearly independent PRCs for 3D stress components extraction with full temperature compensation. Figure 2-5 shows a microscopic image of the developed single polarity ten-element 3D stress rosette. Single-polarity (n-type) rosette provides a simpler micro-fabrication process compared to a dual-polarity (n-type and p-type) since there is no need for the p-type doping equipment. Also, it has the potential of fabricating a rosette with a smaller footprint due to the absence of the n-well [59]. However, this rosette showed high sensitivity to process noise while extracting stresses due to the fabrication non-uniformity [15]. Lwo *et al.* [86], [87] recommended the use of all n-type rosettes as *in-situ* stress sensors for electronic packaging applications, because of their lower standard deviation on the extracted PRCs compared to the p-type ones.

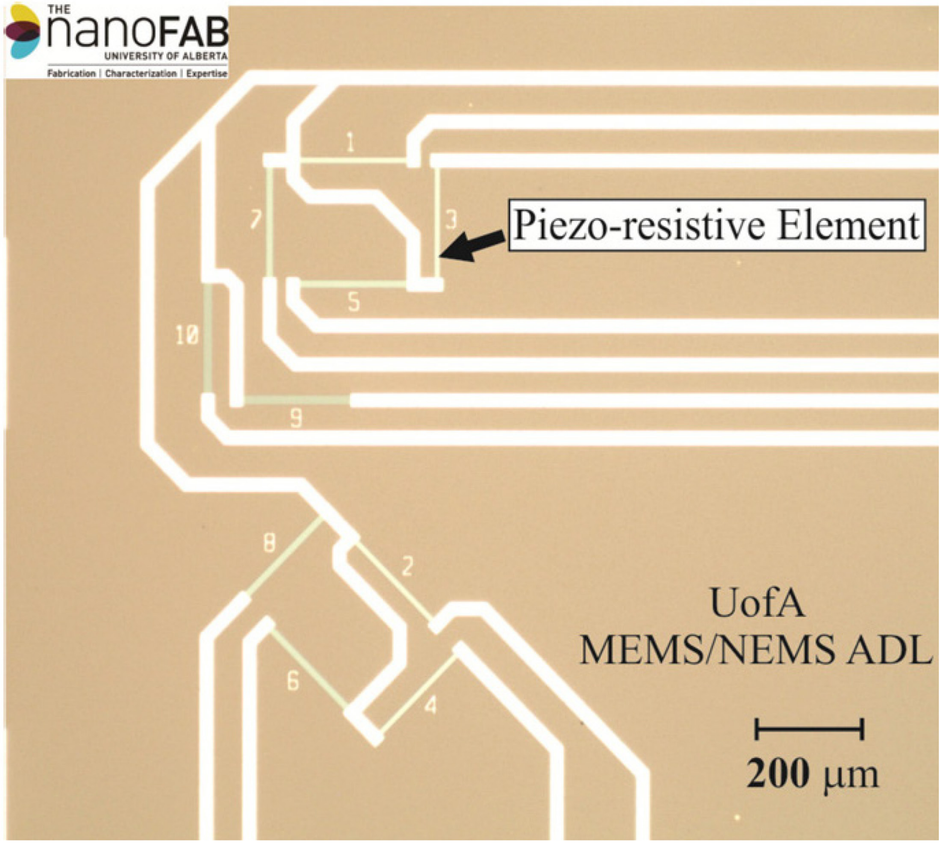

Figure 2-5 Single polarity ten-element piezoresistive 3D stress sensing rosette developed by Gharib [59], Copyright © 2011 IEEE

2.6 Temperature Compensation Systems for Piezoresistive Sensors

Piezoresistive stress sensors are sensitive to temperature variation, which changes the mobility and number of carriers of piezoresistors [3]. The small temperature change may lead to serious deviations in the sensor's acquired signals while measuring stress within structure [4], [88].

An early study of the temperature dependence of the piezoresistance of high-purity silicon and germanium was provided by Morin et *al.* [54]. They measured the change of resistance due to uniaxial compression for a number of single-crystal specimens of high-resistivity n-type and p-type germanium and silicon over the temperature ranges from 5 K to 350 K (Ge) and 20 K to 350 K (Si). Kurtz [89] investigated the effect of dopant concentration on PRCs, temperature coefficient of sensitivity (TCS), resistivity (ρ), temperature coefficient of resistivity (TCR) and strain nonlinearity. It was found that the temperature dependence of sensitivity decreases with increasing dopant concentration. The increase in doping concentration also sacrifices the sensitivity of the piezoresistors. However, the temperature coefficient of sensitivity drops off faster than sensitivity. Also at higher doping levels, the strain and temperature nonlinearities of sensitivity, and temperature change of resistance are very much reduced. Tufte and Stelzer [52], [53] subsequently discussed the temperature dependence of the large PRCs, π_{44} for p-type and π_{11} for n-type silicon, on layers having surface concentration values from 10^{18} to 10^{21} cm^{-3}. The results showed less temperature dependence of PRC with increasing impurity concentration. Kozlovskiy and Boiko [90] presented analytical expressions for the values of π_{44} in p-type and π_{11} in n-type silicon as a function of temperature for different impurity concentrations. Theoretical calculations of PRCs change versus dopant concentration were carried out by Kanda [51]. At high doping levels, a deviation between his calculations and the experimental data has been observed. Kanda calculated the PRC by multiplying the piezoresistive factor, P(N, T), shown in Figure 2-6 and Figure 2-7, by the value of PRC at the room temperature [19], [56], given in Table 2-2. The calculated values of the P(N, T), successfully match the experimental values obtained by Mason [91] for doping concentrations less than 1×10^{17} cm^{-3}, over the temperature range of −50 to 150 °C, but differ by 21% at a concentration of 3×10^{19} cm^{-3} at room temperature. The error was attributed to the ignorance of dopant ions scattering in P(N, T) calculations for high dopant concentrations, whereas the lattice scattering was only considered.

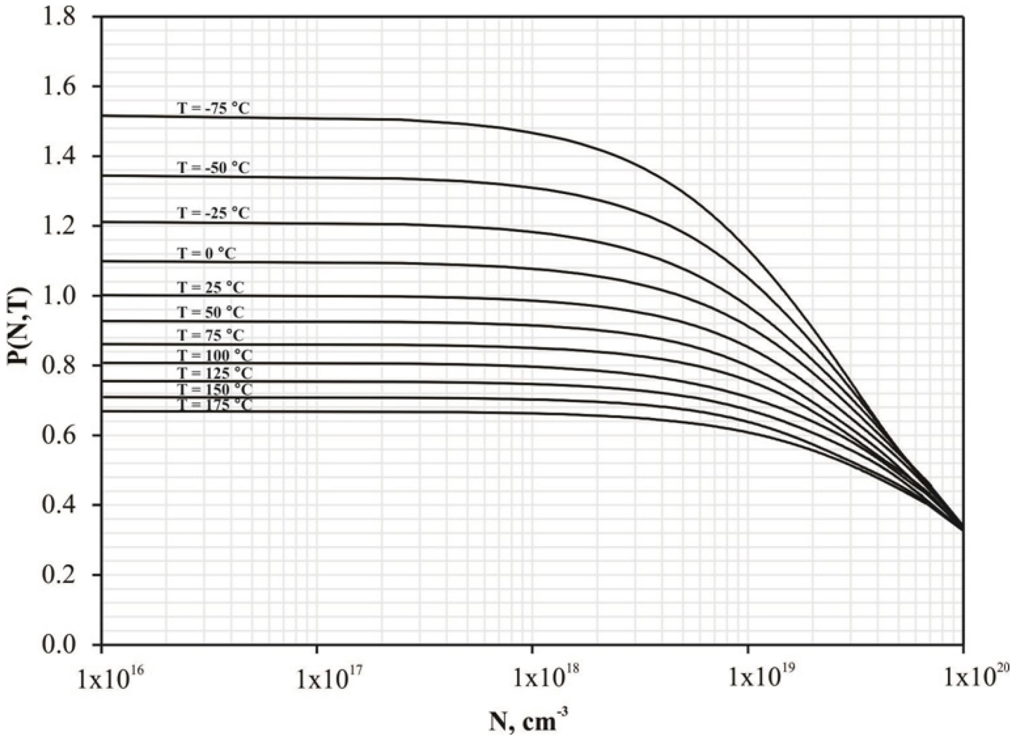

Figure 2-6 Piezoresistive factor P(N,T) as a function of impurity concentration and temperature in n-Si (re-plotted from [51]), Copyright © 1982 IEEE

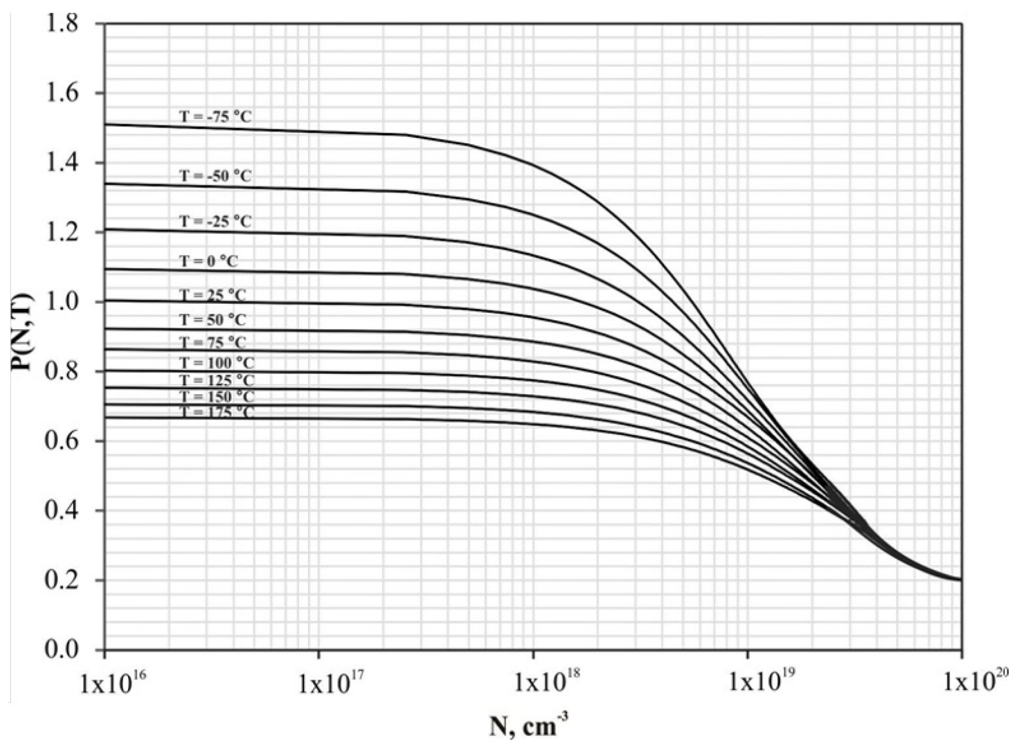

Figure 2-7 Piezoresistive factor P(N,T) as a function of impurity concentration and temperature in p-Si (re-plotted from [51]), Copyright © 1982 IEEE

Table 2-2: PRCs for lightly doped silicon at room temperature, TPa^{-1}

	n-type Silicon	p-type Silicon
π_{11}	-1022	66
π_{12}	534	-11
π_{44}	-136	1381

Ultimately, the temperature-induced signal during typical operation can be larger than the intended sensor output. To this end, a temperature compensation system is required to reduce the thermal impact on sensor accuracy. Many temperature compensation techniques have been proposed for piezoresistive devices, which can be classified into three main categories: passive compensation at the sensor, active compensation in the signal-conditioning electronics, and software compensation [92].

Passive compensation integrates two or four nominally identical piezoresistors in a Wheatstone bridge configuration. When these piezoresistors are exposed to the same environmental conditions, specifically, temperature change, a common-mode signal is generated that can be canceled using an instrumentation amplifier. This approach compensates for resistance but not sensitivity changes with temperature [93].

For active compensation, the passive approach is integrated with a temperature sensor and compensation circuit to eliminate the thermal effect on both resistance and sensitivity of piezoresistors. Active compensation is used in applications where a high level of accuracy is required. For analaog circuitry, trim resistors were utilized in temperature compensation circuits for piezoresistive sensors[94]. The need for smaller, more accurate, cheaper and low power sensors was a motive for the transition to CMOS [95]. In terms of cost per power per functionality, digital technology offer superior functionality than analog technologies. There are two main architectures for piezoresistor temperature compensation using CMOS:

fully digital compensation and digitally controlled analog compensation [24]. The fully digital signal compensation uses an analog-to-digital converter (ADC) to digitize signals of both piezoresistive senor and temperature sensor, before performing signal compensation. Finally, if an analog output is needed then the compensated digital data are sent to digital-to-analog converter (DAC). This architecture is the most flexible but has some intrinsic problems that limit its use in control loops. Since, the ADC, the microprocessor, and the DAC all need processing time, this delay time may not be tolerated in feedback control. In contrast, the digitally controlled analog compensation system benefits from the fact that temperature is a slow signal so that latency is not generally a problem.

Software schemes are based on data processing according to an inverse function algorithm or artificial neural networks (ANNs) [6], [7]. Several software approaches based on ANNs have been proposed to reduce the temperature effect on the accuracy of piezoresistive sensors readout [9], [10]. However, ANN-based approaches were not clarified in the performances and configuration of neural networks.

2.7 Conclusions

This chapter presented the development of the theory of piezoresistivity and specifically towards the design of piezoresistive stress/strain sensors. Different types of piezoresistive sensors i.e. metal, non-metal and doped silicon stress/strain sensors are discussed. The successful approaches to developing 3D piezoresistive stress sensing rosettes with full temperature compensation are limited. These approaches mainly utilized a dual-polarity and single-polarity rosettes of diffused resistors on (111) silicon to extract stress components with temperature compensation. Finally, an overview of the temperature compensation systems for piezoresistive stress/strain sensors was discussed.

CHAPTER 3: THE PIEZORESISTIVE THREE-DIMENSIONAL STRESS SENSING ROSETTE

3.1 Piezoresistance Fundamentals of Doped Crystalline Silicon

3.1.1 General Expressions of a Piezoresistor with Arbitrary Orientation

This section introduces the fundamental relations describing the change in electrical resistance of a piezoresistive filament due to applied mechanical and thermal loads, which have been presented earlier by Bittle *et al*. [2] and Suhling *et al*. [96]. The capability of a piezoresistive sensing rosette, fabricated into crystalline silicon, to extract the three-dimensional (3D) state of stress depends on the orientation of the sensing elements with respect to the principal crystallographic axes of the silicon cubic crystal. Uniform piezoresistive filament at a general orientation with respect to the silicon principal crystallographic directions is shown in Figure 3-1.

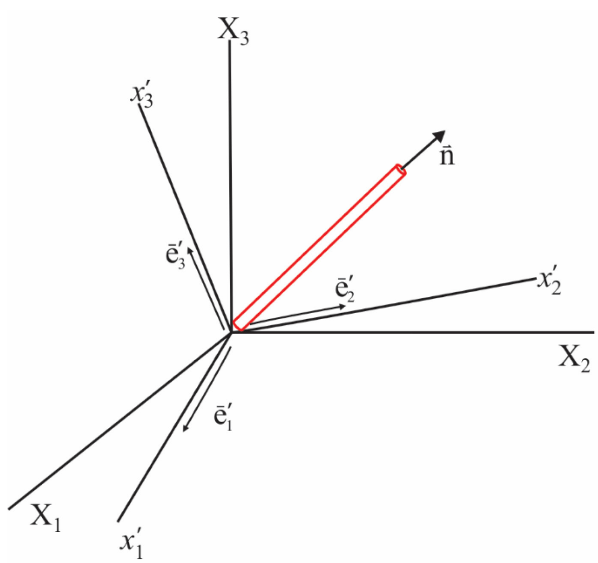

Figure 3-1 Silicon conductor with arbitrary orientation

The unprimed coordinates (on-axis) represent the principal crystallographic directions X_1 = [100], X_2 = [010], and X_3 = [001] of a cubic crystal. It is more convenient to have the change in resistance defined in terms of stress components which are resolved in different coordinate system, i.e. the primed axes, than the one aligned with the principal crystallographic axes. The primed axes (off-axis) represent an arbitrary rotated coordinate system with respect to the unprimed coordinate system. The change in electrical resistance of a piezoresistive element due to applied stress and temperature along the primed axes can be expressed as follows [11]:

$$\begin{aligned}\frac{\Delta R}{R} &= \frac{R(\sigma,T)-R(0,0)}{R(0,0)}\\ &=\left(\pi'_{1\beta}\sigma'_{\beta}\right)l'^2+\left(\pi'_{2\beta}\sigma'_{\beta}\right)m'^2+\left(\pi'_{3\beta}\sigma'_{\beta}\right)n'^2\\ &\quad+2\left(\pi'_{4\beta}\sigma'_{\beta}\right)l'n'+2\left(\pi'_{5\beta}\sigma'_{\beta}\right)m'n'\\ &\quad+2\left(\pi'_{6\beta}\sigma'_{\beta}\right)l'm'+\alpha\Delta T\end{aligned} \tag{3-1}$$

Where,

$R(\sigma, \Delta T)$	= electrical resistance of a piezoresistor subjected to stress and temperature change
$R(0, 0)$	= reference resistance of a piezoresistor at zero load ($\sigma = 0$) at reference temperature ($\Delta T = 0$)
$\pi'_{\gamma\beta}$	= off-axis piezoresistive coefficients (γ, β equals 1,2,…6)
σ'_{β}	= stress in the off-axis coordinate system, β = 1,2,..,6
α	= Temperature coefficients of resistance (TCR)
ΔT	= Temperature change
l', m', n'	= direction cosines of the piezoresistor orientation with respect to the x'_1, x'_2, and x'_3 axes (off-axis)

In equation (3-1), the stresses are given in reduced index notation, where:

$$\sigma_1' = \sigma_{11}',\ \sigma_2' = \sigma_{22}',\ \sigma_3' = \sigma_{33}'$$
$$\sigma_4' = \sigma_{13}',\ \sigma_5' = \sigma_{23}',\ \sigma_6' = \sigma_{12}' \tag{3-2}$$

Silicon has a diamond structure with a face-centered cubic cell, which allows for simplification of the crystallographic piezoresistivity tensor to a reduced matrix defined by the three unique on-axis piezoresistive coefficients π_{11}, π_{12}, and π_{44} .

$$\left[\pi_{\alpha\beta}\right] = \begin{bmatrix} \pi_{11} & \pi_{12} & \pi_{12} & 0 & 0 & 0 \\ \pi_{12} & \pi_{11} & \pi_{12} & 0 & 0 & 0 \\ \pi_{12} & \pi_{12} & \pi_{11} & 0 & 0 & 0 \\ 0 & 0 & 0 & \pi_{44} & 0 & 0 \\ 0 & 0 & 0 & 0 & \pi_{44} & 0 \\ 0 & 0 & 0 & 0 & 0 & \pi_{44} \end{bmatrix} \tag{3-3}$$

Transforming the piezoresistive coefficients from the unprimed coordinates ($\pi_{\alpha\beta}'$) to the primed coordinates ($\pi_{\gamma\delta}$) can be done by:

$$\pi_{\alpha\beta}' = T_{\alpha\gamma}\pi_{\gamma\delta}T_{\delta\beta}^{-1} \tag{3-4}$$

Where the transformation matrix $T_{\alpha\gamma}$ is given by:

$$\left[T_{\alpha\beta}\right] = \begin{bmatrix} l_1^2 & m_1^2 & n_1^2 & 2l_1n_1 & 2m_1n_1 & 2l_1m_1 \\ l_2^2 & m_2^2 & n_2^2 & 2l_2n_2 & 2m_2n_2 & 2l_2m_2 \\ l_3^2 & m_3^2 & n_3^2 & 2l_3n_3 & 2m_3n_3 & 2l_3m_3 \\ l_1l_3 & m_1m_3 & n_1n_3 & l_1n_3 + l_3n_1 & m_1n_3 + m_3n_1 & l_1m_3 + l_3m_1 \\ l_2l_3 & m_2m_3 & n_2n_3 & l_2n_3 + l_3n_2 & m_2n_3 + m_3n_2 & l_2m_3 + l_3m_2 \\ l_1l_2 & m_1m_2 & n_1n_2 & l_1n_2 + l_2n_1 & m_1n_2 + m_2n_1 & l_1m_2 + l_2m_1 \end{bmatrix} \tag{3-5}$$

Where quantities l_i, m_i, n_i, i= 1, 2 and 3, are the direction cosines of the primed axes with respect to the unprimed axes. Also, the off-axis stress is related to the on-axis crystallographic stress by:

$$\sigma'_\alpha = T_{\alpha\beta}\sigma_\beta$$

Or

$$\begin{bmatrix} \sigma'_1 \\ \sigma'_2 \\ \sigma'_3 \\ \sigma'_4 \\ \sigma'_5 \\ \sigma'_6 \end{bmatrix} = \begin{bmatrix} l_1^2 & m_1^2 & n_1^2 & 2l_1n_1 & 2m_1n_1 & 2l_1m_1 \\ l_2^2 & m_2^2 & n_2^2 & 2l_2n_2 & 2m_2n_2 & 2l_2m_2 \\ l_3^2 & m_3^2 & n_3^2 & 2l_3n_3 & 2m_3n_3 & 2l_3m_3 \\ l_1l_3 & m_1m_3 & n_1n_3 & l_1n_3+l_3n_1 & m_1n_3+m_3n_1 & l_1m_3+l_3m_1 \\ l_2l_3 & m_2m_3 & n_2n_3 & l_2n_3+l_3n_2 & m_2n_3+m_3n_2 & l_2m_3+l_3m_2 \\ l_1l_2 & m_1m_2 & n_1n_2 & l_1n_2+l_2n_1 & m_1n_2+m_2n_1 & l_1m_2+l_2m_1 \end{bmatrix} \begin{bmatrix} \sigma_1 \\ \sigma_2 \\ \sigma_3 \\ \sigma_4 \\ \sigma_5 \\ \sigma_6 \end{bmatrix} \qquad (3\text{-}6)$$

If the off-axis coordinate system coincides with the on-axis coordinate system, the transformation matrix $T_{\alpha\beta}$ becomes a 6x6 identity matrix, which results in $\pi'_{\alpha\beta} = \pi_{\gamma\delta}$. Thus, applying this to equation (3-1) yields the following relation for the resistance change along the crystallographic directions:

$$\begin{aligned} \frac{\Delta R}{R} &= \left[\pi_{11}\sigma_{11} + \pi_{12}\left(\sigma_{22}+\sigma_{33}\right)\right]l^2 + \left[\pi_{11}\sigma_{22} + \pi_{12}\left(\sigma_{11}+\sigma_{33}\right)\right]m^2 \\ &+ \left[\pi_{11}\sigma_{33} + \pi_{12}\left(\sigma_{11}+\sigma_{22}\right)\right]n^2 \\ &+ 2\pi_{44}\left[\sigma_{12}lm + \sigma_{13}ln + \sigma_{23}mn\right] + \alpha\Delta T \end{aligned} \qquad (3\text{-}7)$$

Where, *l*, *m*, and *n* are the direction cosines of the arbitrary piezoresistive conductor with respect to the on-axis coordinate system. Equation (3-7) shows that the change in resistance of an arbitrarily oriented piezoresistive filament depends on the six stress components, the three piezoresistive coefficients, and temperature. To this end, developing a piezoresistive sensing rosette consisting of multi-elements with different orientations on a specific silicon plane determines the number of stress components that can be extracted.

3.1.2 Piezoresistive conductor along (001) and (111) Silicon Plane

The two most common single crystal silicon wafers are (001) and (111), thus the feasibility of utilizing a specific orientation to successfully develop a 3D stress sensing rosette is driven by these available orientations of silicon wafers.

For a piezoresistor oriented over (001) silicon plane, the $x_1 = [100]$ and $x_2 = [010]$ axes lie in the plane of the wafer, while the $x_3 = [001]$ is normal to the surface of the wafer. The general expression of the change in electrical resistance with respect to the on-axis coordinate system can be obtained from Equation (3-7) by setting $n = 0$, $l = \cos\theta$, and $m = \sin\theta$, which yields:

$$\begin{aligned}\frac{\Delta R}{R} &= \left(\pi_{11}\cos^2\theta + \pi_{12}\sin^2\theta\right)\sigma_{11} + \left(\pi_{12}\cos^2\theta + \pi_{11}\sin^2\theta\right)\sigma_{22} + \pi_{12}\sigma_{33} \\ &\quad + \pi_{44}\sin 2\theta\sigma_{12} + \alpha\Delta T\end{aligned} \tag{3-8}$$

Where θ is the angle between x_1'-axis and the piezoresistor orientation as shown in Figure 3-3. It is clearly seen that the out-of-plane shear stress components σ_{13} and σ_{23} have no influence on the resistance value of the sensing element, oriented over (001), as given in equation (3-8). This means that a rosette oriented over the (001) plane can, at most, extract only four components of the 3D stress tensor, namely the three in-plane components (σ_{11}, σ_{22}, and σ_{12}) and the out-of-plane normal component (σ_{33}).

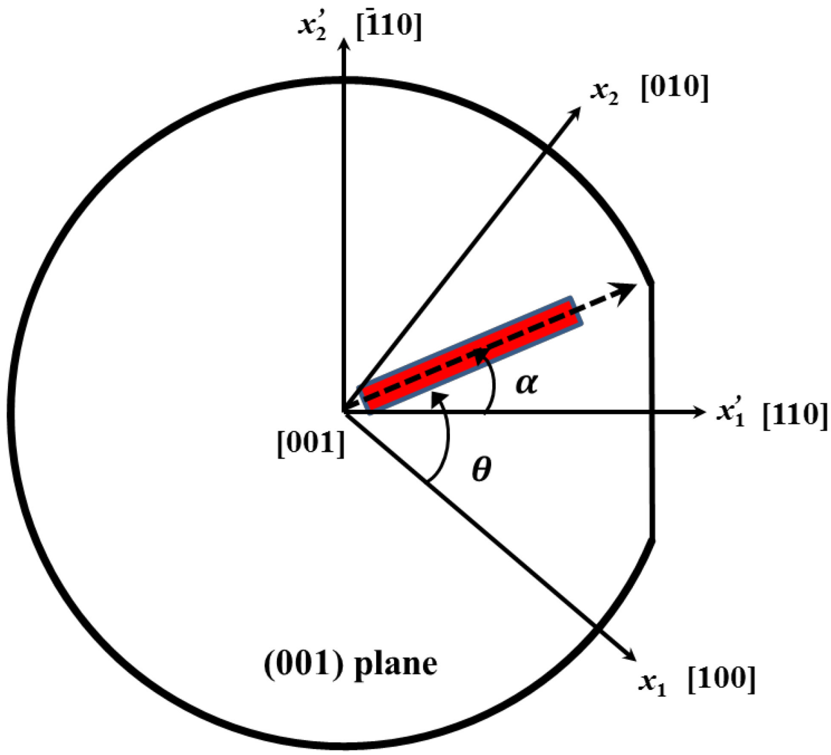

Figure 3-2 (001) silicon wafer with filament orientation

On the other hand, a resistor oriented over the (111), where the $x_1' = [\bar{1}10]$ and $x_2' = [\bar{1}\bar{1}2]$ axes lie in the plane of the wafer, while the $x_3' = [111]$ is normal to the surface of the wafer. To obtain the change in resistance expression along the (111) plane, the piezoresistive coefficients need to be evaluated with respect to the primed axes. The primed axes, of plane (111), are oriented relative to the crystallographic directions (unprimed axes) as shown in Figure 3-3, thus the direction cosines are given by:

$$\left[\beta_{ij}\right] = \cos(X_i', X_j) = \begin{bmatrix} l_1 & m_1 & n_1 \\ l_2 & m_2 & n_2 \\ l_3 & m_3 & n_3 \end{bmatrix} = \begin{bmatrix} -\frac{1}{\sqrt{2}} & \frac{1}{\sqrt{2}} & 0 \\ -\frac{1}{\sqrt{6}} & -\frac{1}{\sqrt{6}} & \frac{2}{\sqrt{6}} \\ \frac{1}{\sqrt{3}} & \frac{1}{\sqrt{3}} & \frac{1}{\sqrt{3}} \end{bmatrix} \tag{3-9}$$

The direction cosines in equation (3-9) are used to calculate the piezoresistive coefficients along the (111) plane is obtained through the matrix transformation in equation (3-4).

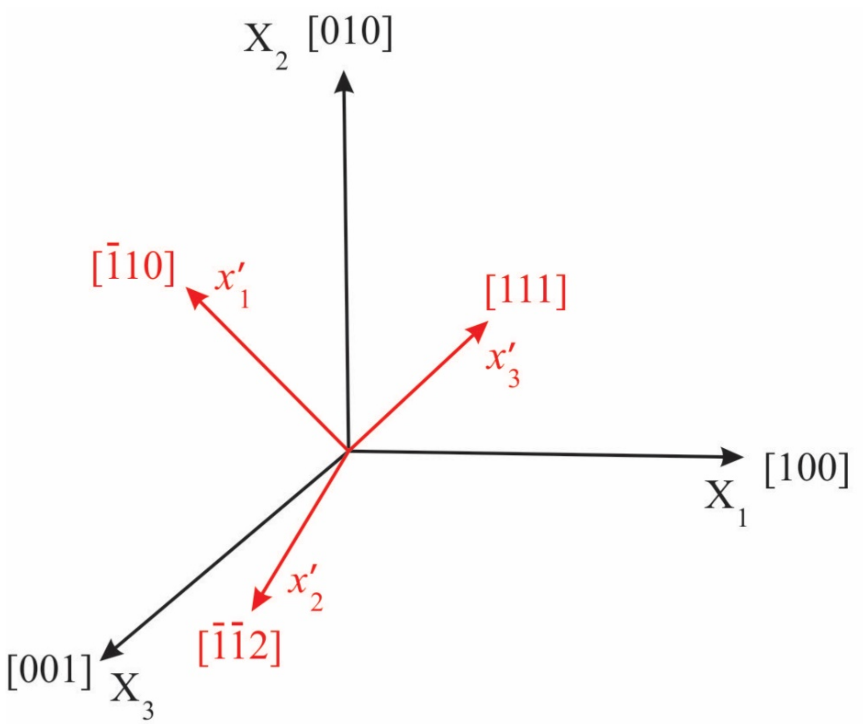

Figure 3-3 Orientation of (111) axes to the crystallographic coordinate system

The change in resistance expression of a piezoresistor oriented over (111) silicon plane can be derived from equation (3-1) by substituting the resulting piezoresistive coefficients from transformation as follows:

$$\begin{aligned}\frac{\Delta R}{R} &= (B_1\cos^2\phi + B_2\sin^2\phi)\sigma'_{11} + (B_2\cos^2\phi + B_1\sin^2\phi)\sigma'_{22} + B_3\sigma'_{33} \\ &+ 2\sqrt{2}(B_2 - B_3)(\cos^2\phi - \sin^2\phi)\sigma'_{23} + 2\sqrt{2}(B_2 - B_3)\sin(2\phi)\sigma'_{13} \\ &+ (B_1 - B_2)\sin(2\phi)\sigma'_{12} + \alpha\, T\end{aligned} \tag{3-10}$$

The stress components applied to the piezoresisor, in equation (3-10), are assumed to be aligned with the primed axes. Also, ϕ is the angle defining the orientation of the sensing element over the (111) plane as shown in Figure 3-4 and related to the direction cosines in equation (3-1) as $l' = \cos\phi$, $m' = \sin\phi$ and $n' = 0$. Moreover, B_i (i=1,2,3) is a function of the crystallographic piezoresistive coefficients as follows:

$$B_1 = \frac{\pi_{11} + \pi_{12} + \pi_{44}}{2}, \quad B_2 = \frac{\pi_{11} + 5\pi_{12} - \pi_{44}}{6}, \quad \text{and} \quad B_3 = \frac{\pi_{11} + 2\pi_{12} - \pi_{44}}{3} \tag{3-11}$$

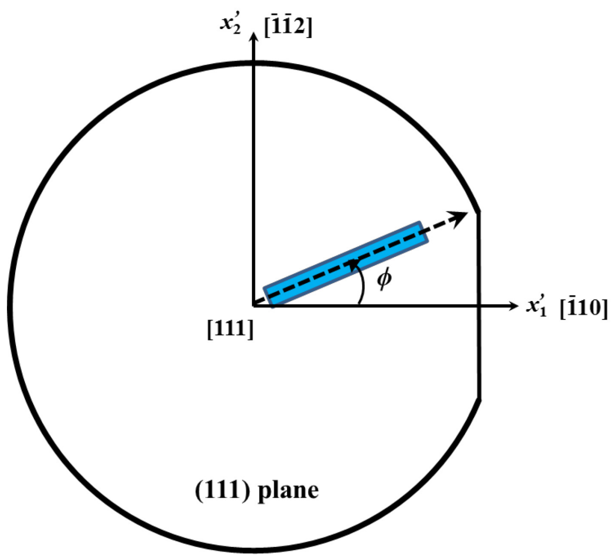

Figure 3-4 (111) silicon wafer with filament orientation

3.2 Three-dimensional (3D) Stress Sensing Rosette

3.2.1 The Eight-Element Rosette

As provided in the previous section, the resistance of a piezoresistor oriented over (111) silicon plane is related to the six components of the 3D stress tensor. Therefore, the orientation of a sufficient number of sensing elements on the (111) silicon plane creates a sensing rosette that can measure all the six stress components. The early attempt to develop a 3D stress sensing rosette of piezoresistive elements along the (111) silicon plane was first provided by Bittle and developed by Suhling *et al.* [2], [11]. This rosette consists of eight piezoresistors, with dual-polarity (n- and p-type), where the sensing elements are oriented at 45 degrees increments starting from R_1 at $[\bar{1}10]$ direction, as shown in Figure 3-5. According to their analysis, (111), dual-polarity rosette provides two sets of independent piezoresistive coefficients (π) and temperature coefficients of resistance (α) that can be utilized to form a set of independent linear equations to solve for the six stress components.

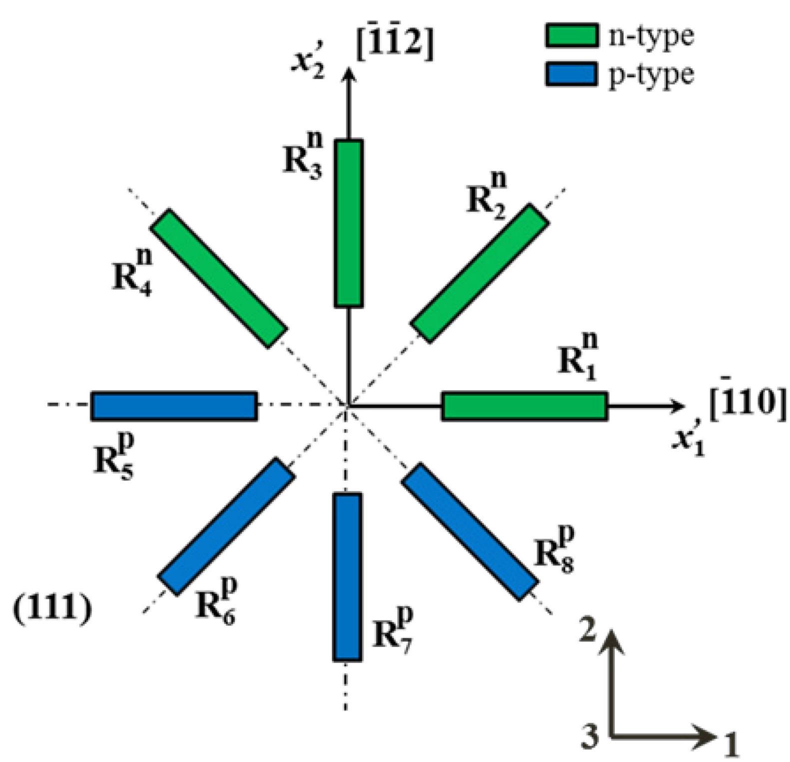

Figure 3-5 Eight-element dual polarity rosette along (111) silicon plane

Application of equation (3-10) along the directions of the eight-sensing elements and assuming the linearity of temperature coefficients of resistance (α) generates the following equations for the eight-element rosette [11], which relate the change in resistance with the applied stresses and temperature:

$$\left(\frac{\Delta R_1}{R_1}\right) = B_1^n\sigma'_{11} + B_2^n\sigma'_{22} + B_3^n\sigma'_{33} + 2\sqrt{2}(B_2^n - B_3^n)\sigma'_{23} + \alpha^n\Delta\mathrm{T}$$

$$\left(\frac{\Delta R_2}{R_2}\right) = \left(\frac{B_1^n + B_2^n}{2}\right)\sigma'_{11} + \left(\frac{B_1^n + B_2^n}{2}\right)\sigma'_{22} + B_3^n\sigma'_{33}$$
$$+2\sqrt{2}(B_2^n - B_3^n)\sigma'_{13} + (B_1^n - B_2^n)\sigma'_{12} + \alpha^n\Delta \mathrm{T}$$
$$\left(\frac{\Delta R_3}{R_3}\right) = B_2^n\sigma'_{11} + B_1^n\sigma'_{22} + B_3^n\sigma'_{33} - 2\sqrt{2}(B_2^n - B_3^n)\sigma'_{23} + \alpha^n\Delta \mathrm{T}$$

$$\left(\frac{\Delta R_4}{R_4}\right) = \left(\frac{B_1^n + B_2^n}{2}\right)\sigma'_{11} + \left(\frac{B_1^n + B_2^n}{2}\right)\sigma'_{22} + B_3^n\sigma'_{33}$$
$$-2\sqrt{2}(B_2^n - B_3^n)\sigma'_{13} - (B_1^n - B_2^n)\sigma'_{12} + \alpha^n\Delta \mathrm{T}$$
$$\left(\frac{\Delta R_5}{R_5}\right) = B_1^p\sigma'_{11} + B_2^p\sigma'_{22} + B_3^p\sigma'_{33} + 2\sqrt{2}(B_2^p - B_3^p)\sigma'_{23} + \alpha^p\Delta \mathrm{T}$$
$$\left(\frac{\Delta R_6}{R_6}\right) = \left(\frac{B_1^p + B_2^p}{2}\right)\sigma'_{11} + \left(\frac{B_1^p + B_2^p}{2}\right)\sigma'_{22} + B_3^p\sigma'_{33}$$
$$+2\sqrt{2}(B_2^p - B_3^p)\sigma'_{13} + (B_1^p - B_2^p)\sigma'_{12} + \alpha^p\Delta \mathrm{T}$$
$$\left(\frac{\Delta R_7}{R_7}\right) = B_2^p\sigma'_{11} + B_1^p\sigma'_{22} + B_3^p\sigma'_{33} - 2\sqrt{2}(B_2^p - B_3^p)\sigma'_{23} + \alpha^p\Delta \mathrm{T}$$
$$\left(\frac{\Delta R_8}{R_8}\right) = \left(\frac{B_1^p + B_2^p}{2}\right)\sigma'_{11} + \left(\frac{B_1^p + B_2^p}{2}\right)\sigma'_{22} + B_3^p\sigma'_{33} \qquad (3\text{-}12)$$
$$-2\sqrt{2}(B_2^p - B_3^p)\sigma'_{13} - (B_1^p - B_2^p)\sigma'_{12} + \alpha^p\Delta \mathrm{T}$$

Where, the superscripts n and p refer to the n- and p-type doping, respectively. Also, the stress components are assumed to be aligned with (111) plane directions. Through addition and subtraction of equations (3-11), the following stress equations are generated [11], that can be used to extract the six stress components**:**

$$\sigma'_{11} = \frac{\left(B_3^p - B_2^p\right)\left(\frac{\Delta R_1}{R_1} - \frac{\Delta R_3}{R_3}\right) - \left(B_3^n - B_2^n\right)\left(\frac{\Delta R_5}{R_5} - \frac{\Delta R_7}{R_7}\right)}{2\left[\left(B_2^p - B_1^p\right)B_3^n + \left(B_1^p - B_3^p\right)B_2^n + \left(B_3^p - B_2^p\right)B_1^n\right]}$$
$$+\frac{B_3^p\left[\frac{\Delta R_1}{R_1} + \frac{\Delta R_3}{R_3} - 2\alpha_1^n T\right] - B_3^n\left[\frac{\Delta R_5}{R_5} + \frac{\Delta R_7}{R_7} - 2\alpha_1^p T\right]}{2\left[\left(B_1^n + B_2^n\right)B_3^p - \left(B_1^p + B_2^p\right)B_3^n\right]}$$

$$\sigma'_{22} = -\frac{\left(B_3^p - B_2^p\right)\left(\frac{\Delta R_1}{R_1} - \frac{\Delta R_3}{R_3}\right) - \left(B_3^n - B_2^n\right)\left(\frac{\Delta R_5}{R_5} - \frac{\Delta R_7}{R_7}\right)}{2\left[\left(B_2^p - B_1^p\right)B_3^n + \left(B_1^p - B_3^p\right)B_2^n + \left(B_3^p - B_2^p\right)B_1^n\right]} + \frac{B_3^p\left[\frac{\Delta R_1}{R_1} + \frac{\Delta R_3}{R_3} - 2\alpha_1^n T\right] - B_3^n\left[\frac{\Delta R_5}{R_5} + \frac{\Delta R_7}{R_7} - 2\alpha_1^p T\right]}{2\left[\left(B_1^n + B_2^n\right)B_3^p - \left(B_1^p + B_2^p\right)B_3^n\right]}$$

$$\sigma'_{33} = \frac{-\left(B_1^p + B_2^p\right)\left[\frac{\Delta R_1}{R_1} + \frac{\Delta R_3}{R_3} - 2\alpha_1^n T\right] + \left(B_1^n + B_2^n\right)\left[\frac{\Delta R_5}{R_5} + \frac{\Delta R_7}{R_7} - 2\alpha_1^p T\right]}{2\left[\left(B_1^n + B_2^n\right)B_3^p - \left(B_1^p + B_2^p\right)B_3^n\right]}$$

$$\sigma'_{23} = \frac{\sqrt{2}}{8}\left[\frac{-\left(B_2^p - B_1^p\right)\left(\frac{\Delta R_1}{R_1} - \frac{\Delta R_3}{R_3}\right) + \left(B_2^n - B_1^n\right)\left(\frac{\Delta R_5}{R_5} - \frac{\Delta R_7}{R_7}\right)}{\left(B_2^p - B_1^p\right)B_3^n + \left(B_1^p - B_3^p\right)B_2^n + \left(B_3^p - B_2^p\right)B_1^n}\right]$$

$$\sigma'_{13} = \frac{\sqrt{2}}{8}\left[\frac{-\left(B_2^p - B_1^p\right)\left(\frac{\Delta R_2}{R_2} - \frac{\Delta R_4}{R_4}\right) + \left(B_2^n - B_1^n\right)\left(\frac{\Delta R_6}{R_6} - \frac{\Delta R_8}{R_8}\right)}{\left(B_2^p - B_1^p\right)B_3^n + \left(B_1^p - B_3^p\right)B_2^n + \left(B_3^p - B_2^p\right)B_1^n}\right]$$

$$\sigma'_{12} = \left[\frac{\left(B_3^p - B_2^p\right)\left(\frac{\Delta R_2}{R_2} - \frac{\Delta R_4}{R_4}\right) - \left(B_3^n - B_2^n\right)\left(\frac{\Delta R_6}{R_6} - \frac{\Delta R_8}{R_8}\right)}{2\left[\left(B_2^p - B_1^p\right)B_3^n + \left(B_1^p - B_3^p\right)B_2^n + \left(B_3^p - B_2^p\right)B_1^n\right]}\right] \tag{3-13}$$

As given by equation (3-13), the eight-element rosette is only capable of extracting 3 stresses with temperature-compensation, namely σ'_{12}, σ'_{13} and σ'_{23} which are the shear stress components applied on the sensing chip. While, the other 3 stress components, the normal stress components σ'_{11}, σ'_{22}, and σ'_{33}, are with temperature-dependence. Therefore, an additional temperature measurement is needed to accurately capture accurately the normal stress components using the eight-element rosette.

3.2.2 The Ten-Element Rosette

The capability of having a rosette with two groups of sensing elements (not necessarily dual-polarity) with independent piezoresistive coefficients (PRCs) and temperature coefficient of resistance (TCR), the partially temperature-compensated six stress components can be extracted. Gharib [13], [14] found that a single polarity (n-type) silicon rosette made up of groups of sensing elements with different doping concentration levels can result in having linearly independent sets of PRCs and TCR. They benefit from the independence of impurity concentration for the n-type shear PRC (π_{44}), unlike the other PRCs π_{11} and π_{12}, which are dependent on the doping level.

Therefore, they successfully developed a single polarity (n-type) ten-element sensing rosette over the (111) wafer plane as shown in Figure 3-6. The developed rosette is divided into three groups (a, b, and c), where each group has linearly independent PRCs and TCR. Eight of these elements, forming groups a and b, are used to solve for the four temperature-compensated stresses similar to the dual-polarity rosette of Suhling et al. The extra two sensing elements forming the third group c is used to solve for the remaining temperature-compensated stress components. The single polarity sensing rosette (n-type) provides simpler micro-fabrication process compared to a dual-polarity (n-type and p-type) since there is no need for the p-type doping equipment. Also, it has the potential of fabricating a rosette with a smaller footprint due to the absence of the n-well [59].

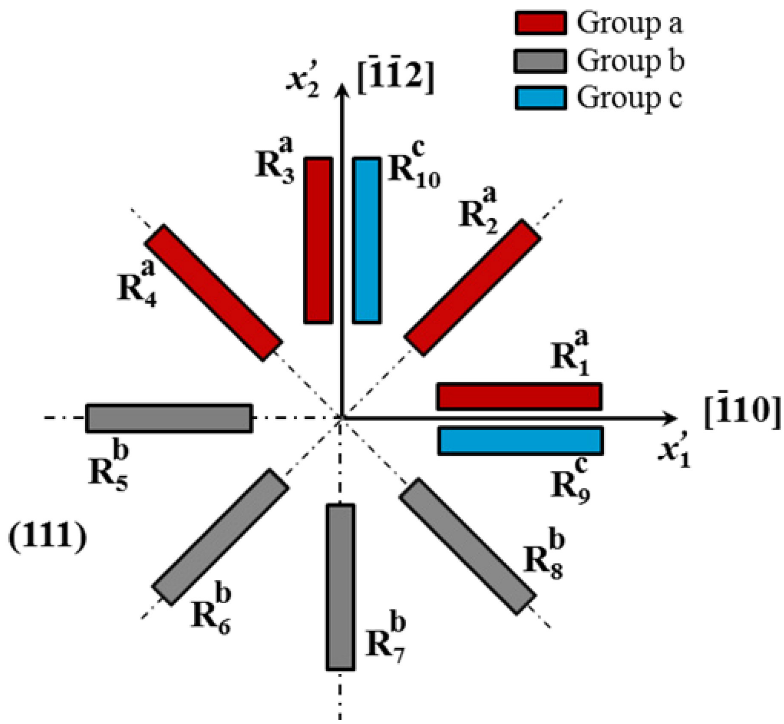

Figure 3-6 Ten-element single polarity rosette on (111) silicon

Application of equation (3-10) to the 10-element rosette provides ten equations describing the change in resistance of each sensing element with the applied stress and temperature:

$$\left(\frac{\Delta R_1}{R_1}\right) = B_1^a\sigma'_{11} + B_2^a\sigma'_{22} + B_3^a\sigma'_{33} + 2\sqrt{2}(B_2^a - B_3^a)\sigma'_{23} + \alpha^a\Delta T$$

$$\left(\frac{\Delta R_2}{R_2}\right) = \left(\frac{B_1^a + B_2^a}{2}\right)\sigma'_{11} + \left(\frac{B_1^a + B_2^a}{2}\right)\sigma'_{22} + B_3^a\sigma'_{33} + 2\sqrt{2}(B_2^a - B_3^a)\sigma'_{13} + (B_1^a - B_2^a)\sigma'_{12} + \alpha^a\Delta T$$

$$\left(\frac{\Delta R_3}{R_3}\right) = B_2^a\sigma'_{11} + B_1^a\sigma'_{22} + B_3^a\sigma'_{33} - 2\sqrt{2}(B_2^a - B_3^a)\sigma'_{23} + \alpha^a\Delta T$$

$$\left(\frac{\Delta R_4}{R_4}\right) = \left(\frac{B_1^a + B_2^a}{2}\right)\sigma'_{11} + \left(\frac{B_1^a + B_2^a}{2}\right)\sigma'_{22} + B_3^a\sigma'_{33} - 2\sqrt{2}(B_2^a - B_3^a)\sigma'_{13} - (B_1^a - B_2^a)\sigma'_{12} + \alpha^a\Delta T$$

$$\left(\frac{\Delta R_5}{R_5}\right) = B_1^b\sigma'_{11} + B_2^b\sigma'_{22} + B_3^b\sigma'_{33} + 2\sqrt{2}(B_2^b - B_3^b)\sigma'_{23} + \alpha^b\Delta T$$

$$\left(\frac{\Delta R_6}{R_6}\right)=\left(\frac{B_1^b+B_2^b}{2}\right)\sigma'_{11}+\left(\frac{B_1^b+B_2^b}{2}\right)\sigma'_{22}+B_3^b\sigma'_{33}+2\sqrt{2}(B_2^b-B_3^b)\sigma'_{13}+(B_1^b-B_2^b)\sigma'_{12}+\alpha^b\Delta T$$

$$\left(\frac{\Delta R_7}{R_7}\right)=B_2^b\sigma'_{11}+B_1^b\sigma'_{22}+B_3^b\sigma'_{33}-2\sqrt{2}(B_2^b-B_3^b)\sigma'_{23}+\alpha^b\Delta T$$

$$\left(\frac{\Delta R_8}{R_8}\right)=\left(\frac{B_1^b+B_2^b}{2}\right)\sigma'_{11}+\left(\frac{B_1^b+B_2^b}{2}\right)\sigma'_{22}+B_3^b\sigma'_{33}-2\sqrt{2}(B_2^b-B_3^b)\sigma'_{13}-(B_1^b-B_2^b)\sigma'_{12}+\alpha^b\Delta T$$

$$\left(\frac{\Delta R_9}{R_9}\right)=B_1^c\sigma'_{11}+B_2^c\sigma'_{22}+B_3^c\sigma'_{33}+2\sqrt{2}(B_2^c-B_3^c)\sigma'_{23}+\alpha^c\Delta T$$

$$\left(\frac{\Delta R_{10}}{R_{10}}\right)=B_2^c\sigma'_{11}+B_1^c\sigma'_{22}+B_3^c\sigma'_{33}-2\sqrt{2}(B_2^c-B_3^c)\sigma'_{23}+\alpha^c\Delta T \qquad (3\text{-}14)$$

Where the superscripts a, b, and c indicate the different groups of elements. Moreover, the stress components are assumed to be aligned with (111) plane directions. Using addition and subtraction of equations (3-14), the following stress equations are obtained, which can be used to calculate all the six stress components and the temperature:

$$\sigma'_{11}=\frac{1}{2D_2}\left[\left(B_3^c\alpha^b-B_3^b\alpha^c\right)\left(\frac{\Delta R_1}{R_1}+\frac{\Delta R_3}{R_3}\right)+\left(B_3^a\alpha^c-B_3^c\alpha^a\right)\left(\frac{\Delta R_5}{R_5}+\frac{\Delta R_7}{R_7}\right)\right.$$
$$\left.+\left(B_3^b\alpha^a-B_3^a\alpha^b\right)\left(\frac{\Delta R_9}{R_9}+\frac{\Delta R_{10}}{R_{10}}\right)\right]$$
$$+\frac{1}{2D_1}\left[\left(B_2^b-B_3^b\right)\left(\frac{\Delta R_1}{R_1}-\frac{\Delta R_3}{R_3}\right)-\left(B_2^a-B_3^a\right)\left(\frac{\Delta R_5}{R_5}-\frac{\Delta R_7}{R_7}\right)\right]$$

$$\sigma'_{22}=\frac{1}{2D_2}\left[\left(B_3^c\alpha^b-B_3^b\alpha^c\right)\left(\frac{\Delta R_1}{R_1}+\frac{\Delta R_3}{R_3}\right)+\left(B_3^a\alpha^c-B_3^c\alpha^a\right)\left(\frac{\Delta R_5}{R_5}+\frac{\Delta R_7}{R_7}\right)\right.$$
$$\left.+\left(B_3^b\alpha^a-B_3^a\alpha^b\right)\left(\frac{\Delta R_9}{R_9}+\frac{\Delta R_{10}}{R_{10}}\right)\right]$$
$$-\frac{1}{2D_1}\left[\left(B_2^b-B_3^b\right)\left(\frac{\Delta R_1}{R_1}-\frac{\Delta R_3}{R_3}\right)-\left(B_2^a-B_3^a\right)\left(\frac{\Delta R_5}{R_5}-\frac{\Delta R_7}{R_7}\right)\right]$$

$$\left(\sigma'_{11}-\sigma'_{22}\right)=\frac{1}{D_1}\left[\left(B_2^b-B_3^b\right)\left(\frac{\Delta R_1}{R_1}-\frac{\Delta R_3}{R_3}\right)-\left(B_2^a-B_3^a\right)\left(\frac{\Delta R_5}{R_5}-\frac{\Delta R_7}{R_7}\right)\right]$$

$$\begin{aligned}\sigma'_{33}=\frac{1}{2D_2}\Bigg[&\left((B_1^b+B_2^b)\alpha^c-(B_1^c+B_2^c)\alpha^b\right)\left(\frac{\Delta R_1}{R_1}+\frac{\Delta R_3}{R_3}\right)\\&+\left((B_1^c+B_2^c)\alpha^a-(B_1^a+B_2^a)\alpha^c\right)\left(\frac{\Delta R_5}{R_5}+\frac{\Delta R_7}{R_7}\right)\\&+\left((B_1^a+B_2^a)\alpha^b-(B_1^b+B_2^b)\alpha^a\right)\left(\frac{\Delta R_9}{R_9}+\frac{\Delta R_{10}}{R_{10}}\right)\Bigg]\end{aligned}$$

$$\sigma'_{23}=\frac{1}{D_1}\left[-\frac{\left(B_1^b-B_2^b\right)}{4\sqrt{2}}\left(\frac{\Delta R_1}{R_1}-\frac{\Delta R_3}{R_3}\right)+\frac{\left(B_1^a-B_2^a\right)}{4\sqrt{2}}\left(\frac{\Delta R_5}{R_5}-\frac{\Delta R_7}{R_7}\right)\right]$$

$$\sigma'_{13}=\frac{1}{D_1}\left[\frac{-\left(B_1^b-B_2^b\right)}{4\sqrt{2}}\left(\frac{\Delta R_2}{R_2}-\frac{\Delta R_4}{R_4}\right)+\frac{\left(B_1^a-B_2^a\right)}{4\sqrt{2}}\left(\frac{\Delta R_6}{R_6}-\frac{\Delta R_8}{R_8}\right)\right]$$

$$\sigma'_{12}=\frac{1}{D_1}\left[\frac{\left(B_2^b-B_3^b\right)}{2}\left(\frac{\Delta R_2}{R_2}-\frac{\Delta R_4}{R_4}\right)-\frac{\left(B_2^a-B_3^a\right)}{2}\left(\frac{\Delta R_6}{R_6}-\frac{\Delta R_8}{R_8}\right)\right]$$

$$\begin{aligned}\Delta T=\frac{1}{2D_2}\Bigg[&\left((B_1^c+B_2^c)B_3^b-(B_1^b+B_2^b)B_3^c\right)\left(\frac{\Delta R_1}{R_1}+\frac{\Delta R_3}{R_3}\right)\\&+\left((B_1^a+B_2^a)B_3^c-(B_1^c+B_2^c)B_3^a\right)\left(\frac{\Delta R_5}{R_5}+\frac{\Delta R_7}{R_7}\right)\\&+\left((B_1^b+B_2^b)B_3^a-(B_1^a+B_2^a)B_3^b\right)\left(\frac{\Delta R_9}{R_9}+\frac{\Delta R_{10}}{R_{10}}\right)\Bigg]\end{aligned}\tag{3-15}$$

Where,

$$D_1=B_1^a\left(B_2^b-B_3^b\right)+B_2^a\left(B_3^b-B_1^b\right)+B_3^a\left(B_1^b-B_2^b\right)\tag{3-16}$$

$$\begin{aligned}D_2=&B_3^a\left[(B_1^b+B_2^b)\alpha^c-(B_1^c+B_2^c)\alpha^b\right]+B_3^b\left[(B_1^c+B_2^c)\alpha^a-(B_1^a+B_2^a)\alpha^c\right]\\&+B_3^c\left[(B_1^a+B_2^a)\alpha^b-(B_1^b+B_2^b)\alpha^a\right]\end{aligned}\tag{3-17}$$

3.3 The New Developed Stress Sensing Rosette

In this section, a developed n-type piezoresistive 3D stress sensor with full temperature compensation is presented. The proposed sensing rosette benefits from the unique behavior of shear piezoresistive coefficient (π_{44}) of n-Si to construct a piezoresistive stress sensing rosette over (111) silicon plane that is capable of extracting 3D stress components. Moreover, a new temperature transducer is integrated into the stress sensing rosette to capture the temperature changes in close proximity to stress sensing rosette for compensation.

3.3.1 Stress Sensing Rosette

Since the eight-element rosette provides, in general, reduced equation forms compared to the ten-element rosette over (111), thus less process noise which results in more accurate stress measurements [97]. On the other hand, the single polarity rosette provides a simpler microfabrication process than the dual polarity rosette. To this end, the proposed stress rosette is made up of single-polarity (n-type) eight piezoresistive elements oriented over (111) with 45° increments, as shown in Figure 3-7. These piezoresistors are divided into two groups, *a* and *b*, with two different doping concentration levels which provide linearly independent PRCs and TCR. These sensing elements are used to solve for the six stress components.

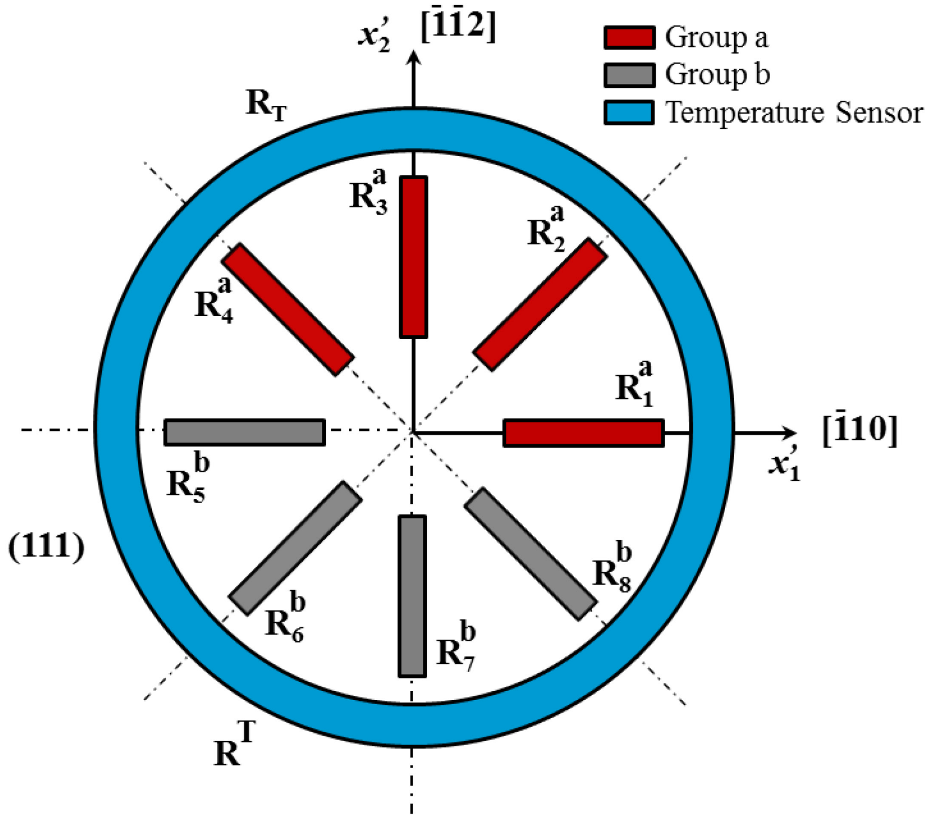

Figure 3-7 Eight-element n-type rosette with temperature compensation along (111) silicon plane

Like the eight-element dual polarity rosette, the stress equations of the proposed stress rosette are given in equation (3-18), but the superscripts *n* and *p*, which indicate the n-type and p-type, are replaced by superscripts *a* and *b*, which refer to the different impurity concentrations. Since the eight-element rosette, in general, extract normal stress components (σ'_{11}, σ'_{22}, and σ'_{33}) with temperature-dependence, an accurate independent measurement of the temperature is needed.

.

$$\sigma'_{11}=\frac{\left(B_3^b-B_2^b\right)\left(\frac{\Delta R_1}{R_1}-\frac{\Delta R_3}{R_3}\right)-\left(B_3^a-B_2^a\right)\left(\frac{\Delta R_5}{R_5}-\frac{\Delta R_7}{R_7}\right)}{2\left[\left(B_2^b-B_1^b\right)B_3^a+\left(B_1^b-B_3^b\right)B_2^a+\left(B_3^b-B_2^b\right)B_1^a\right]}$$

$$+\frac{B_3^b\left[\frac{\Delta R_1}{R_1}+\frac{\Delta R_3}{R_3}-2\alpha_1^a\Delta T\right]-B_3^a\left[\frac{\Delta R_5}{R_5}+\frac{\Delta R_7}{R_7}-2\alpha_1^b\Delta T\right]}{2\left[\left(B_1^a+B_2^a\right)B_3^b-\left(B_1^b+B_2^b\right)B_3^a\right]}$$

$$\sigma'_{22}=-\frac{\left(B_3^b-B_2^b\right)\left(\frac{\Delta R_1}{R_1}-\frac{\Delta R_3}{R_3}\right)-\left(B_3^a-B_2^a\right)\left(\frac{\Delta R_5}{R_5}-\frac{\Delta R_7}{R_7}\right)}{2\left[\left(B_2^b-B_1^b\right)B_3^a+\left(B_1^b-B_3^b\right)B_2^a+\left(B_3^b-B_2^b\right)B_1^a\right]}$$

$$+\frac{B_3^b\left[\frac{\Delta R_1}{R_1}+\frac{\Delta R_3}{R_3}-2\alpha_1^a\Delta T\right]-B_3^a\left[\frac{\Delta R_5}{R_5}+\frac{\Delta R_7}{R_7}-2\alpha_1^b\Delta T\right]}{2\left[\left(B_1^a+B_2^a\right)B_3^b-\left(B_1^b+B_2^b\right)B_3^a\right]}$$

$$\sigma'_{33}=\frac{-\left(B_1^b+B_2^b\right)\left[\frac{\Delta R_1}{R_1}+\frac{\Delta R_3}{R_3}-2\alpha_1^a\Delta T\right]+\left(B_1^a+B_2^a\right)\left[\frac{\Delta R_5}{R_5}+\frac{\Delta R_7}{R_7}-2\alpha_1^b\Delta T\right]}{2\left[\left(B_1^a+B_2^a\right)B_3^b-\left(B_1^b+B_2^b\right)B_3^a\right]}$$

$$\sigma'_{23}=\frac{\sqrt{2}}{8}\left[\frac{-\left(B_2^b-B_1^b\right)\left(\frac{\Delta R_1}{R_1}-\frac{\Delta R_3}{R_3}\right)+\left(B_2^a-B_1^a\right)\left(\frac{\Delta R_5}{R_5}-\frac{\Delta R_7}{R_7}\right)}{\left(B_2^b-B_1^b\right)B_3^a+\left(B_1^b-B_3^b\right)B_2^a+\left(B_3^b-B_2^b\right)B_1^a}\right]$$

$$\sigma'_{13}=\frac{\sqrt{2}}{8}\left[\frac{-\left(B_2^b-B_1^b\right)\left(\frac{\Delta R_2}{R_2}-\frac{\Delta R_4}{R_4}\right)+\left(B_2^a-B_1^a\right)\left(\frac{\Delta R_6}{R_6}-\frac{\Delta R_8}{R_8}\right)}{\left(B_2^b-B_1^b\right)B_3^a+\left(B_1^b-B_3^b\right)B_2^a+\left(B_3^b-B_2^b\right)B_1^a}\right]$$

$$\sigma'_{12}=\left[\frac{\left(B_3^b-B_2^b\right)\left(\frac{\Delta R_2}{R_2}-\frac{\Delta R_4}{R_4}\right)-\left(B_3^a-B_2^a\right)\left(\frac{\Delta R_6}{R_6}-\frac{\Delta R_8}{R_8}\right)}{2\left[\left(B_2^b-B_1^b\right)B_3^a+\left(B_1^b-B_3^b\right)B_2^a+\left(B_3^b-B_2^b\right)B_1^a\right]}\right] \tag{3-18}$$

In this research, a novel temperature transducer using full-circular n-type piezoresistor over (111) is proposed to be integrated into the stress rosette for temperature compensation. The principle of operation of the proposed temperature compensation technique is presented in the next section.

3.3.2 Temperature Sensor

In this study, the n-type full circular piezoresistor over (111) silicon plane is found to have near-zero response under 3D state of stress and its resistance is only affected by the temperature changes. In the next sections, the principle of operation and analytical verification of the new temperature sensor are introduced.

3.3.2.1 Principal of operation

To evaluate the total resistance of a circular piezoresistor oriented over (111) silicon plane, shown in Figure 3-8, the resistance of an infinitesimally small portion of the piezoresistor needs first to be calculated. The piezoresistive effect in the principal crystallographic directions of silicon can be described by:

$$\begin{pmatrix} \rho_1 \\ \rho_2 \\ \rho_3 \\ \rho_4 \\ \rho_5 \\ \rho_6 \end{pmatrix} = \rho_0 \begin{pmatrix} 1 \\ 1 \\ 1 \\ 0 \\ 0 \\ 0 \end{pmatrix} + \rho_0 \begin{pmatrix} \pi_{11} & \pi_{12} & \pi_{12} & 0 & 0 & 0 \\ \pi_{12} & \pi_{11} & \pi_{12} & 0 & 0 & 0 \\ \pi_{12} & \pi_{12} & \pi_{11} & 0 & 0 & 0 \\ 0 & 0 & 0 & \pi_{44} & 0 & 0 \\ 0 & 0 & 0 & 0 & \pi_{44} & 0 \\ 0 & 0 & 0 & 0 & 0 & \pi_{44} \end{pmatrix} \begin{pmatrix} \sigma_1 \\ \sigma_2 \\ \sigma_3 \\ \sigma_4 \\ \sigma_5 \\ \sigma_6 \end{pmatrix} \quad (3\text{-}19)$$

Where ρ_i and σ_i represent the second-order resistivity and stress tensors, respectively, written in column vector forms, while ρ_0 represents the stress-free resistance.

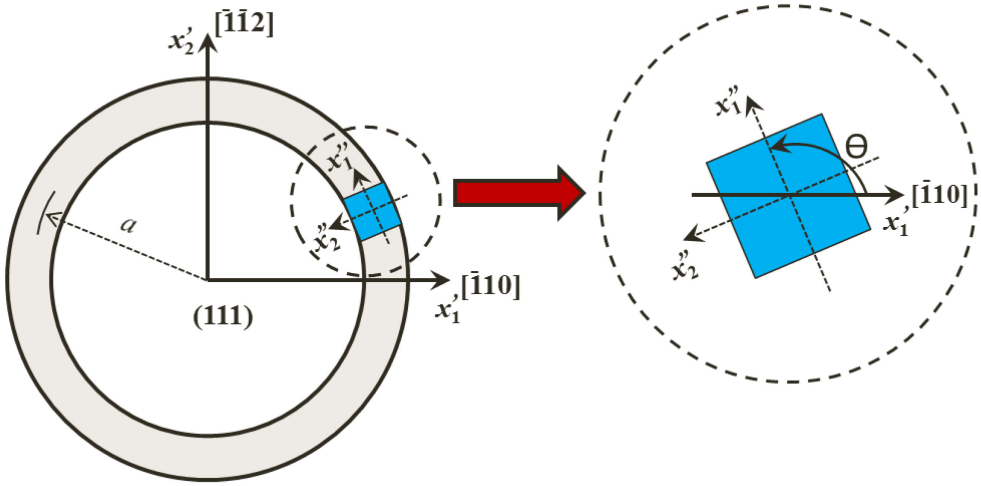

Figure 3-8 Circular n-type piezoresistor over (111) silicon plane.

The resistance of an infinitesimally small portion of the piezoresistor, shown in Figure 3-8, along the x_1'' axis (direction of integration path) over (111) plane is calculated as follows:

$$dR = \rho_1'' \frac{1}{A} ds = \rho_1'' \frac{a}{A} d\theta \tag{3-20}$$

Where ρ_1'' is a component of the resistivity tensor representing the resistivity along the x_1'' axis. While a is the mean radius of the resistor, A is the cross-section area of the resistor and Θ is the angle between the infinitesimal resistor element and the crystallographic direction $[\bar{1}10]$. Integrating dR yields the total resistance of the circular piezoresistor yields:

$$R = \int_0^{2\pi} \rho_1'' \frac{1}{A} ds = \frac{a}{A} \int_0^{2\pi} \rho_1'' d\theta \tag{3-21}$$

To calculate the integral in equation (3-21), the PRCs and stress components need to be evaluated in the resistor coordinate system x_1'' - x_2''. Transforming the PRCs from the silicon crystallographic coordinate system to (111) silicon plane directions can be done using equations (3-4) and (3-5).

The direction cosines in equation (3-9) are used first to transform the piezoresistive coefficients from the silicon crystallographic coordinate system to the coordinate system of (111) plane. Then another transformation is performed from the coordinate system of (111) plane to the resistor coordinate system $x_1'' - x_2''$ using the following direction cosines:

$$\left[\gamma_{ij}\right] = \cos(X_i'', X_j') = \begin{bmatrix} l_1 & m_1 & n_1 \\ l_2 & m_2 & n_2 \\ l_3 & m_3 & n_3 \end{bmatrix} = \begin{pmatrix} \cos\theta & \sin\theta & 0 \\ -\sin\theta & \cos\theta & 0 \\ 0 & 0 & 1 \end{pmatrix} \tag{3-22}$$

The stress components applied to the resistor are assumed to be in the coordinate system of (111) plane, thus a transformation from the stress coordinate system to the resistor coordinate system is performed using equation (3-6) and direction cosines in equation (3-22). Substituting the transformed PRCs and stress components into equation (3-21), and then performing the integration, result in:

$$\frac{\Delta R}{R_0} = \frac{R - R_0}{R_0} = \frac{(\pi_{11} + 2\pi_{12})}{3}\left(\sigma_{11}' + \sigma_{22}' + \sigma_{33}'\right) + \frac{\pi_{44}}{6}(\sigma_{11}' + \sigma_{22}' - 2\sigma_{33}') \tag{3-23}$$

Where $R_0 = \rho_0 \frac{2\pi a}{A}$ is the stress-free resistance of the annulus piezoresistor. If the full-circular piezoresistor is also subjected to temperature changes, the electrical resistance will be:

$$\frac{\Delta R}{R_0} = \frac{(\pi_{11} + 2\pi_{12})}{3}\left(\sigma_{11}' + \sigma_{22}' + \sigma_{33}'\right) + \frac{\pi_{44}}{6}(\sigma_{11}' + \sigma_{22}' - 2\sigma_{33}') + \alpha\Delta T \tag{3-24}$$

Where α is the TCR and ΔT is the change in temperature. For n-type silicon, the relationship between π_{11} and π_{12} is approximately given by $\pi_{11} + 2\pi_{12} \approx 0$ as confirmed experimentally by Tufte *et al.* [53]. In addition, π_{44} was found experimentally to have a small value compared with other coefficients π_{11} and π_{12} [98].

Therefore, the first term and second term in equation (3-24) can be ignored, which results in:

$$\frac{\Delta R}{R_0} \cong \alpha \Delta T \tag{3-25}$$

To this end, the full-circular n-type piezoresistor over (111) silicon plane is stress-insensitive and its resistance is only affected by the temperature changes. This allows it to be placed in the vicinity of stress-sensitive elements, as temperature transducer, to capture the local temperature changes for compensation.

3.3.3 Stress Insensitivity of Temperature Sensor

To verify the insensitivity of the circular piezoresistor over (111) silicon plane to the applied stress, a numerical analysis was carried out to investigate the piezoresistive sensitivity (S) of the full-circular piezoresistor. The piezoresistive stress sensitivity (S) is given by:

$$S = \frac{\partial(\Delta R / R_0)}{\partial \sigma} \tag{3-26}$$

In this analysis, S was evaluated for both full-circular piezoresistor and straight piezoresistor over (111) silicon chip subjected to uniaxial stress. As shown in Figure 3-9 and Figure 3-10, two different loads, longitudinal and transverse uniaxial stress, were applied to the silicon chip. A MATLAB code was developed to calculate S over a range of concentrations from $1\text{x}10^{17}$ to $1\text{x}10^{20}$ cm^{-3}. This analysis is based on the analytical values of π_{11} and π_{12} for n-type silicon given by Kanda [51] and the experimental value of π_{44} for n-type silicon given by Tufte *et al*. [53]. In addition, the accuracy of the circular piezoresistor to capture the change in temperature at the sensing chip was investigated. We studied the effect of the doping concentration of the circular piezoresitor on the accuracy of the temperature sensor (full-circular piezoresistor). A MATLAB code was developed to evaluate the accuracy of the temperature sensor over a range of concentrations from $1x10^{17}$ to $1x10^{20}$ cm^{-3}. The sensing chip was assumed to be subjected to uniaxial stress up to 60 MPa at different temperatures from 0 °C to 50 °C.

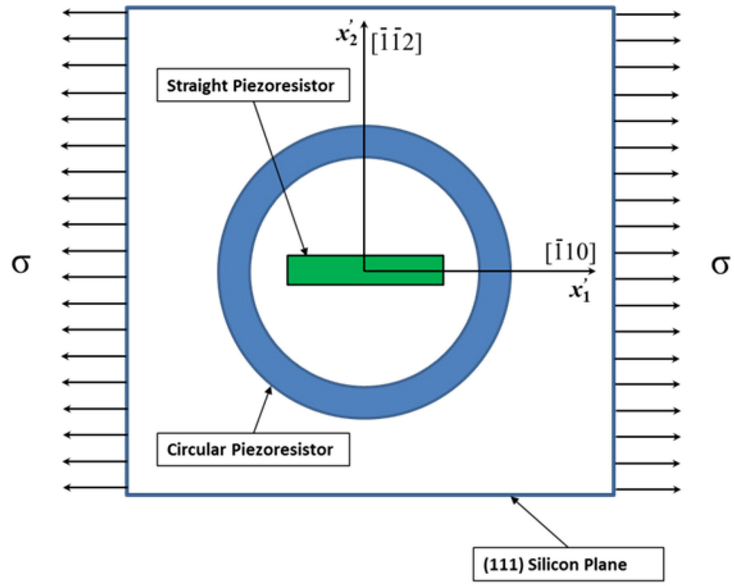

Figure 3-9 Circular and straight piezoresistor over (111) silicon subjected to longitudinal uniaxial stress

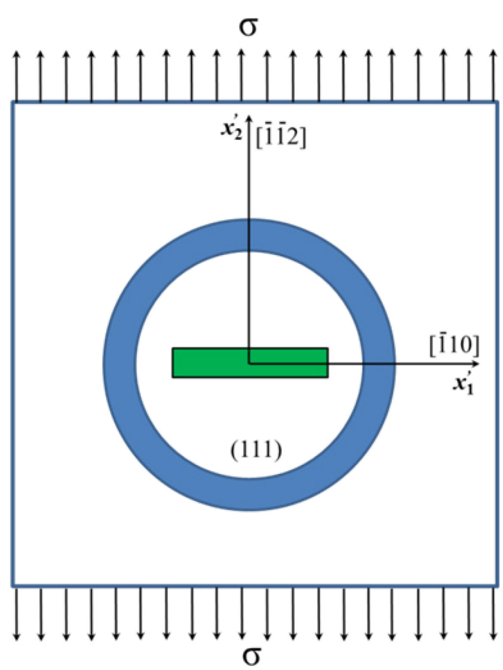

Figure 3-10 Circular and straight piezoresistor over (111) silicon subjected to transverse uniaxial stress

The evaluation of piezoresistive sensitivity (S) to longitudinal and transverse uniaxial stress at different concentrations for both the circular and straight piezoresistors over (111) silicon plane is shown in Figure 3-11 and Figure 3-12. It is clearly seen that the piezoresitive stress sensitivity of straight piezoresistor is much higher than of the circular piezoresistor, specifically, at lower concentrations. As we can see, at low concentrations (1x 10^{17} to 1x10^{18} cm^{-3}), the S value of straight piezoresistor is 50 times larger than of the circular piezoresistor. The results of this analysis confirm that the circular piezoresistor over (111) silicon plane is stress-insensitive compared with the straight piezoresistor on the same plane.

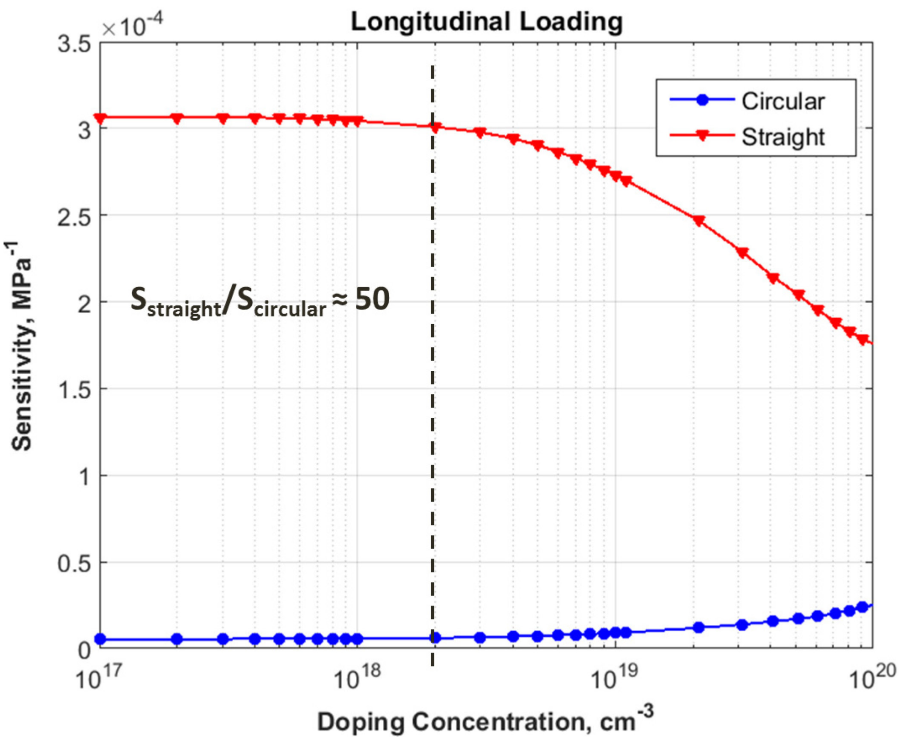

Figure 3-11 Piezoresistive sensitivity (S) to longitudinal uniaxial stress

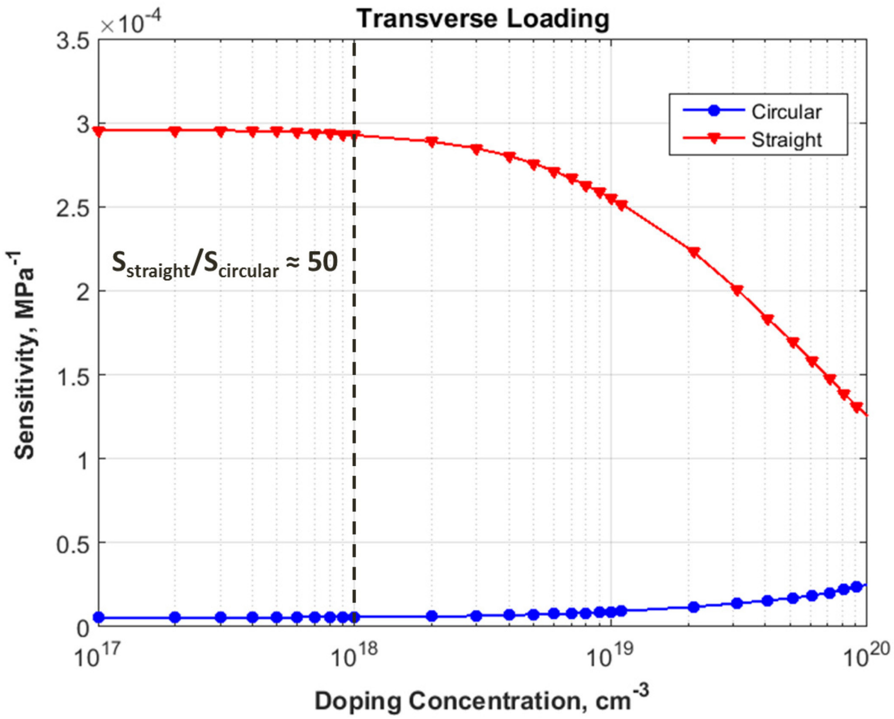

Figure 3-12 Piezoresistive sensitivity (*S*) to transverse uniaxial stress

In this numerical analysis, the accuracy of the temperature sensor, to detect the temperature changes within the sensing chip, was also evaluated while it is subjected to both in-plane and out-of-plane norml stresses. The error resulted from ignoring the effect of the applied stress on the electrical resistance of the circular piezoresistor was calculated using equation (3-27), where ΔT_{exact} and $\Delta T_{approx.}$ are calculated from equations (3-24) and (3-25), respectively. This analysis was carried out over over a range of the doping concentration from 1x10^{17} to 1x10^{20} cm^{-3}.

$$Error = \Delta T_{approx.} - \Delta T_{exact} \tag{3-27}$$

As shown in Figure 3-13, the accuracy of the temperature sensor depends on the impurity concentration. It is clearly seen that, at low concentrations (up to 10^{18} cm^{-3}), circular piezoresistor can accurately capture the change in temperature that occurs at the sensing chip. As maximum absolute error of ±0.3 °C can be obtained with in-plane normal stress application up to 60 MPa at different temperatures from 0 °C to 50 °C. At high concentration levels (above $2x10^{19}$ cm^{-3}), the temperature sensor is still capable of extracting the temperature change with high accuracy (maximum absolute error of about ±0.8 °C) for applied stress up to 60 MPa. On the other side, poor accuracy (absolute error as large as ±3.8 °C) can be obtained over the range of concentrations from $3x10^{18}$ to $2x10^{19}$ cm^{-3} due to the low values of TCR over this range [99]. Therefore, it is important to avoid that range of concentrations while fabricating the temperature sensor.

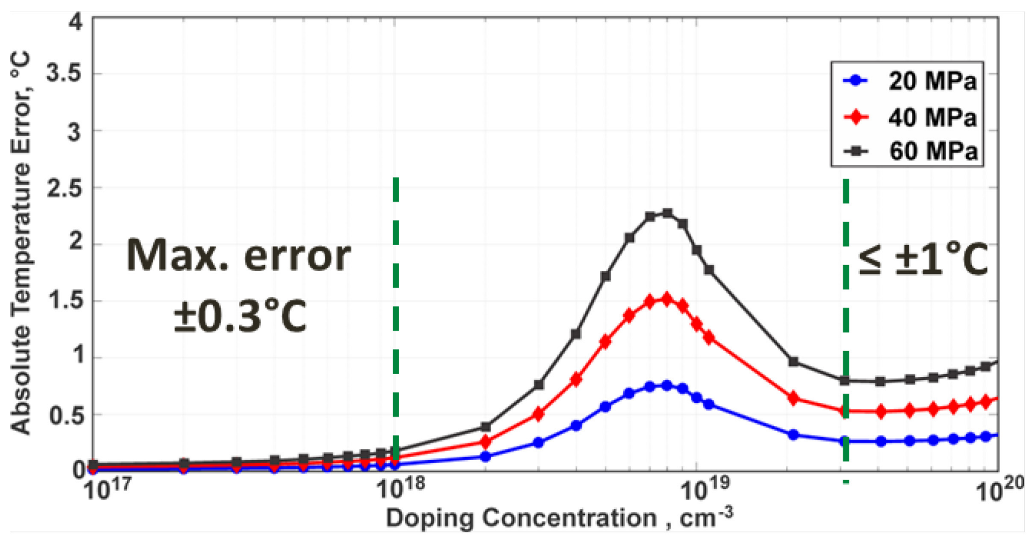

Figure 3-13 Absolute temperature error obtained by the proposed temperature sensor subjected to in-plane loads up to 60 MPa

Figure 3-14 shows the effect of out-of-plane normal stress up to 20 MPa on the proposed temperature transducer's accuracy at different concentration levels. An absolute error of about ±0.8°C or less can be obtained at concentration levels below 10^{18} cm^{-3} or above $7x10^{19}$ cm^{-3}.

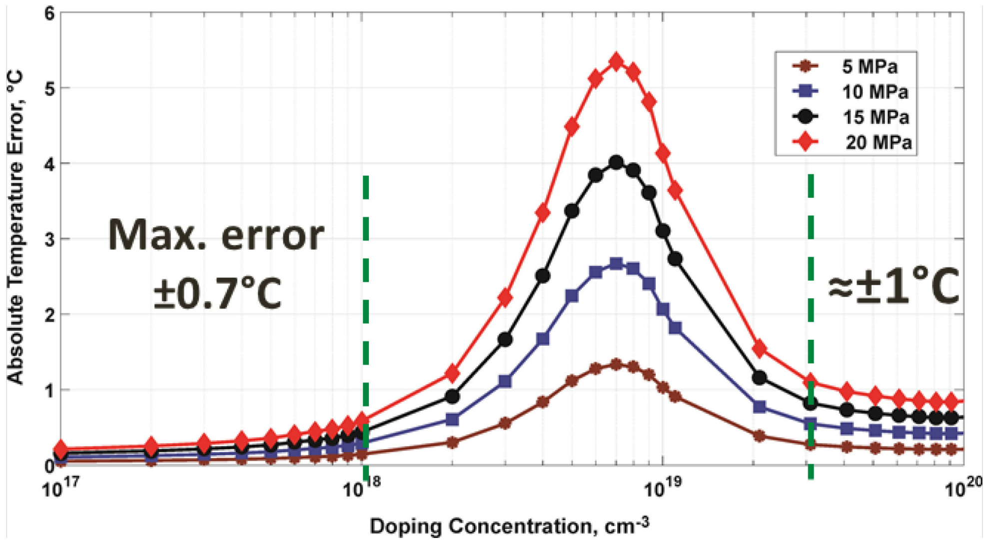

Figure 3-14 Absolute temperature error obtained by the proposed temperature sensor subjected to out-of-plane normal loads up to 20 MPa

3.3.4 The Fabrication Non-uniformity Effect on Stress Measurement

Numerical sensitivity analysis was conducted to study the stress measurement error due to fabrication non-uniformity and the uncertainties in the values of PRCs and TCR for both eight-element and ten-element sensing rosettes presented in earlier sections (Figure 3-6 and Figure 3-7). Jaeger et al. found that uncertainties of 10% or more in PRCs values might be obtained from experimental calibration, which in turn could produce large errors in extracted stress values [80], [82].

In this analysis, random data sets of PRCs and TCR have been generated, for the sensing elements of eight-element and ten-element rosettes, with relative standard deviation (RSD) of 10% to simulate the uncertainty in PRCs. Figure 3-15 shows the flow diagram of the numerical sensitivity analysis utilized to investigate the effect of fabrication non-uniformity and the uncertainty in PRCs and TCR values on the sensor's capability to extract the stress applied.

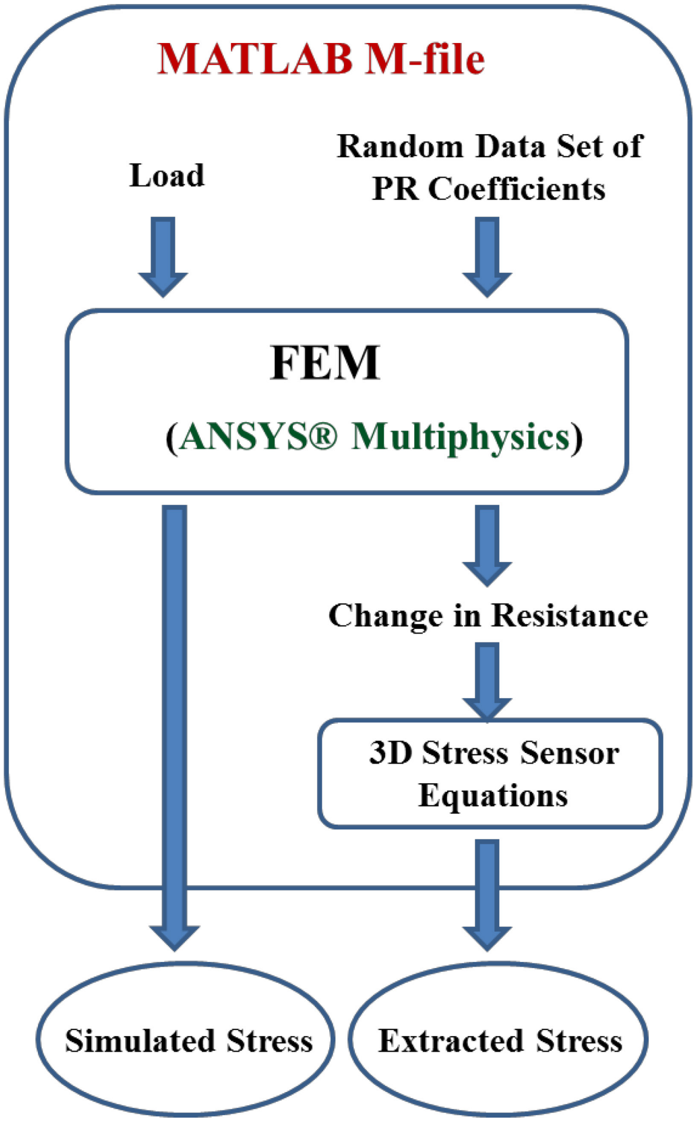

Figure 3-15 Numerical sensitivity analysis flow diagram

3.3.4.1 Finite Element Model

A finite element model (FEM) of the 3D stress sensing chip, with both rosettes configuration (eight-element and ten-element), attached to a structure under four-point bending was developed using ANSYS® Multiphysics. Also, it models the piezoresistive sensing elements on the chip surface of both rosettes to obtain the resistance change occurred in the sensing element due to the stress exerted on the chip due to the applied load. The piezoresistors were modeled as a block with length, width, and thickness measuring 100 μm x 20 μm x 6 μm, respectively. Below are the assumptions that were made in the FEM:

- The change in piezoresistive coefficients only comes from the variation in doping levels due to microfabrication issues.
- There is no loss in strain between the monitored structure and the sensor attached to it.
- The residual stresses generated during the microfabrication of the sensor were ignored in the FE model.
- In this analysis, a temperature-controlled environment is assumed ($\Delta T=0$).
- Only uniaxial stress is assumed to be generated between the two supports of the four-point bending fixture.

The monitored structure was model as isotropic material (i.e. Steel), while that of the silicon chip was considered anisotropic. The stiffness constants of silicon along the crystallographic directions used in FEM is provided in Table 1. However, these stiffness constants were transformed along the (111) direction to simulate the actual sensing rosettes plane. The dimensions of the FEM and its material properties are given in Table 3-1.

Table 3-1: Material properties and geometry of the FEM model

	Dimensions, mm	Material Properties
Sensing chip (Silicon)	7x7x0.3	C_{11}=165.7 GPa
		C_{12}=63.9 GPa
		C_{44}=79.6 GPa
Monitored Structure	300x45x3	E=200 GPa, ν=0.3

E = elastic modulus, ν = Poisson's Ratio, C_{11}, C_{12}, and C_{44}= stiffness constants

The FEM was based on static structural-piezoresistive analysis and was developed using SOLID187 10-noded tetrahedral elements for the structural components and SOLID226 10-noded structural-piezoresistive coupled tetrahedral elements for the piezoresistive sensing elements. Each piezoresistor was connected in a Wheatstone bridge configuration with three matching CIRCU124 resistor elements to measure the differential output voltage due to the applied load and input voltage to the bridge.

The nodes at the terminals of the piezoresistors were coupled in terms of voltage degree of freedom to obtain a uniform voltage value at the terminals. The change in resistance for each piezoresistor is calculated from the change in voltage from the Wheatstone bridge as follows [100]:

$$\frac{\Delta R}{R_0} = \frac{4(\Delta V / V_s)}{1 - 2(\Delta V / V_s)} \tag{3-28}$$

Where, *Vs* is the voltage source to the bridge, which equals 5 V and ΔV is the change in voltage from the initial state. The boundary conditions and loads applied to FEM are shown in Figure 3-16. The vertical loads and supports were located at 125 mm and 35 mm from the center of the beam, respectively. The beam was fixed in the x_2 direction along the supports and in the x_1 direction along the beam's center-line. Also Figure 3-17 and Figure 3-18 show the meshing of both rosettes, the proposed eight-element rosette with a temperature sensor and the ten-element rosette (Gharib's rosette). The FEM model is provided in Appendix B and Appendix C

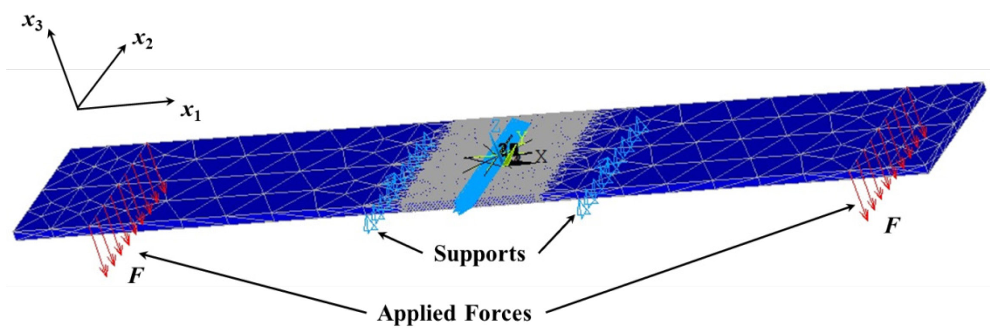

Figure 3-16 Applied loads and boundary conditions of the FE model

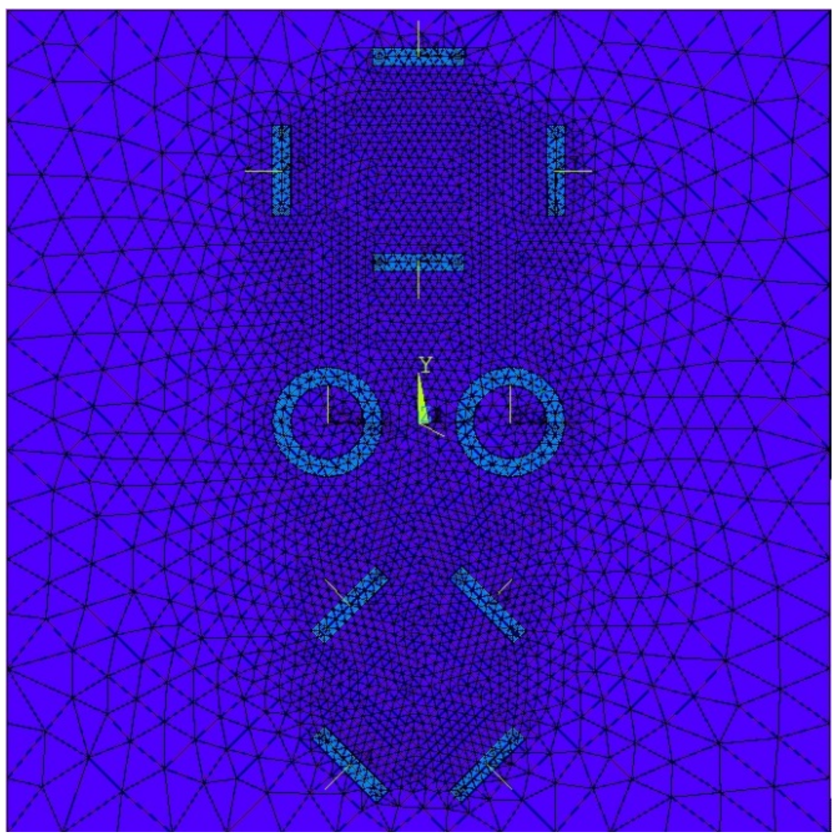

Figure 3-17 Planar view of the meshing of the eight-element stress rosette and temperature sensor

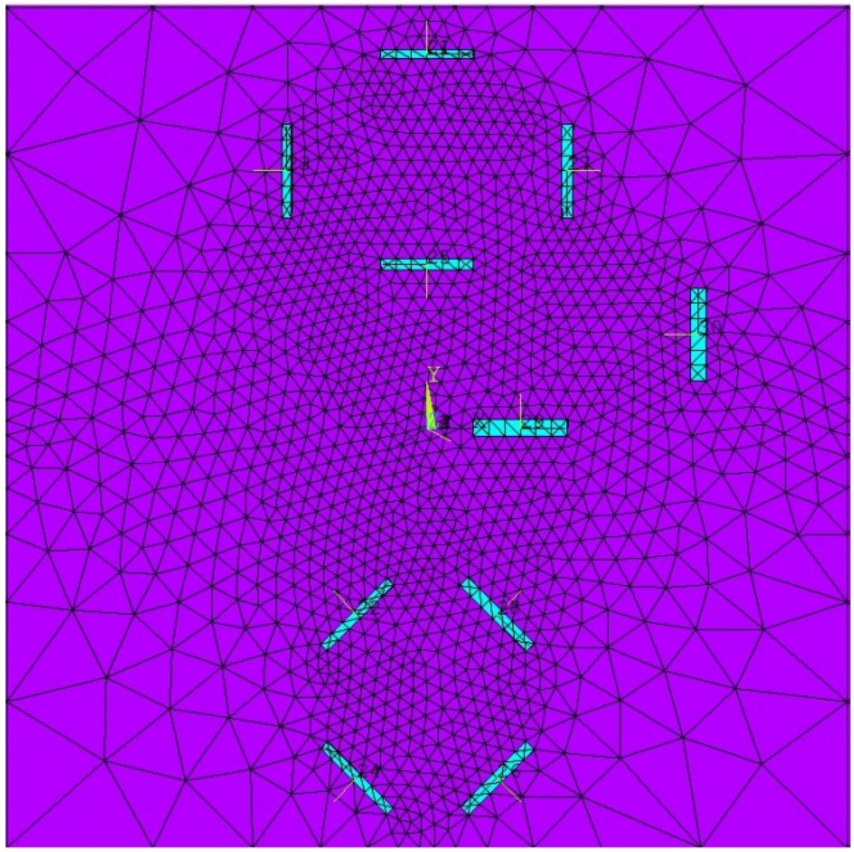

Figure 3-18 Planar view of the meshing of ten-element stress rosette

3.3.4.2 Results

Figure 3-19 and Figure 3-20 show the stress measurement error obtained while extracting the stress components due to a random variation in the PRCs values with 10% RSD from the nominal value. In both figures, the Targeted Stress (σ_T) is the stress value on the surface of the sensing chip, which is obtained from the structural analysis using ANSYS APDL. While the Extracted Stress (σ_E) is the stress value (σ_{11}) calculated using equations (3-15) and (3-18) of both rosettes the eight-element and ten-element, respectively. To calculate the Extracted Stress, the corresponding change in electrical resistance to the applied load was obtained first, from the structure-piezpresistivity coupled FEM using ANSYS APDL, then substituted in the equations.

It is clear that the eight-element rosette is less sensitive to the fabrication non-uniformity (maximum error ~ 17% full scales) compared with the ten-element rosette (maximum error ~ 39% full scales). This low process noise of the eight-element configuration is attributed to the reduced equation forms obtained from this configuration, while the ten-element configuration offers more complex equation forms. To this end, utilizing the eight-element rosette in stress measurement produces less process noise and improves measurement accuracy compared with the ten-element rosette.

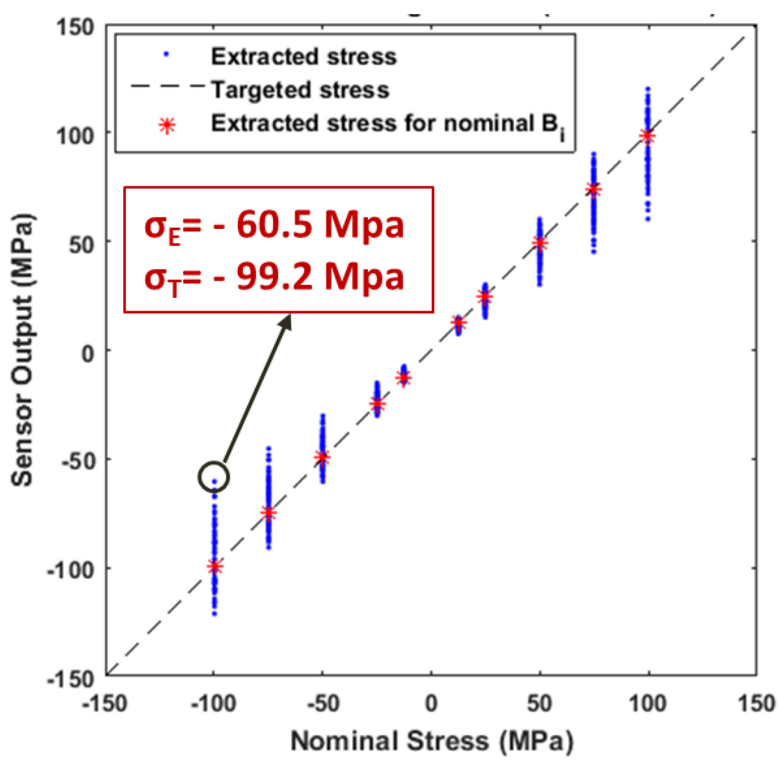

Figure 3-19 Stress measurement error of Gharib's ten-element rosette

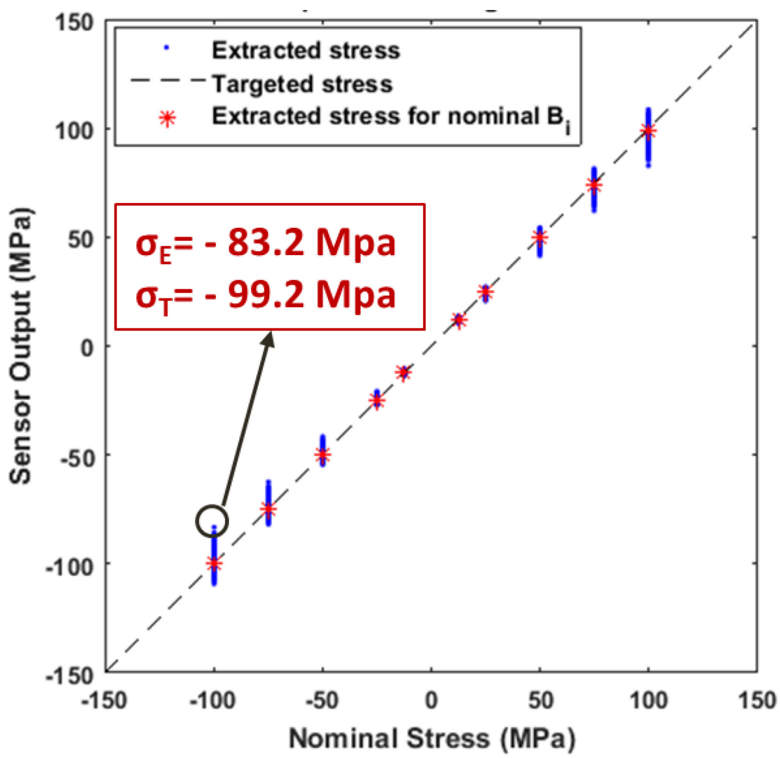

Figure 3-20 Stress measurement error of the proposed eight-element rosette

3.4 Conclusions

This chapter introduced the theoretical background of the piezoresistive multi-element stress rosette and application to the (111) silicon plane. Moreover, the equations relating stresses with the resistance change for the previous state of the art 3D stress sensing rosettes, namely the dual polarity eight-element rosette and the single polarity ten-element rosette. The proposed single polarity eight-element rosette with temperature compensation was introduced as well, where the stress insensitivity of the n-type full circular piezoresistor over (111) silicon plane was studied analytically. This was followed by a discussion of the process noise, of both the proposed eight-element and ten-element sensing rosettes, due to the fabrication non-uniformity that may exist.

CHAPTER 4: MICROFABRICATION OF THE STRESS/STRAIN SENSOR

4.1 Overview

The eight-element single-polarity rosette with temperature compensation was fabricated using semiconductors microfabrication techniques. A number of developing runs, to prototype the proposed sensing chip, were carried out in nanoFab and MEMS/NEMS Advanced Design Laboratory (ADL) at the University of Alberta. This chapter presents the microfabrication processes utilized to prototype the developed sensor. In addition, the fabrication process flow is provided with a detailed description of each fabrication step. Moreover, the mathematical modeling of the diffusion process, used in this research is presented. Finally, the characterization of the fabricated chip is provided in this chapter.

4.2 Doping of semiconductors

Doping means the deliberate introduction of impurities into a semiconductor crystal (i.e. silicon) to change the electrical properties of the semiconductor. For silicon, boron (p-type) and phosphorus (n-type) are the most important doping materials. N-doping of silicon with phosphorus (5-valent dopant) results in a free electron to move to serve as a charge carrier. This free electron requires much less energy to move into the conduction band than the electrons which cause the intrinsic conductivity of silicon, thus a better electrical conductivity is obtained.

On the other hand, the p-doping of silicon with boron (3-valent dopant) can attract an additional outer electron from silicon leaving a hole in the valence band of silicon atoms. This makes the electrons in the valence band more mobile. Since the dopant is fixed to the crystal lattice, only the positive charges (the holes) can move in the opposite direction to the movement of the electrons leading to a change in the electrical properties of the silicon.

The two most widely used doping processes are diffusion and ion implantation. Diffusion is a cheap and accessible method of doping, while ion-implantation provides a more controlled and uniform impurity levels

In the current research, the diffusion process was used in the fabrication of the developed sensor to introduce phosphorus ions into boron-doped crystalline silicon to create n-doped piezoresistors of the sensing rosette. The diffusion equipment is available in MEMS/NEMS Advanced Design Laboratory (ADL) at the University of Alberta.

4.2.1 Diffusion

In the diffusion process, the silicon wafer is placed inside a quartz tube furnace with controlled elevated temperature (800 °C to 1200 °C), while a mixture of dopants and carrier gas (nitrogen) is passing on the wafer surface. For n-type doping (phosphorus), the dopants can be introduced either by using solid sources (Phosphorus Pentoxide, P_2O_5), liquid sources (Phosphoryl Chloride, $POCl_3$), or gaseous sources (Phosphine, PH_3).

In this work, a phosphorus solid source (PhosPlus® TP-250) from TechneGlas Inc. was used, which is a combination of Phosphorus Pentoxide (P_2O_5) and Lanthanum Oxide (La_2O_3). The diffusion process was conducted in two steps; pre-deposition and drive-in steps.

In pre-deposition diffusion, a non-uniform shallow doped region, near the surface, is created at high concentrations and temperatures (800 °C - 900 °C). While the dopants' drive-in step is used to diffuse the dopants more uniformly to the desired depth. The doping profile and junction depth, for each step, are determined mainly by the temperature and diffusion time.

In this research, diffusion modeling was conducted to provide approximate guidance to define the parameters needed for each step. This modeling is based on a one-dimensional diffusion that follows the Fick's second law [101]

$$\frac{\partial C(x,t)}{\partial t} = D\frac{\partial^2 C(x,t)}{\partial x^2} \tag{4-1}$$

Where C is the doping concentration, x is the distance from the silicon surface, t is the diffusion time, and D is the diffusion coefficient. To determine the doping profile, from equation (4-1), two sets of boundary conditions are used; Constant-Surface-Concentration Diffusion (pre-deposition) and Constant-Total-Dopant Diffusion (drive-in).

4.2.1.1 Constant-Surface-Concentration Diffusion

In the pre-deposition stage, an unlimited source of dopants is available during the process. Therefore, the surface concentration remains constant and equals to the solid solubility limit. The doping profile, through a silicon wafer, follows a complementary error function (erfc) [101] given by:

$$C(x,t) = C_{ss} erfc\left(\frac{x}{2\sqrt{(Dt)_{tot}^{p}}}\right) \tag{4-2}$$

Where, $C(x,t)$ is the doping distribution at distance x from the surface after time t of pre-deposition diffusion, C_{SS} is the solid limit for the dopants at the process temperature. While $(Dt)_{tot}^{p}$ is the total product of the diffusion coefficient and time, if multiple pre-deposition stages are conducted, and is calculated by:

$$(Dt)_{tot}^{p} = \sum_i (Dt)_i^{p} = \sum D_0 t_i^{p} \exp\left(\frac{-E_A}{kT_i^{p}}\right) \tag{4-3}$$

In which, D_0 is diffusion constant (for phosphorus dopants, D_0 = 10.5 cm^2/sec), E_A is Arrhenius activation energy (E_A = 3.69 eV, for phosphorus dopant), and k is Boltzmann constant (k = 8.62x10^{-5} eV/K). While, t_i^p and T_i^p are time and temperature, respectively, for each pre-deposition stage. Also, the junction depth X_j^p of the dopant profile, during pre-deposition, can be obtained from equation (4-2) when $C(x,t)$ equals the background doping (C_B) of the wafer as follows:

$$X_j^p = 2\sqrt{(Dt)_{tot}^p}\, erf^{-1}\left(1-\frac{C_B}{C_{ss}}\right) \tag{4-4}$$

The total number of impurity atoms introduced to silicon per unit area, known as the dose, is given by:

$$Q = \int_0^\infty C(x,t)dx = 2C_{ss}\sqrt{\frac{(Dt)_{tot}^p}{\pi}} \tag{4-5}$$

4.2.1.2 Constant-Total-Dopant Diffusion

In the drive-in stage, where the dopant source is not available, thus constant total impurities are assumed. The impurities profile, through a silicon wafer, follows a Gaussian distribution function [101] given by:

$$C(x,t) = \frac{Q}{\sqrt{\pi (Dt)_{tot}^d}} \exp\left(\frac{-x^2}{4(Dt)_{tot}^d}\right) \tag{4-6}$$

Where Q is the dose of impurities introduced during the pre-deposition step and is calculated from equation (4-5). While $(Dt)_{tot}^d$ is the total, which includes all subsequent elevated temperature processes (e.g. thermal oxidation) and can be calculated from equation (4-3). The junction depth, for drive-in step, also can be obtained from:

$$X_j^d = \sqrt{-4\left(Dt\right)_{tot}^d \ln\left(\frac{C_B\sqrt{\pi\left(Dt\right)_{tot}^d}}{Q}\right)} \tag{4-7}$$

4.2.2 Chip Design

A prototype of the proposed stress sensing rosette with temperature compensation needs to be fabricated to test the capability of the developed sensor to accurately extract the stresses applied to structures at different thermal environments. As shown in Figure 4-1, the sensing chip dimensions are 7 mm x 7 mm x 0.3 mm. The stress sensing elements (the eight elements) are designed as straight piezoresistors since the calibration of the PRCs (B_i) is directly related to the crystallographic PRCs (π_{ij}). All piezoresistors have a length of 250 μm and a width of 10 μm. For the temperature sensor, the annulus piezoresistor has an inner diameter of 250 μm and an outer diameter of 300 μm. For characterization, test structures are designed on the same wafer to measure contact resistance using the transfer line method (TLM). In addition, two large open windows, measuring 7 mm x 2 mm, are used for characterization of the phosphorus doping of groups *a* and *b*. First, the sheet resistance of the two groups is measured through these two large windows using a four-point probe.

4.2.3 Process flow

The microfabrication of the sensing chip involves several steps including silicon oxide growth, photolithography, dry and wet etching, phosphorus diffusion and metal sputtering as given in Figure 4-2. The most sensitive step is the phosphorus diffusion, which introduces impurity atoms into silicon that satisfy the operational requirements of sensing rosette.

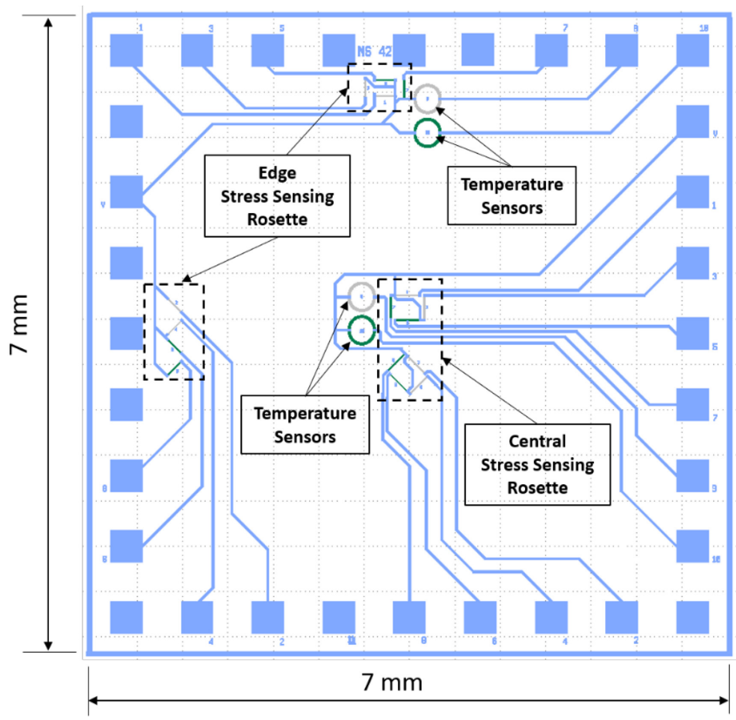

Figure 4-1 Layout of the sensing chip

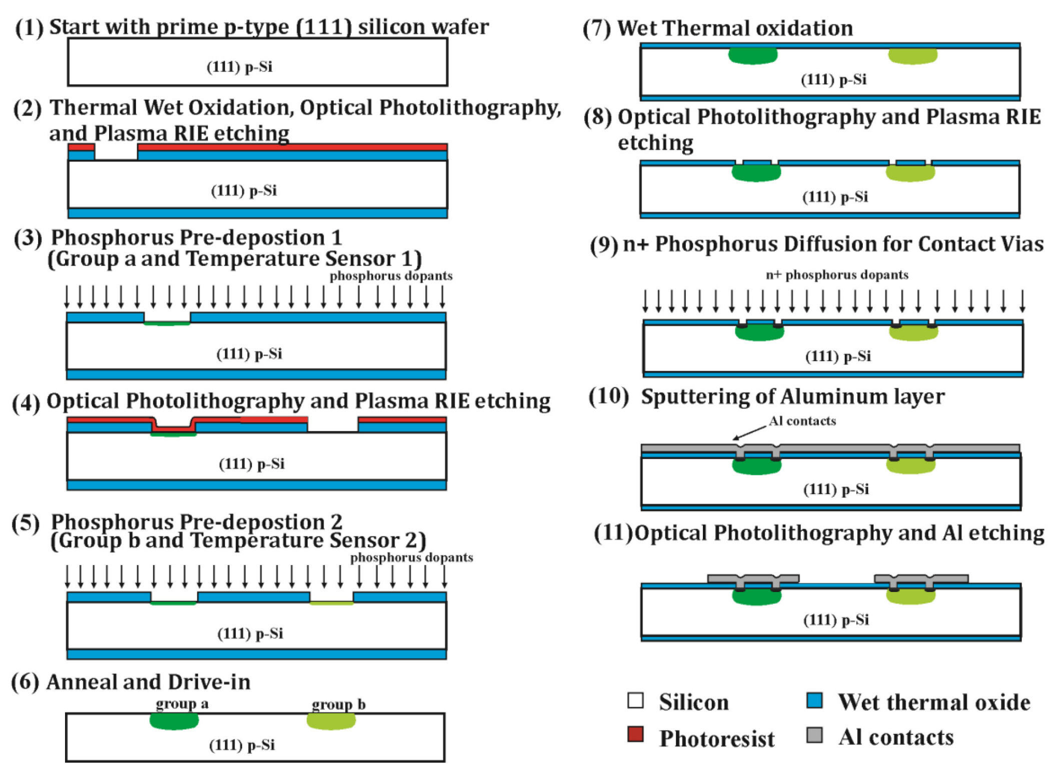

Figure 4-2 Microfabrication process flow of the proposed sensing chip

All processes were carried out in the nanoFab at the University of Alberta except the doping process, which was conducted in the MEMS/NEMS Advanced Design Lab (ADL) at the University of Alberta. The detailed microfabrication process flow of the developed sensing chip is as follows:

STEP 1.0: WAFER PREPARATION	
1.1 Starting Material	• 100 mm prime p-type wafer • Orientation: (111) ± 0.1° • Thickness: 300 ± 25 μm • Bulk resistivity: 10 ± 2 Ω.cm
1.2 Wafer Cleaning	1.2.1 Piranha: (H_2SO_4: H_2O_2, 3:1) • Clean: 15 minutes in piranha • Dump rinse • Spin-rinse-dry 1.2.2 Buffered Oxide Etch (BOE) • Etch: 2 minutes in BOE • Dump rinse • Spin-rinse-dry
STEP 2.0: Define Alignment Marks	
2.1 Lithography	2.1.1 HMDS Prime: • Standard HMDS prime recipe (program 1) 2.1.2 Photo Resist Coat: • Photoresist: HPR 504 • Spread: 500 rpm for 10 seconds • Spin: 4000 rpm for 40 seconds • Soft-bake: 115 °C for 90 seconds on hotplate • Rehydration: 15 minutes 2.1.3 Expose Photo Resist: • Mask layer: 10 • UV light (365 nm + 405 nm) • Dose: ~140 mJ/cm^2 2.1.4 Develop Photo Resist: • Developer: 354 • Time: ~18-20 seconds (visual endpoint) • DI H_2O rinse

2.2 Silicon Etch	• Tool: ICP RIE (Oxford Estrelas) • Recipe: unswitched process • Condition: 5 minutes • Etch: 1 minute
2.3 Photo Resist Strip	• Tool: Branson 3000 Barrel Etcher • time: 20 minutes
STEP 3.0: Oxide Mask for Doping	
3.1 Wafer Cleaning	• Piranha: (H_2SO_4: H_2O_2, 3:1) • Clean: 15 minutes in piranha • Dump rinse • Spin-rinse-dry
3.2 Thermal Wet Oxidation	• Tool: Minibrute Middle Furnace • Temperature set-point: 1000 °C • Ramp up to 998 °C then start timer • Time: 110 minutes • Thickness: ~ 550 nm
STEP 4.0: Doping group a (Pre-deposition 1)	
4.1 Lithography	4.1.1 HMDS Prime: • Standard HMDS prime recipe (program 1) 4.1.2 Photo Resist Coat: • Photoresist: HPR 504 • Spread: 500 rpm for 10 seconds • Spin: 4000 rpm for 40 seconds • Soft-bake: 115 °C for 90 seconds on hotplate • Rehydration: 15 minutes 4.1.3 Expose Photo Resist: • Mask layer: 11 • UV light (365 nm + 405 nm) • Dose: ~140 mJ/cm^2 4.1.4 Develop Photo Resist: • Developer: 354 • Time: ~18-20 seconds (visual endpoint) • DI H_2O rinse
4.2 Oxide Etch	• Open group a windows • Tool: Trion RIE • Cleaning Recipe: 20 minutes • Oxide Etch Recipe: 20 minutes • Over Etch: 30%

4.2 Photo Resist Strip	• Tool: Branson 3000 Barrel Etcher • time: 20 minutes
4.4 Phosphorus Pre-deposition	• Tool: Diffusion Furnace • Doping Source: PhosPlus® TP-250 • Doping Temperature: 845 °C • Wafer Insertion Temperature: 700 °C • Time: 2 hours (start timer at 843 °C)
STEP 5.0: Doping groups a & b (Pre-deposition 2)	
5.1 Lithography	5.1.1 HMDS Prime: • Standard HMDS prime recipe (program 1) 5.1.2 Photo Resist Coat: • Photoresist: HPR 504 • Spread: 500 rpm for 10 seconds • Spin: 4000 rpm for 40 seconds • Soft-bake: 115 °C for 90 seconds on hotplate • Rehydration: 15 minutes 5.1.3 Expose Photo Resist: • Mask layer: 12 • UV light (365 nm + 405 nm) • Dose: ~140 mJ/cm^2 5.1.4 Develop Photo Resist: • Developer: 354 • Time: ~18-20 seconds (visual endpoint) • DI H_2O rinse
5.2 Oxide Etch	• Open group a windows • Tool: Trion RIE • Condition Recipe: O_2 Clean • Condition Time: 20 minutes • Etch Recipe: Oxide Etch • Etch Time: 20 minutes (~550 nm oxide etch) • Over Etch: 30% of etch time
5.3 Photo Resist Strip	• Tool: Branson 3000 Barrel Etcher • time: 20 minutes
5.4 Phosphorus Pre-deposition	• Tool: Diffusion Furnace • Doping Source: PhosPlus® TP-250 • Doping Temperature: 845 °C • Wafer Insertion Temperature: 700 °C • Time: 2 hours (start timer at 843 °C) • Nitrogen Flow Rate: 40 Liter/minute

5.4 Oxide and PSG Etch	• Wet Etch using BOE • Etch rate: 44 nm/min • Etch Time: 12 minutes and 30 seconds • Over etch: 30% of etch time • Dump rinse • Spin-rinse-dry
STEP 6.0: Annealing, Drive-In, and Oxidation	
6.1 Annealing and Drive-in	• Tool: Minibrute Middle Furnace • Temperature set-point: 1050 °C • Switch set to Anneal (Nitrogen only) • Nitrogen Flow Rate: 40 Liter/ minute • Ramp up to 1048 °C then start timer • Hold for 30 minutes • Proceed immediately to the next step
6.2 Oxidation	• Turn switch from Anneal to Oxidation • Turn on bubbler and heater • Hold for 30 minutes • Turn off bubbler and heater • Turn off the furnace main switch • Cool for 200 °C or less to remove • Oxide thickness: ~ 250 nm
STEP 7.0: n^+ Phosphorus Doping of Contact Vias	
7.1 Lithography	7.1.1 HMDS Prime: • Standard HMDS prime recipe (program 1) 7.1.2 Photo Resist Coat: • Photoresist: HPR 504 • Spread: 500 rpm for 10 seconds • Spin: 4000 rpm for 40 seconds • Soft-bake: 115 °C for 90 seconds on hotplate • Rehydration: 15 minutes 7.1.3 Expose Photo Resist: • Mask layer: 13 • UV light (365 nm + 405 nm) • Dose: ~140 mJ/cm^2 7.1.4 Develop Photo Resist: • Developer: 354 • Time: ~18-20 seconds (visual endpoint) • DI H_2O rinse

7.2 Oxide Etch	• Open group a windows • Tool: Trion RIE • Condition Recipe: O_2 Clean • Condition Time: 20 minutes • Etch Recipe: Oxide Etch • Etch Time: 7 minutes (~250 nm oxide etch) • Over Etch: 30% of etch time
7.3 Photo Resist Strip	• Tool: Branson 3000 Barrel Etcher • time: 20 minutes
7.4 Phosphorus Doping	• Tool: Diffusion Furnace • Doping Source: PhosPlus® TP-250 • Doping Temperature: 875 °C • Wafer Insertion Temperature: 700 °C • Time: 1 hour (start timer at 873 °C) • Nitrogen Flow Rate: 40 Liter/minute
STEP 8.0: Aluminum Sputtering	
8.1 Oxide and PSG Etch	• Wet Etch using BOE • Etch rate: 44 nm/min • Etch Time: 3 minutes and 30 Seconds • Dump rinse • Spin-rinse-dry • Proceed immediately to the next step
8.2 Wafer Dehydration Bake	• Tool: Hot plate • Temperature: 115 °C • Time: 90 seconds • Proceed immediately to the next step
8.3 Aluminum Deposition	• Tool: Floyd Magnetron sputtering • Burn-in time: 120 seconds • Deposition Time: 3135 seconds
STEP 9.0: Patterning Aluminum Traces and Pads	
8.1 Lithography	8.1.1 HMDS Prime: • Standard HMDS prime recipe (program 1) 8.1.2 Photo Resist Coat: • Photoresist: HPR 504 • Spread: 500 rpm for 10 seconds • Spin: 4000 rpm for 40 seconds • Soft-bake: 115 °C for 90 seconds on hotplate • Rehydration: 15 minutes

	8.1.3 Expose Photo Resist: • Mask layer: 14 • UV light (365 nm + 405 nm) • Dose: ~140 mJ/cm^2 8.1.4 Develop Photo Resist: • Developer: 354 • Time: ~18-20 seconds (visual endpoint) • DI H_2O rinse
8.2 Aluminum Etch	• Wet Etch using commercial Al Etchant • Etch Rate: 35 nm/min • Etching Time: 20 minutes • Over Etch: 20% of etch time
8.3 Photo Resist Strip	• Acetone Bath • time: 5 minutes • Dump rinse • Spin-rinse-dry
8.4 Annealing	• Tool: Diffusion Furnace • Wafer insertion at room temperature • Nitrogen Flow Rate: 40 Liter/ minute • Set Temperature: 450 °C • Ramp up to 453 °C then start timer • Time: 15 minutes

A photograph of the final diced prototype chip is shown in Figure 4-3, while microscopic image of the fabricated sensing 8-element sensing rosette and temperature sensor is shown in Figure 4-4.

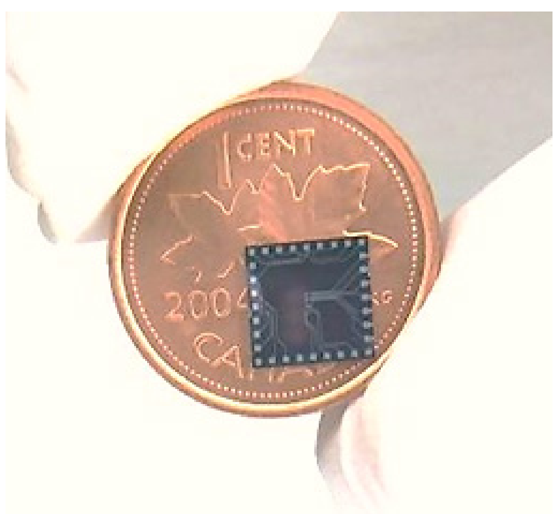

Figure 4-3 Photograph of the microfabricated sensing chip

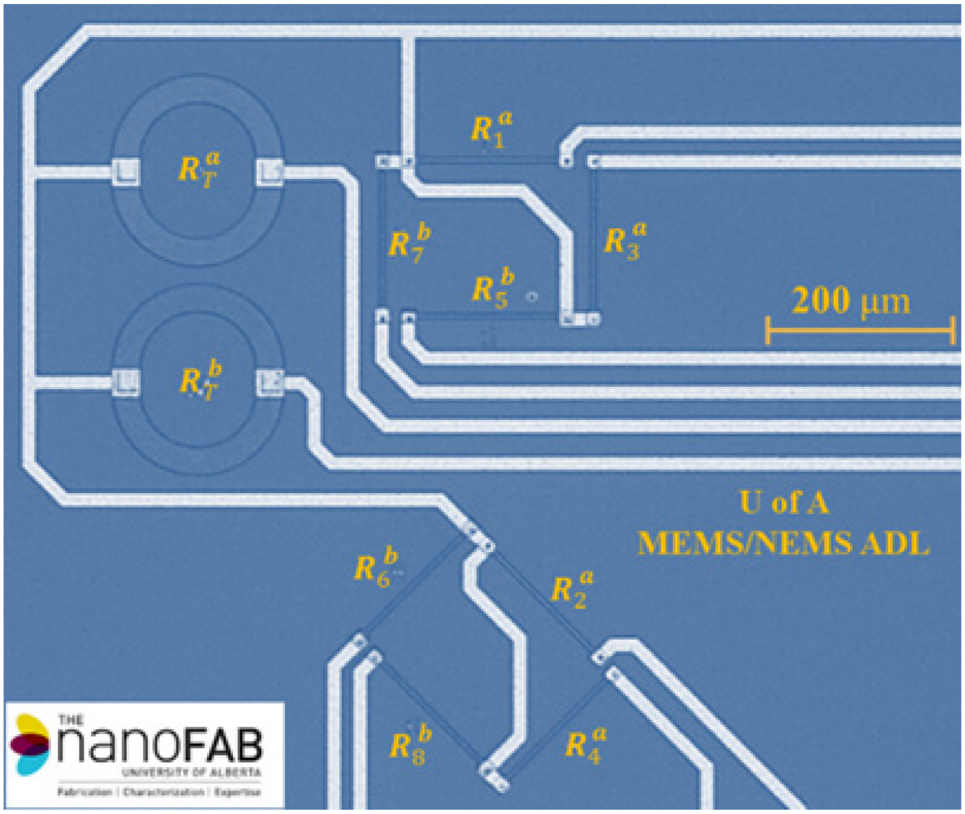

Figure 4-4 Microscopic image of the fabricated chip; the 8-element stress rosette with a circular temperature sensor.

4.2.4 Microfabrication Tools

In this section, a brief introduction, to all the tools used in fabricating the developed sensing rosette, is provided. Some of the tools are available in the nanofab facility at the University of Alberta, while others are located at NEMS/MEMS Advanced Design Lab at the University of Alberta.

4.2.4.1 Diffusion Tube Furnace

For phosphorus doping, the Carbolite Horizontal Tube Furnace Single Zone (GHA 12/450) was used which is available in NEMS/MEMS Advanced Design Lab at the University of Alberta. This furnace uses free radiating wire elements that are embedded within the insulation layer of the furnace. The maximum operating temperature is 1200 °C with a heated length of 450 mm. As a carrier gas of phosphorous dopants, a stream of nitrogen flows inside the furnace during the doping process. The furnace has a power of 3120 Watts with a maximum current of 15 Amps. The diffusion furnace uses solid doping sources for phosphorus pre-deposition. The solid source, used in this study, is PhosPlus® TP-250 from TechneGlas Inc., which is a combination of Phosphorus PentaOxide (P_2O_5) and Lanthanum Oxide (La_2O_3) that releases phosphorous dopants when the source is heated to the diffusion temperature. Figure 4-5 shows the diffusion furnace used in this research.

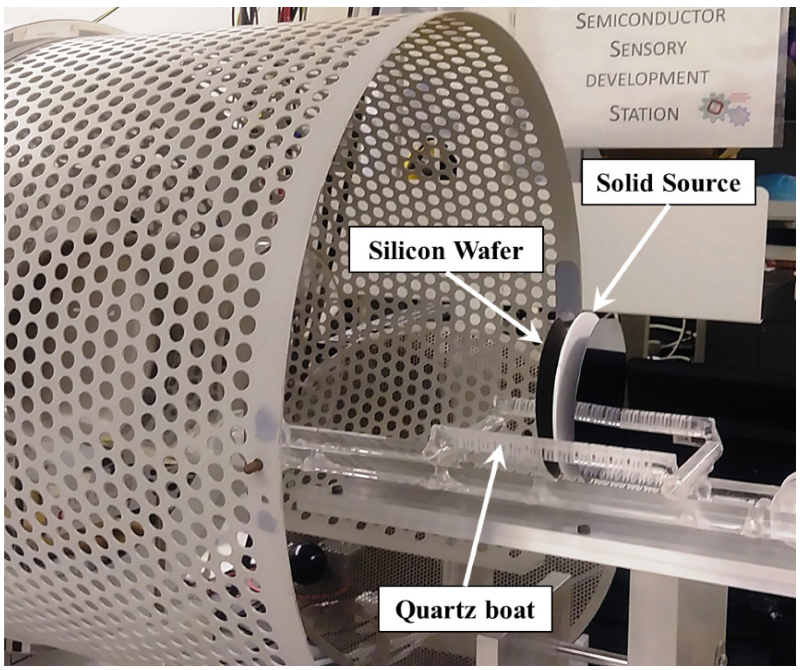

Figure 4-5 Phosphorus diffusion furnace

4.2.4.2 Thermal Wet Oxidation Furnace

The MiniBrute furnaces, shown in Figure 4-6, are used to grow thermal silicon oxide layer (SiO_2) on silicon substrates and for annealing as well. For thermal silicon oxide growth, the following wet oxidation reaction at high temperature (up to 1100 °C) occurs:

$$Si_{(s)} + 2H_2O_{(g)} \rightarrow SiO_{2(s)} + 2H_{2(g)}$$

A mix of oxygen (O2) and water vapor is provided inside the furnace through a bubbler heated up to 94 °C located at the back of the furnace. The oxidation process occurs in an ambient of nitrogen gas which works a carrier gas and sweeps out impurities as well.

Figure 4-6 Thermal wet oxidation furnace
Source: https://www.nanofab.ualberta.ca/capabilities/our-equipment/minibrute-middle-furnace-thermal-oxide-and-general-annealing/

4.2.4.3 ICP-RIE Plasma Etching

Inductively Coupled Plasma Reactive Ion Etching (ICP-RIE) Oxford Estrelas tool, shown in Figure 4-7, is used for etching silicon to feature the alignment marks in the early step of the fabrication of the developed sensor. This tool is capable of performing versatile silicon etching, from Bosch high-rate-through-wafer etching, using inductively coupled high-density plasma, to thin SOI device layers etching. The cryogenic etch mode (-110 °C to +100 °C), using liquid N_2 cooling system, is also available. A mix of process gases SF_6, C_4F_8, O_2, and Ar are available. The Oxford Estrelas ICP-RIE tool can handle both 150 mm and 100 mm wafers using a single-wafer load lock. For Bosch etch process, high selectivity to both, a photoresist (~100:1) and oxide (~250:1) can be achieved.

Figure 4-7 Oxford Estrelas ICP-RIE Plasma Etching
Source: https://www.nanofab.ualberta.ca/capabilities/our-equipment/icprie-oxford-estrelas/

4.2.4.4 CCP-RIE Plasma Etching

Etching both doping windows and contact vias, through the oxide mask layer, is performed using the Capacitive Coupled Plasma Reactive Ion Etching (CCP-RIE) Trion tool, as shown in Figure 4-8. The Trion etching tool offers a mix of process gases of SF_6 CF_4, CHF_3, and O_2. This tool can also etch silicon nitride layers and isotropic silicon as well. For chamber conditioning, O_2 plasma is used. For oxide etching, an acceptable selectivity to photoresist (3:1) and silicon (2:1) is obtained using a mix of CHF_3 and O_2.

Figure 4-8 Trion CCP RIE Plasma Etching
Source: https://www.nanofab.ualberta.ca/capabilities/our-equipment/rie-trion/

4.2.4.5 Magnetron Sputter System

In this research, a load-locked planar magnetron sputter system (Floyd) is used to deposit a layer of the aluminum for metallization. This sputter system is computer-controlled with four sputter guns and RF etch-back. It has four 3" planar magnetron sources. The aluminum deposition is carried out in a vacuum chamber with a base pressure of less than 1×10^{-7} Torr using a cryogenic pump. Up to 6 wafers, 150 mm in diameter or less, can be deposited per single load. Typical uniformity less than 5% over a 150 mm substrate is achievable using Floyd sputtering tool. Figure 4-9 shows the Floyd sputter system used for aluminum deposition which is available in the nanoFAB at the University of Alberta.

Figure 4-9 Floyd Magnetron Sputter System
Source: https://www.nanofab.ualberta.ca/capabilities/our-equipment/sputtering-system-3-floyd/

4.2.5 Characterization

In this work, the characterization of the prototype sensing chip went through two major aspects: I-V characteristics and the contact resistance measurements of the piezoresistive sensing elements of both groups *a* and *b*.

4.2.5.1 I-V Characteristics

A piezoresistor exhibits an Ohmic behavior that means having a linear I-V relationship which provides constant electrical resistance. This linear relationship, for a piezoresistor, is needed to have its electrical resistance change only with the applied mechanical and thermal loads. To characterize the I-V relationship of the prototype sensor, in this study, A current sweep over a range from -200 μA to 200 μA was carried out using a Keithley 2400 source meter. While the voltage response of both, the stress sensing elements and temperature sensors, of groups *a* and *b*, is obtained. As shown in Figure 4-10, good linearity was achieved that confirms a good Ohmic contact.

4.2.5.2 Contact Resistance

Contact resistance is a measure of the quality of the metal-semiconductor interface and the ease with which current can flow across this interface. For better performance of devices, the minimum contact resistance is required. A transfer line method (TLM) was employed to evaluate the contact resistance of the sensing elements of each group of doping. Two TLM test structures made up of a straight doped region with 8 contact points along its length, as shown in Figure 4-11, was created on the wafer for both groups *a* and *b* of piezoresistors. The distance between two successive contact points keeps increasing from the first point to the last point.

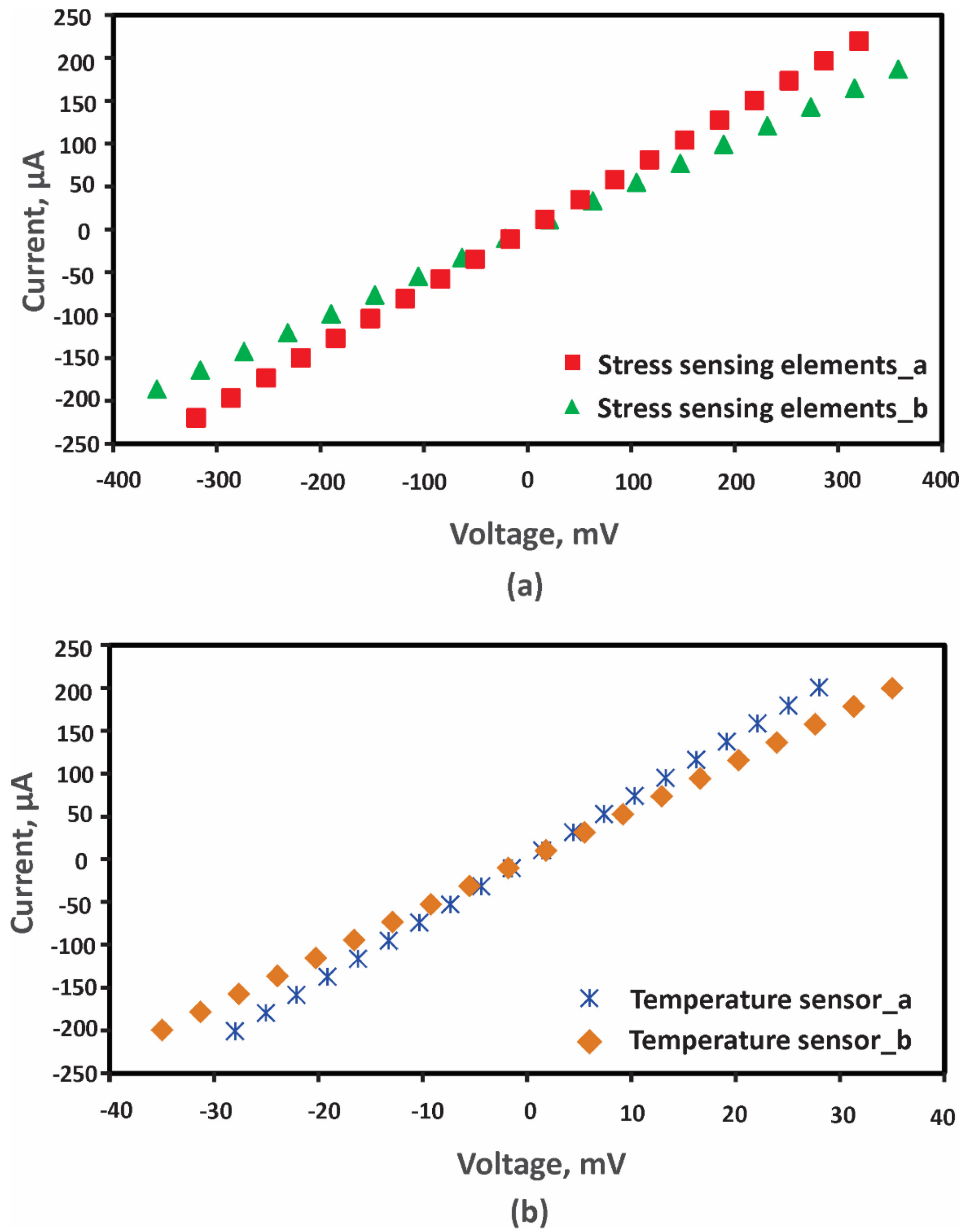

Figure 4-10 Sample I-V curve of (a) stress sensing elements of groups *a* and *b* (b) Temperature sensors of groups *a* and *b*

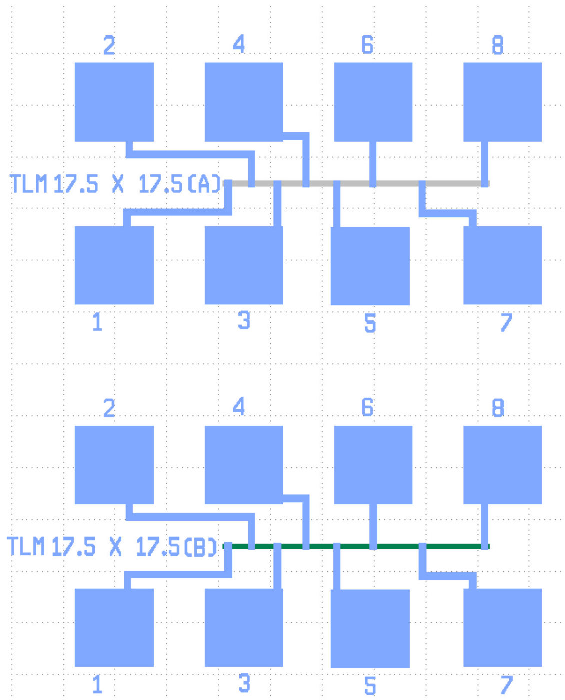

Figure 4-11 The Transfer Line Method (TLM) test structure for groups *a* and *b*

Using TLM structure, the measured total resistance between every two points is as follows:

$$R_{Total} = R_{semi} + 2R_{metal} + 2R_{contact} \tag{4-8}$$

Where, R_{semi} is the resistance of the semiconductor piezoresistor, while R_{metal} is the resistance of the contact metal, and $R_{contact}$ is the associated contact resistance at the metal/semiconductor interface. Since the resistivity of metal is so low which results in $R_{contact} \gg R_{metal}$, thus R_{metal} can be ignored to have:

$$R_{Total} = R_{semi} + 2R_{contact} = \frac{R_s}{W} L + 2R_{contact} \tag{4-9}$$

R_s is the sheet resistance of the doped piezoresistor, while L *and* W are the length and width of the piezoresistor respectively. To measure the contact resistance, the total resistance between contact point 1 and other points from 2 to 8 is measured first then plotted versus the distance between the two contact points, as shown in Figure 4-12. Since these measured resistances have different lengths, keeping all other parameters given in equation 4-15 the same, the y-intercept is equal to twice the contact resistance. The contact resistance of the piezoresistors, within the prototype sensing chip, was found to be around 1 Ω, which is considered small compared to the resistor value which is in order of 1K Ω.

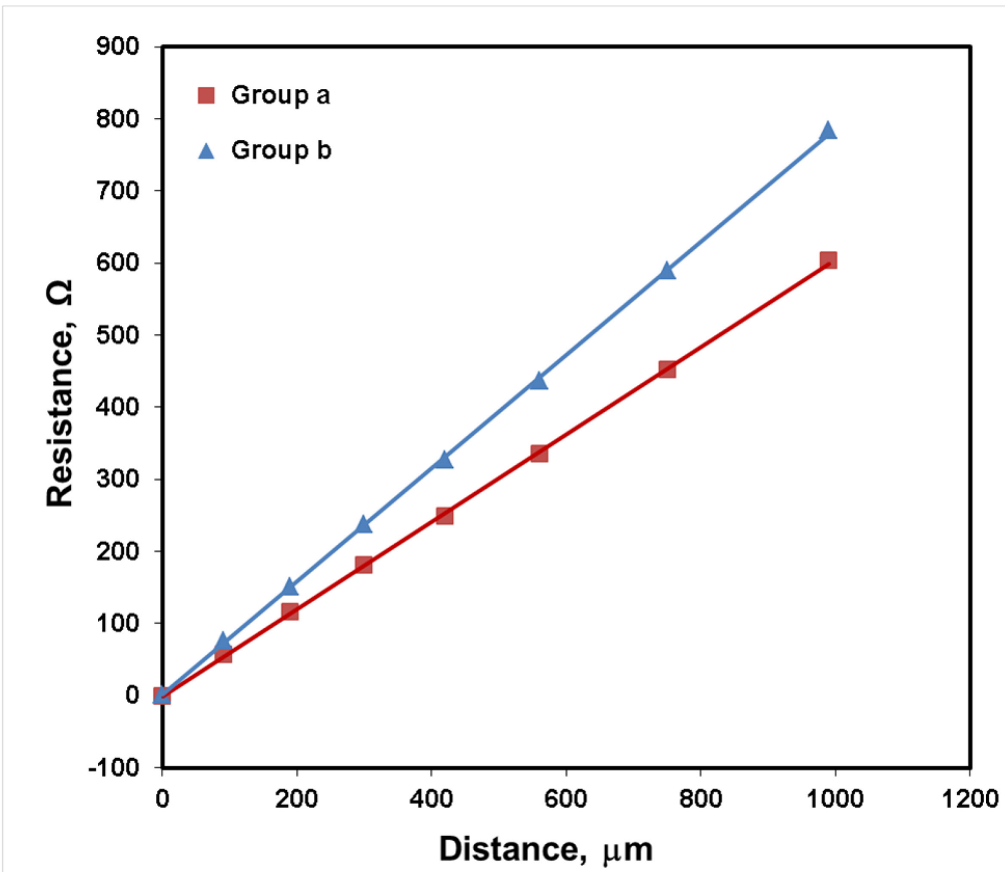

Figure 4-12 Resistance measurements of each group using the TLM structure.

4.3 Challenges

During the microfabrication phase, a number of challenges have been experienced to come up with a successful developing run of fabricated sensors. Since all the fabrication processes were personally carried out, there was a need for earning sufficient understanding along with hands-on experience in semiconductors fabrication techniques. In addition, other challenges had to deal with the control of some processes, specifically doping and etching processes to achieve a good Ohmic contact for piezoresistors which was the main challenge faced to prototype the proposed sensor.

For several fabrication trials, there was inconsistency in the Ohmic behavior of the resulting piezoresistors. Through troubleshooting runs and tests, to resolve this problem, it was found that this non-Ohmic contact resulted from having an insulating layer at the interface between the doped silicon and the aluminum layer. To remove this layer, firstly wet processes, namely Piranha cleaning and BOE etching were used prior to sputtering to ensure a clean and oxide-free interface. However, after a long period of trials, the problem still existed. Since we are not sure about the composition of this insulating layer, it is hard to select the proper wet etching chemistry, thus this layer needs to be physically etched. To this end, over-etching of 30% was carried while opening the contact vias using the Trion RIE tool to make sure of removing the interfacial insulating layer before aluminum sputtering. Finally, we were able to have consistent and good Ohmic behavior for all piezoresistive sensing elements.

4.4 Conclusions

A simpler fabrication process is presented, compared to the other reported 3D stress sensors in the literature [11], [13], with only two n-type doping steps with no need for the p-type doping equipment. Also, this chapter introduced the detailed microfabrication process flow used to prototype the proposed sensing chip. In addition, analytical modeling for both doping profile and sheet resistance obtained from the diffusion process, which was utilized in this research. Finally, the characterization of the prototype sensor was presented in terms of the piezoresistors' I-V characteristics, contact resistance, which are the important characteristic parameters of the piezoresistors.

CHAPTER 5: CALIBRATION AND TESTING OF THE SENSING CHIP

5.1 Overview

In order to employ the developed sensing rosette in stress measurement, accurate values for the PRCs and TCR must be obtained. Two different calibration techniques were utilized in this research; Linear Calibration and Smart Calibration. This chapter presents the linear calibration, while the smart calibration algorithm is introduced in the next chapter. Moreover, the capability of the prototype sensing chip, to extract different mechanical loads at different temperatures, was experimentally evaluated in this chapter.

5.2 Linear Calibration

In this study, the same procedure, presented by Gharib [59], was adopted to calibrate B_1, B_2, B_3, and α, of groups, *a* and *b*, to correctly capture the in-plane stress components, as denoted in equation (3-18). The calibration of B_1 and B_2 is carried out using a four-point bending setup, to apply known uniaxial stress to a silicon beam with calibration resistors which are identical to the measurement elements, while B_3 is calibrated by applying a known hydrostatic pressure. Lastly, α is calibrated by applying a stress-free temperature load using an environmental chamber to control the thermal load.

5.2.1 Uni-axial loading

Known uniaxial stress (σ'_{11}) using a four-point bending fixture, shown in Figure 5-1, is applied at the sensing rosette along the x'_1-axis in Figure 3-6. This loading generates a state of uniform bending stress within the load span in the middle section of the beam. Therefore, a tensile uniaxial stress field is developed on one side of the beam, while, it is compressive on the other side [102]. The generated uniaxial stress can be calculated as follows:

$$\sigma_{11} = \frac{3F(L-d)}{wh^2} \tag{5-1}$$

Where F is the applied force, L is the support span, d is the load span, while w and h are the width and the thickness of the beam, respectively.

Then, the measurement of the corresponding resistance change of the piezoresistors, oriented with 0 and 90 degrees from x_1' -axis, is used to calibrate B_1 and B_2 of groups a and b as follows:

$$\left(\frac{\Delta R_0}{R_0}\right) = B_1 \sigma_{11}'$$
$$\left(\frac{\Delta R_{90}}{R_{90}}\right) = B_2 \sigma_{11}' \tag{5-2}$$

For group a, piezoresistors R_1 and R_3 are used to calibrate B_1 and B_2, respectively. While, elements R_5 and R7 are used to calibrate B_1 and $B_{2,}$ respectively, for group b of piezoresistors. The geometry and loading conditions of the four-point fixture, for calibration, are given in Table 5-1.

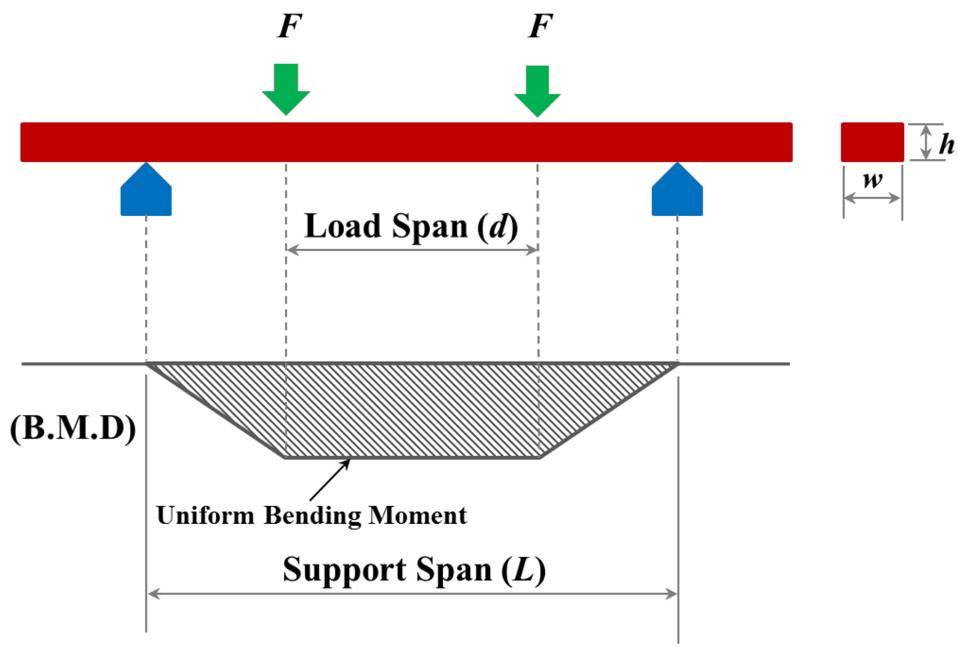

Figure 5-1 Four-point bending fixture and its bending moment diagram.

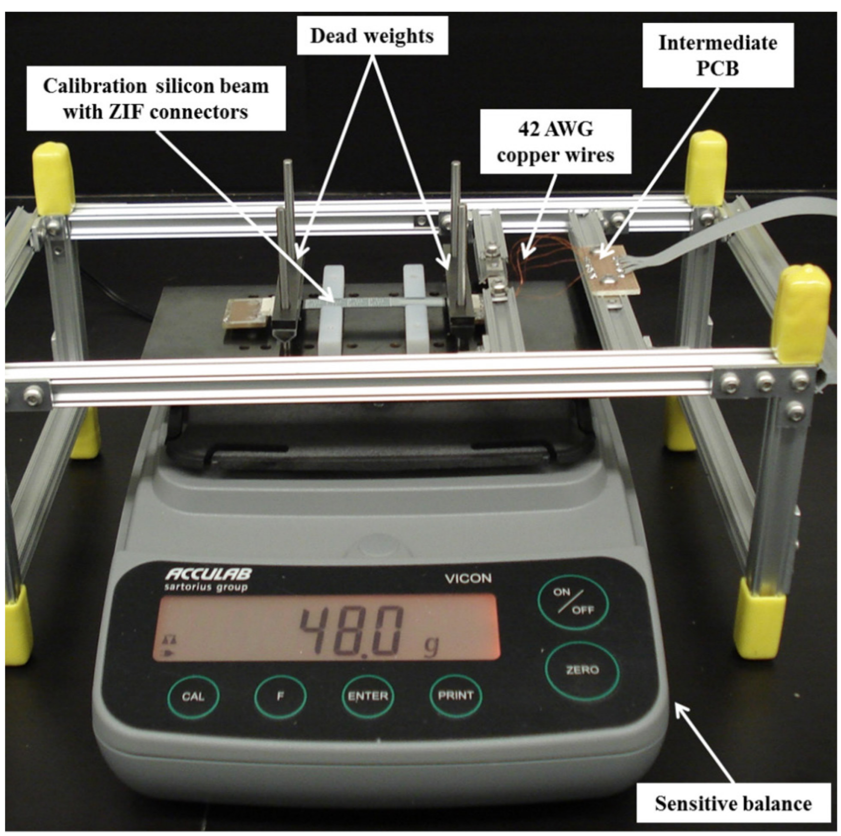

Figure 5-2 Actual four-point bending loading setup for calibration

Table 5-1: Geometry and loading conditions of four-point loading for calibration

L	d	w	h	F (increment)
56 mm	28 mm	7 mm	7 mm	117.7 mN

5.2.2 Thermal loading

A stress-free thermal load needs to be applied to the calibration beam to measure the TCR (α) of stress sensing of groups *a* and *b* and temperature sensor as well. In this research, a controlled temperature chamber (TestEQUITY, Model 115A system), is used to apply temperature variations over a range from -25 °C to 60 °C with uniformity of ±0.2°C. For stress-free condition, the resistance change of a piezoresistor is related to temperature changes as follows:

$$\frac{\Delta R}{R} = \alpha T \tag{5-3}$$

5.2.3 Hydrostatic loading

In this work, the PR coefficient B_3 was calibrated through hydrostatic pressure loading. A uniformly distributed pressure was applied using a pressure vessel with a non-compressible fluid, like hydraulic oil, as shown in Figure 5-4. The resistance change equation for a piezoresistor undergoing hydrostatic pressure is given by:

$$\left(\frac{\Delta R}{R}\right) = \pi_p P + \alpha T \tag{5-4}$$

Where, P = the applied hydrostatic pressure and π_p is the piezoresistive pressure coefficient which equals:

$$\pi_p = -\left(B_1 + B_2 + B_3\right) \tag{5-5}$$

Figure 5-3 Thermal load calibration setup including environmental chamber, source meter, and switch box

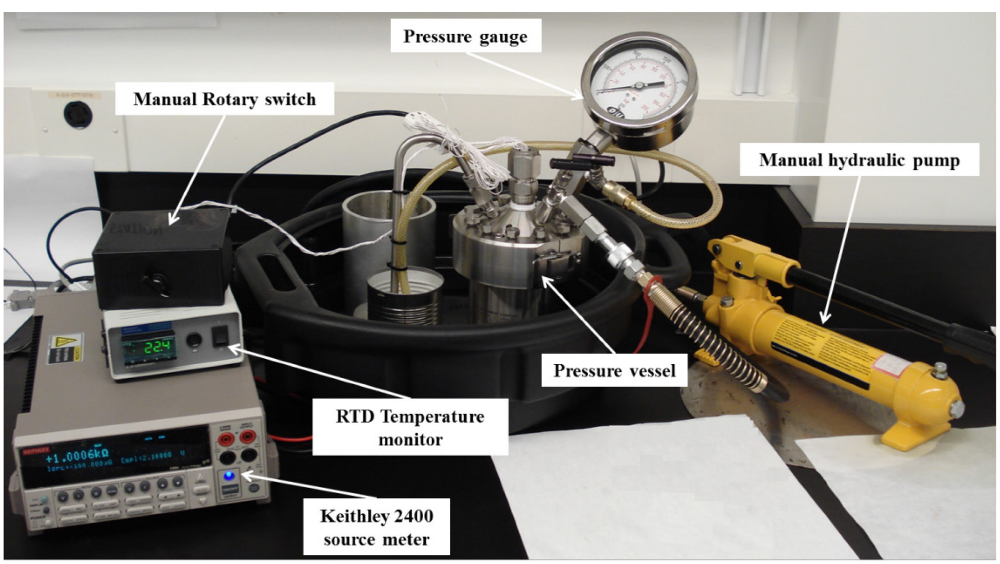

Figure 5-4 Hydrostatic pressure vessel calibration setup

As it is shown in equation (5-4), the temperature increase in the compressible fluid changes the resistance of piezoresistors by (αT). Therefore, the temperature effect needs to be evaluated and compensated first, to accurately measure B_3.

5.2.4 Measurement setup and calibration results

For calibration, a silicon beam, measures 70 mm x 7 mm x 0.3 mm, was diced off from the microfabricated wafer. The calibration sensing rosette is connected to the measurement equipment via ZIF connector (TE Connectivity, part No. 1-1734839-3), as shown in Figure 5-5. All PRCs and TCR were measured using the 0° and 90° sensing elements and circular piezoresistors, i.e. the six sensing elements R_1, R_3, R_5, R_7, R_9, and R_{10}. Therefore, seven aluminum traces was sputtered over the surface of the calibration beam, where 6 traces provide the bias voltage to the six calibrated piezoresistors. While, the seventh is a common ground to supply 100 μA, using Keithley 2400 source meter, to each piezoresistor. A manual rotary switch box was used to switch between the sensing elements to measure the corresponding voltage drop. A schematic of the measurement setup for the calibration is shown in Figure 5-6, which was used in the three calibration setups. The final calibrated coefficients, obtained from the linear calibration algorithm, are given in Table 5-2.

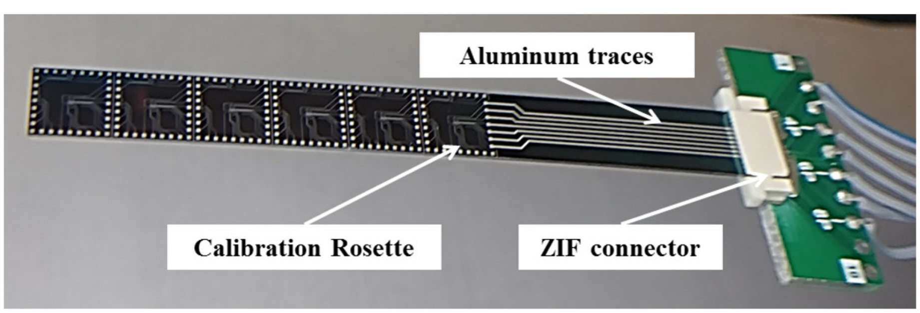

Figure 5-5 Silicon calibration beam with ZIF connector

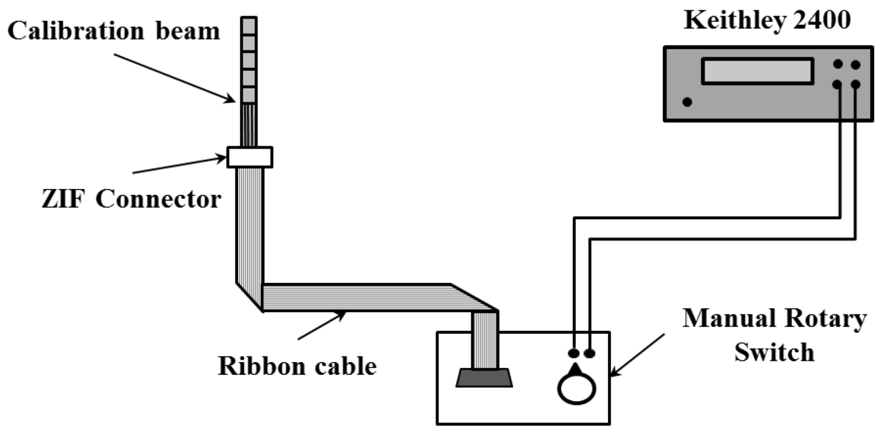

Figure 5-6 Measurement Setup for the calibration beam

Table 5-2: Experimental values for B_i and α of groups *a* and *b*

Group	*a*	*b*
N, cm^{-3}	6.7×10^{19}	5.8×10^{19}
B_1, TPa^{-1}	-191.4	-198.1
B_2, TPa^{-1}	147.7	162.7
π_p, TPa^{-1}	-6.4	16.2
B_3, TPa^{-1}	8.6	19.9
α, ppm/°C	2184.1	1868.5

5.3 Testing of Prototype Sensor

The capability of multi-element single polarity (n-type) piezoresistive stress sensing rosette over (111) silicon plane to extract the 3D stress components has been already studied by the authors' group in previous work [103]. This study aims to investigate the feasibility of the integration between the temperature compensation system, using n-type full circular piezoresistor, and multi-element single polarity (n-type) piezoresistive 3D stress sensing rosette over (111) silicon plane. To this end, the testing of the prototype sensor, in this work, focuses on applying different mechanical loads at different thermal environments to evaluate the sensor's capability to extract the induced stress with temperature compensation. The selected approach was the four-point bending of a chip-on-beam, as shown in the schematic in Figure 5-7, because of the ease of setup, specimen preparation, and measurement at different temperatures. Also, many stress components could be induced, using the selected approach, by changing the orientation of the sensing chip over the beam. The beam is a standard printed circuit board (PCB) connected to the measurement equipment using edge connectors. In the meantime, the PCB beam is used as a structure to apply mechanical load using four-point bending. Moreover, the PCB transfers signals from the sensing chip flipped on it to the measurement equipment using edge connectors. The sensing chip flipped and bonded to the PCB beam using an anisotropic conductive adhesive (ACA). The ACA is made up of conductive metal particles floating in an epoxy resin matrix.

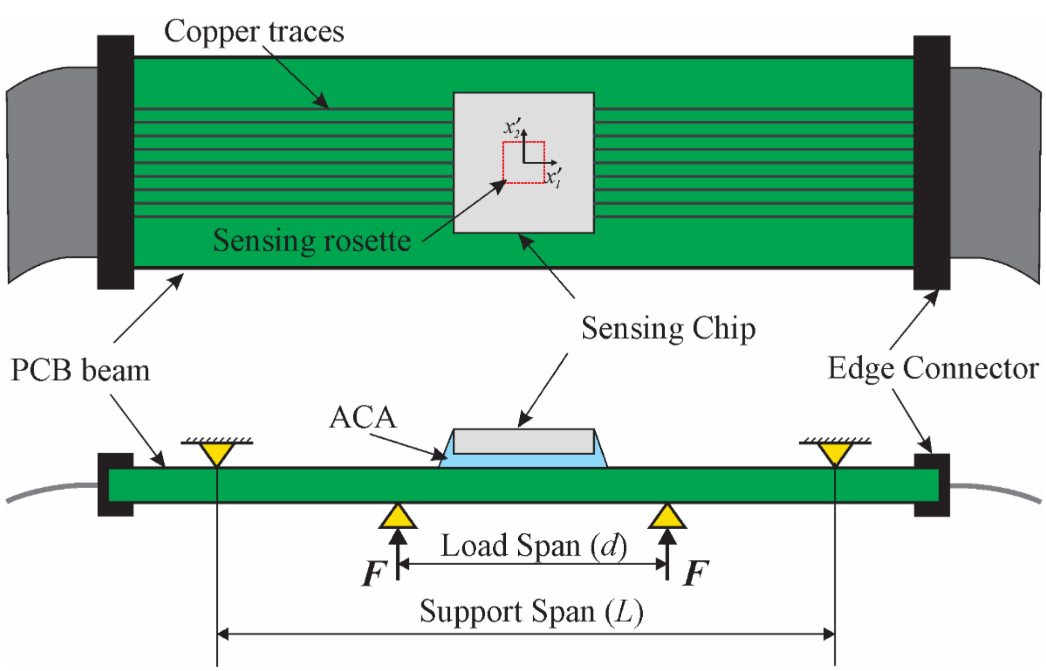

Figure 5-7 Schematic of the testing specimen subjected to four-point bending

5.3.1 Test Specimen Preparation

Prior to bonding, a number of gold stud bumps need to be bonded on the chip's aluminum pads to improve the conduction in the vertical direction and avoid having a short circuit between adjacent traces on the chip surface. In this work, 5 stud bumps were first bonded to cover the aluminum pad area, followed by a coining process to flatten the gold bumps to provide good conduction with the metal particles in the ACA. A wire-bonder, West.Bond® 7476E, shown in Figure 5-8, which is available in the MEMS/NEMS ADL, was used for gold stud bumping and coining processes.

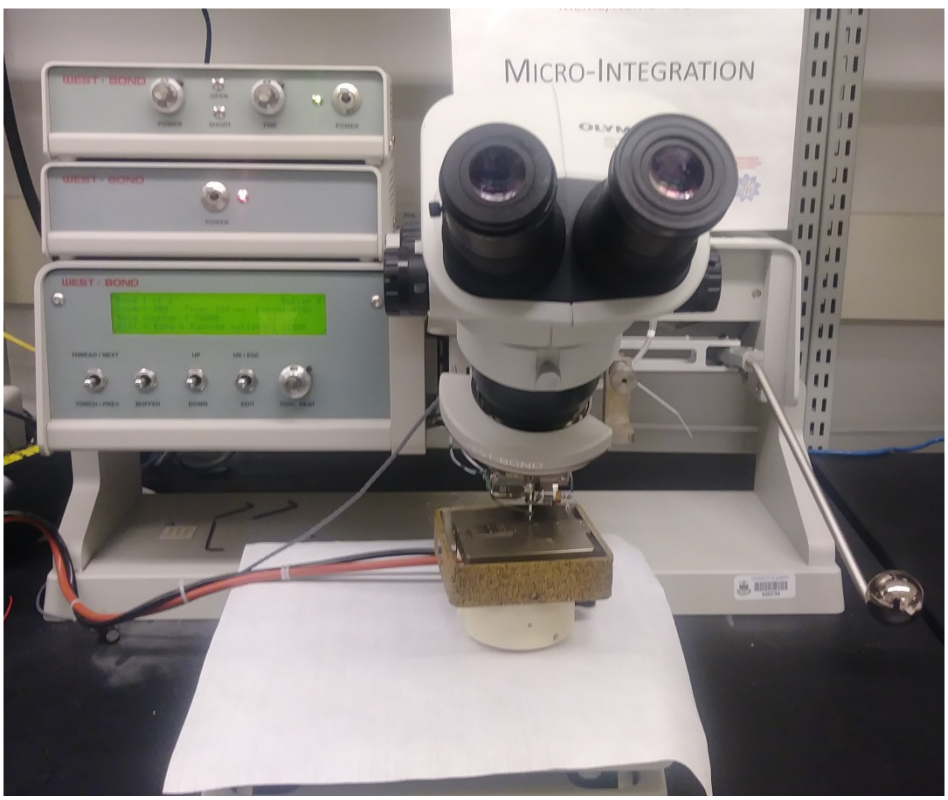

Figure 5-8 A wire-bonder, West.Bond® 7476E

A FinePlacer® pico flip-chipper, available at the MEMS/NEMS ADL, was used to flip the prototype chip on the PCB beam. But, the adhesive 102-32, from CREATIVEMATERIALS®, was first applied between the chip and PCB for electrical conduction and structural bonding This was followed by applying a force of 10 N, using the flip-chipper pivot arm, to produce a pressure of 0.5 MPa which is needed along with a temperature of 160 °C for 5 minutes to cure the adhesive as recommended by the manufacturer. Figure 5-9 shows thermo-compression bonding process between the flipped sensing chip and the PCB beam using the flip-chipper tool. To make sure that the flip-chipping process is performed properly without having short-circuited resistors, we need to measure the resistance of each piezoresistor of groups *a* and *b* before and after the flipping and compare the values.

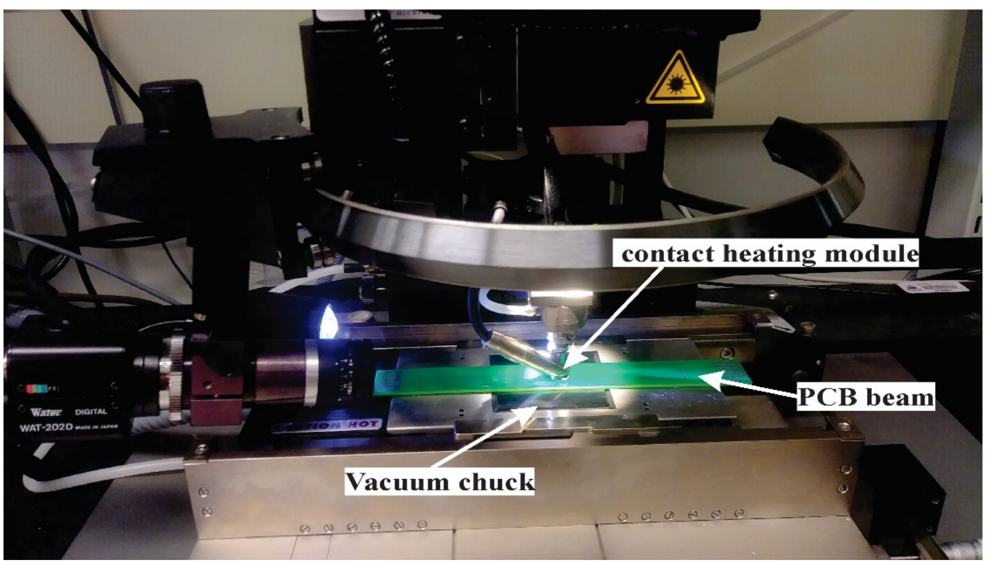

Figure 5-9 Image showing the flip-chipping process of the chip on the PCB beam

The sensing chip was flipped and bonded to the PCB with two different angles, 0 and 45 degrees, namely S0 and S45 respectively, as shown in Figure 5-10 Specimens S0 and S45 are used to induce different stress components, specifically in-plane normal and shear components, on the sensing rosette under four-point bending loading.

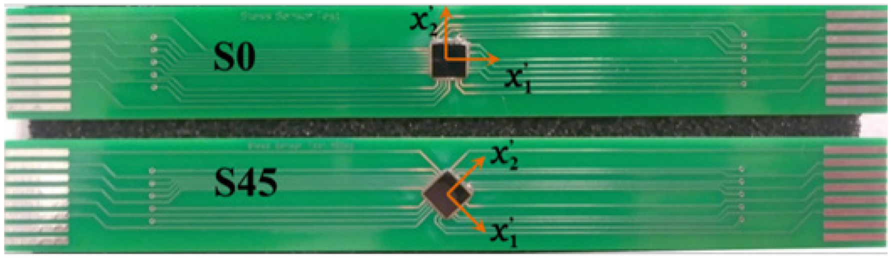

Figure 5-10 The orientation of the sensing chip on the two test specimens, S0 and S45

5.3.2 Measurement Setup

To test the capability of the developed sensor to extract the stresses with full temperature compensation, the test was conducted inside an environmental chamber to apply temperature changes with uniformity of ±0.2°C. The load (*F*) on the PCB beam was applied using a screw jack turned by a stepper motor and a load-cell is used to measure the applied load on the beam. The four-point bending rig was able to produce uniaxial stress up to ~ 60 MPa.

The resistance measurement of each sensing element was carried out by supplying a constant current of 100 μA for each piezoresistor using a current source integrated circuit (LM234). The potential difference $V = I \times R$ was measured using a 24-bit data acquisition system (OMB-DAQ-2416). Measurements were obtained for each piezoresistor at aggregate frequency of 1000 Hz and 10 number of samples were collected at each load. A smooth average function was applied to further reduce noise. Figure 5-11and Figure 5-12 shows the setup used for testing the developed sensor.

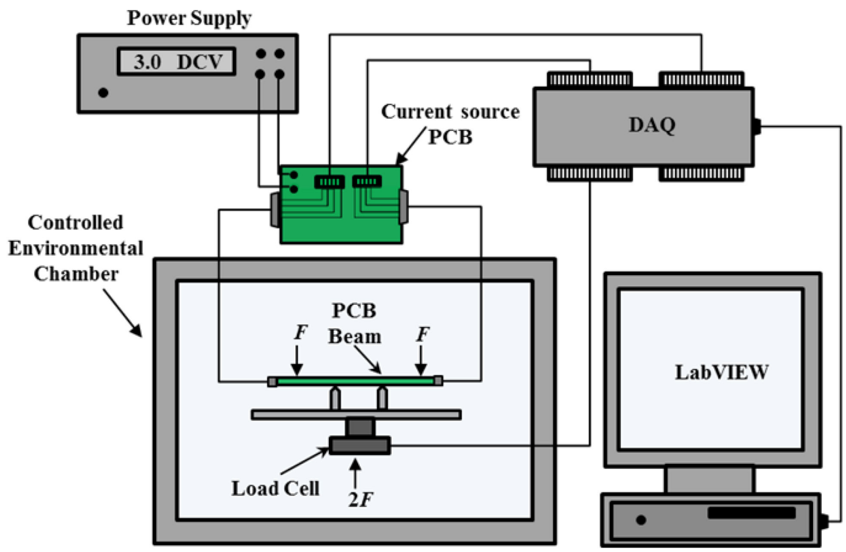

Figure 5-11 Test measurement setup

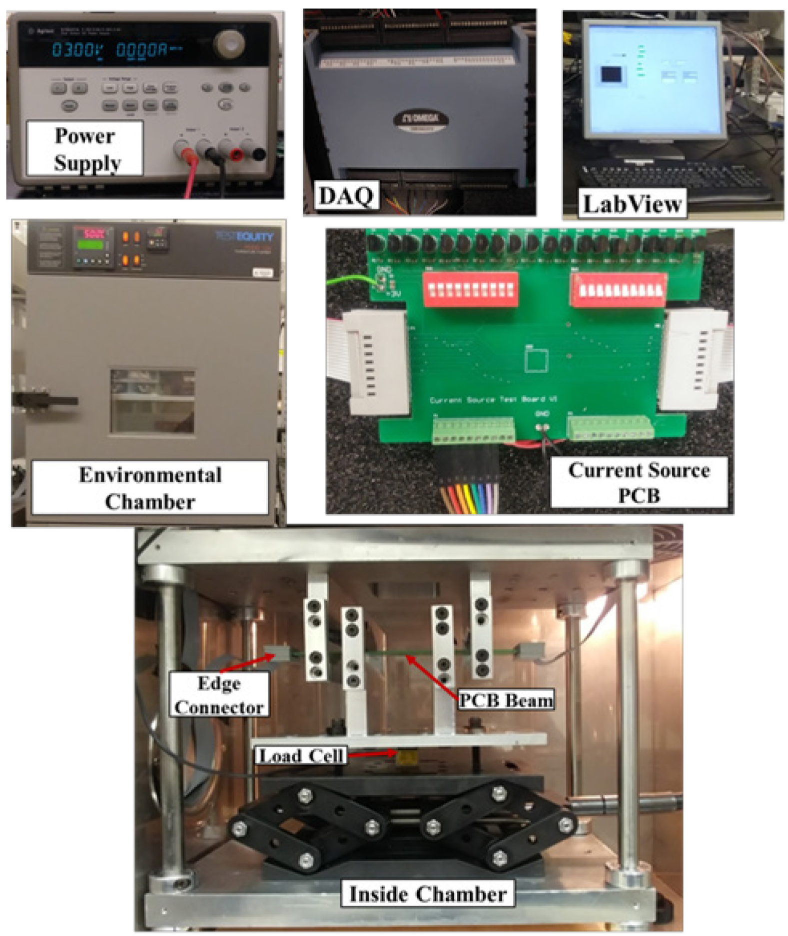

Figure 5-12 Experimental test setup

5.3.3 Results

The testing results are divided into three parts; the first is the temperature sensor response with temperature changes at both, stress-free and applied stress conditions, to prove the stress-insensitivity of the n-type circular piezoresistor featured over (111) silicon plane. While the second part is the stress sensing rosette response when it is subjected to certain stress at different thermal environments. The last part shows the experimental stress output at different mechanical loads and temperatures.

5.3.3.1 Temperature Sensor

The TCR (α) of the n-type circular piezoresoitor was firstly calibrated by applying a stress-free temperature load using an environmental chamber to control the thermal load. The temperature was varied over a range from 0 °C to 50 °C. As shown in Figure 5-13, the circular piezoresistor exhibits an excellent linear relationship between the temperature and its resistance change. To prove the stress-insensitivity of the temperature transducer, a uniaxial-stress up to 50 MPa was applied. In Figure 5-14, the temperature transducer demonstrated a linear response with temperature change despite the 50 MPa mechanical stress applied. It has been noticed that a very slight shift in α occurs due to the effect of the applied mechanical stress. However, the proposed temperature transducer succeeded in capturing accurately the local changes in temperature. A maximum absolute error of ~ ±0.8 °C in the measured temperature was obtained while the micro-fabricated device was subjected to stress up to 50 MPa, as in Figure 5-15. The experimental results showed an excellent agreement with the analytical prediction in Chapter 3.

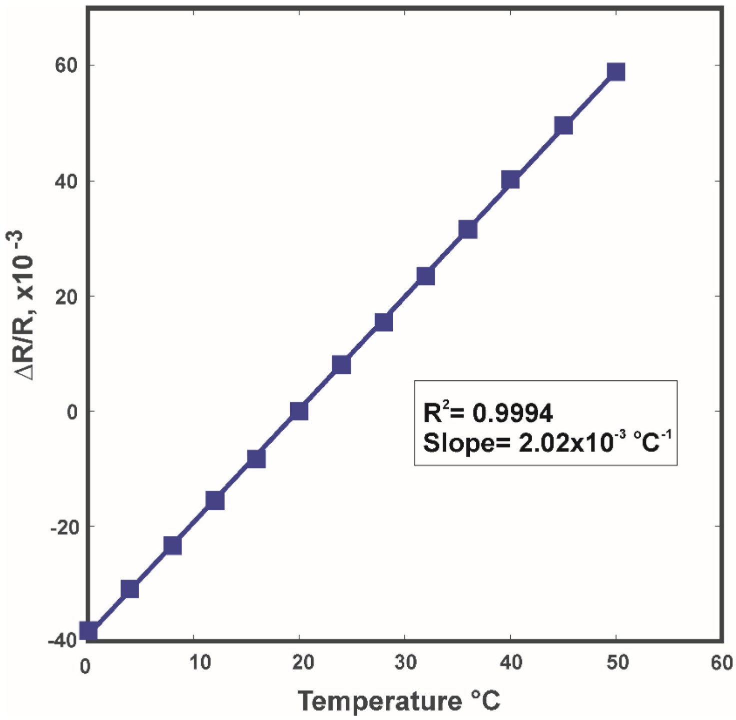

Figure 5-13 Typical results for temperature versus resistance change of n-type circular piezoresistor over (111) plane

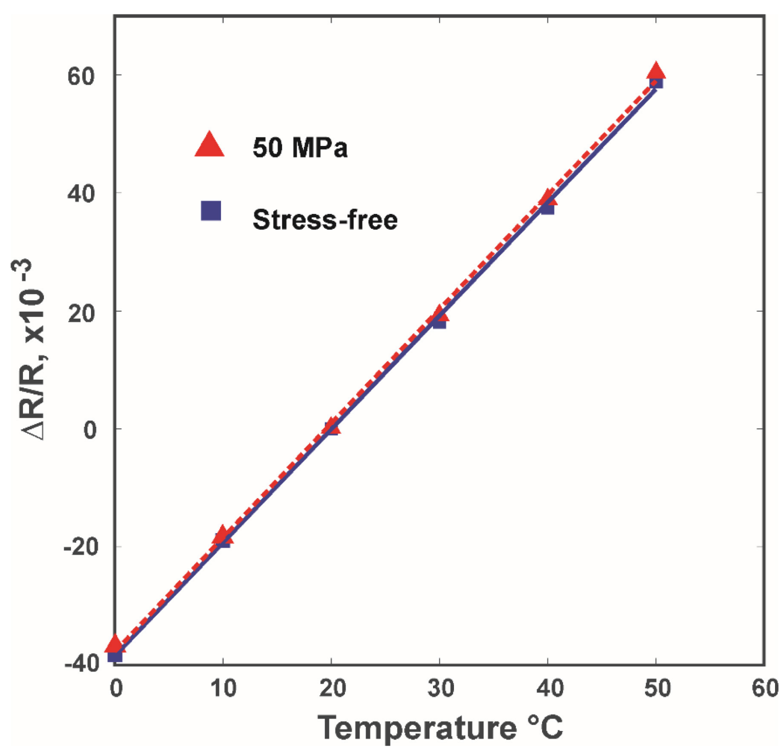

Figure 5-14 Measured response of the temperature transducer subjected to mechanical stress up to 50 MPa

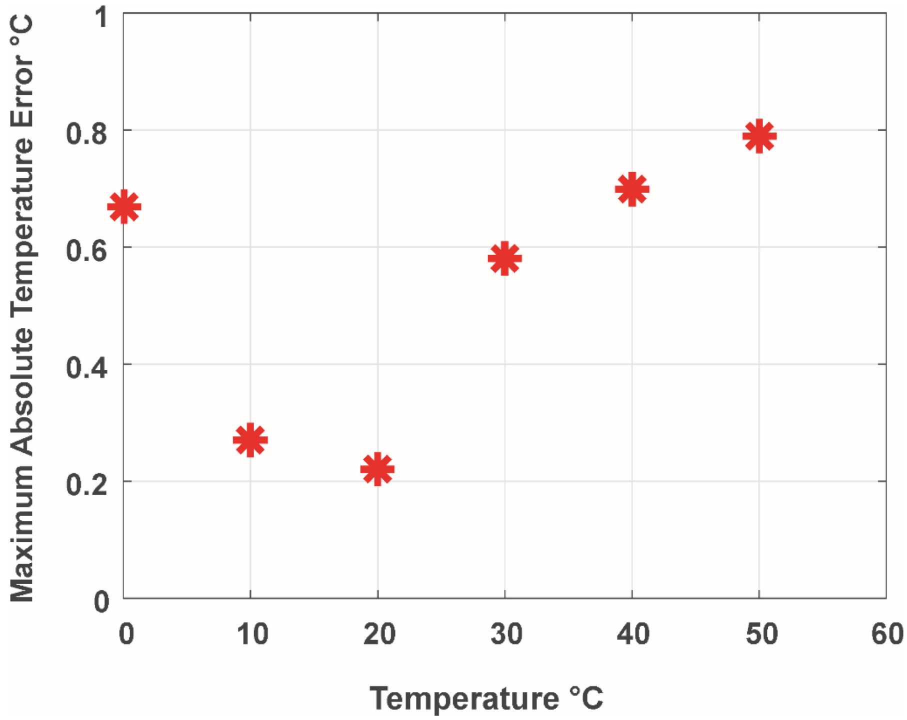

Figure 5-15 Maximum absolute temperature error for loaded test device up to 50 MPa

5.3.3.2 Stress Sensor output

Two different procedures were used to evaluate the capability of the developed stress senor to capture the stress components with temperature compensation. Firstly, the two specimens S0 and S45 were subjected to constant mechanical load while a temperature sweep from 0 °C to 50 °C was carried out. Figure 5-16 and Figure 5-17 show the real-time response of both S0 and S45 specimens subjected to uniaxial stress of ~21 and ~44 MPa, respectively. It can be clearly seen that the developed sensing chip successfully captured the applied stress with temperature compensation. For S0 specimen, the compensated in-plane normal stress, using temperature sensor to compensate for the thermal effect, has an average of 23.4 MPa and relative standard deviation (RSD) of 9.3%. On the other hand, the uncompensated signal resulted in a large error exceeded 300%. For in-plane shear stress exerted on S45, the developed sensing chip was capable of extracting the applied stress with an average of 23.6 MPa and RSD of 3.2%.

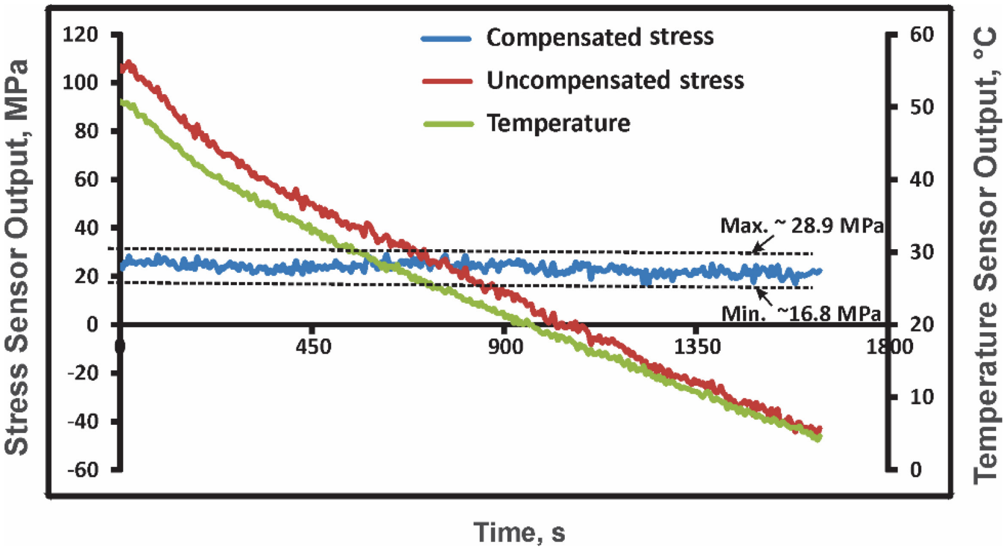

Figure 5-16 Real-time response of sensing chip S0 subjected to uniaxial stress of ~21 MPa and temperature change from 50 °C to 0 °C

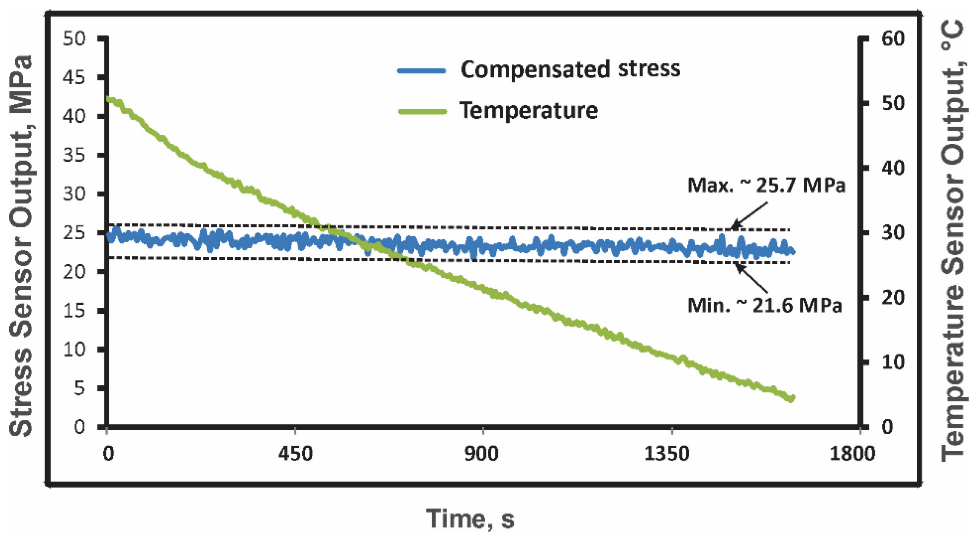

Figure 5-17 Real-time response of sensing chip S45 subjected to uniaxial stress of ~44 MPa and temperature change from 50 °C to 0 °C

For further evaluation of the developed stress sensor, both specimens S0 and S45 were subjected to four different loads that produce uniaxial stress upon the PCB beam within a range from 0 to around 60 MPa. These loads are applied at different temperatures over a range from 0 °C to 50 °C. Figure 5-18 and Figure 5-19 show both measured in-plane normal stress (σ_{11}) and in-plane shear stress (σ_{12}) at different temperatures. The developed sensing chip successfully captured the applied stress with a maximum absolute error of ~16% FS with temperature compensation. However, this error doesn't only arise from the accuracy of the compensation system, but also from the change of PR coefficients values with temperature. In this study, PR coefficients' values are assumed to be constant with temperature changes. For higher accuracy for such multi-element sensing rosette, it is recommended to take into consideration the effect of temperature on PR coefficients' values and compensate it.

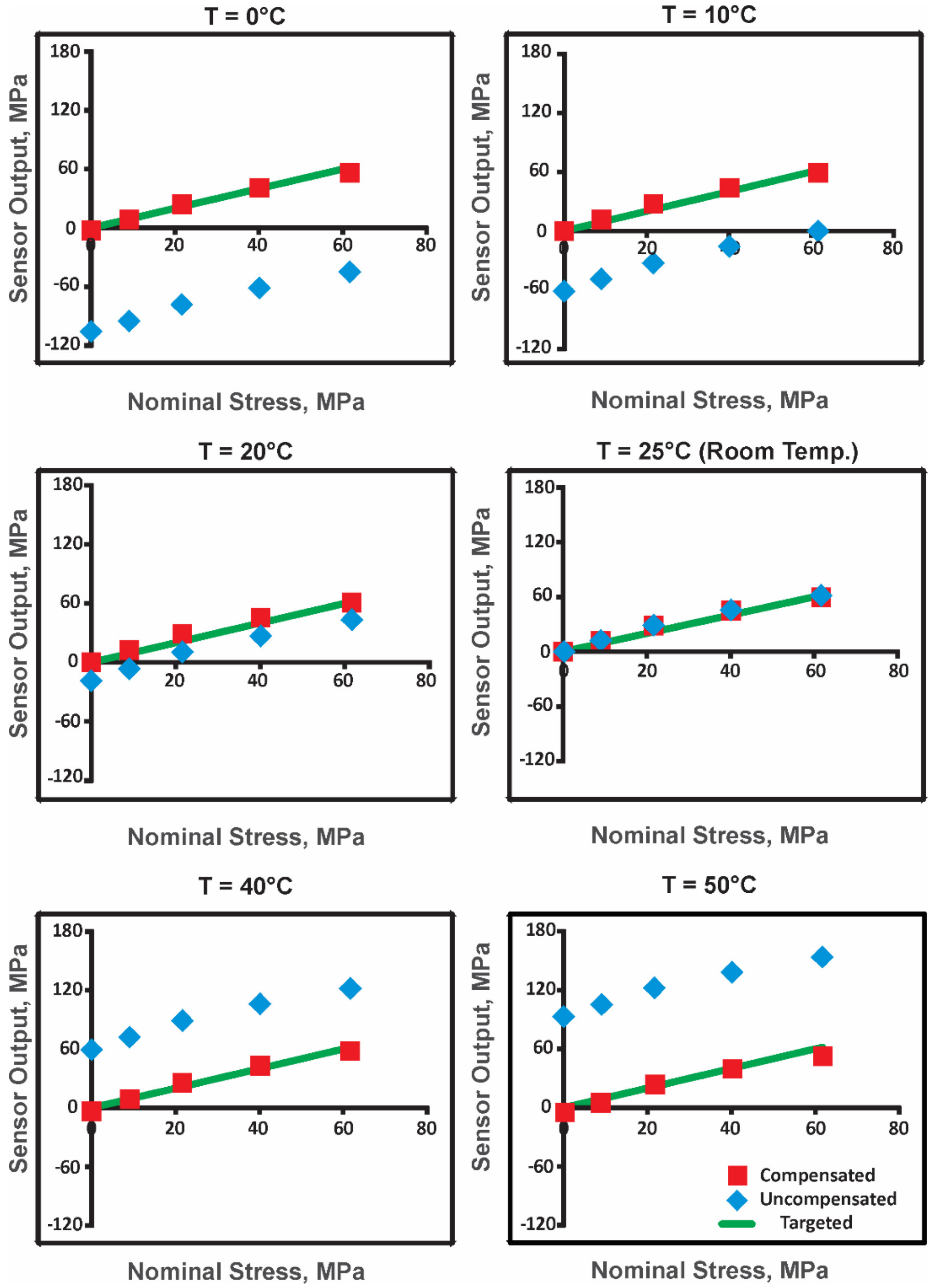

Figure 5-18 Measured stress output of the S0 specimen before and after temperature compensation.

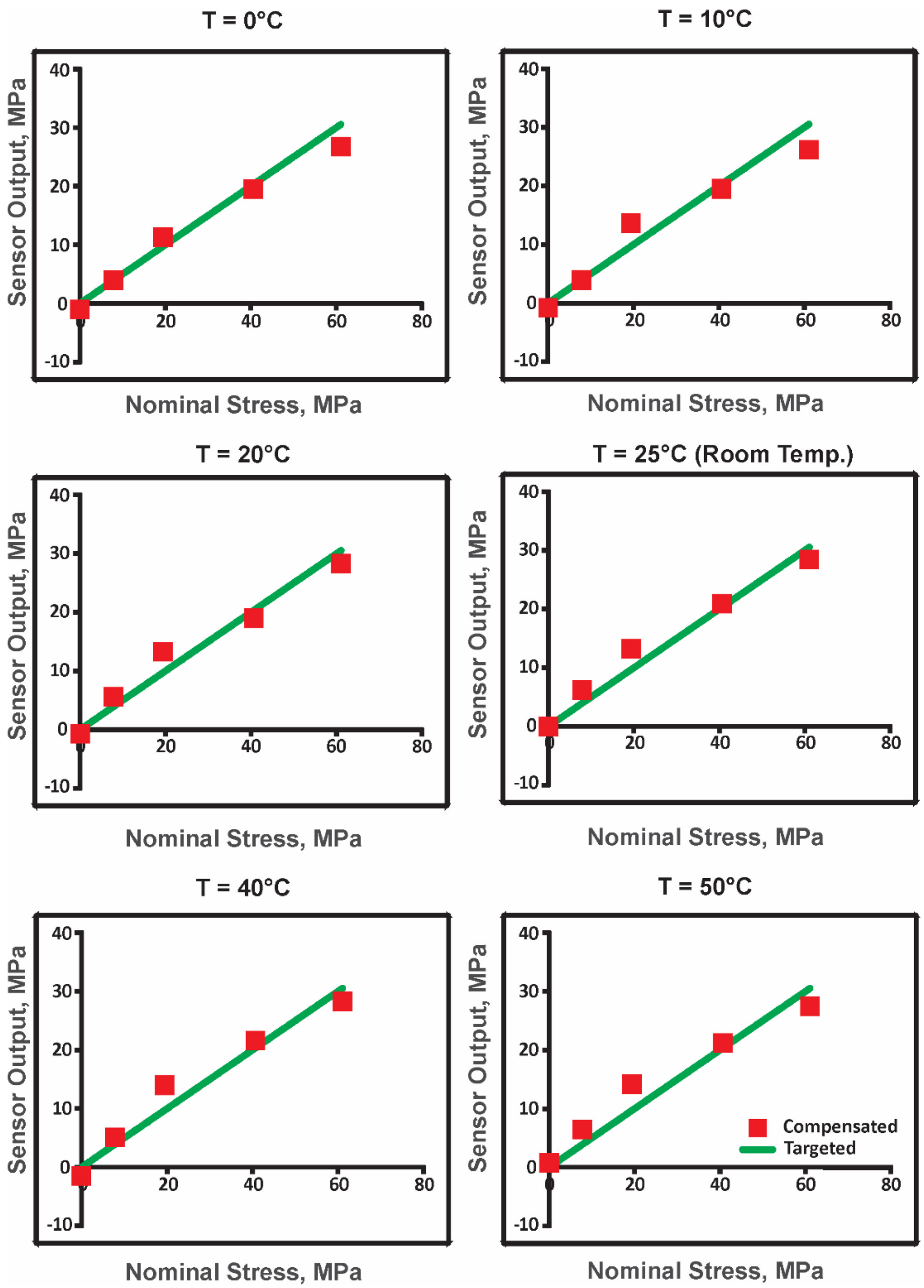

Figure 5-19 Measured stress output of the S45 specimen before and after temperature compensation.

5.4 Conclusions

This chapter presented first the linear calibration process conducted to extract PR coefficients (B_i) and the TCR (α) for the two groups of stress sensing elements and the temperature sensor as well. In this calibration process, the PR coefficients were considered constant and their temperature dependency was ignored. This assumption is valid for the highly doped piezoresistors (Reference needed), which is the case for the developed sensor. Moreover, for all the sensing elements within each group, the PR coefficients and TCR were assumed the same to be able to use the sensor's stress equations provided in chapter 3.

Then the prototype sensing chip was experimentally tested through three different testing procedures. The first test was conducted for the proposed temperature to prove the stress-insensitivity of the n-type circular piezoresistor over (111) silicon plane through capturing its response with temperature changes at both, the stress-free and applied stress conditions. The second test was carried to evaluate the temperature compensation system while extracting applied stress. In this test, the stress sensing chip was subjected to certain stress, using four-point bending loading, at different thermal environments. Finally, the developed sensor's capability to extract different mechanical loads at different temperatures was evaluated in this chapter. The sensing chip was flipped and bonded to the PCB with two different orientations, 0 and 45 degrees, namely S0 and S45 respectively, to induce a number of different stress components, specifically in-plane normal and shear components, on the sensing rosette under four-point bending loading.

The results showed that the temperature sensor can successfully extract the temperature changes occur on the surface of the sensing chip with a maximum error of ~ ±0.8 °C. In the meantime, the stress sensing rosette was able to capture the applied stress at the different thermal environments with a maximum absolute error of ~16% FS. However, this error doesn't only arise from the accuracy of the compensation system, but also from the assumptions made through the linear calibration process. Therefore, there is a need for an accurate calibration algorithm to consider the nonlinearity and temperature dependency of the PRCs that may exist for more accurate stress measurements. A smart with high accuracy calibration algorithm using artificial intelligence, i.e. artificial neural networks (ANNs), is presented in the next chapter, for such multi-element stress sensors.

CHAPTER 6: SMART HIGH ACCURACY CALIBRATION ALGORITHM

6.1 Overview

This chapter presents a smart calibration technique utilizing the artificial neural network (ANN) to eliminate the error in stress measurement, due to the fabrication non-uniformity within wafer, wafer-to-wafer, and batch-to-batch, for multi-element piezoresistive sensing rosettes. In this study, sensing chips from two different batches were integrated into building the ANN and testing its performance. The proposed calibration technique employs the Neural Network Fitting Toolbox in Matlab to generate a two-layer feed-forward network, with sigmoid hidden neurons and linear output neurons.

In addition, a new hybrid temperature compensation system that integrates the full-circular n-type piezoresistor (temperature sensor) with the artificial neural networks (ANNs) is introduced in this chapter. The extracted temperature changes, using the temperature transducer, along with the resistance changes, are fed, as inputs, to the ANNs to compensate the temperature effect on the acquired signals for more accurate stress measurement. This proposed compensation system is used to smartly compensate for the temperature effect on both resistance and sensitivity of the piezoresistive element.

Finally, as an improvement to the sensitivity of the out-of-plane stress/strain measurement, a strained silicon technique was integrated into the proposed sensing rosette during the microfabrication process. A prototype sensing chip was microfabricated to test the capability of the developed sensing rosette to accurately extract stress applied on structures at different thermal environments.

6.2 Sources of Error for Multi-element Sensing Rosette

Previous efforts were conducted to analyze the sources of error accompanying stress measurements using doped silicon multi-element piezoresistive sensing rosettes. Jaeger et al. [80], [82] studied the errors associated with the calibration of the piezoresistive stress sensors. Their results indicate that uncertainties of 10% or more in PR coefficients' values might be obtained from experimental calibration, which in turn could produce large errors in extracted stress values. Moreover, error analysis was conducted to study the effect of measurement and calibration errors on the output of the (111) stress sensors by Hussain et al. [84]. They concluded that the sensitivity is dependent on the stress distribution over the surface of the sensing chip. Their findings also confirmed the utilization of temperature compensated rosette configurations, since they are less sensitive to measurement uncertainty.

6.2.1 Fabrication Non-uniformity

During the derivation of the stress equations of the developed rosette, the PRCs and TCR are assumed the same for each group of piezoresistors (*a* and *b*). However, a variation in PRCs values may exist, within the same group of piezoresistors, chip-to-chip, or wafer-to-wafer due to the fabrication non-uniformity. To study the change PRCs due to the fabrication uniformity, different chips diced off from different wafers of single batch were collected and tested in a temperature-controlled environment ($\Delta T = 0$) using the four-point bending setup, introduced in Chapter 5. The typical responses of 0 and 90 degree oriented piezoresistors, of different chips, subjected to uniaxial stress are shown in Figure 6-1 toFigure 6-4Figure 6-8. The PRCs, B_1, and B_2 are the slope of the 0 and 90 degree piezoresistors' responses, respectively. It's clearly seen that the value of B_1 and B_2, of groups *a* and *b*, varies due to the fabrication non-uniformity from chip-to-chip and wafer-to-wafer. This variation in PRCs values may lead to a large error in stress measurements for such multi-element sensing rosettes [15]. In the linear calibration process, provided in Chapter 5, the change in PRCs from fabrication non-uniformity wasn't considered, since only a single resistor of each group was utilized to calibrate PRCs and TCR. Moreover, the calibration samples, in linear calibration, were different from the chips employed for the testing provided in Chapter 5, as it was challenging to dice off the calibrated rosette from the calibration beam. To this end, a new calibration algorithm is needed to consider the variation in PRCs and TCR, within the same group, chip-to-chip, wafer-to-wafer or batch-to-batch, for more accurate stress measurements.

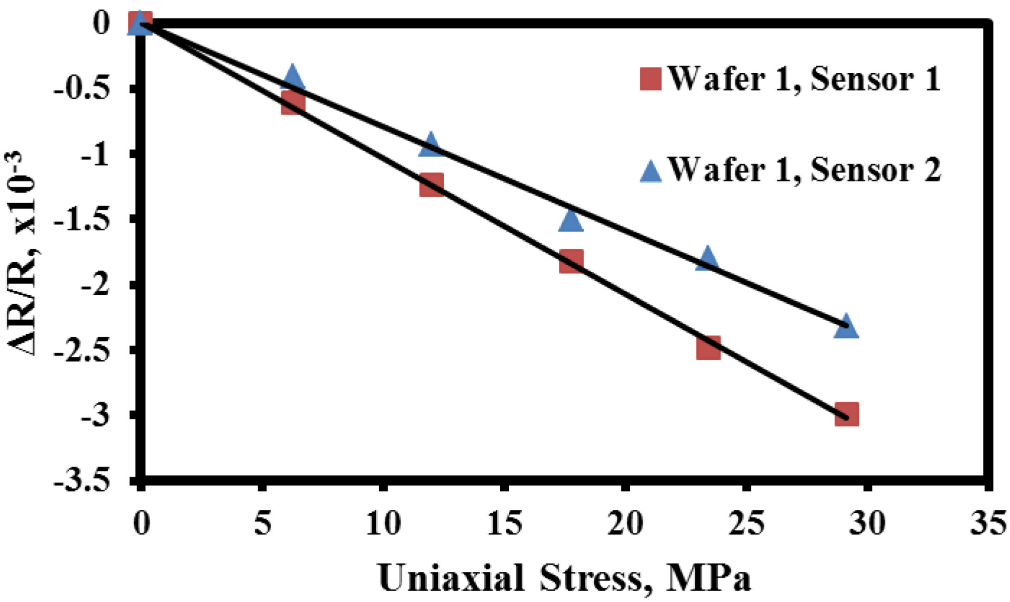

Figure 6-1 Typical response of resistor R_1 subjected to uniaxial stress (slope is B_1 for group a) for two different sensors diced off from the same wafer.

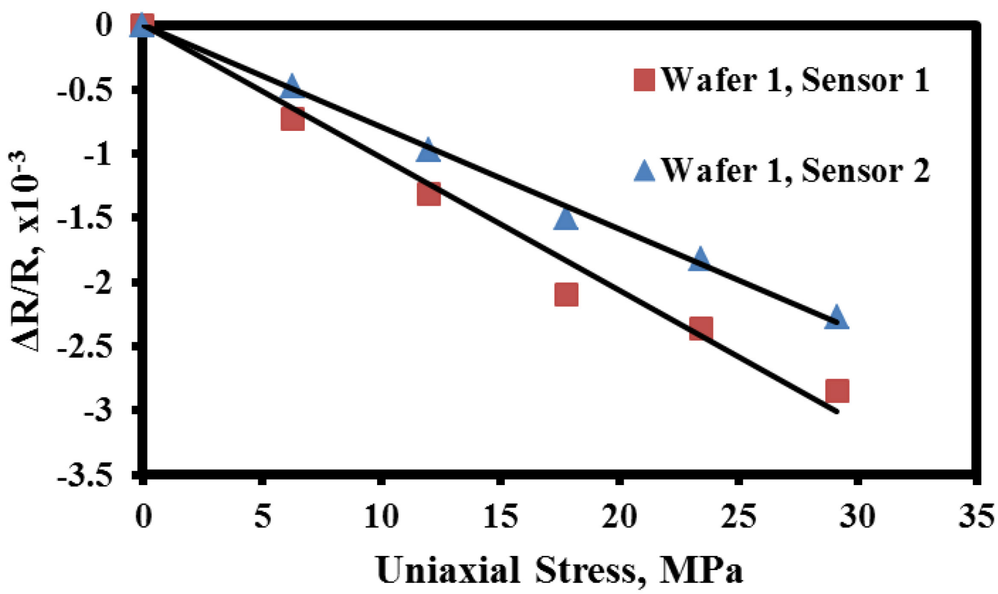

Figure 6-2 Typical response of resistor R_5 subjected to uniaxial stress (slope is B_1 for group b) for two different sensors diced off from the same wafer.

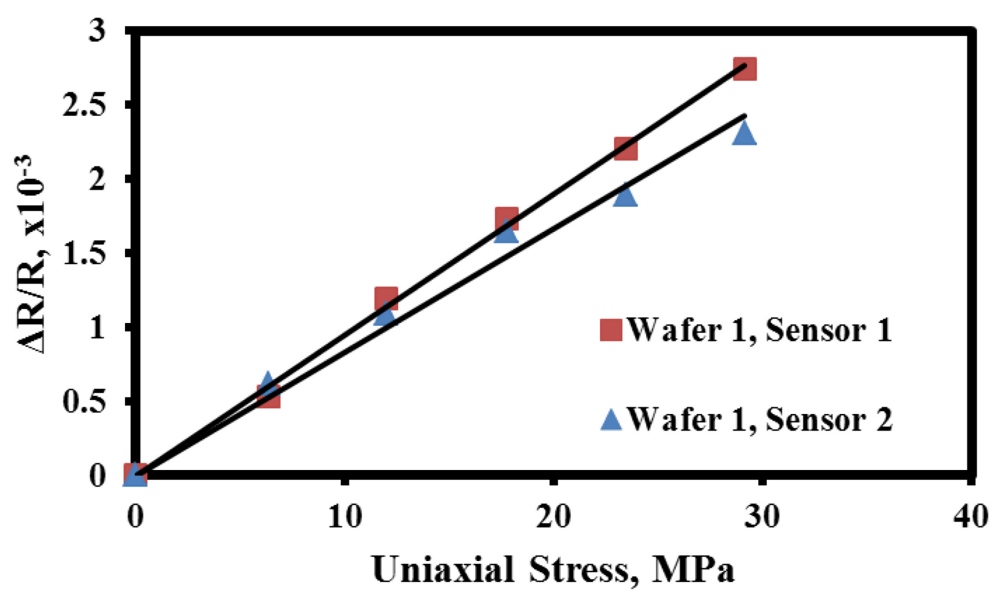

Figure 6-3 Typical response of resistor R_3 subjected to uniaxial stress (slope is B_2 for group a) for two different sensors diced off from the same wafer.

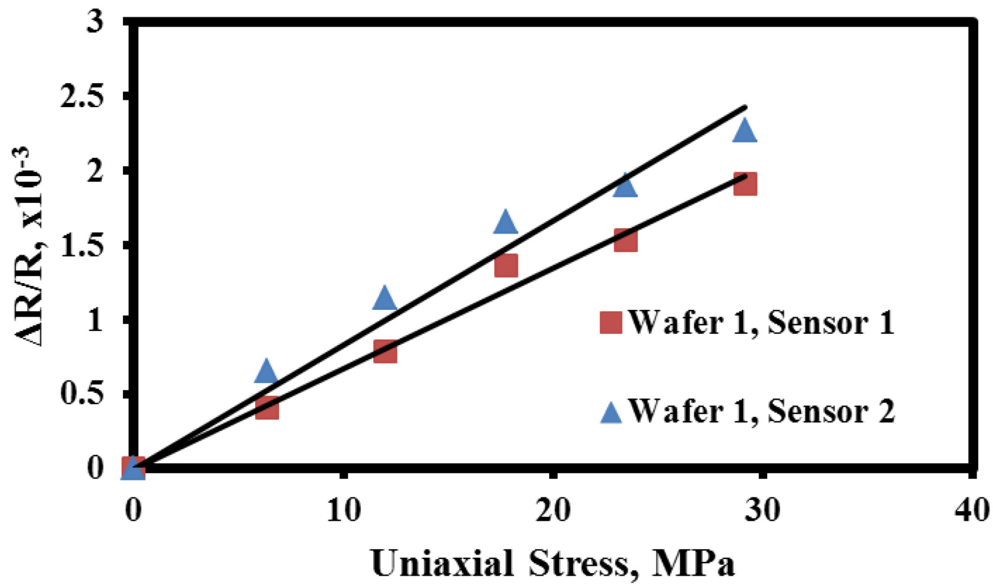

Figure 6-4 Typical response of resistor R_7 subjected to uniaxial stress (slope is B_2 for group b) for two different sensors diced off from the same wafer.

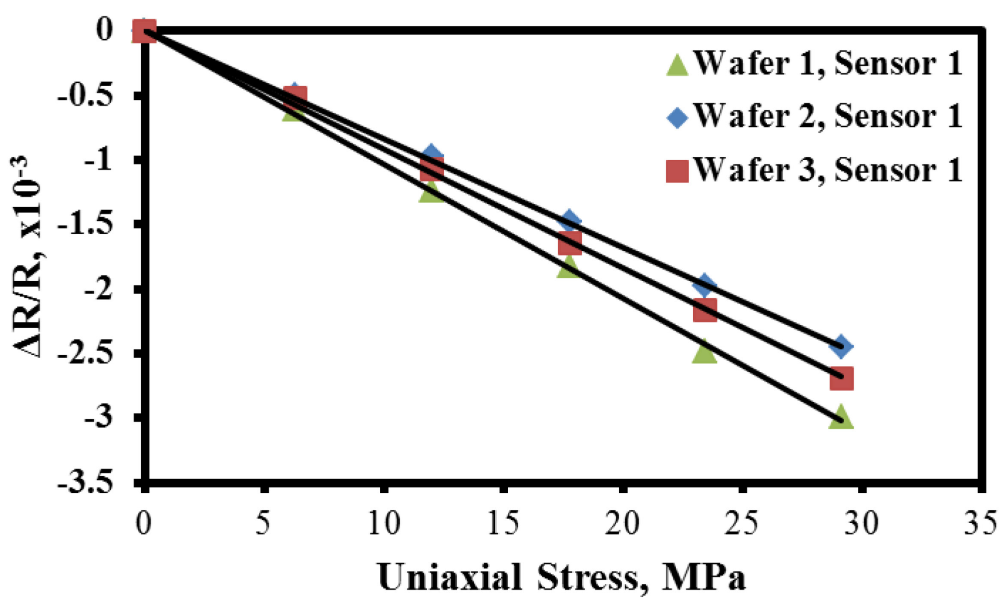

Figure 6-5 Typical response of resistor R_1 subjected to uniaxial stress (slope is B_1 for group a) for three sensors diced off from the three different wafers.

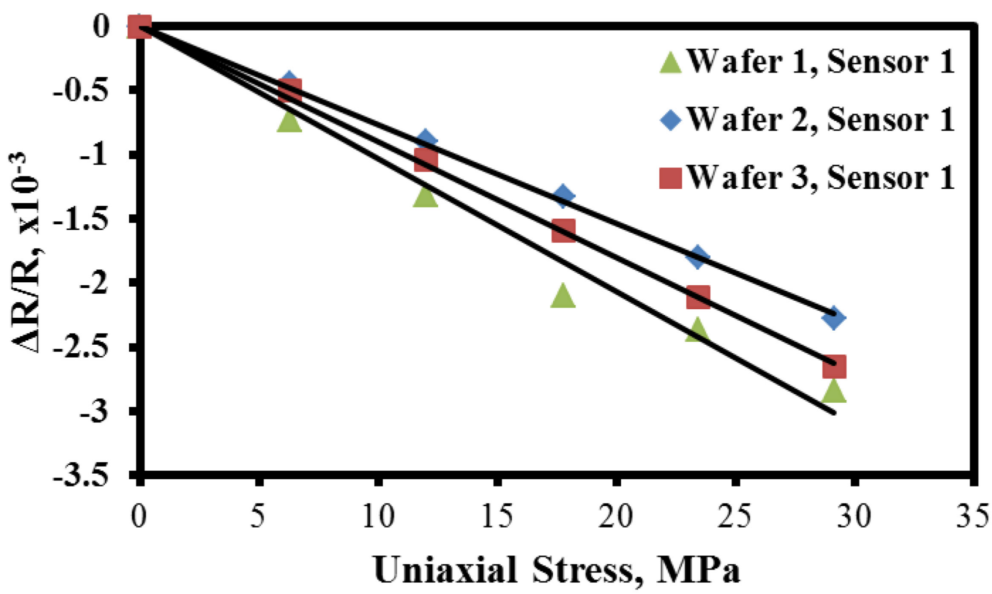

Figure 6-6 Typical response of resistor R_5 subjected to uniaxial stress (slope is B_1 for group b) for three sensors diced off from the three different wafers.

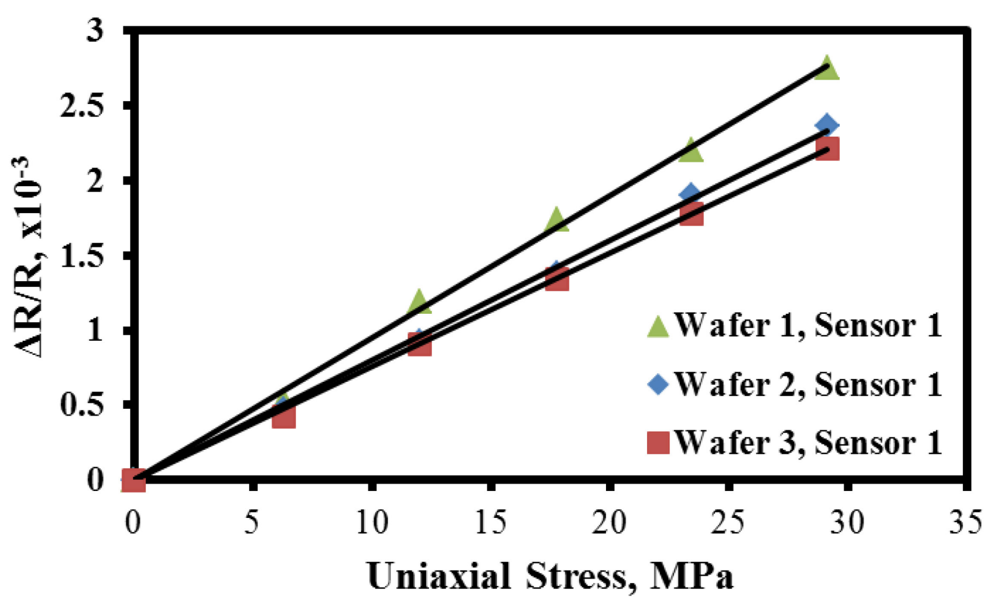

Figure 6-7 Typical response of resistor R_3 subjected to uniaxial stress (slope is B_2 for group a) for three sensors diced off from the three different wafers.

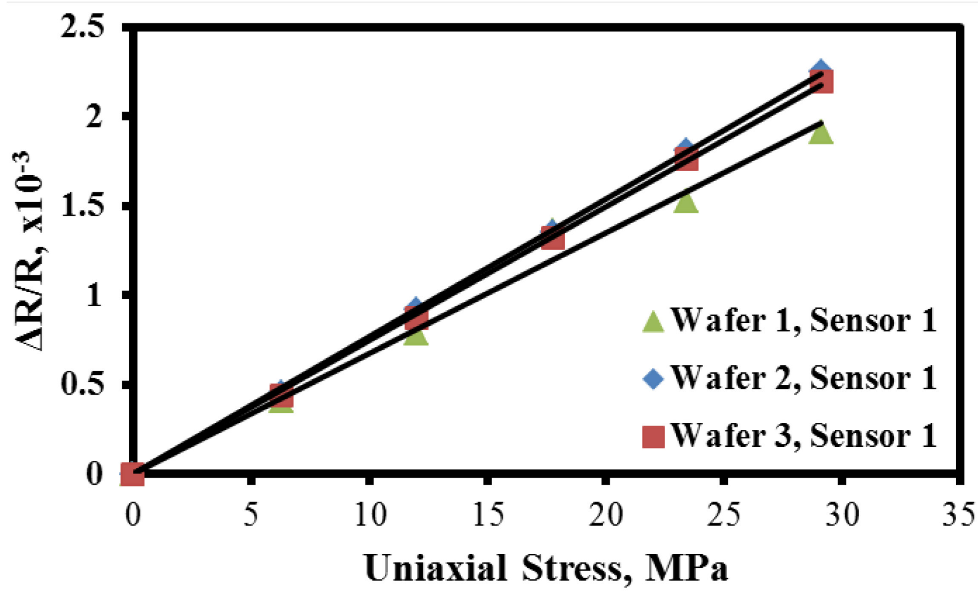

Figure 6-8 Typical response of resistor R_7 subjected to uniaxial stress (slope is B_2 for group b) for three sensors diced off from the three different wafers.

6.2.2 The Temperature Dependency of PRCs

Piezoresistive stress sensors are sensitive to temperature variation, which changes the mobility and number of carriers of piezoresistors, resulting in a change in resistivity and piezoresistive coefficients (PRCs) [3]. This temperature-induced signal during typical operation can be larger than the intended sensor output. Tufte and Stelzer discussed the temperature dependence of the large PRCs, π_{11} for n-type and π_{44} for p-type silicon, on layers having surface concentration values from 10^{18} to 10^{21} cm^{-3} [52], [53]. For n-type silicon, it was found that π_{11} decreases with increasing temperature as given in Table 6-1. Therefore, there is a need for developing a more accurate calibration algorithm, in which the temperature dependency and nonlinearity of PRCs is considered, for more accurate stress measurements. Cho et al. [83] experimentally characterized the temperature dependency of the large n-type PRCs, $B_{1,}$ and B_2, on (111) silicon plane. They found that all the coefficients linearly decrease with increasing temperature at constant doping concentration, as shown in Figure 6-9.

Table 6-1: π_{11} for n-type silicon measured by Tufte et *al* [52], [53]

	Doping Concentration (cm^{-3})				
T(°C)	1.3x10^{16}	1.8x10^{18}	8.8x10^{18}	5.0x10^{19}	9.0x10^{19}
-200	-3200	-	-	-590	-500
-150	-2200	-	-	-585	-510
-100	-1800	-	-1100	-570	-500
-50	-1400	-1020	-780	-530	-490
0	-1300	-925	-690	-500	-450
25	-1156	-870	-635	-490	-435
50	-1000	-790	-590	-480	-420
75	-800	-710	-555	-470	-415
100	-	-660	-540	-	-

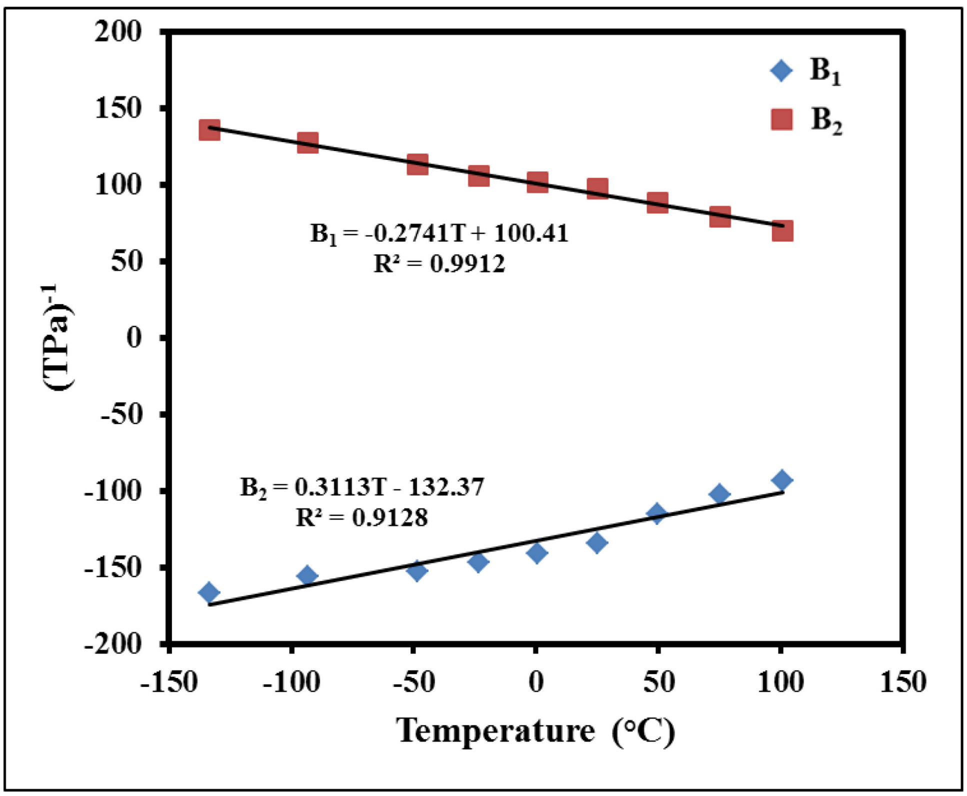

Figure 6-9 Extracted n-type PRCs (B_1 and B_2) with temperature changes for (111) silicon plane [83]

6.3 Neural Networks Calibration Algorithm

Some researchers proposed novel designs and some fabrication processes as compensation systems to overcome the sources of error associated with the measurement and thus enhance the accuracy of sensors [104], [105]. But, other smart compensation approaches have been provided using signal-conditioning interfaces, hardware-based and software-based, for thermal drifts and nonlinearity issues in piezoresistive sensors [7], [92]. For software-based smart calibration systems, the artificial neural networks (ANNs) provide an efficient tool for sensor compensation and linearity correction [106]. The ANNs were successfully utilized as an inverse modeling method for mapping nonlinear input-output relations of sensor signals [107]–[111].

In this work, a new calibration algorithm is proposed, using ANNs, to improve the proposed stress sensor's performance by eliminating the measurement error due to the uncertainties in the values of PRCs and TCR obtained from conventional experimental calibration techniques. The ANNs can be used to build a smart calibration system that would be able to compensate for all errors arise during fabrication and calibration that may lead to uncertainty in knowing the exact values of the PRCs. This proposed calibration algorithm abolishes the need for a costly and time-consuming calibration process for each sensor in a fabricated batch.

6.3.1 Testing setup

To consider the non-uniformity within the wafer, the sensing chips used in building and testing ANNs were selected from different locations across the wafer, specifically, around the periphery of the wafer and the middle of the wafer where the maximum non-uniformity within the wafer appears [112]. In addition, to include the non-uniformity from wafer-to-wafer or batch-to-batch, sensing chips from different wafers of two different batches were utilized to evaluate the calibration capabilities of ANNs. All collected sensing chip was flipped and bonded to the PCB with two different angles, 0 and 45 degrees, to provide two sets of S0 and S45 specimens shown in Figure 5-10. These two configurations of specimens are used to induce both in-plane normal and shear stress components, on the sensing rosette under four-point bending loading.

To measure the resistance change of the stress sensing elements and the corresponding applied load on the beam at each loading increment, the testing setup, shown in Figure 5-12, was used. An incremental load from 0 to around 7.5 N was applied to the chip-on-PCB beam. For each load, the corresponding average stresses, exerted at the center of the sensing chip, were estimated from FEM using ANSYS APDL. The FEM is provided in Appendix C.

6.3.2 Software Setup

A double layer feedforward ANNs function was constructed using the ANNs fitting toolbox in MATLAB software. Five specific steps: Collect Data, Divide Data, Train ANN, Validate ANN, and ANN Analysis, are followed to build the smart calibration algorithm using ANNs, as shown in Figure 6-10. In the Data Collection step, different known stresses (σ) are applied to the sensing chip and the corresponding resistance changes ($\Delta R/R$) of the sensing elements are obtained. For the collected calibration points, the resistance changes are the ANNs inputs, while the corresponding stresses are the ANNs targets. All calibration points are collected at a thermally controlled environment ($\Delta T = 0$) to only investigate the capability of the ANNs to compensate for the uncertainties in PRCs arise from the fabrication non-uniformity. The collected data was then randomly divided into training data and testing data with a ratio of 3 to 2. To configure and train the network, the training data was only used, while the testing data was employed to validate the configured ANN. Some analyses of the network response (i.e. network performance and linear regression), were performed during the training and validation phases to evaluate the configured network. Finally, the network was retrained until a satisfactory small Mean Square Error (MSE) between the network outputs and targets was obtained. The MATLAB code, used to generate ANNs function, is provided in Appendix D.

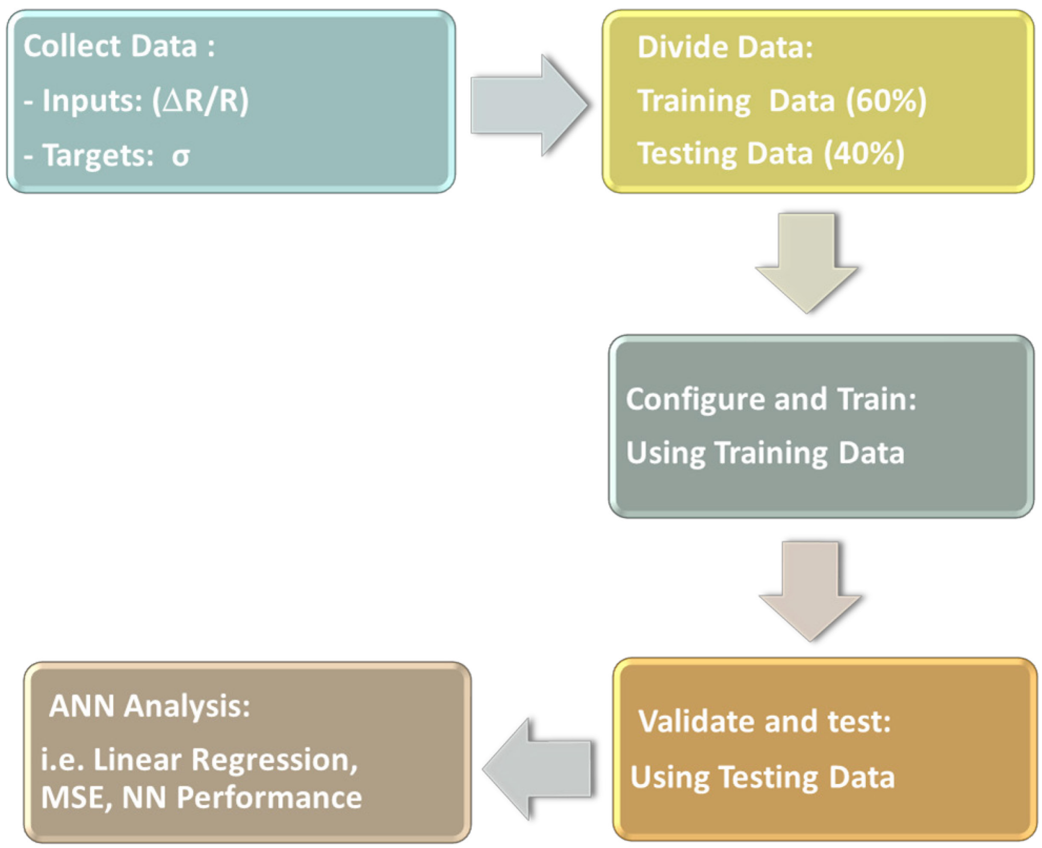

Figure 6-10 Steps of building ANNs calibration algorithm

6.3.3 The Configurations of ANNs Calibration Points

Since the size of the training set has a great influence on the generalization ability of the ANNs [113]. Three different configurations of calibration 4x10, 6x10, and 8x10, were designed to investigate the effect of sample size on the accuracy of the ANNs calibration algorithm to predict the in-plane stress components σ_{11}, σ_{12}. In the 4x10 configuration, 40 calibration points obtained from the experimental testing of 4 different sensing chips were used to build ANN. While, in 6x10 configuration, 60 calibration points were collected from testing 6 different sensors under the same loading conditions of 4x10 configuration. Finally, using 8 different sensors, 80 calibration points were provided to construct ANN of 8x10 configuration.

In all three configurations, the sensing chip is attached to a PCB beam that is subjected to10 different loads within a range from -7.5 to 7.5 N that produce 10 corresponding average stress values within a range from -40 to 40 MPa on the sensing chip surface.

6.3.4 Results and Discussion

To test the accuracy of the ANNS calibration algorithm in predicting the stresses, new experimental data set were collected using new 5 randomly selected testing sensing chips. Each sensor of the 5 testing chips was subjected to 10 different loads within a range from -7.5 N to 7.5 N. The change in electrical resistance of each sensing element of the ten-element sensing rosette and the corresponding stresses, due to the applied load, were measured. Using these resistance change measurements as an input for the ANNs calibration algorithm, the predicted corresponding stresses, which are the ANNs output, can be calculated. Finally, these predicted stresses were compared with the actual stresses and the error was quantified. Moreover, the stress applied was also extracted from equation (3-18), using the PRCs and TCR obtained from the linear calibration process, for comparison and obtaining reliable assessment on using the proposed ANNs for calibration of multi-element sensing rosettes.

As shown in Figure 6-11, a stress error as large as 50% *FS* while extracting in-plane normal stress (σ_{11}), has been obtained from the linear calibration process. Also, the results show that the proposed sensing rosette is less sensitive to the variation in PRCs while extracting the in-plane shear stress (σ_{12}) compared to the in-plane normal stress components (σ_{11}).

On the other hand, Figure 6-12 and Figure 6-13 show the maximum absolute stress error between the predicted in-plane stress components σ_{11} and σ_{22}, using the proposed ANNs calibration algorithm, and the in-plane stresses obtained from FEM for the same load. It can be found that the configuration 4x10 has the maximum error in extracting stresses compared to the other configurations, 6x10 and 8x10, since fewer calibration points were used in building ANN. In the 4x10 configuration, the maximum stress error can reach 9% FS. It can also be clearly seen that increasing the sample size improves the accuracy of the constructed ANNs. As in 8x10 configuration, the maximum absolute stress error dropped to 1.5% FS while extracting the in-plane stress component σ_{11} and σ_{12} using the proposed ANNs calibration algorithm. The results also show that σ_{12} can be predicted with very high accuracy, unlike σ_{11}. As shown in Figure 6-13, for stress range from -20 to 20 MPa, the maximum error in σ_{12} doesn't exceed 0.25% *FS*.

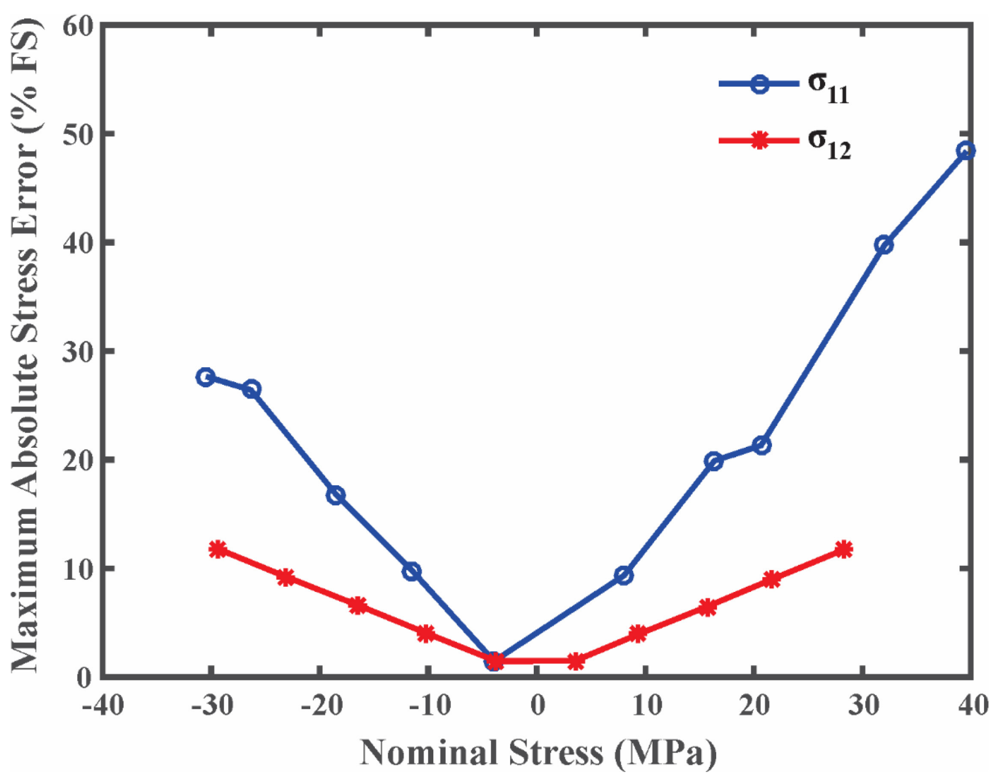

Figure 6-11 Stress measurement error of the proposed sensor using the linear calibration

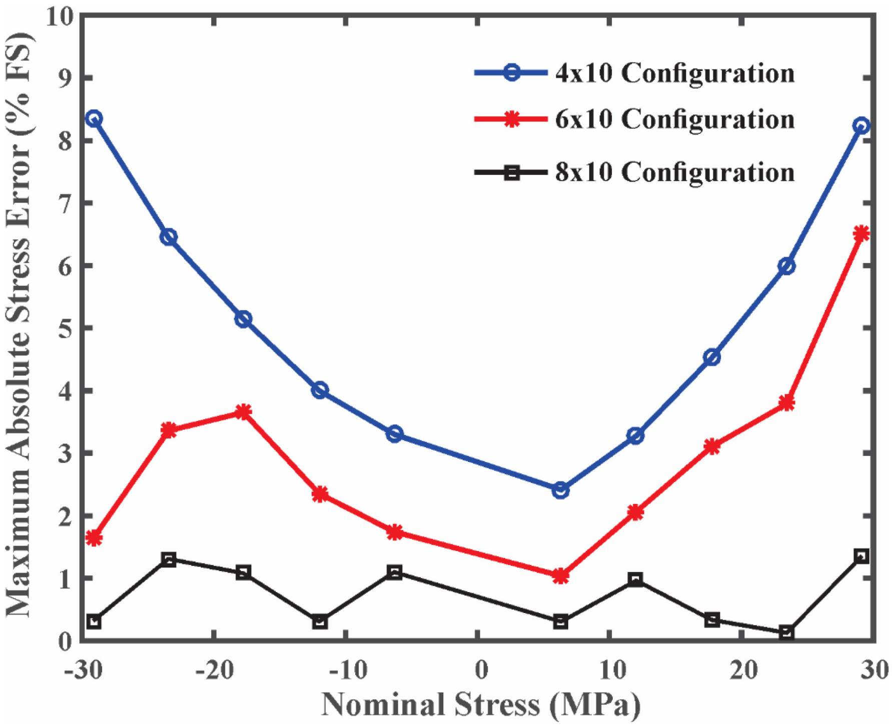

Figure 6-12 Errors in measuring σ_{11} using ANNs calibration algorithm

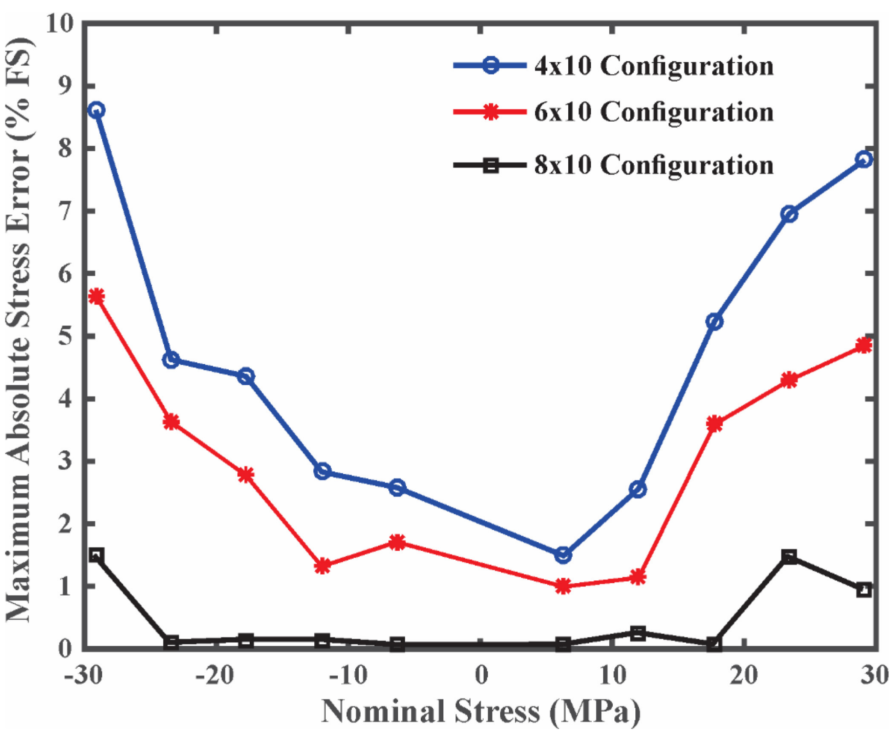

Figure 6-13 Errors in measuring σ_{12} using ANNs calibration algorithm

6.4 Hybrid Temperature Compensation System

As it was presented in Chapter 5, the linear calibration process may result in relatively large error in stress measurements, specifically in-plane normal stress components, since the nonlinearity and temperature dependency of the PRCs are unconsidered. To this end, a hybrid temperature compensation system, which integrates the new proposed temperature sensor (n-type circular piezoresistor) into ANNs, is proposed in this work. The circular piezoresistor was utilized to capture the local temperature changes within the sensing rosette to feed it, as an input, to the ANNs to compensate the temperature effect on both the resistance and sensitivity. To collect the data needed to train and test the ANNs, the developed sensor was subjected to uniaxial stress up to 60 MPa using the setup shown in Figure 5-12, at different temperatures within a range from 0 °C to 50 °C.

6.4.1 Software Setup

A single layer feedforward ANNs function was constructed using the ANNs fitting toolbox in MATLAB software. Figure 6-14 shows the specific steps of creating the smart calibration algorithm using ANNs. In the data collection step, different known stresses (σ) are applied to the sensing chip at different thermal environments and the corresponding resistance changes ($\Delta R/R$) of the sensing elements are obtained. In regards to the ANNs data collected, the resistance changes and temperature are the inputs of the ANNs, while the corresponding stresses are the targets. The collected ANNs data are randomly divided into training data and testing data with ration of 7:3. Three different configurations of 5x5, 7x5 and 11x5, as listed in Table 6-2, were designed to investigate the effect of sample size on the accuracy of the proposed temperature algorithm to predict the stress applied at different temperatures.

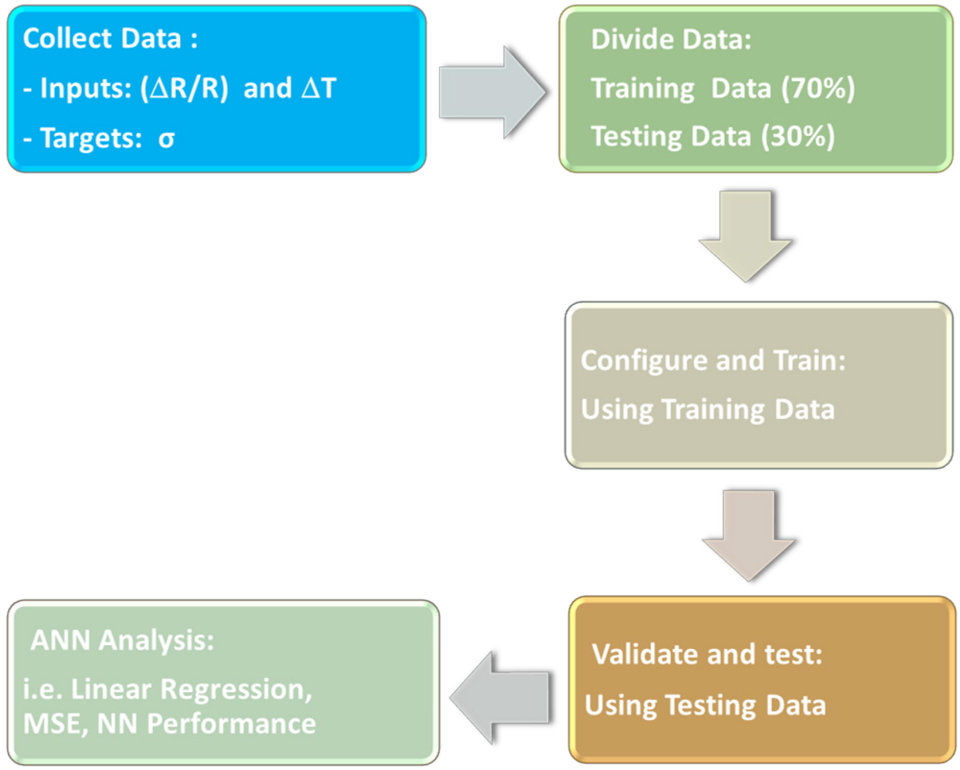

Figure 6-14 Steps of building a hybrid temperature compensation system

Table 6-2: The configurations of the ANNs data

Configuration	Temperature and Stress
5x5	(0,15,25,35,50) °C (0,9,22,24,62) MPa
7x5	(0,10,20,25,30,40,50) °C (0,9,22,24,62) MPa
11x5	(0,5,10,15,20,25,30,35,40,45,50) °C (0,9,22,24,62) MPa

6.4.2 Results and Discussion

Figure 6-15 shows the maximum absolute stress error between the predicted stress using the proposed ANNs calibration algorithm, and the actual stress applied on the sensing chip. It can be found that the configuration 5x5 has the maximum error in extracting stresses compared to the other configurations, 7x5 and 11x5, since fewer calibration points were used in building ANNs. In 5x5configuration, the maximum stress error can reach to ~ 7.5% FS. It can also be clearly seen that increasing the sample size improves the accuracy of the constructed ANNs. As in 11x5 configuration, the maximum absolute stress error dropped to 5.5% FS.

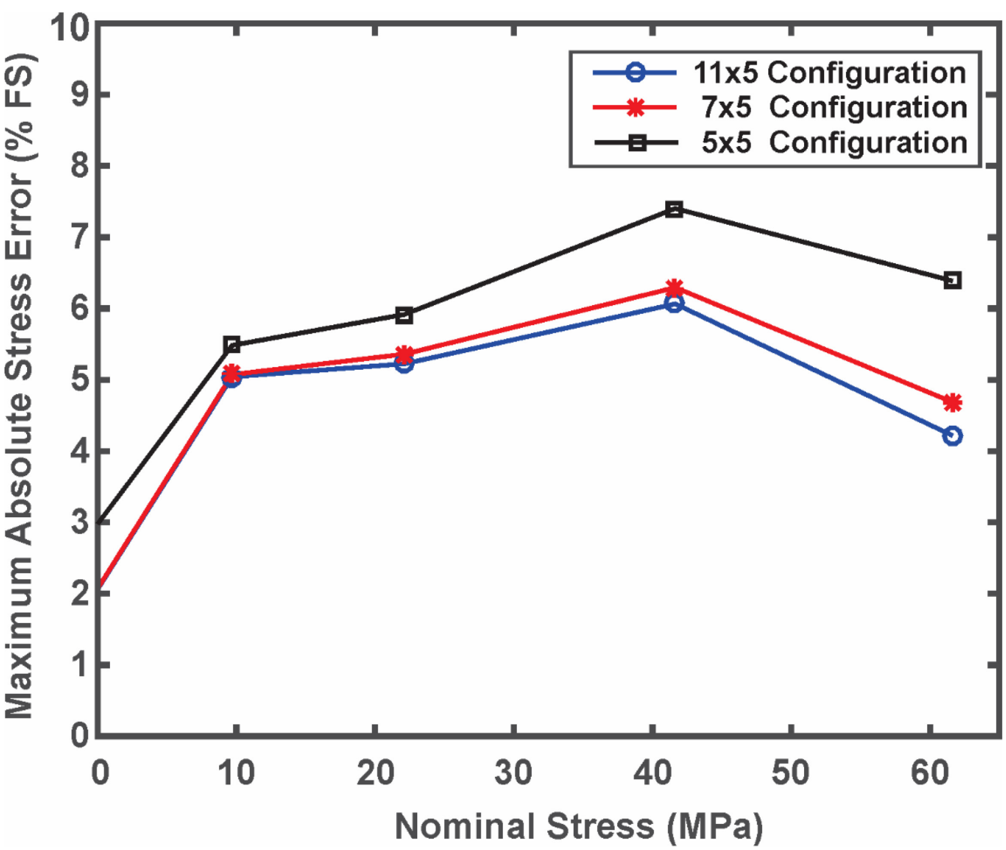

Figure 6-15 Error in stress measurement using the hybrid temperature compensation system for the different configurations 5x5, 7x5, and 11x5

To evaluate the capability of the ANNs compensation algorithm to predict the stress applied, sensing chip S0 was subjected to an in-plane normal stress of ~41 MPa at different temperatures from 50 °C to 0 °C. Figure 6-16 shows the real-time response of sensing chip S0 using both linear and ANNs calibration. It's clearly seen that the ANNs resulted in a significant improvement in the accuracy of the developed sensor with only ~1.5% RSD compared to the stress measurement using the linear calibration, in which ~9.3% RSD was obtained.

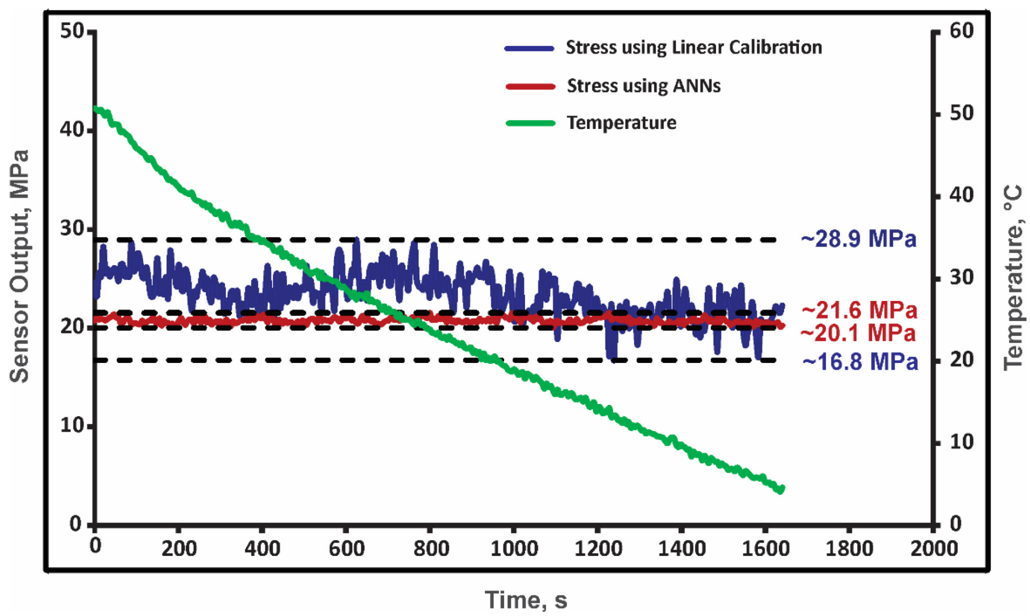

Figure 6-16 Real-time response of sensing chip S0 subjected to in-plane stress of ~21 MPa and temperature change from 50 °C to 0 °C

For further evaluation of the developed compensation system, the test specimen was subjected to four different loads that induce different uniaxial stresses within a range from 0 to around 60 MPa. This test was conducted at different thermal environments over a range from 0 °C to 50 °C. Figure 6-17 to Figure 6-28 show the measured in-plane normal stress (σ_{11}) and the maximum error obtained at different temperatures. For linear calibration, a relatively large error of ~14.5% FS was obtained since only the temperature effect on resistance is compensated using the temperature sensor (circular piezoresistor). On the other hand, the proposed compensation system was successfully able to reduce the error to only ~6.5% FS, as the influence of temperature on both the resistance and PRCs is compensated. Moreover, the proposed compensation system was able to reduce the maximum zero error measured from ~8.8% FS (for linear calibration) to only ~2.1% FS.

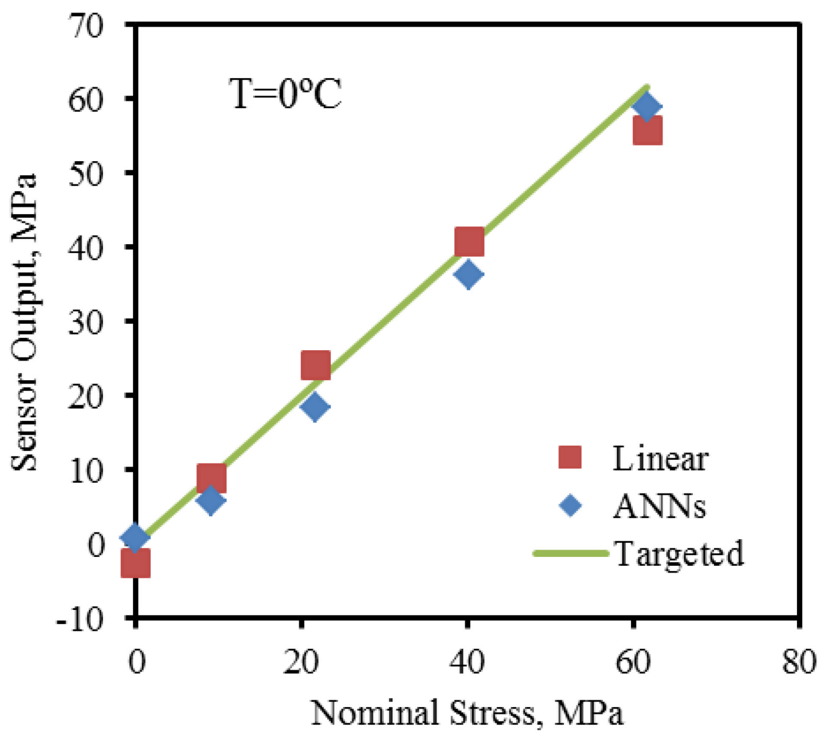

Figure 6-17 Measured stress output using linear calibration and ANNs at 0 °C

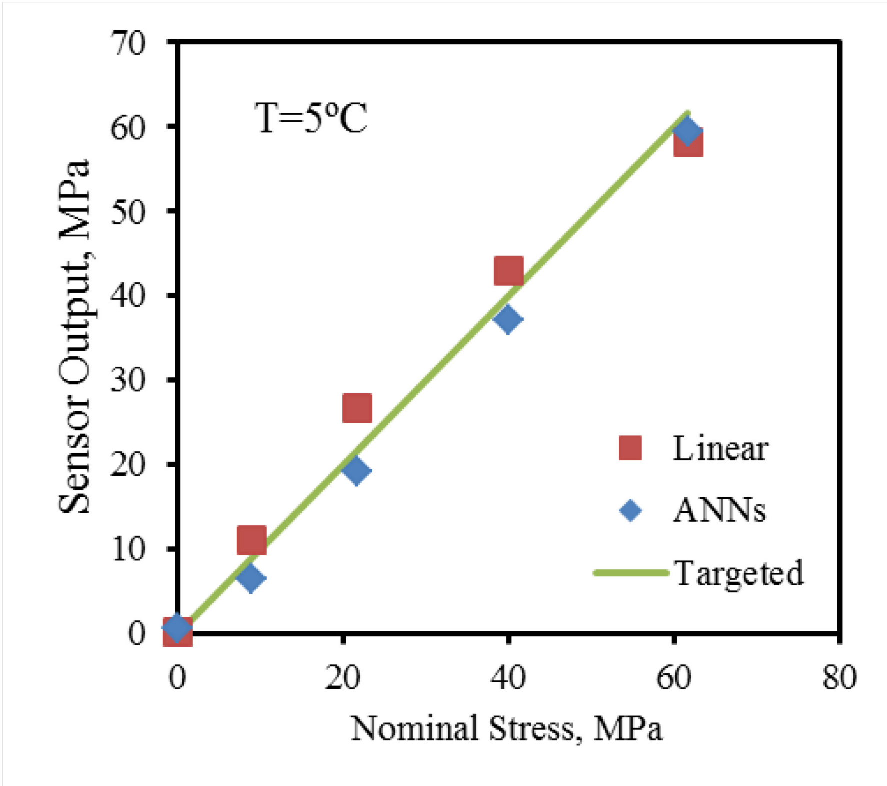

Figure 6-18 Measured stress output using linear calibration and ANNs at 5 °C

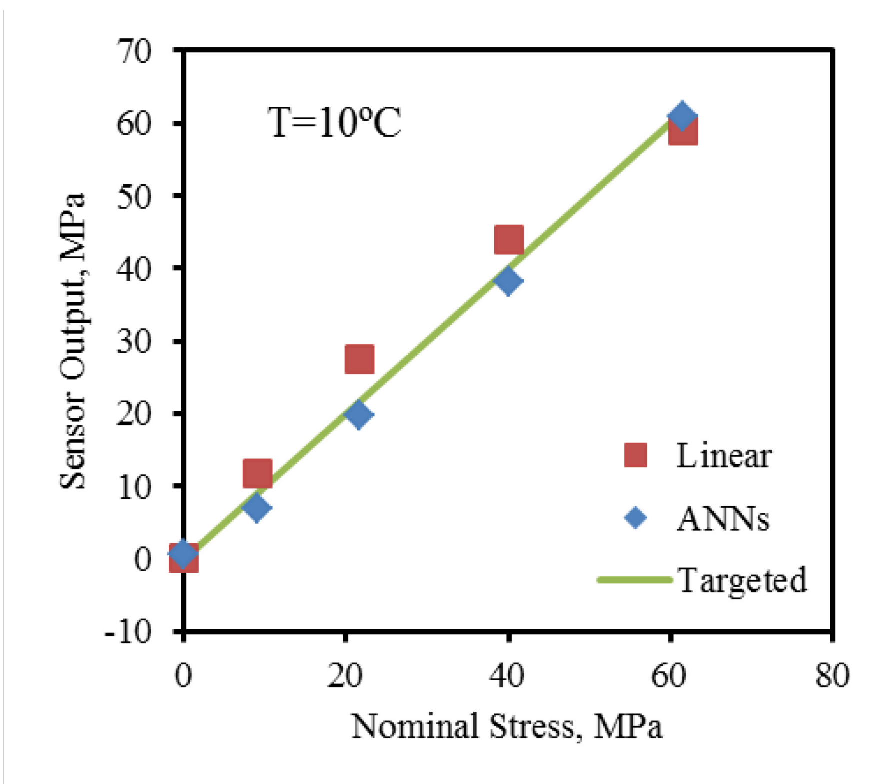

Figure 6-19 Measured stress output using linear calibration and ANNs at 10 °C

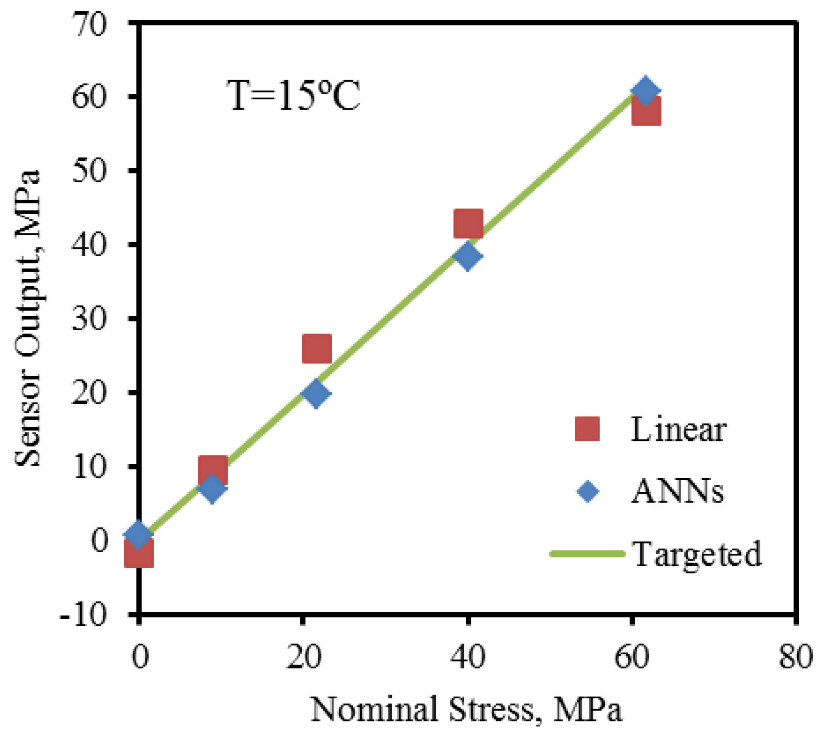

Figure 6-20 Measured stress output using linear calibration and ANNs at 15 °C

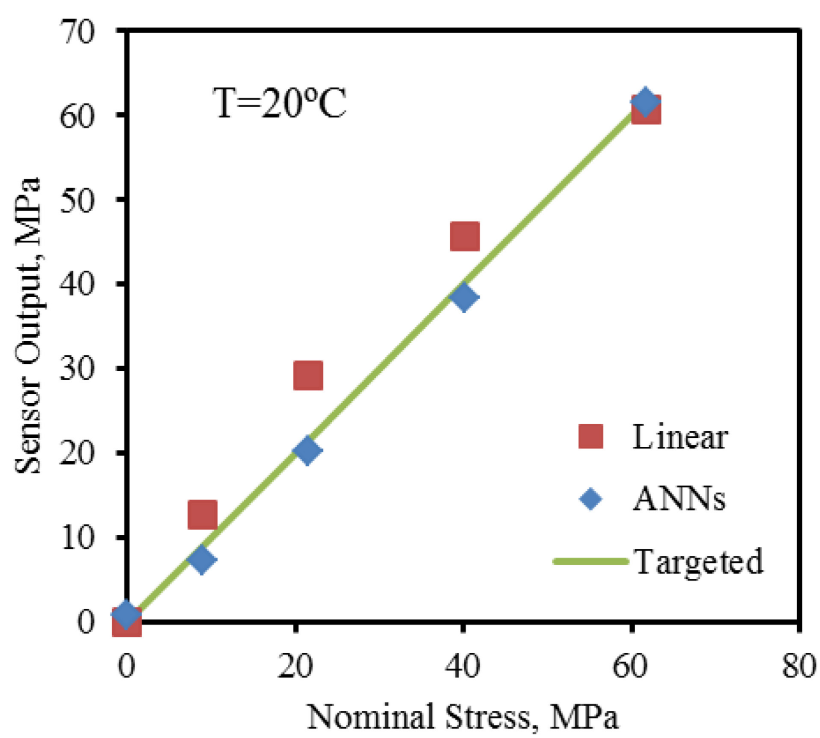

Figure 6-21 Measured stress output using linear calibration and ANNs at 20 °C

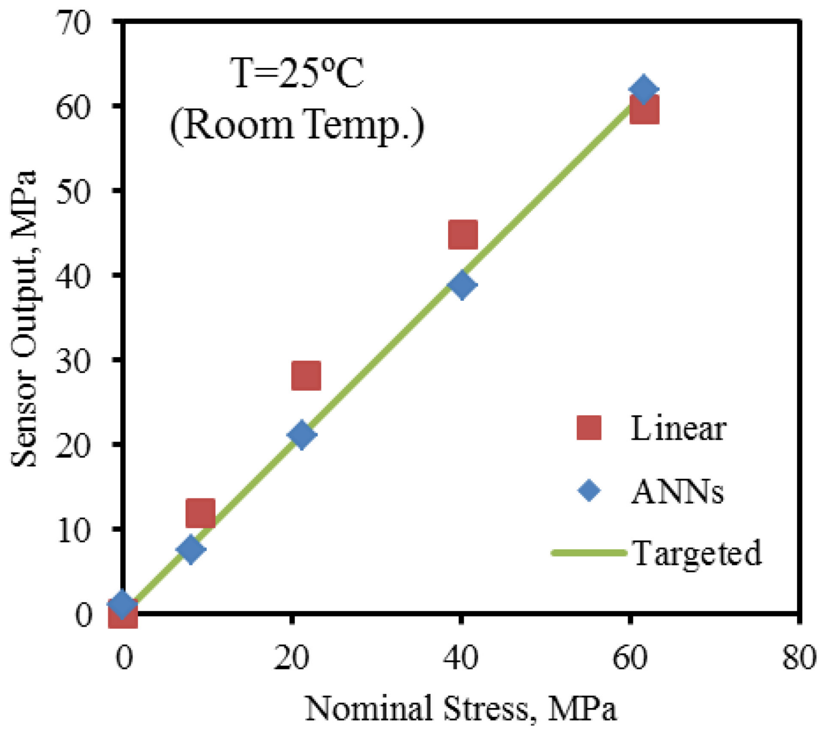

Figure 6-22 Measured stress output using linear calibration and ANNs at 25 °C

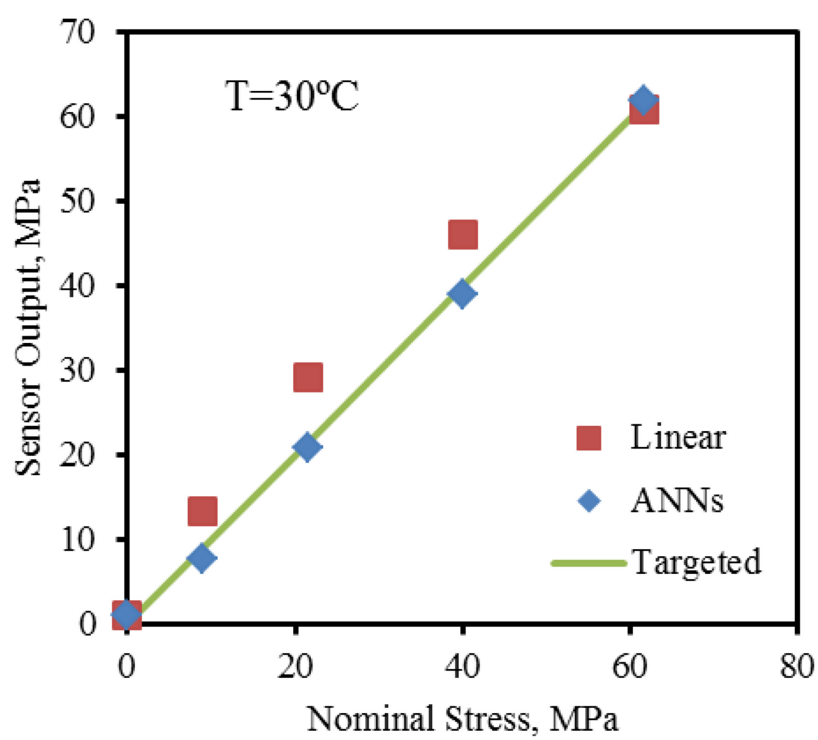

Figure 6-23 Measured stress output using linear calibration and ANNs at 30 °C

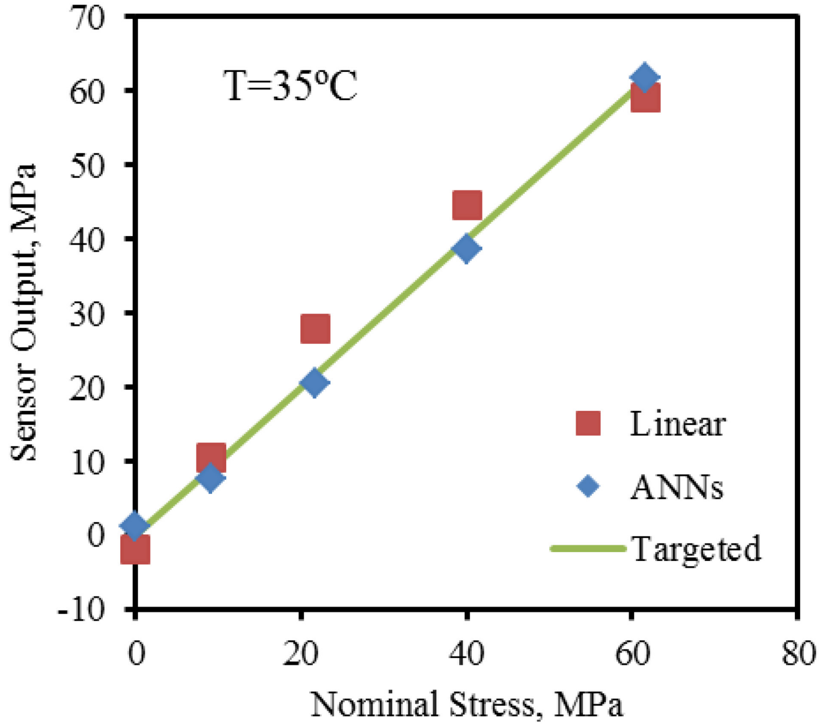

Figure 6-24 Measured stress output using linear calibration and ANNs at 35 °C

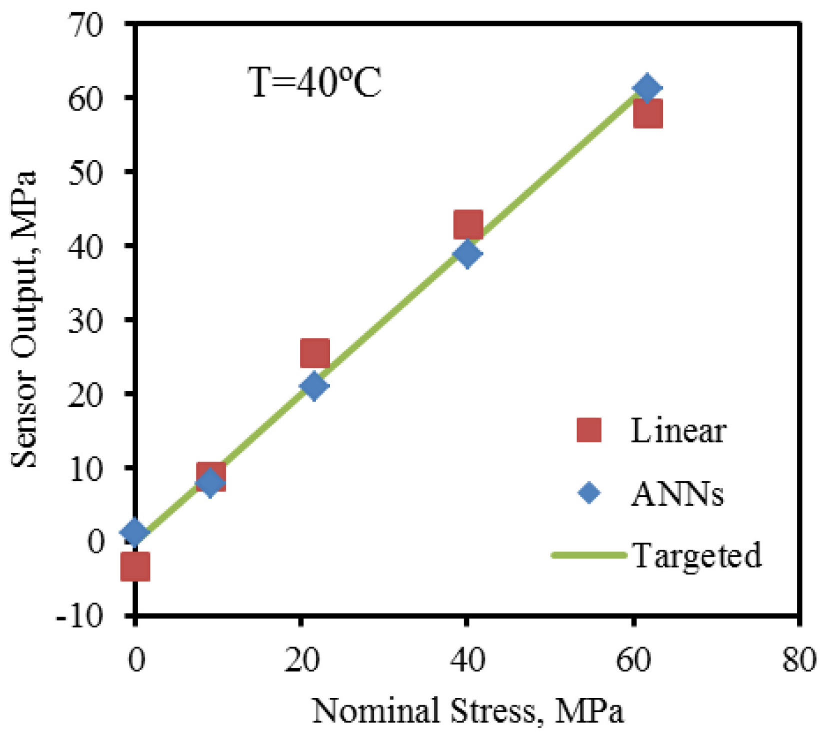

Figure 6-25 Measured stress output using linear calibration and ANNs at 40 °C

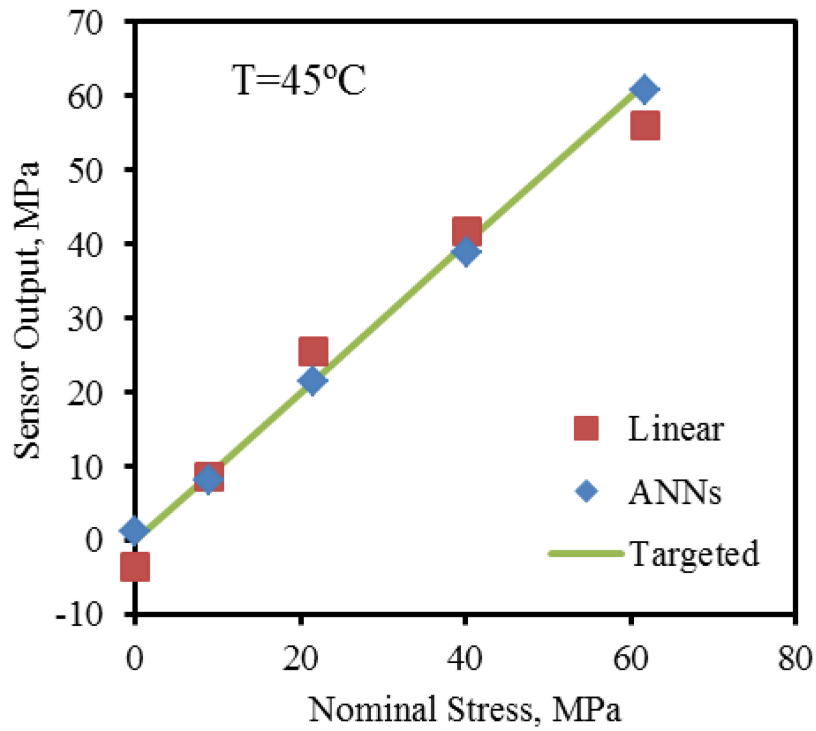

Figure 6-26 Measured stress output using linear calibration and ANNs at 45 °C

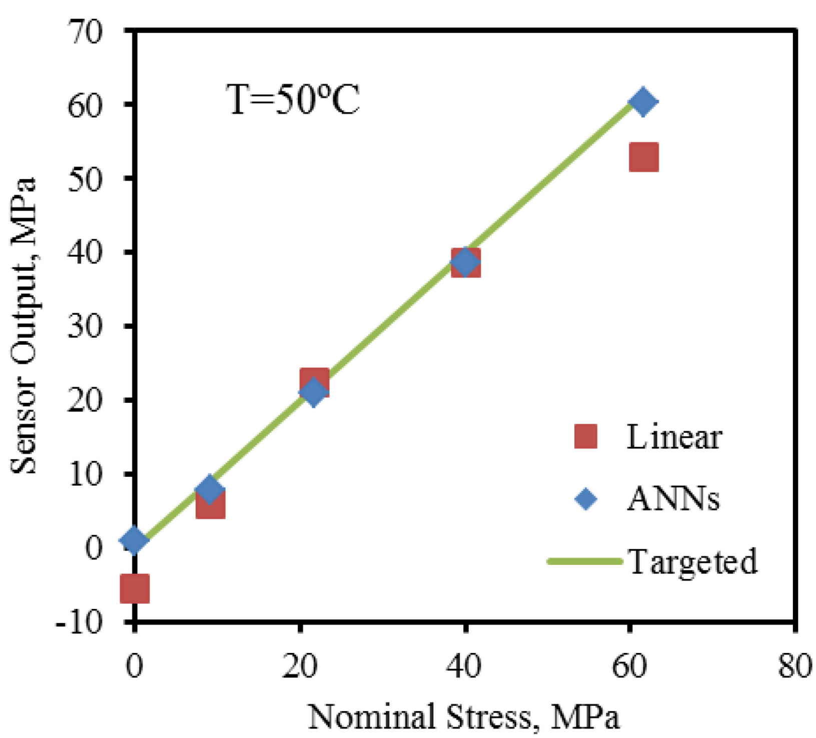

Figure 6-27 Measured stress output using linear calibration and ANNs at 50 °C

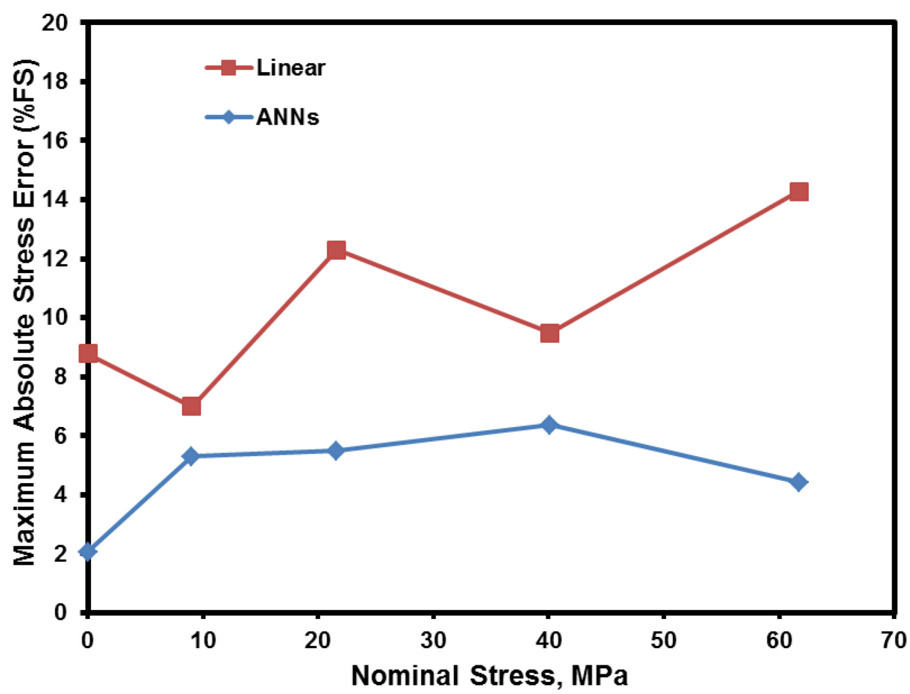

Figure 6-28 Error in stress measurement using both the linear calibration and the ANNs.

6.5 Integration of Strain Engineering into Stress/Strain Sensing Rosette

The single-polarity (n-type) silicon-based rosette provides simpler micro-fabrication process compared to the dual-polarity (n-type and p-type), since there is no need for the p-type doping equipment. Moreover, the use of all n-type rosettes, as in-situ stress sensors for electronic packaging applications, is recommended because of their lower standard deviation on the extracted piezoresistive (PR) coefficients compared to the p-type ones, according to Lwo et al. [86], [87]. However, the n-type silicon-based 3D stress sensors have low sensitivity to the out-of-plane stress components compared to the in-plane ones.

Strained silicon technique has a high potential for enhancing the doped silicon piezoresistive sensing rosette. For instance, biaxial strain could improve the sensitivity of piezoresistive n-type based stress sensors by 30 percent [114].

6.5.1 Microfabrication

In this research work, a highly compressive silicon nitride film produced by the Plasma Enhanced Chemical Vapor Deposition (PECVD), was integrated into the proposed sensing chip to enhance the sensitivity of the sensor to the out-of-plane components. This layer induces a tensile strain at the front side of the substrate where the sensing elements were fabricated. A strained sensing chip was fabricated on (111) silicon plane as shown in Figure 6-29. The biaxial tensile strain on (111) silicon plane also reduce both the longitudinal and the transverse piezoresistive coefficients for n-type piezoresistors [114]. Therfore, an experimental evaluation of the proposed strained-based sensor is necessary to investigate its capability to extract the in-plane stress/strain components along with the out-of-plane components. The detailed microfabrication process flow of the strained silicon-based sensing chip is provided in Appendix E.

6.5.2 Testing and Results

In this testing, we followed the same the testing procedure mentioned in section 7 to apply a uniaxial normal load, however, we attached a normal strain gauge to the opposite side of the chip-on-PCB beam as shown in Figure 6-30, to be used for comparison, instead of the load cell we used earlier. In addition, to test the capability of the developed sensing chip to capture the out-of-plane stress component (σ_{33}), the test rig, pictured in Figure 6-31, is used. The loading mechanism includes a 3D printed dimple that was mounted on the testing frame, while the specimen was placed on a movable plate. An inline load cell was installed between this movable plate and a dual-pantograph mechanism that uses a leadscrew to shorten the distance between its bars and lift this plate. The test was conducted inside the environmental chamber to apply incremental force, using a stepper motor, at different temperatures.

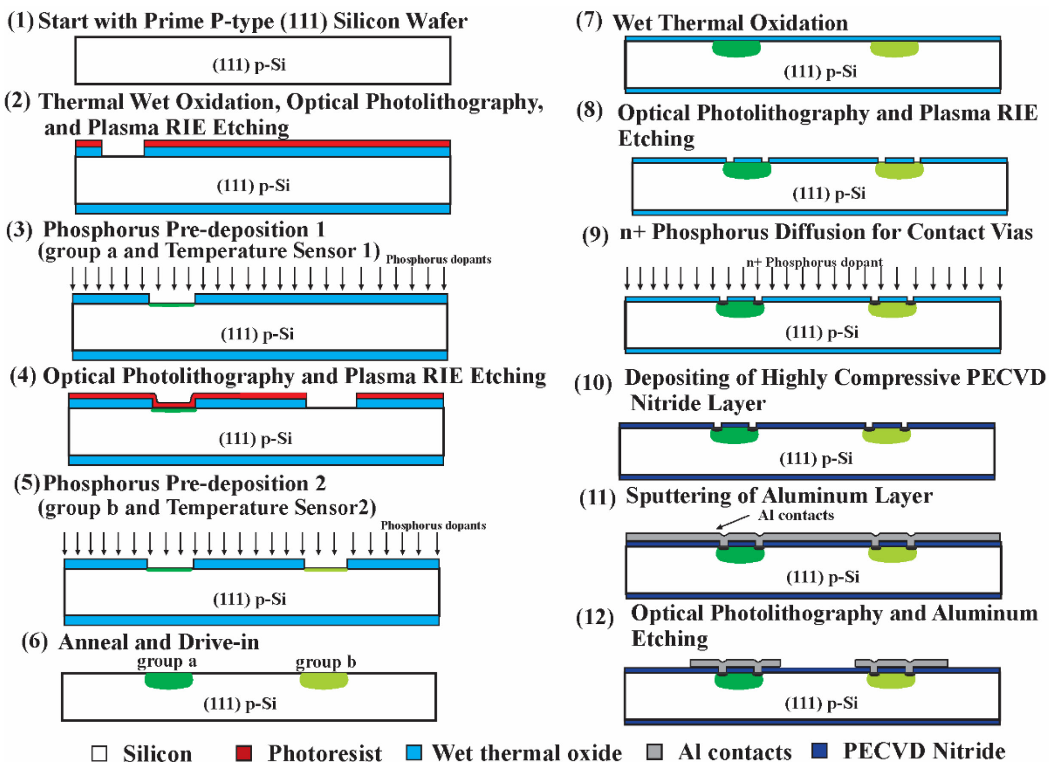

Figure 6-29 Microfabrication process flow of strained sensing chip

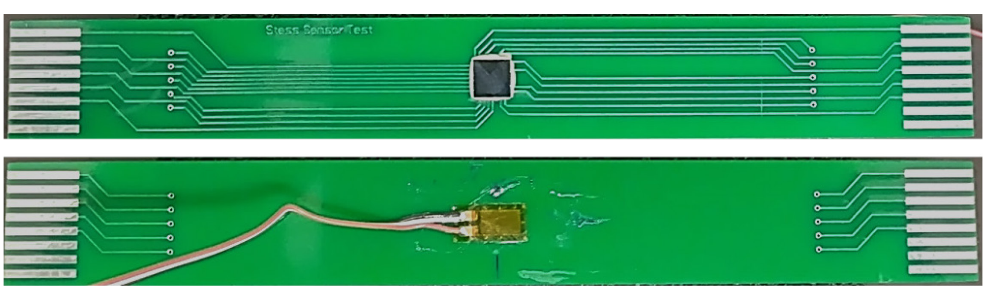

Figure 6-30 Actual image shows both the strained sensing chip and normal strain gauge attached to the PCB beam’s opposite sides

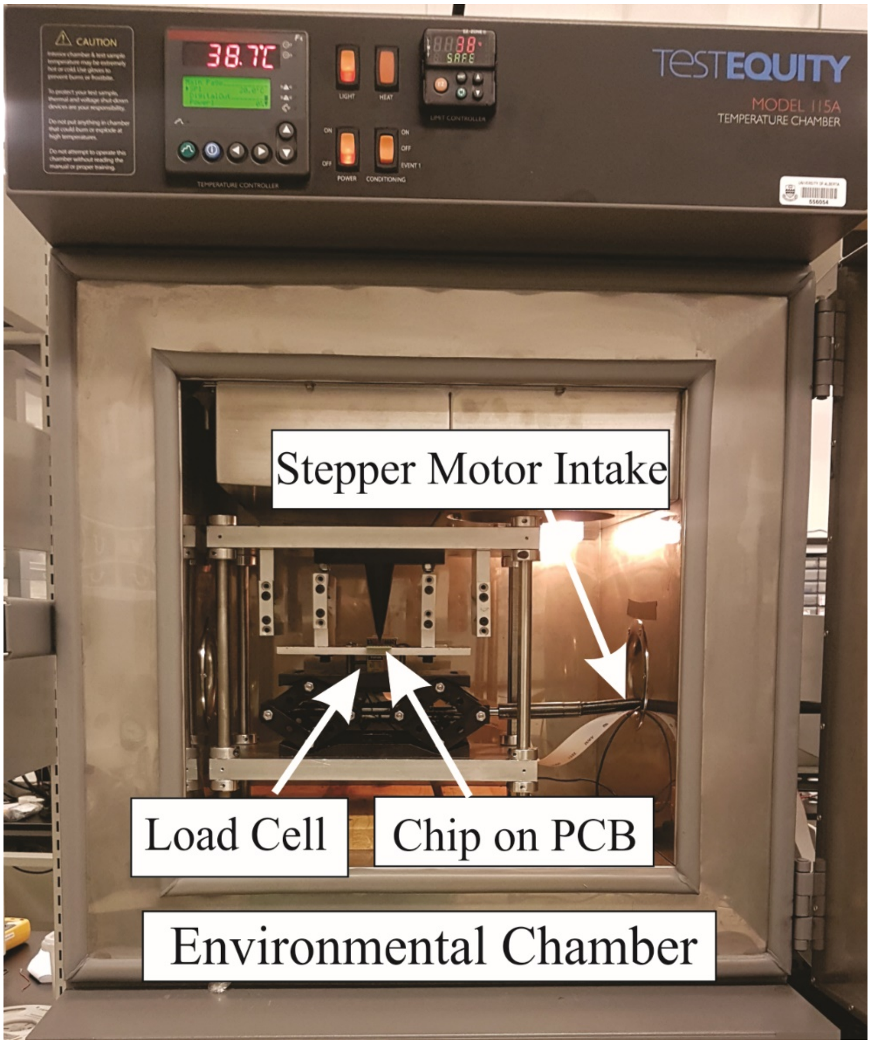

Figure 6-31 The out-of-plane normal loading setup

Figure 6-32 shows the real-time response of S0 specimen subjected to dynamic uniaxial strain that varies from 2500 to -1500 µstrain, while the temperature changes from 60 to -20 °C. It can be clearly seen that the developed sensing chip successfully captured the applied strain with temperature compensation with a maximum absolute error percentage of ~10% FS.

For further evaluation of the proposed sensing rosette, the test specimen was subjected to dynamic out-of-normal stress within a range from 0 to ~20 MPa. This test was conducted at different thermal environments over a range from -15 °C to

40 °C. As shown in Figure 6-33, the sensing chip is capable of extracting the applied out-of-normal load with a maximum absolute error of ~20% FS. This relatively large error is attributed to the low sensitivity of such sensors to the out-of-plane components compared to the in-plane components.

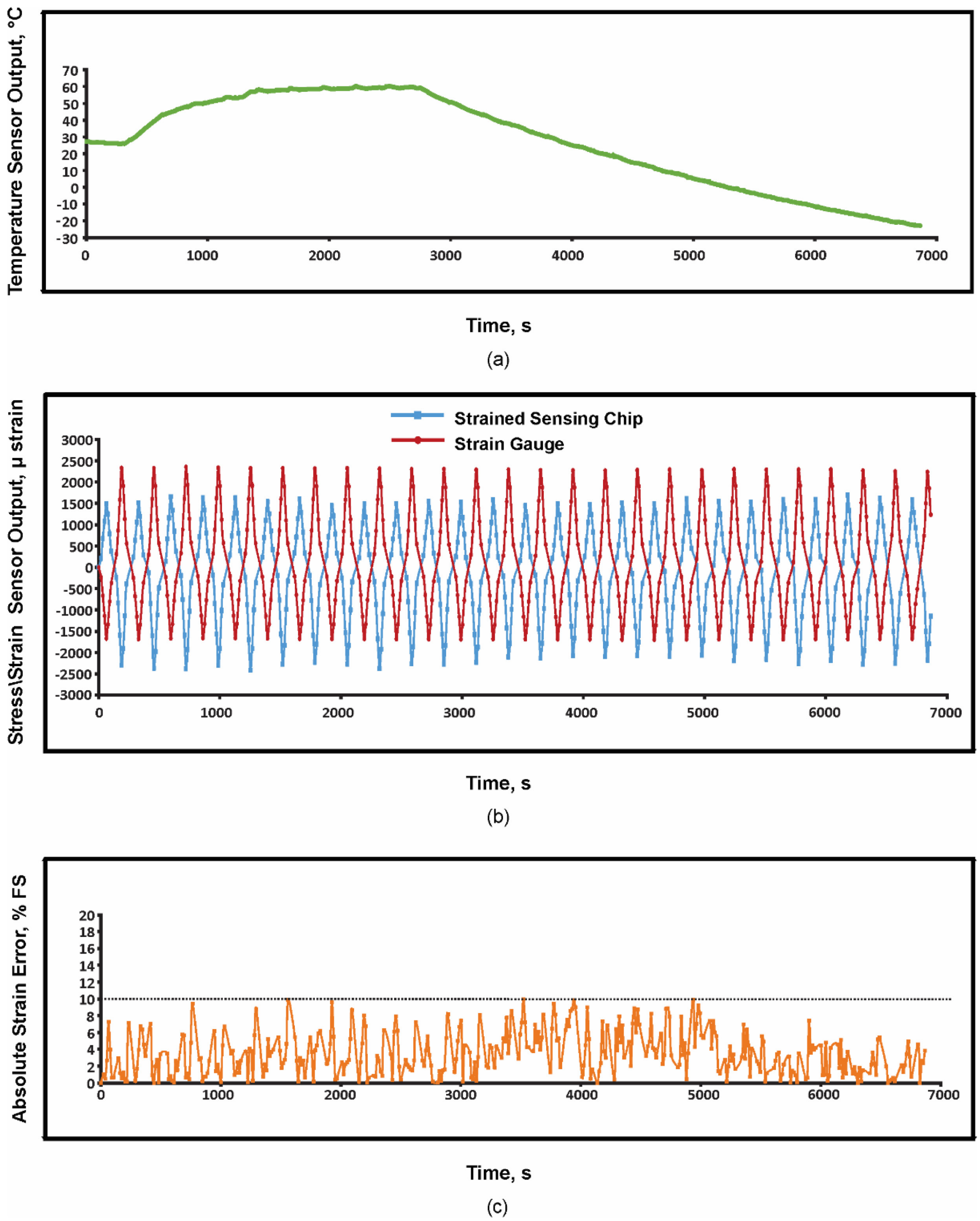

Figure 6-32 Real-time response of in-plane normal strain: a) Temperature sensor b) Strained sensing chip and standard strain gauge and c) Absolute strain error %

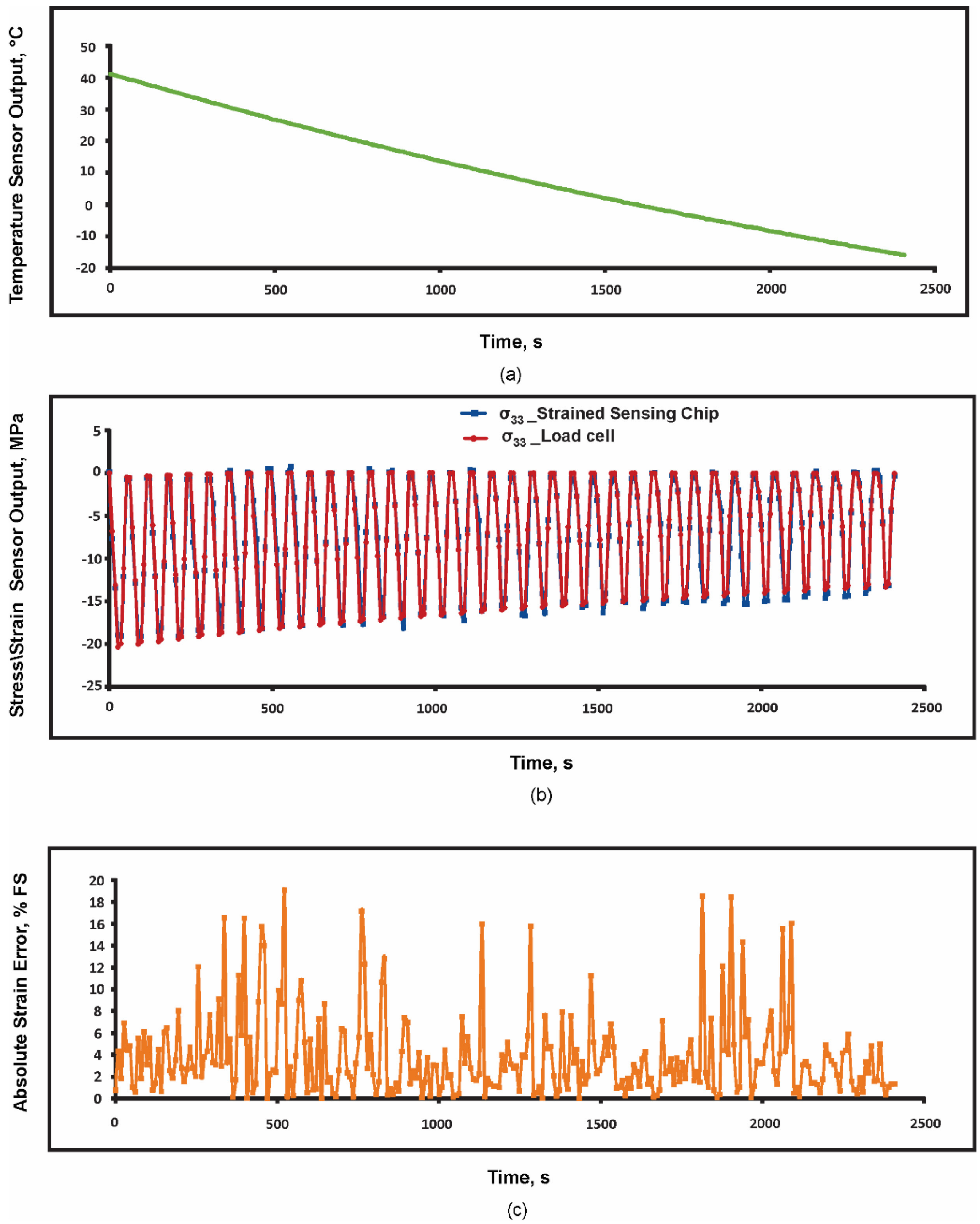

Figure 6-33 Real-time response of out-of-plane normal stress: a) Temperature sensor b) Strained sensing chip and load cell and c) Absolute stress error %

6.6 Conclusions

A smart high accuracy calibration algorithm for 3D piezoresistive stress sensors is presented chapter. A program was developed on MATLAB which incorporates the Neural Network Fitting Toolbox to build an ANNs that are capable of predicting the stresses generated on the sensing chip surface. Three different configurations of calibration were designed to test the generalization abilities of the ANNs in capturing the in-plane stress components exerted on the sensor's surface. The sensors used in training and testing ANNs are the same sensors employed in the experimental sensitivity analysis. The experimental results showed that the proposed algorithm can successfully extract the stresses with high accuracy of 1.5% *FS* despite the presence of the microfabrication non-uniformity.

In addition, a new temperature compensation algorithm that combines a temperature sensor with the ANNs is introduced. The proposed compensation system utilizes a full-circular n-type piezoresistor over (111) silicon plane, as a temperature sensor, to extract the temperature changes in close proximity to stress sensing rosettes. The measured temperature changes along with the resistance changes are provided to the ANNs to compensate for both resistance and sensitivity of the piezoresistive sensing elements. The experimental evaluation demonstrated an excellent performance for the proposed compensation system since only ~1.5% relative standard deviation (RSD) compared to the stress measurement using the linear calibration, in which ~9.3% RSD was obtained. The developed compensator was also able to reduce the maximum zero error measured from ~8.8% FS (for linear calibration) to only ~2.1% FS. This introduced compensation system is advantageous since the employed temperature sensor has the same thermal environment with the stress sensing elements. Moreover, there is no need for additional circuitry for the sensing chip.

Finally, this chapter investigated the impact of integration between strain engineering and the proposed sensing rosette to improve the sensitivity of such sensors to the out-of-plane components. A highly compressive silicon nitride film produced by plasma enhanced chemical vapor deposition (PECVD), was integrated into the proposed sensor during the microfabrication process to improve the sensitivity of the out-of-plane stress/strain measurement. A prototype stress sensing chip was microfabricated to test the capability of the developed sensing rosette to accurately extract stress applied on structures at different thermal environments. The fabricated sensing chip was subjected to different mechanical loads, namely in-plane and out-of-plane normal loads. The testing was carried out over a temperature range of -20 to 60 °C. The results showed that the developed sensing chip successfully captured the applied load with temperature compensation with a maximum absolute error percentage of ~10% FS and ~20% FS for in-plane normal and out-of-plane normal components, respectively.

CHAPTER 7: CONCLUSION AND FUTURE WORK

7.1 Research Contributions

This research concerns about developing a new 3D stress sensing rosette with robust temperature compensation system, simpler fabrication process, and less process noise due to the fabrication non-uniformity. The previous state of the art 3D stress sensors are capable of extracting the stress applied with compensation for the thermal effect on the resistance only. This is considered partial temperature compensation since the temperature has an impact on the sensitivity (i.e., piezoresistive coefficients) of piezoresistors as well. In this research work, a new 3D stress sensing rosette with full temperature compensation (for both resistance and sensitivity of the piezoresistor), is presented. The current research work involved the design, microfabrication, calibration, and testing of the developed sensing rosette. The following are the major research contributions:

1. The previous state of the art dual-poalrity eight-element and single polarity ten-element were studied first to find an alternative approach of developing a 3D stress sensing rosette capable of stress measurement with full temperature compensation and offering simpler microfabrication process. A new single polarity (n-type) eight-element sensing rosette with a temperature compensation system is developed. The proposed sensing rosette integrates a novel temperature transducer into n-type eight-element piezoresistive rosette to detect the temperature changes within the stress sensing rosette.
2. A novel temperature transducer using full-circular n-type piezoresistor over (111) silicon plane is proposed as an accurate solution for local temperature compensation for piezoresistive 3D stress sensors. The stress-insensitivity of the n-type circular piezoresistor was studied both

analytically and experimentally. In addition, the capability of the developed temperature sensor to accurately extract the temperature changes was experimentally evaluated.

3. A simpler fabrication process is provided, compared to the other reported 3D stress sensors in the literature [11], [13], since the proposed sensing rosette has only two n-type doping steps with no need for the p-type doping equipment.
4. A smart calibration approach using the ANNs to reduce the error in stress measurement, due to the fabrication non-uniformity of such 3D stress sensing rosettes, was investigated both numerically and experimentally. The proposed technique avoided the need for individual, expensive and time-consuming calibration processes for each sensor.
5. A new hybrid smart temperature compensation system that integrates the n-type circular piezoresistor (temperature sensor) with the ANNs, was developed, to smartly compensate the temperature effect on both resistance and sensitivity of the piezoresistive element. The proposed compensation system showed an improvement in stress measurement in different thermal environments.

7.2 Suggested Future Work

The current research dealt with different study areas; Design of new sensing rosette, development of novel smart temperature compensation system and full experimental study for the proposed approach. However, there are still more areas that need more investigation to enhance the performance of the developed approach. Below is the suggested future work:

1. In this research, the diffusion process was used for doping while fabricating the developed sensing chip for experimental evaluation. However, it is recommended to use the ion implantation to dope the sensing elements since it has a privilege over diffusion due to its high uniformity and reproducibility of impurity ions and its lower processing

temperature. Moreover, higher resistance values can be obtained since the ion implantation offers lower junction depths and higher sheet resistances, compared to diffusion, for the doped regions. They may result in an improvement in the sensor's performance.

2. Experimentally evaluate the capability of the circular piezoresistor, fabricated over (111) silicon plane at low doping concentrations (below 10^{18} cm^{-3}), to detect the temperature changes with high accuracy as obtained numerically in this study.
3. Investigate the potential of using other types of neural networks, for the proposed hybrid temperature compensation system, to eliminate the temperature effect and the nonlinearity of the PRCs with higher accuracy or fewer calibration points compared to the feedforward neural network used in this research.
4. The current research did not involve testing of the out-of-plane shear stress/strain components under varying thermal loads. This should be accompanied by preparing a test setup to apply a controlled load on the chip to induce enough out-of-plane shear stress. This is an important continuation to evaluate the capability of the proposed rosette to capture all the six stress components.
5. Test the proposed sensor at a broader range of temperatures, as the current research only included testing of the developed sensor over a range from 60 ºC to -20 ºC. This is due to the limited capability of the testing setup, used in this study, to apply mechanical loads at a wider range of temperatures.

BIBLIOGRAPHY

[1] Alberta, “Report 2013-B: Pipeline Performance in Alberta 1990-2012,” 1990.

[2] D. a. Bittle, J. C. Suhling, R. E. Beaty, R. C. Jaeger, and R. W. Johnson, “Piezoresistive Stress Sensors for Structural Analysis of Electronic Packages,” *J. Electron. Packag.*, vol. 113, no. September 1991, p. 203, 1991.

[3] A. A. Barlian, W. Park, J. R. M. Jr, A. J. Rastegar, B. L. Pruitt, and M. Engineering, “Review: Semiconductor Piezoresistance for Microsystems,” in *IEEE Inst Electr Electron Eng.*, 2009, vol. 97, no. 3, pp. 513–552.

[4] M. K. Rahim, J. C. Suhling, R. C. Jaeger, P. Lall, and R. W. Johnson, “Measurement of thermally induced die stresses in flip chip on laminate assemblies,” in *The Ninth Intersociety Conference on Thermal and Thermomechanical Phenomena in Electronic Systems, ITHERM 2004*, 2004, pp. 219–230.

[5] M. H. Bao and S. Middelhoek, *Micro Mechanical Transducers: Pressure Sensors, Accelerometers and Gyroscopes*. 2000.

[6] C. Pramanik, T. Islam, and H. Saha, “Temperature compensation of piezoresistive micro-machined porous silicon pressure sensor by ANN,” *Microelectron. Reliab.*, vol. 46, no. 2–4, pp. 343–351, 2006.

[7] G. Zhou, Y. Zhao, F. Guo, and W. Xu, “A smart high accuracy silicon piezoresistive pressure sensor temperature compensation system,” *Sensors (Switzerland)*, vol. 14, no. 7, pp. 12174–12190, 2014.

[8] J. C. Patra, A. C. Kot, S. Member, and G. Panda, “An Intelligent Pressure Sensor Using Neural Networks,” *Instrumentation*, vol. 49, no. 4, pp. 829–834, 2000.

[9] J. C. J. Patra, a van den Bos, and A. Van Den Bos, “Modeling of an intelligent pressure sensor using functional link artificial neural networks.,” *ISA Trans.*, vol. 39, pp. 15–27, 2000.

[10] N. P. Futane, S. R. Chowdhury, C. R. Chowdhury, and H. Saha, “ANN based CMOS ASIC design for improved temperature-drift compensation of piezoresistive micro-machined high resolution pressure sensor,” *Microelectron. Reliab.*, vol. 50, no. 2, pp. 282–291, 2010.

[11] J. C. Suhling and R. C. Jaeger, “Silicon piezoresistive stress sensors and their application in electronic packaging,” *IEEE Sens. J.*, vol. 1, no. 1, pp. 14–30, 2001.

[12] T. Huynh, “Fundamentals of Thermal Sensors,” in *Thermal Sensors*, C. M. Jha, Ed. Springer, New York, NY, 2015, pp. 5–42.

[13] H. H. Gharib and W. A. Moussa, “On the feasibility of a new approach for developing a piezoresistive 3D stress sensing rosette,” *IEEE Sens. J.*, vol. 11, no. 9, pp. 1861–1871, 2011.

[14] H. H. Gharib and W. A. Moussa, “A single-polarity piezoresistive three-dimensional stress-sensing rosette,” *J. Microelectromechanical Syst.*, vol. 20, no. 3, pp. 555–557, 2011.

[15] M. O. Kayed, A. A. Balbola, and W. A. Moussa, “A Smart High Accuracy Calibration Algorithm for 3D Piezoresistive Stress Sensor,” *IEEE Sens. J.*, vol. 17, no. 5, pp. 1255–1263, 2017.

[16] W. Thomson, “On the electro-dynamicqualities of metals : effects of

magnetization on the electric conductivity of nickel and of iron," *Philosophical Transactions of the Royal Society of London*, vol. 8. pp. 546–550, 1856.

[17] J. H. Taylor, "Pressure dependence of resistance of germanium [31]," *Physical Review*, vol. 80, no. 5. pp. 919–920, 1950.

[18] P. W. Bridgman, "The Effect of Pressure on the Electrical Resistance of Certain Semiconductors," in *proceedings of the American Academy of Arts and Sciences*, 1951, pp. 127–148.

[19] C. S. Smith, "Piezoresistance effect in germanium and silicon," *Phys. Rev.*, vol. 94, no. 1, pp. 42–49, 1954.

[20] W. Paul and G. L. Pearson, "Pressure dependence of the resistivity of silicon," *Phys. Rev.*, vol. 98, no. 6, pp. 1755–1757, 1955.

[21] H. Rolnick, "Tension coefficient of resistance of metals," *Phys. Rev.*, vol. 36, pp. 506–513, 1930.

[22] S. Keil, "On the strain gage's 50th jubulee – a review of its evolution and of 33 years strain gage production at Darmstadte," *RAM*, vol. 4, no. 2, pp. 39–48, 1988.

[23] *BLH-Measurement Topics*, vol. 5. 1967.

[24] F. G. Tantall, "Tantal on Testing," *Am. Soc. Met.*, vol. 2nd printi, p. 60, 1967.

[25] A. S. Fiorillo, C. D. Critello, and A. S. Pullano, "Theory, technology and applications of piezoresistive sensors: A review," *Sensors Actuators, A Phys.*, vol. 281, pp. 156–175, 2018.

[26] E. E. Simmons, "Material Testing Apparatus," 2292549, 1942.

[27] A. C. Ruge, “Strain Gauge,” 2350972, 1944.

[28] C. Pang *et al.*, “A flexible and highly sensitive strain-gauge sensor using reversible interlocking of nanofibres,” *Nat. Mater.*, vol. 11, no. 9, pp. 795–801, Sep. 2012.

[29] H. P. Wang, D. Zhou, J. Cao, and R. Lindeke, “A Skin-Like Pressure Sensor Array Based on Silver Nanowires and Conductive Elastomer,” in *Volume 1: Development and Characterization of Multifunctional Materials; Modeling, Simulation and Control of Adaptive Systems; Integrated System Design and Implementation*, 2013, p. V001T01A010.

[30] S. Gong *et al.*, “A wearable and highly sensitive pressure sensor with ultrathin gold nanowires,” *Nat. Commun.*, vol. 5, no. 1, p. 3132, Dec. 2014.

[31] Y. Zang, F. Zhang, C. Di, and D. Zhu, “Advances of flexible pressure sensors toward artificial intelligence and health care applications,” *Mater. Horizons*, vol. 2, no. 2, pp. 140–156, Feb. 2015.

[32] S.-H. Zhang *et al.*, “Flexible bifunctional sensor based on porous copper nanowires@IonGels composite films towards high-resolution stress/deformation detection,” *J. Mater. Chem. C*, 2020.

[33] C. Celle *et al.*, “Oxidation of copper nanowire based transparent electrodes in ambient conditions and their stabilization by encapsulation: application to transparent film heaters,” *Nanotechnology*, vol. 29, no. 8, p. 085701, Feb. 2018.

[34] X. Ye, Z. Yuan, H. Tai, W. Li, X. Du, and Y. Jiang, “A wearable and highly sensitive strain sensor based on a polyethylenimine–rGO layered nanocomposite thin film,” *J. Mater. Chem. C*, vol. 5, no. 31, pp. 7746–7752, Aug. 2017.

[35] H. Chen *et al.*, “Fingertip-inspired electronic skin based on triboelectric sliding sensing and porous piezoresistive pressure detection,” *Nano Energy*, vol. 40, pp. 65–72, Oct. 2017.

[36] T. Yamada *et al.*, “A stretchable carbon nanotube strain sensor for human-motion detection,” *Nat. Nanotechnol.*, vol. 6, no. 5, pp. 296–301, May 2011.

[37] D. Cho *et al.*, “Three-Dimensional Continuous Conductive Nanostructure for Highly Sensitive and Stretchable Strain Sensor,” *ACS Appl. Mater. Interfaces*, vol. 9, no. 20, pp. 17369–17378, May 2017.

[38] J. Li, Y. Lu, and M. Meyyappan, “Nano Chemical Sensors With Polymer-Coated Carbon Nanotubes,” *IEEE Sens. J.*, vol. 6, no. 5, pp. 1047–1051, Oct. 2006.

[39] B. Philip, J. K. Abraham, A. Chandrasekhar, and V. K. Varadan, “Carbon nanotube/PMMA composite thin films for gas-sensing applications,” *Smart Mater. Struct.*, vol. 12, no. 6, pp. 935–939, 2003.

[40] T. Gurunathan, C. R. K. Rao, R. Narayan, and K. V. S. N. Raju, “Polyurethane conductive blends and composites: synthesis and applications perspective,” *J. Mater. Sci.*, vol. 48, no. 1, pp. 67–80, Jan. 2013.

[41] X. Sun *et al.*, “Carbon nanotubes reinforced hydrogel as flexible strain sensor with high stretchability and mechanically toughness,” *Chem. Eng. J.*, vol. 382, p. 122832, Feb. 2020.

[42] W. Zhang, J. Suhr, and N. Koratkar, “Carbon nanotube/polycarbonate composites as multifunctional strain sensors,” *J. Nanosci. Nanotechnol.*, vol. 6, no. 4, pp. 960–964, Apr. 2006.

[43] G. T. Pham, Y. Bin Park, Z. Liang, C. Zhang, and B. Wang, “Processing and modeling of conductive thermoplastic/carbon nanotube films for strain sensing,” *Compos. Part B Eng.*, vol. 39, no. 1, pp. 209–216, Jan. 2008.

[44] J. G. Rocha, A. J. Paleo, F. W. J. Van Hattum, and S. Lanceros-Mendez, “Polypropylene-carbon nanofiber composites as strain-gauge sensor,” *IEEE Sens. J.*, vol. 13, no. 7, pp. 2603–2609, 2013.

[45] K. J. Loh, J. P. Lynch, B. S. Shim, and N. A. Kotov, “Tailoring Piezoresistive Sensitivity of Multilayer Carbon Nanotube Composite Strain Sensors,” *J. Intell. Mater. Syst. Struct.*, vol. 19, no. 7, pp. 747–764, Jul. 2008.

[46] T. Yasuoka, Y. Shimamura, and A. Todoroki, “Electrical resistance change under strain of CNF/flexible-epoxy composite,” *Adv. Compos. Mater.*, vol. 19, no. 2, pp. 123–138, Apr. 2010.

[47] N. Wang *et al.*, “A tunable strain sensor based on a carbon nanotubes/electrospun polyamide 6 conductive nanofibrous network embedded into poly(vinyl alcohol) with self-diagnosis capabilities,” *J. Mater. Chem. C*, vol. 5, no. 18, pp. 4408–4418, 2017.

[48] L. Han *et al.*, “Polydopamine/polystyrene nanocomposite double-layer strain sensor hydrogel with mechanical, self-healing, adhesive and conductive properties,” *Mater. Sci. Eng. C*, vol. 109, p. 110567, Apr. 2020.

[49] J. Chen, Y. Zhu, and W. Jiang, “A stretchable and transparent strain sensor based on sandwich-like PDMS/CNTs/PDMS composite containing an ultrathin conductive CNT layer,” *Compos. Sci. Technol.*, vol. 186, p. 107938, Jan. 2020.

[50] P. Zhao *et al.*, “Electrically conductive graphene-filled polymer composites with well organized three-dimensional microstructure,” *Mater. Lett.*, vol.

121, pp. 74–77, Apr. 2014.

[51] Y. Kanda, "A Graphical Representation Of The Piezoresistance Coefficients In Silicon," *IEEE Trans. Electron Devices*, vol. 29, no. 1, pp. 64–70, 1982.

[52] O. N. Tufte and E. L. Stelzer, "Piezoresistive Properties of Silicon Diffused Layers," *J. Appl. Phys.*, vol. 34, no. 2, pp. 313–318, 1963.

[53] O. N. Tufte and E. L. Stelzer, "piezoresistive Properties of Heavily Doped n-Type Silicon," *Phys. Rev.*, vol. 133, no. 6a, pp. A1705–A1716, 1964.

[54] F. J. Morin, T. H. Geballe, and C. Herring, "Temperature dependence of the piezoresistance of high-purity silicon and germanium," *Phys. Rev.*, vol. 105, no. 2, pp. 525–539, 1957.

[55] J. Richter, O. Hansen, A. Nylandsted Larsen, J. Lundsgaard Hansen, G. F. Eriksen, and E. V. Thomsen, "Piezoresistance of silicon and strained Si0.9Ge0.1," *Sensors Actuators A Phys.*, vol. 123–124, pp. 388–396, Sep. 2005.

[56] W. P. Mason and R. N. Thurston, "Use of piezoresistive materials in the measurement of displacement, force, and torque," *J. Acoust. Soc. Am.*, vol. 29, no. 10, p. 1096, 1957.

[57] J. A. Hoerni, "Planar silicon diodes and transistors," in *International Electron Devices Meeting*, 1960, pp. 50–50.

[58] A. A. Balbola, M. O. Kayed, and W. A. Moussa, "Studying the Influence of n-type Strained (111) Silicon on the Piezoresistive Coefficients," *IEEE Sens. J.*, vol. 17, no. 2, pp. 1–1, 2016.

[59] H. H. Gharib and W. A. Moussa, "Microfabrication and calibration of a single-polarity piezoresistive three-dimensional stress sensing chip," *J.*

Micromechanics Microengineering, vol. 23, no. 3, p. 35019, 2013.

[60] S. S. Li and W. R. Thurder, "The dopant density and temperature dependence of electron mobility and resistivity in n-type silicon," *Solid State Electron.*, vol. 20, no. 7, pp. 609–616, 1977.

[61] D. Benfield, E. Lou, and W. A. Moussa, "A packaging solution utilizing adhesive-filled TSVs and flip-chip methods," *J. Micromechanics Microengineering*, vol. 22, no. 6, Jun. 2012.

[62] T. C. Duc, J. F. Creemer, and P. M. Sarro, "Piezoresistive cantilever beam for force sensing in two dimensions," *IEEE Sens. J.*, vol. 7, no. 1, pp. 96–104, Jan. 2007.

[63] A. Tibrewala, A. Phataralaoha, and S. Büttgenbach, "Simulation, fabrication and characterization of a 3D piezoresistive force sensor," *Sensors Actuators, A Phys.*, vol. 147, no. 2, pp. 430–435, Oct. 2008.

[64] X. Li, Q. Liu, S. Pang, K. Xu, H. Tang, and C. Sun, "High-temperature piezoresistive pressure sensor based on implantation of oxygen into silicon wafer," *Sensors Actuators, A Phys.*, vol. 179, pp. 277–282, Jun. 2012.

[65] C. T. Peng, J. C. Lin, C. Te Lin, and K. N. Chiang, "Performance and package effect of a novel piezoresistive pressure sensor fabricated by front-side etching technology," *Sensors Actuators, A Phys.*, vol. 119, no. 1, pp. 28–37, Mar. 2005.

[66] S. Sugiyama, M. Takigawa, and I. Igarashi, "Integrated piezoresistive pressure sensor with both voltage and frequency output," *Sensors and Actuators*, vol. 4, no. C, pp. 113–120, 1983.

[67] D. Li, T. Zhao, Z. Yang, and D. Zhang, "Monolithic integration of a micromachined piezoresistive flow sensor," *J. Micromechanics*

Microengineering, vol. 20, no. 3, 2010.

[68] M. A. Schmidt, S. D. Senturia, R. T. Howe, and J. H. Haritonidis, “Design and Calibration of a Microfabricated FloatingElement Shear Stress Sensor,” *IEEE Trans. Electron Devices*, vol. 35, no. 6, pp. 750–757, 1988.

[69] Karl Hoffmann, *An Introduction to Measurements Using Strain Gages*. Hottinger Baldwin Messtechnik, 1989.

[70] A. L. Window, *Strain gauge technology*. Elsevier Applied Science, 1992.

[71] W. N. Sharpe, *Springer handbook of experimental solid mechanics*. Springer Science+Business Media, 2008.

[72] J. K. Abraham, B. Philip, A. Witchurch, V. K. Varadan, and C. C. Reddy, “A compact wireless gas sensor using a carbon nanotube/PMMA thin film chemiresistor,” 2004.

[73] J. Yang, X. Li, X. Lu, W. Bao, and R. Chen, “Three-Dimensional Interfacial Stress Sensor Based on Graphene Foam,” *IEEE Sens. J.*, vol. 18, no. 19, pp. 7956–7963, Oct. 2018.

[74] B. Lemke, M. Baumann, P. Gieschke, R. Baskaran, and O. Paul, “Piezoresistive CMOS-compatible sensor for out-of-plane shear stress,” *Sensors Actuators, A Phys.*, vol. 189, pp. 488–495, 2013.

[75] B. Lemke, R. Baskaran, and O. Paul, “Piezoresistive CMOS sensor for out-of-plane normal stress,” *Sensors Actuators, A Phys.*, vol. 176, pp. 10–18, 2012.

[76] B.Lemke, K.Kratt, O.Paul, and R.Baskaran, “Towards CMOS sensors FOR OUT-OF-PLANE STRESS,” in *Proceedings of the IEEE International Conference on Micro Electro Mechanical Systems (MEMS)*, 2009, pp. 7–10.

[77] K. D. Wise, “Integrated sensors, MEMS, and microsystems: Reflections on a fantastic voyage,” *Sensors Actuators, A Phys.*, vol. 136, no. 1, pp. 39–50, 2007.

[78] R. A. Cordes, J. C. Suhling, Y. Kang, and R. C. Jaeger, “Optimal temperature compensated piezoresistive stress sensor rosettes,” in *the 1995 ASME International Mechanical Engineering Congress and Exposition*, 1995, pp. 109–116.

[79] R. C. Jaeger, J. C. Suhling, and R. Ramani, “Errors Associated With the Design, Calibration and Application of Piezoresistive Stress Sensors in (100) Silicon,” *IEEE Trans. Components Packag. Manuf. Technol. Part B*, vol. 17, no. 1, pp. 97–107, 1994.

[80] C. Chun-Hyung, J. C. Richard, and J. C. Suhling, “The effect of the transverse sensitivity on measurement of the piezoresistive coefficients of silicon,” *Jpn. J. Appl. Phys.*, vol. 47, no. 5 PART 1, pp. 3647–3656, 2008.

[81] C. H. Cho, R. C. Jaeger, and J. C. Suhling, “Characterization of the temperature dependence of the piezoresistive coefficients of silicon from -150 °C to +125 °C,” *IEEE Sens. J.*, vol. 8, no. 8, pp. 1455–1468, 2008.

[82] R. C. Jaeger, C.-H. Cho, S. Hussain, and J. C. Suhling, “Impact of piezoresistive coefficient uncertainity on stress measurement using silicon multi-resistor sensor rosettes,” in *Proceedings of IMECE2008*, 2008, no. 100, pp. 1–12.

[83] C. H. Cho, R. C. Jaeger, and J. C. Suhling, “Experimental characterization of the temperature dependence of the piezoresistive coefficients of silicon,” in *Thermal and Thermomechanical Proceedings 10th Intersociety Conference on Phenomena in Electronics Systems, 2006. ITHERM 2006.*, 2006, pp. 928–935.

[84] S. Hussain, R. C. Jaeger, J. C. Suhling, J. C. Roberts, M. A. Motalab, and C. H. Cho, “Error analysis for piezoresistive stress sensors used in flip chip packaging,” *2010 12th IEEE Intersoc. Conf. Therm. Thermomechanical Phenom. Electron. Syst. ITherm 2010*, no. 111, pp. 1–12, 2010.

[85] J. C. Suhling, R. C. Jaeger, P. Lall, M. K. Rahim, J. C. Roberts, and S. Hussain, “Application of stress sensing test chips to area array packaging,” in *2009 10th International Conference on Thermal, Mechanical and Multi-Physics Simulation and Experiments in Microelectronics and Microsystems, EuroSimE 2009*, 2009.

[86] B.-J. Lwo, C.-H. Kao, T.-S. Chen, and Y.-S. Chen, “On the Study of Piezoresistive Stress Sensors for Microelectronic Packaging,” *J. Electron. Packag.*, vol. 124, no. 1, p. 22, 2002.

[87] B.-J. Lwo, T.-S. Chen, C.-H. Kao, and Y.-L. Lin, “In-Plane Packaging Stress Measurements Through Piezoresistive Sensors,” *J. Electron. Packag.*, vol. 124, no. 2, p. 115, 2002.

[88] M. O. Kayed, A. A. Balbola, and W. A. Moussa, “A New Temperature Transducer for Local Temperature Compensation for Piezoresistive 3-D Stress Sensors,” *IEEE/ASME Trans. Mechatronics*, vol. 24, no. 2, pp. 832–840, Apr. 2019.

[89] A. D. Kurtz, “Adjusting crystal characteristics to minimize temperature dependency,” in *Semiconductor and Conventional Strain Gages.*, M. Dean, Ed. New York: Academic Press, 1962, pp. 259–272.

[90] S. I. Kozlovskiy and I. I. Boiko, “First-order piezoresistance coefficients in silicon crystals,” *Sensors Actuators, A Phys.*, vol. 118, no. 1, pp. 33–43, 2005.

[91] W. P. Mason, J. J. Forst, and L. M. Tornillo, “Recent developments in

semiconductor strain transducers," in *15th Annual Conference of The Instrument Society of America: New York*, 1962, pp. 110–120.

[92] E. Perraud, "Theoretical model of performance of a silicon piezoresistive pressure sensor," *Sensors Actuators, A Phys.*, vol. 57, no. 3, pp. 245–252, Dec. 1996.

[93] B. W. Chui *et al.*, "Advanced temperature compensation for piezoresistive sensors based on crystallographic orientation," *Rev. Sci. Instrum.*, vol. 78, no. 4, 2007.

[94] M. El Gibari *et al.*, "Thermal drift compensation of piezoresistive implantable blood pressure sensors with low cost analog solutions," in *Proceedings of the International Conference on Microelectronics, ICM*, 2018, vol. 2017-December, pp. 1–4.

[95] D. Lee *et al.*, "A Highly Linear, AEC-Q100 Compliant Signal Conditioning IC for Automotive Piezo-Resistive Pressure Sensors," *IEEE Trans. Ind. Electron.*, vol. 65, no. 9, pp. 7363–7373, Sep. 2018.

[96] J. C. Suhling, R. E. Beaty, R. C. Jaeger, and R. W. Johnson, "Piezoresistive sensors for measurement of thermally-induced stresses in microelectronics," in *SEM Spring Conference on Experimental Mechanics*, 1991, pp. 683–694.

[97] M. O. Kayed, A. A. Balbola, E. Lou, and W. A. Moussa, "Development of Doped Silicon Multi-element Stress Sensor Rosette with Temperature Compensation," *IEEE Sens. J.*, vol. 20, no. 3, pp. 1176–1183, Oct. 2019.

[98] Y. Kanda and K. Suzuki, "Origin of the shear piezoresistance coefficient 44 of n-type silicon," *Phys. Rev. B*, vol. 43, no. 8, pp. 6754–6756, 1991.

[99] P. Norton and J. Brandt, "Temperature coefficient of resistance for p- and

n-type silicon," *Solid. State. Electron.*, vol. 21, no. 7, pp. 969–974, Jul. 1978.

[100] S. N. Atluri, A. S. Kobayashi, R. J. Allemang, K. G. McConnell, J. W. Dally, and R. J. Allemang, *Handbook on experimental mechanics*, vol. 16: Experi. Society for Experimental Mechanics (SEM), 1993.

[101] J. C. Richard, "Introduction to Microelectronic Fabrication," G. W. Neudeck and R. F. Pierret, Eds. Prentice Hall, 2002.

[102] R. E. Beaty, R. C. Jaeger, R. W. Johnson, R. D. Butler, and J. C. Suhling, "Evaluation of Piezoresistive Coefficient Variation in Silicon Stress Sensors Using a Four-Point Bending Test Fixture," *IEEE Trans. Components, Hybrids, Manuf. Technol.*, vol. 15, no. 5, pp. 904–914, 1992.

[103] H. H. Gharib and W. A. Moussa, "Testing of a single-polarity piezoresistive three-dimensional stress-sensing chip," *J. Micromechanics Microengineering*, vol. 23, no. 9, p. 095036, 2013.

[104] J. Scott and E. T. Enikov, "Novel temperature compensation technique for force-sensing piezoresistive devices," *J. Micromechanics Microengineering*, vol. 21, no. 11, p. 115017, 2011.

[105] M. Aryafar, M. Hamedi, and M. M. Ganjeh, "A novel temperature compensated piezoresistive pressure sensor," *Meas. J. Int. Meas. Confed.*, vol. 63, pp. 25–29, 2015.

[106] D. Sonowal and M. Bhuyan, "Multi Channel Sensor Linearization in Field Programmable Gate Array for Real Time Applications," *Sensors & Transducers*, vol. 191, no. 8, pp. 135–151, 2015.

[107] J. C. Patra, G. Chakraborty, and P. K. Meher, "Neural-Network-Based Robust Linearization and Compensation Technique for Sensors Under

Nonlinear Environmental Influences," *IEEE Trans. Circuits Syst. I Regul. Pap.*, vol. 55, no. 5, pp. 1316–1327, Jun. 2008.

[108] H. Erdem, "Implementation of software-based sensor linearization algorithms on low-cost microcontrollers.," *ISA Trans.*, vol. 49, no. 4, pp. 552–8, Oct. 2010.

[109] N. J. Medrano-Marques and Martin-del-Brio, "A general method for sensor linearization based on neural networks," in *IEEE International Symposium on Circuits and Systems. Emerging Technologies for the 21st Century. Proceedings (IEEE Cat No.00CH36353)*, 2000, vol. 2, pp. 497–500.

[110] N. J. Medrano-Marques and B. Martin-del-Brio, "Sensor linearization with neural networks," *IEEE Trans. Ind. Electron.*, vol. 48, no. 6, pp. 1288–1290, 2001.

[111] S. A. Khan, D. T. Shahani, and A. K. Agarwala, "Sensor calibration and compensation using artificial neural network," *ISA Trans.*, vol. 42, no. 3, pp. 337–352, 2003.

[112] A. G. Nagy, "Radial Etch Rate Nonuniformity in Reactive Ion Etching."

[113] E. L. Richards, "Generalization in Neural Networks: Experiments in Speech Recognition ; CU-CS-538-91," 1991.

[114] A. A. Balbola, M. O. Kayed, and W. A. Moussa, "Studying the Influence of n-type Strained (111) Silicon on the Piezoresistive Coefficients," *IEEE Sens. J.*, vol. 17, no. 2, pp. 302–310, 2016.

[115] E. V. Thomsen, K. Reck, G. Skands, C. Bertelsen, and O. Hansen, "Silicon as an anisotropic mechanical material: Deflection of thin crystalline plates," *Sensors Actuators, A Phys.*, vol. 220, pp. 347–364, Dec. 2014.

APPENDIX A: REFORMULATION OF THE STRESS EQUATIONS INTERMS OF STRAIN

To reformulate the stress equation (3-18) in terms of strain, the elastic stress-strain relation is used:

$$\sigma_i = K_{ij}\varepsilon_j \tag{A-1}$$

Where the following are based on the primed coordinate system,

ε_j = Strain components

K_{ij} = Stiffness Matrix

For silicon, the stiffness matrix in [100]-crystal axis (unprimed axis) is given by (in GPa) [115]:

$$K_{ij} = \begin{bmatrix} K_{11} & K_{12} & K_{12} & 0 & 0 & 0 \\ K_{12} & K_{11} & K_{12} & 0 & 0 & 0 \\ K_{12} & K_{12} & K_{11} & 0 & 0 & 0 \\ 0 & 0 & 0 & K_{44} & 0 & 0 \\ 0 & 0 & 0 & 0 & K_{44} & 0 \\ 0 & 0 & 0 & 0 & 0 & K_{44} \end{bmatrix}$$

$$= \begin{bmatrix} 165.6 & 63.9 & 63.9 & 0 & 0 & 0 \\ 63.9 & 165.6 & 63.9 & 0 & 0 & 0 \\ 63.9 & 63.9 & 165.6 & 0 & 0 & 0 \\ 0 & 0 & 0 & 79.5 & 0 & 0 \\ 0 & 0 & 0 & 0 & 79.5 & 0 \\ 0 & 0 & 0 & 0 & 0 & 79.5 \end{bmatrix} \tag{A-2}$$

The transformed elasticity tensor along the [111]-crystal axis (primed axis) is given by:

$$K_{ij}^{'} = T_{ik} K_{kl} T_{lj}^{-1} \tag{A-3}$$

Where $T_{\alpha\gamma}$ is presented in (3-5), while the direction cosines in equation (3-9) are used to transform from the silicon crystallographic coordinate system to the coordinate system of (111) plane. Then, transforming the elasticity matrix along the (111) silicon plane using equation (A-3) gives (in GPa):

$$K_{ij}^{'} = \begin{bmatrix} K_{11}^{'} & K_{12}^{'} & K_{13}^{'} & K_{14}^{'} & 0 & 0 \\ K_{12}^{'} & K_{11}^{'} & K_{13}^{'} & K_{14}^{'} & 0 & 0 \\ K_{13}^{'} & K_{13}^{'} & K_{33}^{'} & 0 & 0 & 0 \\ K_{14}^{'} & K_{14}^{'} & 0 & K_{44}^{'} & 0 & 0 \\ 0 & 0 & 0 & 0 & K_{44}^{'} & K_{14}^{'} \\ 0 & 0 & 0 & 0 & K_{14}^{'} & K_{66}^{'} \end{bmatrix}$$

$$= \begin{bmatrix} 194.3 & 54.4 & 44.8 & 13.5 & 0 & 0 \\ 54.4 & 194.3 & 44.8 & -13.5 & 0 & 0 \\ 44.8 & 44.8 & 203.9 & 0 & 0 & 0 \\ 13.5 & -13.5 & 0 & 60.4 & 0 & 0 \\ 0 & 0 & 0 & 0 & 60.4 & 13.5 \\ 0 & 0 & 0 & 0 & 13.5 & 70 \end{bmatrix} \tag{A-4}$$

Therfore, the stress-strain relation, with respect to the [111]-crystal axis, is as follows:

$$\sigma_i^{'} = K^{'}_{ij} \varepsilon_j^{'} \tag{A-5}$$

Equation (A-5) is used when all of the strains are known and the values of stress are to be calculated. However, for piezoresistive element, the stress is known since there is a direct relation with the electrical resistance change. In this case, the strains need to be determined using:

$$\varepsilon_j^{'} = K_{ij}^{'-1}\sigma_i^{'} \tag{A-6}$$

Where $K_{ij}^{'-1}$ is the compliance matrix of the silicon based on the primed coordinate system.

APPENDIX B: ANSYS FINITE ELEMENT CODE FOR EIGHT-ELEMENT SENSING ROSETTE

```
/title, 3D Eight-element Stress Sensor with Temperature
Compensation
!/com, Geometrical Parameters (um)
/com,
!SENSOR
!#######
ls = 7000 !Length of sensor (um)
ws = 7000 !Width of sensor (um)
ts = 300 !Thickness of sensor (um)
theta=0   ! Sensor Orientation With respect to X-axis
!Sensing Rosette
!#############
c=50
r=200
a=100 ! length of piezoresistors, um
b=20 ! width of piezoresistors, um
TP=6 ! depth of doping, um
pi=3.14
phi=pi/4
!Sensing Rosette positions
! ####################
!Element 1
xc1=0
yc1=400
sc1=0
!Element 2
xc2=-75
yc2=-200
sc2=45
!Element 3
xc3=-150
yc3=275
sc3=90
!Element 4
xc4=-75
yc4=-375
sc4=135
!Element 5
xc5=0
yc5=175
sc5=180
!Element 6
xc6=75
yc6=-375
sc6=225
!Element 7
xc7=150
yc7=275
sc7=270
!Element 8
xc8=75
yc8=-200
sc8=315
!Element 9 (Circular a)
xc9=-100
yc9=0
sc9=0
!Element 10 (Circular b)
xc10=100
yc10=0
sc10=0
/com, Supply voltage, Volt
Vs=5
/com, Applied LOAD, MPa
F=50
/NOPR
!MATERIAL PROPERTIES
!#####################
/COM,
/COM, MATERIAL PROPERTIES (Si):
/COM,
/COM, Young's modulus, MPa
E=165e3
/COM, Poisson's ratio
nu=0.25
/COM,
/com, Stiffness, MN/m^2
/com, [c11 c12 c12 0 0 0 ]
/com, [c12 c11 c12 0 0 0 ]
/com, [c12 c12 c11 0 0 0 ]
/com, [ 0 0 0 c44 0 0 ]
/com, [ 0 0 0 0 c44 0 ]
/com, [ 0 0 0 0 0 c44]
c11= 16.57e4
c12= 6.39e4
c44= 7.96e4
/com,
!Piezoresistive properties of group a
/COM, Resistivity (group a), TOhm*um
rhoa= (60*8.88e-12)  !rhoa= 9.84e-10
/COM,
/COM, Piezoresistive coefficients (n-Si), (MPa)^-1
/COM, [p11 p12 p12 0 0 0 ]
/COM, [p12 p11 p12 0 0 0 ]
/COM, [p12 p12 p11 0 0 0 ]
/COM, [ 0 0 0 p44 0 0 ]
/COM, [ 0 0 0 0 p44 0 ]
/COM, [ 0 0 0 0 0 p44]
/COM,
p11a=-547.6e-6  !p11a=-547.6e-6  -0.00036792
p12a=0.5*547.6e-6   !p12a=286.1e-6   0.00019224
p44a=-150.9E-6  !p44a=-150.9E-6      -175E-6
!Piezoresistive properties of group b
/COM, Resistivity (group b), TOhm*um
rhob= (60*1.294e-11)  !rhob= 1.14e-9
/COM, Piezoresistive coefficients (n- Si), (MPa)^-1
/COM, [p11 p12 p12 0 0 0 ]
/COM, [p12 p11 p12 0 0 0 ]
/COM, [p12 p12 p11 0 0 0 ]
/COM, [ 0 0 0 p44 0 0 ]
/COM, [ 0 0 0 0 p44 0 ]
/COM, [ 0 0 0 0 0 p44]
/COM,
p11b=-873.3e-6  !p11b=-873.3e-6  -0.00049056
p12b=0.5*873.3e-6   !p12b=456.3e-6   0.00025632
p44b=-131.5e-6  !p44b=-131.5e-6      -156e-6

!##############################
```

```
/PREP7

! Define (111) Silicon Plane
!###################
LOCAL,11,0
K,1000,0,0,0
K,1001,-1/sqrt(2),-1/sqrt(6),1/sqrt(3)
K,1002,1/sqrt(2),-1/sqrt(6),1/sqrt(3)
CSKP, 12, 0, 1000, 1001, 1002

!Chip and sensing elements Orientation
!#############################

LOCAL,14,0,0,0,0,theta,0,0
CSYS,14
WPCSYS,1,14
block, -ls/2, ls/2, -ws/2, ws/2, 0, ts ! Silicon Chip

!Sensing Rosette CS
CSYS,14
CLOCAL, 21, 0, xc1,yc1,ts,sc1, 0, 0
CSYS,14
CLOCAL, 22, 0, xc2,yc2,ts,sc2, 0, 0
CSYS,14
CLOCAL, 23, 0, xc3,yc3,ts,sc3, 0, 0
CSYS,14
CLOCAL, 24, 0, xc4,yc4,ts,sc4, 0, 0
CSYS,14
CLOCAL, 25, 0, xc5,yc5,ts,sc5, 0, 0
CSYS,14
CLOCAL, 26, 0, xc6,yc6,ts,sc6, 0, 0
CSYS,14
CLOCAL, 27, 0, xc7,yc7,ts,sc7, 0, 0
CSYS,14
CLOCAL, 28, 0, xc8,yc8,ts,sc8, 0, 0
CSYS,14
CLOCAL, 29, 0, xc9,yc9,ts,sc9, 0, 0
CSYS,14
CLOCAL, 30, 0, xc10,yc10,ts,sc10, 0, 0
CSYS,0
WPCSYS,1,0
/trlcy,volu,0.50
/replot
!######################
!Sensing Rosette
!######################
! Sensing Element 1
WPCSYS, , 21
CSYS,21
Block,-a/2,a/2,-b/2,b/2,0,-TP ! Resistor 1
K,1011,-a/2,-b,0
K,1012,a/2,-b,0
! Sensing Element 2
WPCSYS, , 22
CSYS,22
Block,-a/2,a/2,-b/2,b/2,0,-TP ! Resistor 2
K,2011,-a/2,-b,0
K,2012,a/2,-b,0
! Sensing Element 3
WPCSYS, , 23
CSYS,23
Block,-a/2,a/2,-b/2,b/2,0,-TP ! Resistor 3
K,3011,-a/2,-b,0
K,3012,a/2,-b,0
! Sensing Element 4
WPCSYS, , 24
CSYS,24
Block,-a/2,a/2,-b/2,b/2,0,TP ! Resistor 4
K,4011,-a/2,-b,0
K,4012,a/2,-b,0
! Sensing Element 5
WPCSYS, , 25
CSYS,25
Block,-a/2,a/2,-b/2,b/2,0,-TP ! Resistor 5
K,5011,-a/2,-b,0
K,5012,a/2,-b,0
! Sensing Element 6
WPCSYS, , 26
CSYS,26
Block,-a/2,a/2,-b/2,b/2,0,-TP ! Resistor 6
K,6011,-a/2,-b,0
K,6012,a/2,-b,0
! Sensing Element 7
WPCSYS, , 27
CSYS,27
Block,-a/2,a/2,-b/2,b/2,0,-TP ! Resistor 7
K,7011,-a/2,-b,0
K,7012,a/2,-b,0
! Sensing Element 8
WPCSYS, , 28
CSYS,28
Block,-a/2,a/2,-b/2,b/2,0,-TP ! Resistor 8
K,8011,-a/2,-b,0
K,8012,a/2,-b,0
! Sensing Element 9
WPCSYS, , 29
CSYS,29
cyl4,0,0,(a-b)/2,0,(a+b)/2,359,-TP! Circular Group a
K,9011,(a+b)/2,2*b,0
K,9012,(a+b)/2,-2*b,0
! Sensing Element 10
WPCSYS, , 30
CSYS,30
cyl4,0,0,(a-b)/2,0,(a+b)/2,359,-TP! Circular Group b
K,10011,(a+b)/2,2*b,0
K,10012,(a+b)/2,-2*b,0
WPCSYS, 1, 0
CSYS,0
WPCSYS,,14
CSYS,14
block, -450, 450, -450, 450, 0, ts
WPCSYS, 1, 0
CSYS,0
/trlcy,volu,0.5
/replot
VOVLAP,all
VGLUE,all

! ELEMENT TYPE
!##############
ET,1,SOLID227,101 ! piezoresistive element type, Tetrahedron - 10 Noded
ET,2,SOLID187 ! structural element type
ET,3,CIRCU124,0 ! electrical resistance element
R,1,(a/(b*TP))*rhoa ! resistance of constant resistors 1,2,3 and 4 group a - TOhm
R,2,(a/(b*TP))*rhob ! resistance of constant resistors 5,6,7 and 8 group b - TOhm
R,3,(2*pi*0.5*a/(b*TP))*rhoa ! resistance of constant resistor (Circular element group a)
R,4,(2*pi*0.5*a/(b*TP))*rhob ! resistance of constant resistor (Circular element group b)

!###############################
! MATERIAL PROPERTIES
!#################################
! 1) Anisotropic elasticity matrix of Silicon
```

```
!^^^^^^^^^^^^^^^^^^^^^^^^^^^^^^^^^^^^^^^^
!a) Group a
tb,ANEL,2,,,0
tbdata,1,c11,c12,c12
tbdata,7,c11,c12
tbdata,12,c11
tbdata,16,c44
tbdata,19,C44,0,C44
!b) Group b
tb,ANEL,3,,,0
tbdata,1,c11,c12,c12
tbdata,7,c11,c12
tbdata,12,c11
tbdata,16,c44
tbdata,19,C44,0,C44
!2) Resistivity
!^^^^^^^^^^^^^^^
!a) Group a
MP,RSVX,2,rhoa ! Resistivity
TB,PZRS,2 ! piezoresistive stress matrix
TBDATA,1,p11a,p12a,p12a
TBDATA,7,p12a,p11a,p12a
TBDATA,13,p12a,p12a,p11a
TBDATA,22,p44a
TBDATA,29,p44a
TBDATA,36,p44a
!b) Group b
MP,RSVX,3,rhob ! Resistivity
TB,PZRS,3 ! piezoresistive stress matrix
TBDATA,1,p11b,p12b,p12b
TBDATA,7,p12b,p11b,p12b
TBDATA,13,p12b,p12b,p11b
TBDATA,22,p44b
TBDATA,29,p44b
TBDATA,36,p44b
/trlcy,volu,0.5
/replot
!#########
!MESHING #
!#########
NUMSTR, NODE, 300
!Chip
VATT,2,1,2,12 !Sensor
vsel,s,volu,,13
ESIZE,20*TP
MOPT,TETEXPND,2
VMESH,all
vsel,all

!Sensing Rosette
VATT,2,1,1,12
ESIZE,2*TP
vsel,s,volu,,2,5,1
vsel,a,volu,,10
VMESH,all ! mesh group a resistor areas
vsel,all

VATT,3,1,1,12
ESIZE,2*TP
vsel,s,volu,,6,9,1
vsel,a,volu,,11
VMESH,all ! mesh group b resistor areas
vsel,all
!Volume Surrounding Rosette
VATT,2,1,2,12
vsel,s,volu,,14
esize,10*TP      ! old value is 10*TP
VMESH,all
vsel,all
allsel,all
!##########################
! BOUNDARY CONDITIONS #
!##########################
NKPT,11, 1011
NKPT,12, 1012
NKPT,21, 2011
NKPT,22, 2012
NKPT,31, 3011
NKPT,32, 3012
NKPT,41, 4011
NKPT,42, 4012
NKPT,51, 5011
NKPT,52, 5012
NKPT,61, 6011
NKPT,62, 6012
NKPT,71, 7011
NKPT,72, 7012
NKPT,81, 8011
NKPT,82, 8012
NKPT,91, 9011
NKPT,92, 9012
NKPT,101, 10011
NKPT,102, 10012

!##########
!LOADING #
!##########
!1)Mechanical Loading
!^^^^^^^^^^^^^^^^^^^
Applied Force
SFA, 5, ,pres,-F
DA,6,all,0

!2) Apply electrical BC:
!^^^^^^^^^^^^^^^^^^^^^^
!##########################
!Bridge 1 - at 0 degrees
!++++++++++++++++++++++
ASEL,S,AREA,,12 ! define supply voltage contact
NSLA,S,1
CP,11,VOLT,ALL
*GET,ns1,NODE,0,NUM,MIN
D,ns1,VOLT,Vs
ALLSEL,ALL
NSEL,S,NODE,,11 ! define ground contact
!CP,12,VOLT,ALL
*GET,ng1,NODE,0,NUM,MIN
D,ng1,VOLT,0
ALLSEL,ALL
NSEL,S,NODE,,12 ! define first output contact
!CP,13,VOLT,ALL
*GET,no11,NODE,0,NUM,MIN
ALLSEL,ALL
ASEL,S,AREA,,11 ! define second output contact
NSLA,S,1
CP,14,VOLT,ALL
*GET,no12,NODE,0,NUM,MIN
ALLSEL,ALL
Type, 3 ! define constant resistors
!MAT, 4
REAL, 1
ESYS,11
E,ns1,no11
E,no11,ng1
E,ng1,no12
!Bridge 2 - at 45 degrees
!++++++++++++++++++++++
ASEL,S,AREA,,18 ! define supply voltage contact
```

```
NSLA,S,1
CP,21,VOLT,ALL
*GET,ns2,NODE,0,NUM,MIN
D,ns2,VOLT,Vs
ALLSEL,ALL
NSEL,S,NODE,,21 ! define ground contact
*GET,ng2,NODE,0,NUM,MIN
D,ng2,VOLT,0
ALLSEL,ALL
NSEL,S,NODE,,22 ! define first output contact
*GET,no21,NODE,0,NUM,MIN
ALLSEL,ALL
ASEL,S,AREA,,17 ! define second output contact
NSLA,S,1
CP,24,VOLT,ALL
*GET,no22,NODE,0,NUM,MIN
ALLSEL,ALL
Type, 3 ! define constant resistors
!MAT, 4
REAL, 1
ESYS,11
E,ns2,no21
E,no21,ng2
E,ng2,no22
!Bridge 3 - at 90 degrees
!++++++++++++++++++++++
ASEL,S,AREA,,24 ! define supply voltage contact
NSLA,S,1
CP,31,VOLT,ALL
*GET,ns3,NODE,0,NUM,MIN
D,ns3,VOLT,Vs
ALLSEL,ALL
NSEL,S,NODE,,31 ! define ground contact
*GET,ng3,NODE,0,NUM,MIN
D,ng3,VOLT,0
ALLSEL,ALL
NSEL,S,NODE,,32 ! define first output contact
*GET,no31,NODE,0,NUM,MIN
ALLSEL,ALL
ASEL,S,AREA,,23 ! define second output contact
NSLA,S,1
CP,34,VOLT,ALL
*GET,no32,NODE,0,NUM,MIN
ALLSEL,ALL
Type, 3 ! define constant resistors
!MAT, 4
REAL, 1
ESYS,11
E,ns3,no31
E,no31,ng3
E,ng3,no32
!Bridge 4 - at 135 degrees
!++++++++++++++++++++++
ASEL,S,AREA,,30 ! define supply voltage contact
NSLA,S,1
CP,41,VOLT,ALL
*GET,ns4,NODE,0,NUM,MIN
D,ns4,VOLT,Vs
ALLSEL,ALL
NSEL,S,NODE,,41 ! define ground contact
*GET,ng4,NODE,0,NUM,MIN
D,ng4,VOLT,0
ALLSEL,ALL
NSEL,S,NODE,,42 ! define first output contact
*GET,no41,NODE,0,NUM,MIN
ALLSEL,ALL
ASEL,S,AREA,,29 ! define second output contact
NSLA,S,1
CP,44,VOLT,ALL
*GET,no42,NODE,0,NUM,MIN
ALLSEL,ALL
Type, 3 ! define constant resistors
!MAT, 4
REAL, 1
ESYS,11
E,ns4,no41
E,no41,ng4
E,ng4,no42
!Bridge 5 - at 180 degrees
!++++++++++++++++++++++
ASEL,S,AREA,,36 ! define supply voltage contact
NSLA,S,1
CP,51,VOLT,ALL
*GET,ns5,NODE,0,NUM,MIN
D,ns5,VOLT,Vs
ALLSEL,ALL
NSEL,S,NODE,,51 ! define ground contact
*GET,ng5,NODE,0,NUM,MIN
D,ng5,VOLT,0
ALLSEL,ALL
NSEL,S,NODE,,52 ! define first output contact
*GET,no51,NODE,0,NUM,MIN
ALLSEL,ALL
ASEL,S,AREA,,35 ! define second output contact
NSLA,S,1
CP,54,VOLT,ALL
*GET,no52,NODE,0,NUM,MIN
ALLSEL,ALL
Type, 3 ! define constant resistors
!MAT, 4
REAL, 2
ESYS,11
E,ns5,no51
E,no51,ng5
E,ng5,no52
!Bridge 6 - at 225 degrees
!++++++++++++++++++++++
ASEL,S,AREA,,42 ! define supply voltage contact
NSLA,S,1
CP,61,VOLT,ALL
*GET,ns6,NODE,0,NUM,MIN
D,ns6,VOLT,Vs
ALLSEL,ALL
NSEL,S,NODE,,61 ! define ground contact
*GET,ng6,NODE,0,NUM,MIN
D,ng6,VOLT,0
ALLSEL,ALL
NSEL,S,NODE,,62 ! define first output contact
*GET,no61,NODE,0,NUM,MIN
ALLSEL,ALL
ASEL,S,AREA,,41 ! define second output contact
NSLA,S,1
CP,64,VOLT,ALL
*GET,no62,NODE,0,NUM,MIN
ALLSEL,ALL
Type, 3 ! define constant resistors
!MAT, 4
REAL, 2
ESYS,11
E,ns6,no61
E,no61,ng6
E,ng6,no62
!Bridge 7 - at 270 degrees
!++++++++++++++++++++++
ASEL,S,AREA,,48 ! define supply voltage contact
NSLA,S,1
CP,71,VOLT,ALL
*GET,ns7,NODE,0,NUM,MIN
```

```
D,ns7,VOLT,Vs
ALLSEL,ALL
NSEL,S,NODE,,71 ! define ground contact
!CP,12,VOLT,ALL
*GET,ng7,NODE,0,NUM,MIN
D,ng7,VOLT,0
ALLSEL,ALL
NSEL,S,NODE,,72 ! define first output contact
!CP,13,VOLT,ALL
*GET,no71,NODE,0,NUM,MIN
ALLSEL,ALL
ASEL,S,AREA,,47 ! define second output contact
NSLA,S,1
CP,74,VOLT,ALL
*GET,no72,NODE,0,NUM,MIN
ALLSEL,ALL
Type, 3 ! define constant resistors
!MAT, 4
REAL, 2
ESYS,11
E,ns7,no71
E,no71,ng7
E,ng7,no72
!Bridge 8 - at 315 degrees
!++++++++++++++++++++++
ASEL,S,AREA,,54 ! define supply voltage contact
NSLA,S,1
CP,81,VOLT,ALL
*GET,ns8,NODE,0,NUM,MIN
D,ns8,VOLT,Vs
ALLSEL,ALL
NSEL,S,NODE,,81 ! define ground contact
!CP,12,VOLT,ALL
*GET,ng8,NODE,0,NUM,MIN
D,ng8,VOLT,0
ALLSEL,ALL
NSEL,S,NODE,,82 ! define first output contact
!CP,13,VOLT,ALL
*GET,no81,NODE,0,NUM,MIN
ALLSEL,ALL
ASEL,S,AREA,,53 ! define second output contact
NSLA,S,1
CP,84,VOLT,ALL
*GET,no82,NODE,0,NUM,MIN
ALLSEL,ALL
Type, 3 ! define constant resistors
!MAT, 4
REAL, 2
ESYS,11
E,ns8,no81
E,no81,ng8
E,ng8,no82
!Bridge 9 - at 0 degrees
!++++++++++++++++++++++
ASEL,S,AREA,,60 ! define supply voltage contact
NSLA,S,1
CP,91,VOLT,ALL
*GET,ns9,NODE,0,NUM,MIN
D,ns9,VOLT,Vs
ALLSEL,ALL
NSEL,S,NODE,,91 ! define ground contact
!CP,12,VOLT,ALL
*GET,ng9,NODE,0,NUM,MIN
D,ng9,VOLT,0
ALLSEL,ALL
NSEL,S,NODE,,92 ! define first output contact
!CP,13,VOLT,ALL
*GET,no91,NODE,0,NUM,MIN
ALLSEL,ALL
ASEL,S,AREA,,59 ! define second output contact
NSLA,S,1
CP,94,VOLT,ALL
*GET,no92,NODE,0,NUM,MIN
ALLSEL,ALL
Type, 3 ! define constant resistors
!MAT, 4
REAL, 3
ESYS,11
E,ns9,no91
E,no91,ng9
E,ng9,no92
!Bridge 10 - at 90 degrees
!++++++++++++++++++++++
ASEL,S,AREA,,66 ! define supply voltage contact
NSLA,S,1
CP,101,VOLT,ALL
*GET,ns10,NODE,0,NUM,MIN
D,ns10,VOLT,Vs
ALLSEL,ALL
NSEL,S,NODE,,101 ! define ground contact
!CP,12,VOLT,ALL
*GET,ng10,NODE,0,NUM,MIN
D,ng10,VOLT,0
ALLSEL,ALL
NSEL,S,NODE,,102 ! define first output contact
!CP,13,VOLT,ALL
*GET,no101,NODE,0,NUM,MIN
ALLSEL,ALL
ASEL,S,AREA,,65 ! define second output contact
NSLA,S,1
CP,104,VOLT,ALL
*GET,no102,NODE,0,NUM,MIN
ALLSEL,ALL
Type, 3 ! define constant resistors
!MAT, 4
REAL, 4
ESYS,11
E,ns10,no101
E,no101,ng10
E,ng10,no102
ALLSEL,ALL
!################

/PBC,u,,1
/PBC,volt,,1
/PBC,cp,,1
/PNUM,TYPE,1
/NUMBER,1
EPLOT

FINISH

!#########
! Solution #
!#########
/SOLU
ANTYPE,STATIC
CNVTOL,VOLT,1,1E-3
autots,on ! auto time stepping
nsubst,5,1000,1 ! Size of first substep=1/5 of the total load, max # substeps=1000, min # substeps=1

SOLVE

FINISH

!############
!Postprocessing#
```

```
!############

/post1

!Calculate Results
!###############
/com, Results at Central Rosette
/com, VOA=%(volt(no11)-volt(no12))*1.e3%, mV
! Calculate ANSYS Result - Bridge1
/com,		dR01=%(4*(volt(no11)-volt(no12))/Vs)/(1-
2*(volt(no11)-volt(no12))/Vs)%
/com,
/com, VOA=%(volt(no21)-volt(no22))*1.e3%, mV
! Calculate ANSYS Result - Bridge2
/com,		dR02=%(4*(volt(no21)-volt(no22))/Vs)/(1-
2*(volt(no21)-volt(no22))/Vs)%
/com,
/com, VOA=%(volt(no31)-volt(no32))*1.e3%, mV
! Calculate ANSYS Result - Bridge3
/com,		dR03=%(4*(volt(no31)-volt(no32))/Vs)/(1-
2*(volt(no31)-volt(no32))/Vs)%
/com,
/com, VOA=%(volt(no41)-volt(no42))*1.e3%, mV
! Calculate ANSYS Result - Bridge4
/com,		dR04=%(4*(volt(no41)-volt(no42))/Vs)/(1-
2*(volt(no41)-volt(no42))/Vs)%
/com,
/com, VOA=%(volt(no51)-volt(no52))*1.e3%, mV
! Calculate ANSYS Result - Bridge5
/com,		dR05=%(4*(volt(no51)-volt(no52))/Vs)/(1-
2*(volt(no51)-volt(no52))/Vs)%
/com,
/com, VOA=%(volt(no61)-volt(no62))*1.e3%, mV
! Calculate ANSYS Result - Bridge6
/com,		dR06=%(4*(volt(no61)-volt(no62))/Vs)/(1-
2*(volt(no61)-volt(no62))/Vs)%
/com,
/com, VOA=%(volt(no71)-volt(no72))*1.e3%, mV
! Calculate ANSYS Result - Bridge7
/com,		dR07=%(4*(volt(no71)-volt(no72))/Vs)/(1-
2*(volt(no71)-volt(no72))/Vs)%
/com,
/com, VOA=%(volt(no81)-volt(no82))*1.e3%, mV
! Calculate ANSYS Result - Bridge8
/com,		dR08=%(4*(volt(no11)-volt(no82))/Vs)/(1-
2*(volt(no81)-volt(no82))/Vs)%
/com,
/com, VOA=%(volt(no91)-volt(no92))*1.e3%, mV
! Calculate ANSYS Result - Bridge9
/com,		dR09=%(4*(volt(no91)-volt(no92))/Vs)/(1-
2*(volt(no91)-volt(no92))/Vs)%
/com,
/com, VOA=%(volt(no101)-volt(no102))*1.e3%, mV
! Calculate ANSYS Result - Bridge10
/com,	dR10=%(4*(volt(no101)-volt(no102))/Vs)/(1-
2*(volt(no101)-volt(no102))/Vs)%
/com,
```

APPENDIX C: ANSYS FINITE ELEMENT CODE FOR CHIP-ON-BEAM SPECIMEN UNDER FOUR POINT BENDING

```
/clear
/input,parameters,inp
/title, Chip-on-beam  Under 4 Point Bending
!/com, Geometrical Parameters (um)
/com,
!MONITORED Steel STRUCTURE
!#######################
lm = 300000 !Length of monitored structure (um)
wm = 45000 !Width of monitored structure (um)
tm = 3000 !Thickness of monitored structure (um)
!SENSOR
!#######
ls = 7000 !Length of sensor (um)
ws = 7000 !Width of sensor (um)
ts = 300 !Thickness of sensor (um)
!Four point bending
!###############
L=250000/2
D=70000/2
!Sensing Rosette
!#############
c=50
r=200
a=100 ! length of piezoresistors, um
b1=10 ! width of piezoresistors group a, um
b2=13 ! width of piezoresistors group b, um
b3=17 ! width of piezoresistors group b, um
TP=6 ! depth of doping, um
pi=3.14
phi=pi/4
!Sensing Rosette positions
! ###################
!1) Center Rosette
!Element 1
xc1=0
yc1=400
sc1=0
!Element 2
xc2=-75
yc2=-200
sc2=45
!Element 3
xc3=-150
yc3=275
sc3=90
!Element 4
xc4=-75
yc4=-375
sc4=135
!Element 5
xc5=0
yc5=175
sc5=180
!Element 6
xc6=75
yc6=-375
sc6=225
!Element 7
xc7=150
yc7=275
sc7=270
!Element 8
xc8=75
yc8=-200
sc8=315
!Element 9
xc9=100
yc9=0
sc9=0
!Element 10
xc10=290
yc10=100
sc10=90
/COM, LOADING CONDITIONS
!F=4*12.71e6 !Check number of nodes along line of
applied load   % F=12.71e6/2
/com, Supply voltage, Volt
Vs=5
/NOPR
!MATERIAL PROPERTIES
!#####################
/COM,
/COM, MATERIAL PROPERTIES (Si):
/COM,
/COM, Young's modulus, MPa
E=165e3
/COM, Poisson's ratio
nu=0.25
/COM,
/com, Stiffness, MN/m^2
/com, [c11 c12 c12 0 0 0 ]
/com, [c12 c11 c12 0 0 0 ]
/com, [c12 c12 c11 0 0 0 ]
/com, [ 0 0 0 c44 0 0 ]
/com, [ 0 0 0 0 c44 0 ]
/com, [ 0 0 0 0 0 c44]
c11= 16.57e4
c12= 6.39e4
c44= 7.96e4
/com,
!Piezoresistive properties of group a
/COM, Resistivity (group a), TOhm*um
rhoa= (60*8.88e-12)  !rhoa= 9.84e-10
/COM,
/COM, Piezoresistive coefficients (n-Si), (MPa)^-1
/COM, [p11 p12 p12 0 0 0 ]
/COM, [p12 p11 p12 0 0 0 ]
/COM, [p12 p12 p11 0 0 0 ]
/COM, [ 0 0 0 p44 0 0 ]
/COM, [ 0 0 0 0 p44 0 ]
/COM, [ 0 0 0 0 0 p44]
/COM,
!p11a=-0.00037953           !p11a=-0.00036792 My Old
simulations  !p11a=-547.6e-6 Hossam
```

```
!p12a=0.00019831           !p12a=0.00019224 My Old
simulations   !p12a=286.1e-6  Hossam
!p44a=-175.79E-6           !p44a=-175E-6  My Old
simulations     !p44a=-150.9E-6 Hossam
!Piezoresistive properties of group b
/COM, Resistivity (group b), TOhm*um
rhob= (60*1.294e-11)  !rhob= 1.14e-9
/COM, Piezoresistive coefficients (n- Si), (MPa)^-1
/COM, [p11 p12 p12 0 0 0 ]
/COM, [p12 p11 p12 0 0 0 ]
/COM, [p12 p12 p11 0 0 0 ]
/COM, [ 0 0 0 p44 0 0 ]
/COM, [ 0 0 0 0 p44 0 ]
/COM, [ 0 0 0 0 0 p44]
/COM,
!p11b=-0.00050111   !p11b=-0.00049056  my old
simulations    !p11b=-873.3e-6       Hossam
!p12b=0.00026183    !p12b=0.00025632   my old
simulations    !p12b=456.3e-6        Hossam
!p44b=-154.93e-6       !p44b=-156e-6      my old
simulations    !p44b=-131.5e-6     Hossam
!Piezoresistive properties of group c
/COM, Resistivity (group c), TOhm*um
rhoc= (60*1.776e-11)  !rhoc= 1.38e-9
/COM, Piezoresistive coefficients (n-Si), (MPa)^-1
/COM, [p11 p12 p12 0 0 0 ]
/COM, [p12 p11 p12 0 0 0 ]
/COM, [p12 p12 p11 0 0 0 ]
/COM, [ 0 0 0 p44 0 0 ]
/COM, [ 0 0 0 0 p44 0 ]
/COM, [ 0 0 0 0 0 p44]
/COM,
!p11c=-0.00059276  !p11c=-0.00059276 my old
simulations       !p11c=-948.3e-6  Hossam
!p12c=0.00030972   !p12c=0.00030972  my old
simylations      !p12c=495.5e-6   Hossam
!p44c=-148e-6      !p44c=-148e-6  my old simulations
!p44c=-128.4e-6     Hossam
!################################
/PREP7
! (111) Silicon Plane orientation
!#################################
LOCAL,11,0
K,1000,0,0,0
K,1001,-1/sqrt(2),-1/sqrt(6),1/sqrt(3)
K,1002,1/sqrt(2),-1/sqrt(6),1/sqrt(3)
CSKP, 12, 0, 1000, 1001, 1002
!Chip Orientation on Steel Structure
!###################################
LOCAL,14,0,0,0,0,theta,0,0
CSYS,14
WPCSYS,1,14
block, -ls/2, ls/2, -ws/2, ws/2, tm, tm+ts ! Silicon Chip
!Sensing Rosette CS
CSYS,14
CLOCAL, 21, 0, xc1,yc1,tm+ts,sc1, 0, 0
CSYS,14
CLOCAL, 22, 0, xc2,yc2,tm+ts,sc2, 0, 0
CSYS,14
CLOCAL, 23, 0, xc3,yc3,tm+ts,sc3, 0, 0
CSYS,14
CLOCAL, 24, 0, xc4,yc4,tm+ts,sc4, 0, 0
CSYS,14
CLOCAL, 25, 0, xc5,yc5,tm+ts,sc5, 0, 0
CSYS,14
CLOCAL, 26, 0, xc6,yc6,tm+ts,sc6, 0, 0
CSYS,14
CLOCAL, 27, 0, xc7,yc7,tm+ts,sc7, 0, 0
CSYS,14
CLOCAL, 28, 0, xc8,yc8,tm+ts,sc8, 0, 0
CSYS,14
CLOCAL, 29, 0, xc9,yc9,tm+ts,sc9, 0, 0
CSYS,14
CLOCAL, 30, 0, xc10,yc10,tm+ts,sc10, 0, 0
CSYS,0
WPCSYS,1,0
!Central Sensing Rosette
!######################
! Sensing Element 1
WPCSYS, , 21
CSYS,21
Block,-a/2,a/2,-b1/2,b1/2,0,-TP ! Resistor 1
K,1011,-a/2,-b1,0
K,1012,a/2,-b1,0
! Sensing Element 2
WPCSYS, , 22
CSYS,22
Block,-a/2,a/2,-b1/2,b1/2,0,-TP ! Resistor 2
K,2011,-a/2,-b1,0
K,2012,a/2,-b1,0
! Sensing Element 3
WPCSYS, , 23
CSYS,23
Block,-a/2,a/2,-b1/2,b1/2,0,-TP ! Resistor 3
K,3011,-a/2,-b1,0
K,3012,a/2,-b1,0
! Sensing Element 4
WPCSYS, , 24
CSYS,24
Block,-a/2,a/2,-b1/2,b1/2,0,-TP ! Resistor 4
K,4011,-a/2,-b1,0
K,4012,a/2,-b1,0
! Sensing Element 5
WPCSYS, , 25
CSYS,25
Block,-a/2,a/2,-b2/2,b2/2,0,-TP ! Resistor 5
K,5011,-a/2,-b2,0
K,5012,a/2,-b2,0
! Sensing Element 6
WPCSYS, , 26
CSYS,26
Block,-a/2,a/2,-b2/2,b2/2,0,-TP ! Resistor 6
K,6011,-a/2,-b2,0
K,6012,a/2,-b2,0
! Sensing Element 7
WPCSYS, , 27
CSYS,27
Block,-a/2,a/2,-b2/2,b2/2,0,-TP! Resistor 7
K,7011,-a/2,-b2,0
K,7012,a/2,-b2,0
! Sensing Element 8
WPCSYS, , 28
CSYS,28
Block,-a/2,a/2,-b2/2,b2/2,0,-TP ! Resistor 8
K,8011,-a/2,-b2,0
K,8012,a/2,-b2,0
! Sensing Element 9
WPCSYS, , 29
CSYS,29
Block,-a/2,a/2,-b3/2,b3/2,0,-TP! Resistor 9
K,9011,-a/2,-b3,0
K,9012,a/2,-b3,0
! Sensing Element 10
WPCSYS, , 30
CSYS,30
Block,-a/2,a/2,-b3/2,b3/2,0,-TP! Resistor 10
K,10011,-a/2,-b3,0
K,10012,a/2,-b3,0
```

```
WPCSYS, 1, 0
CSYS,0
WPCSYS,,14
CSYS,14
block, -450, 450, -450, 450, tm, tm+ts
WPCSYS, 1, 0
CSYS,0
!########
!Structure
!#########
block,-wm/2,wm/2,-wm/2,wm/2,0,tm
block,-lm/2,-wm/2,-wm/2,wm/2,0,tm
block,wm/2,lm/2,-wm/2,wm/2,0,tm
numstr,area,100
!###############
! Partition Structure
!###############
WPLANE, 1, 0, 0, 0, lm/2, 0, 0, 0, 0, tm ! Partitioning
the Sheet
vsel,s,loc,z,0,tm
VSBW, all
WPLANE, 1, 0, 0, 0, 0, wm/2, 0, 0, 0, tm ! Partitioning
the Sheet
VSBW, all
vsel,all
!Location of Four Point Bending
WPLANE, 1, -L, 0, 0, -L, wm/2, 0, -L,0,tm
vsbw,all
WPLANE, 1, L, 0, 0, L, wm/2, 0, L,0,tm
vsbw,all
WPLANE, 1, -D, 0, 0, -D, wm/2, 0, -D,0,tm
vsbw,all
WPLANE, 1, D, 0, 0, D, wm/2, 0, D,0,tm
vsbw,all
WPCSYS, 1, 0
CSYS,0
VOVLAP,all
VGLUE,all
!###############
! ELEMENT TYPE
!###############
ET,1,SOLID227,101 ! piezoresistive element type,
Tetrahedron - 10 Noded
ET,2,SOLID187 ! structural element type
ET,3,CIRCU124,0 ! electrical resistance element
R,1,(a/(b1*TP))*rhoa ! resistance of constant resistors -
TOhm
R,2,(a/(b2*TP))*rhob ! resistance of constant resistors -
TOhm
R,3,(a/(b3*TP))*rhoc ! resistance of constant resistors -
TOhm
!################################
! MATERIAL PROPERTIES
!################################
! 1) Anisotropic elasticity matrix of Silicon
!^^^^^^^^^^^^^^^^^^^^^^^^^^^^^^^^^^^^
!a) Group a
tb,ANEL,2,,,0
tbdata,1,c11,c12,c12
tbdata,7,c11,c12
tbdata,12,c11
tbdata,16,c44
tbdata,19,C44,0,C44
!b) Group b
tb,ANEL,3,,,0
tbdata,1,c11,c12,c12
tbdata,7,c11,c12
tbdata,12,c11
tbdata,16,c44
tbdata,19,C44,0,C44
!c) Group c
tb,ANEL,4,,,0
tbdata,1,c11,c12,c12
tbdata,7,c11,c12
tbdata,12,c11
tbdata,16,c44
tbdata,19,C44,0,C44
!2) Resistivity
!^^^^^^^^^^^^^^
!a) Group a
MP,RSVX,2,rhoa ! Resistivity
TB,PZRS,2 ! piezoresistive stress matrix
TBDATA,1,p11a,p12a,p12a
TBDATA,7,p12a,p11a,p12a
TBDATA,13,p12a,p12a,p11a
TBDATA,22,p44a
TBDATA,29,p44a
TBDATA,36,p44a
!b) Group b
MP,RSVX,3,rhob ! Resistivity
TB,PZRS,3 ! piezoresistive stress matrix
TBDATA,1,p11b,p12b,p12b
TBDATA,7,p12b,p11b,p12b
TBDATA,13,p12b,p12b,p11b
TBDATA,22,p44b
TBDATA,29,p44b
TBDATA,36,p44b
!b) Group c
MP,RSVX,4,rhoc ! Resistivity
TB,PZRS,4 ! piezoresistive stress matrix
TBDATA,1,p11c,p12c,p12c
TBDATA,7,p12c,p11c,p12c
TBDATA,13,p12c,p12c,p11c
TBDATA,22,p44c
TBDATA,29,p44c
TBDATA,36,p44c

!Beam
MP,EX,1,200E3 !  E= 200 GPa, v=0.3
MP,PRXY,1,0.3
!################################
!MESHING #
!#########
!mshape,1,3d
NUMSTR, NODE, 300

!Chip
VATT,2,1,2,12 !Sensor
!vsel,s,volu,,38
!aslv,s
!asel,r,loc,z,tm+tb+ts
!allsel,all
vsel,s,loc,z,tm+tb,tm+tb+ts
vsel,u,volu,,2,11,1
vsel,u,volu,,38
!LESIZE, 5,80*TP ,,,-0.1   !12*TP
!LESIZE, 6,80*TP ,,,-0.1
!LESIZE, 7,80*TP ,,,-0.1
!LESIZE, 8,80*TP ,,,-0.1
!LESIZE, 286,80*TP ,,,-0.1
!LESIZE, 287,80*TP ,,,-0.1
!LESIZE, 297,80*TP ,,,-0.1
!LESIZE, 298,80*TP ,,,-0.1
!LESIZE, 304,80*TP ,,,-0.1
!LESIZE, 305,80*TP ,,,-0.1
!LESIZE, 308,80*TP ,,,-0.1
!LESIZE, 309,80*TP ,,,-0.1
```

```
!Modification
!##########
LESIZE, 137,12*TP ,,,-0.1   !12*TP
LESIZE, 138,12*TP ,,,-0.1
LESIZE, 139,12*TP ,,,-0.1
LESIZE, 140,12*TP ,,,-0.1
LESIZE, 141,12*TP ,,,-0.1
LESIZE, 142,12*TP ,,,-0.1
LESIZE, 143,12*TP ,,,-0.1
LESIZE, 144,12*TP ,,,-0.1
LESIZE, 282,12*TP ,,,-0.1
LESIZE, 283,12*TP ,,,-0.1
LESIZE, 292,12*TP ,,,-0.1
LESIZE, 293,12*TP ,,,-0.1
LESIZE, 299,12*TP ,,,-0.1
LESIZE, 300,12*TP ,,,-0.1
LESIZE, 306,12*TP ,,,-0.1
LESIZE, 307,12*TP ,,,-0.1
esize,2*ts  ! esize,2*ts
MOPT,TETEXPND,2
VMESH,all
vsel,all
!############
!Sensing Rosette
!############
VATT,2,1,1,12
ESIZE,3*TP      ! 3*TP
VMESH,2,5,1 ! mesh group a resistor areas
VATT,3,1,1,12
ESIZE,3*TP   !3*TP
VMESH,6,9,1 ! mesh group b resistor areas
VATT,4,1,1,12
ESIZE,3*TP  !3*TP
VMESH,10,11,1 ! mesh group c resistor areas
!Volume Surrounding Rosette
VATT,2,1,2,12
vsel,s,volu,,38
esize,10*TP   !10*TP
VMESH,all
vsel,all
!###############
!Monitored Structure
!###############
WPCSYS,1,0
CSYS,0
VATT,1,1,2
vsel,s,loc,z,tb,tb+tm
vsel,r,loc,x,-wm/2,wm/2
esize,0.3*tm  ! 0.3*tm
MOPT,TETEXPND,2
VMESH,all
vsel,all
vsel,s,loc,x,-lm/2,-wm/2
vsel,a,loc,x,wm/2,lm/2
esize,5*tm    !5*tm
MOPT,TETEXPND,2
VMESH,all
vsel,all
!#########################
! BOUNDARY CONDITIONS #
!#########################
NKPT,11, 1011
NKPT,12, 1012
NKPT,21, 2011
NKPT,22, 2012
NKPT,31, 3011
NKPT,32, 3012
NKPT,41, 4011
NKPT,42, 4012
NKPT,51, 5011
NKPT,52, 5012
NKPT,61, 6011
NKPT,62, 6012
NKPT,71, 7011
NKPT,72, 7012
NKPT,81, 8011
NKPT,82, 8012
NKPT,91, 9011
NKPT,92, 9012
NKPT,101, 10011
NKPT,102, 10012

!#########
!LOADING #
!#########

!1)Four Point Bending
!^^^^^^^^^^^^^^^^^^
!Edge Supports
nsel,s,loc,x,-D
nsel,a,loc,x,D
nsel,r,loc,z,tb
D,all,UZ,0
allsel,all
nsel,s,loc,x,-D
nsel,a,loc,x,D
nsel,r,loc,z,tb
nsel,r,loc,y,0
D,all,UY,0
allsel,all
nsel,s,loc,x,0
nsel,r,loc,z,tb
D,all,UX,0
allsel,all
!Applied Force
lsel,s,loc,x,-L
lsel,a,loc,x,L
lsel,r,loc,z,tb+tm
nsll,s,1
F, all, FZ, -F/5
allsel,all
!2) Apply electrical BC:
!^^^^^^^^^^^^^^^^^^^^^
!########################
!Bridge 1 - at 0 degrees
!++++++++++++++++++++++
ASEL,S,AREA,,12 ! define supply voltage contact
NSLA,S,1
CP,11,VOLT,ALL
*GET,ns1,NODE,0,NUM,MIN
D,ns1,VOLT,Vs
ALLSEL,ALL
NSEL,S,NODE,,11 ! define ground contact
!CP,12,VOLT,ALL
*GET,ng1,NODE,0,NUM,MIN
D,ng1,VOLT,0
ALLSEL,ALL
NSEL,S,NODE,,12 ! define first output contact
!CP,13,VOLT,ALL
*GET,no11,NODE,0,NUM,MIN
ALLSEL,ALL
ASEL,S,AREA,,11 ! define second output contact
NSLA,S,1
CP,14,VOLT,ALL
*GET,no12,NODE,0,NUM,MIN
ALLSEL,ALL
Type, 3 ! define constant resistors
```

```
!MAT, 4
REAL, 1
ESYS,11
E,ns1,no11
E,no11,ng1
E,ng1,no12
!Bridge 2 - at 45 degrees
!++++++++++++++++++++++
ASEL,S,AREA,,18 ! define supply voltage contact
NSLA,S,1
CP,21,VOLT,ALL
*GET,ns2,NODE,0,NUM,MIN
D,ns2,VOLT,Vs
ALLSEL,ALL
NSEL,S,NODE,,21 ! define ground contact
*GET,ng2,NODE,0,NUM,MIN
D,ng2,VOLT,0
ALLSEL,ALL
NSEL,S,NODE,,22 ! define first output contact
*GET,no21,NODE,0,NUM,MIN
ALLSEL,ALL
ASEL,S,AREA,,17 ! define second output contact
NSLA,S,1
CP,24,VOLT,ALL
*GET,no22,NODE,0,NUM,MIN
ALLSEL,ALL
Type, 3 ! define constant resistors
!MAT, 4
REAL, 1
ESYS,11
E,ns2,no21
E,no21,ng2
E,ng2,no22
!Bridge 3 - at 90 degrees
!++++++++++++++++++++++
ASEL,S,AREA,,24 ! define supply voltage contact
NSLA,S,1
CP,31,VOLT,ALL
*GET,ns3,NODE,0,NUM,MIN
D,ns3,VOLT,Vs
ALLSEL,ALL
NSEL,S,NODE,,31 ! define ground contact
*GET,ng3,NODE,0,NUM,MIN
D,ng3,VOLT,0
ALLSEL,ALL
NSEL,S,NODE,,32 ! define first output contact
*GET,no31,NODE,0,NUM,MIN
ALLSEL,ALL
ASEL,S,AREA,,23 ! define second output contact
NSLA,S,1
CP,34,VOLT,ALL
*GET,no32,NODE,0,NUM,MIN
ALLSEL,ALL
Type, 3 ! define constant resistors
!MAT, 4
REAL, 1
ESYS,11
E,ns3,no31
E,no31,ng3
E,ng3,no32
!Bridge 4 - at 135 degrees
!++++++++++++++++++++++
ASEL,S,AREA,,30 ! define supply voltage contact
NSLA,S,1
CP,41,VOLT,ALL
*GET,ns4,NODE,0,NUM,MIN
D,ns4,VOLT,Vs
ALLSEL,ALL
NSEL,S,NODE,,41 ! define ground contact
*GET,ng4,NODE,0,NUM,MIN
D,ng4,VOLT,0
ALLSEL,ALL
NSEL,S,NODE,,42 ! define first output contact
*GET,no41,NODE,0,NUM,MIN
ALLSEL,ALL
ASEL,S,AREA,,29 ! define second output contact
NSLA,S,1
CP,44,VOLT,ALL
*GET,no42,NODE,0,NUM,MIN
ALLSEL,ALL
Type, 3 ! define constant resistors
!MAT, 4
REAL, 1
ESYS,11
E,ns4,no41
E,no41,ng4
E,ng4,no42
!Bridge 5 - at 180 degrees
!++++++++++++++++++++++
ASEL,S,AREA,,36 ! define supply voltage contact
NSLA,S,1
CP,51,VOLT,ALL
*GET,ns5,NODE,0,NUM,MIN
D,ns5,VOLT,Vs
ALLSEL,ALL
NSEL,S,NODE,,51 ! define ground contact
*GET,ng5,NODE,0,NUM,MIN
D,ng5,VOLT,0
ALLSEL,ALL
NSEL,S,NODE,,52 ! define first output contact
*GET,no51,NODE,0,NUM,MIN
ALLSEL,ALL
ASEL,S,AREA,,35 ! define second output contact
NSLA,S,1
CP,54,VOLT,ALL
*GET,no52,NODE,0,NUM,MIN
ALLSEL,ALL
Type, 3 ! define constant resistors
!MAT, 4
REAL, 2
ESYS,11
E,ns5,no51
E,no51,ng5
E,ng5,no52
!Bridge 6 - at 225 degrees
!++++++++++++++++++++++
ASEL,S,AREA,,42 ! define supply voltage contact
NSLA,S,1
CP,61,VOLT,ALL
*GET,ns6,NODE,0,NUM,MIN
D,ns6,VOLT,Vs
ALLSEL,ALL
NSEL,S,NODE,,61 ! define ground contact
*GET,ng6,NODE,0,NUM,MIN
D,ng6,VOLT,0
ALLSEL,ALL
NSEL,S,NODE,,62 ! define first output contact
*GET,no61,NODE,0,NUM,MIN
ALLSEL,ALL
ASEL,S,AREA,,41 ! define second output contact
NSLA,S,1
CP,64,VOLT,ALL
*GET,no62,NODE,0,NUM,MIN
ALLSEL,ALL
Type, 3 ! define constant resistors
!MAT, 4
REAL, 2
ESYS,11
```

```
E,ns6,no61
E,no61,ng6
E,ng6,no62
!Bridge 7 - at 270 degrees
!++++++++++++++++++++++
ASEL,S,AREA,,48 ! define supply voltage contact
NSLA,S,1
CP,71,VOLT,ALL
*GET,ns7,NODE,0,NUM,MIN
D,ns7,VOLT,Vs
ALLSEL,ALL
NSEL,S,NODE,,71 ! define ground contact
!CP,12,VOLT,ALL
*GET,ng7,NODE,0,NUM,MIN
D,ng7,VOLT,0
ALLSEL,ALL
NSEL,S,NODE,,72 ! define first output contact
!CP,13,VOLT,ALL
*GET,no71,NODE,0,NUM,MIN
ALLSEL,ALL
ASEL,S,AREA,,47 ! define second output contact
NSLA,S,1
CP,74,VOLT,ALL
*GET,no72,NODE,0,NUM,MIN
ALLSEL,ALL
Type, 3 ! define constant resistors
!MAT, 4
REAL, 2
ESYS,11
E,ns7,no71
E,no71,ng7
E,ng7,no72
!Bridge 8 - at 315 degrees
!++++++++++++++++++++++
ASEL,S,AREA,,54 ! define supply voltage contact
NSLA,S,1
CP,81,VOLT,ALL
*GET,ns8,NODE,0,NUM,MIN
D,ns8,VOLT,Vs
ALLSEL,ALL
NSEL,S,NODE,,81 ! define ground contact
!CP,12,VOLT,ALL
*GET,ng8,NODE,0,NUM,MIN
D,ng8,VOLT,0
ALLSEL,ALL
NSEL,S,NODE,,82 ! define first output contact
!CP,13,VOLT,ALL
*GET,no81,NODE,0,NUM,MIN
ALLSEL,ALL
ASEL,S,AREA,,53 ! define second output contact
NSLA,S,1
CP,84,VOLT,ALL
*GET,no82,NODE,0,NUM,MIN
ALLSEL,ALL
Type, 3 ! define constant resistors
!MAT, 4
REAL, 2
ESYS,11
E,ns8,no81
E,no81,ng8
E,ng8,no82
!Bridge 9 - at 0 degrees
!++++++++++++++++++++++
ASEL,S,AREA,,60 ! define supply voltage contact
NSLA,S,1
CP,91,VOLT,ALL
*GET,ns9,NODE,0,NUM,MIN
D,ns9,VOLT,Vs
ALLSEL,ALL
NSEL,S,NODE,,91 ! define ground contact
!CP,12,VOLT,ALL
*GET,ng9,NODE,0,NUM,MIN
D,ng9,VOLT,0
ALLSEL,ALL
NSEL,S,NODE,,92 ! define first output contact
!CP,13,VOLT,ALL
*GET,no91,NODE,0,NUM,MIN
ALLSEL,ALL
ASEL,S,AREA,,59 ! define second output contact
NSLA,S,1
CP,94,VOLT,ALL
*GET,no92,NODE,0,NUM,MIN
ALLSEL,ALL
Type, 3 ! define constant resistors
!MAT, 4
REAL, 3
ESYS,11
E,ns9,no91
E,no91,ng9
E,ng9,no92
!Bridge 10 - at 90 degrees
!++++++++++++++++++++++
ASEL,S,AREA,,66 ! define supply voltage contact
NSLA,S,1
CP,101,VOLT,ALL
*GET,ns10,NODE,0,NUM,MIN
D,ns10,VOLT,Vs
ALLSEL,ALL
NSEL,S,NODE,,101 ! define ground contact
!CP,12,VOLT,ALL
*GET,ng10,NODE,0,NUM,MIN
D,ng10,VOLT,0
ALLSEL,ALL
NSEL,S,NODE,,102 ! define first output contact
!CP,13,VOLT,ALL
*GET,no101,NODE,0,NUM,MIN
ALLSEL,ALL
ASEL,S,AREA,,65 ! define second output contact
NSLA,S,1
CP,104,VOLT,ALL
*GET,no102,NODE,0,NUM,MIN
ALLSEL,ALL
Type, 3 ! define constant resistors
!MAT, 4
REAL, 3
ESYS,11
E,ns10,no101
E,no101,ng10
E,ng10,no102
ALLSEL,ALL
!################
/PBC,u,,1
/PBC,volt,,1
/PBC,cp,,1
/PNUM,TYPE,1
/NUMBER,1
EPLOT
FINISH
!#########
! Solution #
!#########
/SOLU
ANTYPE,STATIC
CNVTOL,VOLT,1,1E-3
autots,on ! auto time stepping
nsubst,5,1000,1
! Size of first substep=1/5 of the total load, max #
!substeps=1000, min # substeps=1
```

```
SOLVE
FINISH
!############
!Postprocessing#
!###########
/post1
!Calculate Results
!##############
/com, Results at Central Rosette
/com, VOA=%(volt(no11)-volt(no12))*1.e3%, mV
 ! Calculate ANSYS Result - Bridge1
/com, R01=%(1-0.5+((volt(no11)-
volt(no12))/5))*888/(0.5-((volt(no11)-volt(no12))/5))%
/com,
/com, VOA=%(volt(no21)-volt(no22))*1.e3%, mV
! Calculate ANSYS Result - Bridge2
/com, R02=%(1-0.5+((volt(no21)-
volt(no22))/5))*888/(0.5-((volt(no21)-volt(no22))/5))%
/com,
/com, VOA=%(volt(no31)-volt(no32))*1.e3%, mV
! Calculate ANSYS Result - Bridge3
/com, R03=%(1-0.5+((volt(no31)-
volt(no32))/5))*888/(0.5-((volt(no31)-volt(no32))/5))%
/com,
/com, VOA=%(volt(no41)-volt(no42))*1.e3%, mV
! Calculate ANSYS Result - Bridge4
/com, R04=%(1-0.5+((volt(no41)-
volt(no42))/5))*888/(0.5-((volt(no41)-volt(no42))/5))%
/com,
/com, VOA=%(volt(no51)-volt(no52))*1.e3%, mV
! Calculate ANSYS Result - Bridge5
/com, R05=%(1-0.5+((volt(no51)-
volt(no52))/5))*995.35/(0.5-((volt(no51)-
volt(no52))/5))%
/com,
/com, VOA=%(volt(no61)-volt(no62))*1.e3%, mV
 ! Calculate ANSYS Result - Bridge6
/com, R06=%(1-0.5+((volt(no61)-
volt(no62))/5))*995.35/(0.5-((volt(no61)-
volt(no62))/5))%
/com,
/com, VOA=%(volt(no71)-volt(no72))*1.e3%, mV
! Calculate ANSYS Result - Bridge7
/com, R07=%(1-0.5+((volt(no71)-
volt(no72))/5))*995.35/(0.5-((volt(no71)-
volt(no72))/5))%
/com,
/com, VOA=%(volt(no81)-volt(no82))*1.e3%, mV
! Calculate ANSYS Result - Bridge8
/com, R08=%(1-0.5+((volt(no81)-
volt(no82))/5))*995.35/(0.5-((volt(no81)-
volt(no82))/5))%
/com,
/com, VOA=%(volt(no91)-volt(no92))*1.e3%, mV
! Calculate ANSYS Result - Bridge9
/com, R09=%(1-0.5+((volt(no91)-
volt(no92))/5))*1044.7/(0.5-((volt(no91)-
volt(no92))/5))%
/com,
/com, VOA=%(volt(no101)-volt(no102))*1.e3%, mV
 ! Calculate ANSYS Result - Bridge10
/com, R010=%(1-0.5+((volt(no101)-
volt(no102))/5))*1044.7/(0.5-((volt(no101)-
volt(no102))/5))%
/com,
*dim,VoB,array,10,2
*set,VoB(1,1),%((1-0.5+((volt(no11)-
volt(no12))/5))*888/(0.5-((volt(no11)-volt(no12))/5))-
888)/888%
*set,VoB(2,1),%((1-0.5+((volt(no21)-
volt(no22))/5))*888/(0.5-((volt(no21)-volt(no22))/5))-
888)/888%
*set,VoB(3,1),%((1-0.5+((volt(no31)-
volt(no32))/5))*888/(0.5-((volt(no31)-volt(no32))/5))-
888)/888%
*set,VoB(4,1),%((1-0.5+((volt(no41)-
volt(no42))/5))*888/(0.5-((volt(no41)-volt(no42))/5))-
888)/888%
*set,VoB(5,1),%((1-0.5+((volt(no51)-
volt(no52))/5))*995.35/(0.5-((volt(no51)-
volt(no52))/5))-995.35)/995.35%
*set,VoB(6,1),%((1-0.5+((volt(no61)-
volt(no62))/5))*995.35/(0.5-((volt(no61)-
volt(no62))/5))-995.35)/995.35%
*set,VoB(7,1),%((1-0.5+((volt(no71)-
volt(no72))/5))*995.35/(0.5-((volt(no71)-
volt(no72))/5))-995.35)/995.35%
*set,VoB(8,1),%((1-0.5+((volt(no81)-
volt(no82))/5))*995.35/(0.5-((volt(no81)-
volt(no82))/5))-995.35)/995.35%
*set,VoB(9,1),%((1-0.5+((volt(no91)-
volt(no92))/5))*1044.7/(0.5-((volt(no91)-
volt(no92))/5))-1044.7)/1044.7%
*set,VoB(10,1),%((1-0.5+((volt(no101)-
volt(no102))/5))*1044.7/(0.5-((volt(no101)-
volt(no102))/5))-1044.7)/1044.7%

*set,VoB(1,2),%volt(no12)%
*set,VoB(2,2),%volt(no22)%
*set,VoB(3,2),%volt(no32)%
*set,VoB(4,2),%volt(no42)%
*set,VoB(5,2),%volt(no52)%
*set,VoB(6,2),%volt(no62)%
*set,VoB(7,2),%volt(no72)%
*set,VoB(8,2),%volt(no82)%
*set,VoB(9,2),%volt(no92)%
*set,VoB(10,2),%volt(no102)%

*CFOPEN,'dRout','txt','D:\My PhD\Research\neural
network\matlab outputs'
*vwrite,VoB(1,1)
(F14.8,' ',F14.8,' ',F14.8' ',F14.8)
*cfclos
*cfopen,dRout,txt
*vwrite,VoB(1,1)
(F14.8,' ',F14.8,' ',F14.8' ',F14.8)
*cfclos

*CFOPEN,'Vout','txt','D:\My PhD\Research\neural
network\matlab outputs'
*vwrite,VoB(1,2)
(F14.8,' ',F14.8,' ',F14.8' ',F14.8)
*cfclos

*cfopen,Vout,txt
*vwrite,VoB(1,2)
(F14.8,' ',F14.8,' ',F14.8' ',F14.8)
*cfclos
```

APPENDIX D: MATLAB CODE TO GENERATE ANNS FUNCTION

```
clear;
clc;
data=xlsread('D:\MyPhD\Research\Testing\New
Training_18July2018\TC_V2_NN_S0_5Loads_Temp0to50_Jul2019.xlsx','NN_building_NS23_S
0_34and5','AT3:BE112');
dr10=data(:,8)'
dT_nn=TC_R10(dr10)
[m,n]=size(data)
data_nn=zeros(m, 5)
data_nn(:,1:4)=data(:,3:6)
data_nn(:,5)=dT_nn'
inputs=transpose(data_nn(:,:))
output=transpose(data(:,2))

x = inputs;
t = output;

% Choose a Training Function
% For a list of all training functions type: help nntrain
% 'trainlm' is usually fastest.
% 'trainbr' takes longer but may be better for challenging problems.
% 'trainscg' uses less memory. Suitable in low memory situations.
%trainFcn = 'trainlm';
% Levenberg-Marquardt backpropagation.
% trainFcn = 'trainbr';
% Bayesian Regulation backpropagation.

% Create a Fitting Network

hiddenLayerSize = 1;
net = fitnet(hiddenLayerSize,trainFcn);

% Choose Input and Output Pre/Post-Processing Functions
% For a list of all processing functions type: help nnprocess

net.input.processFcns = {'removeconstantrows','mapminmax'};
net.output.processFcns = {'removeconstantrows','mapminmax'};

% Setup Division of Data for Training, Validation, Testing
% For a list of all data division functions type: help nndivide

net.divideFcn = 'dividerand';  % Divide data randomly
net.divideMode = 'sample';  % Divide up every sample
net.divideParam.trainRatio = 70/100;
net.divideParam.valRatio = 15/100;
net.divideParam.testRatio = 15/100;
```

```
% Choose a Performance Function
% For a list of all performance functions type: help nnperformance
%net.performFcn = 'mse';
% Mean Squared Error

net.performFcn='msereg';
net.performParam.ratio=0.5;

% Choose Plot Functions
% For a list of all plot functions type: help nnplot

net.plotFcns = {'plotperform','plottrainstate','ploterrhist', ...
    'plotregression', 'plotfit'};

% Train the Network

[net,tr] = train(net,x,t);

% Test the Network

y = net(x);
e = gsubtract(t,y);
performance = perform(net,t,y)

% Recalculate Training, Validation and Test Performance

trainTargets = t .* tr.trainMask{1};
valTargets = t .* tr.valMask{1};
testTargets = t .* tr.testMask{1};
trainPerformance = perform(net,trainTargets,y)
valPerformance = perform(net,valTargets,y)
testPerformance = perform(net,testTargets,y)

% View the Network

view(net)

% Plots
% Uncomment these lines to enable various plots.
%figure, plotperform(tr)
%figure, plottrainstate(tr)
%figure, ploterrhist(e)
%figure, plotregression(t,y)
%figure, plotfit(net,x,t)
% Deployment
% Change the (false) values to (true) to enable the following code blocks.
% See the help for each generation function for more information.

if (true)

    % Generate MATLAB function for neural network for application
    % deployment in MATLAB scripts or with MATLAB Compiler and Builder
    % tools, or simply to examine the calculations your trained neural
    % network performs.
```

```
    genFunction(net,'nn_S0_NS23_11x5samples');
    y = nn_S0_NS23_11x5samples(x);
end
if (false)

    % Generate a matrix-only MATLAB function for neural network code
    % generation with MATLAB Coder tools.

    genFunction(net,'nn_S0_NS23_11x5samples','MatrixOnly','yes');
    y = nn_S0_NS23_11x5samples(x);
end
if (false)

    % Generate a Simulink diagram for simulation or deployment with.
    % Simulink Coder tools.

    gensim(net);
end
```

APPENDIX E: THE MICROFABRICATION PROCESS FLOW OF THE STRAINED SILICON-BASED SENSING ROSETTE

The detailed microfabrication process flow of the developed sensing chip is as follows:

<table>
<tr><th colspan="2">STEP 1.0: WAFER PREPARATION</th></tr>
<tr><td>1.1 Starting Material</td><td>• 100 mm prime p-type wafer
• Orientation: (111) ± 0.1°
• Thickness: 300 ± 25 µm
• Bulk resistivity: 10 ± 2 Ω.cm</td></tr>
<tr><td>1.2 Wafer Cleaning</td><td>1.2.1 Piranha: (H_2SO_4: H_2O_2, 3:1)
• Clean: 15 minutes in piranha
• Dump rinse
• Spin-rinse-dry
1.2.2 Buffered Oxide Etch (BOE)
• Etch: 2 minutes in BOE
• Dump rinse
• Spin-rinse-dry</td></tr>
<tr><th colspan="2">STEP 2.0: Define Alignment Marks</th></tr>
<tr><td>2.1 Lithography</td><td>2.1.1 HMDS Prime:
• Standard HMDS prime recipe (program 1)
2.1.2 Photo Resist Coat:
• Photoresist: HPR 504
• Spread: 500 rpm for 10 seconds
• Spin: 4000 rpm for 40 seconds
• Soft-bake: 115 °C for 90 seconds on hotplate
• Rehydration: 15 minutes
2.1.3 Expose Photo Resist:
• Mask layer: 10
• UV light (365 nm + 405 nm)
• Dose: ~140 mJ/cm^2
2.1.4 Develop Photo Resist:
• Developer: 354
• Time: ~18-20 seconds (visual endpoint)
• DI H_2O rinse</td></tr>
</table>

2.2 Silicon Etch	• Tool: ICP RIE (Oxford Estrelas) • Recipe: unswitched process • Condition: 5 minutes • Etch: 1 minute
2.3 Photo Resist Strip	• Tool: Branson 3000 Barrel Etcher • time: 20 minutes
STEP 3.0: Oxide Mask for Doping	
3.1 Wafer Cleaning	• Piranha: (H_2SO_4: H_2O_2, 3:1) • Clean: 15 minutes in piranha • Dump rinse • Spin-rinse-dry
3.2 Thermal Wet Oxidation	• Tool: Minibrute Middle Furnace • Temperature set-point: 1000 °C • Ramp up to 998 °C then start timer • Time: 110 minutes • Thickness: ~ 550 nm
STEP 4.0: Doping group a (Pre-deposition 1)	
4.1 Lithography	4.1.1 HMDS Prime: • Standard HMDS prime recipe (program 1) 4.1.2 Photo Resist Coat: • Photoresist: HPR 504 • Spread: 500 rpm for 10 seconds • Spin: 4000 rpm for 40 seconds • Soft-bake: 115 °C for 90 seconds on hotplate • Rehydration: 15 minutes 4.1.3 Expose Photo Resist: • Mask layer: 11 • UV light (365 nm + 405 nm) • Dose: ~140 mJ/cm^2 4.1.4 Develop Photo Resist: • Developer: 354 • Time: ~18-20 seconds (visual endpoint) • DI H_2O rinse
4.2 Oxide Etch	• Open group a windows • Tool: Trion RIE • Cleaning Recipe: 20 minutes • Oxide Etch Recipe: 20 minutes • Over Etch: 30%
4.2 Photo Resist Strip	• Tool: Branson 3000 Barrel Etcher

	• time: 20 minutes
4.4 Phosphorus Pre-deposition	• Tool: Diffusion Furnace • Doping Source: PhosPlus® TP-250 • Doping Temperature: 845 °C • Wafer Insertion Temperature: 700 °C • Time: 2 hours (start timer at 843 °C)
STEP 5.0: Doping groups a & b (Pre-deposition 2)	
5.1 Lithography	5.1.1 HMDS Prime: • Standard HMDS prime recipe (program 1) 5.1.2 Photo Resist Coat: • Photoresist: HPR 504 • Spread: 500 rpm for 10 seconds • Spin: 4000 rpm for 40 seconds • Soft-bake: 115 °C for 90 seconds on hotplate • Rehydration: 15 minutes 5.1.3 Expose Photo Resist: • Mask layer: 12 • UV light (365 nm + 405 nm) • Dose: ~140 mJ/cm^2 5.1.4 Develop Photo Resist: • Developer: 354 • Time: ~18-20 seconds (visual endpoint) • DI H_2O rinse
5.2 Oxide Etch	• Open group a windows • Tool: Trion RIE • Condition Recipe: O_2 Clean • Condition Time: 20 minutes • Etch Recipe: Oxide Etch • Etch Time: 20 minutes (~550 nm oxide etch) • Over Etch: 30% of etch time
5.3 Photo Resist Strip	• Tool: Branson 3000 Barrel Etcher • time: 20 minutes
5.4 Phosphorus Pre-deposition	• Tool: Diffusion Furnace • Doping Source: PhosPlus® TP-250 • Doping Temperature: 845 °C • Wafer Insertion Temperature: 700 °C • Time: 2 hours (start timer at 843 °C) • Nitrogen Flow Rate: 40 Liter/minute
5.4 Oxide and PSG Etch	• Wet Etch using BOE • Etch rate: 44 nm/min • Etch Time: 12 minutes and 30 seconds

	• Over etch: 30% of etch time • Dump rinse • Spin-rinse-dry
STEP 6.0: Annealing, Drive-In, and Oxidation	
6.1 Annealing and Drive-in	• Tool: Minibrute Middle Furnace • Temperature set-point: 1050 °C • Switch set to Anneal (Nitrogen only) • Nitrogen Flow Rate: 40 Liter/ minute • Ramp up to 1048 °C then start timer • Hold for 30 minutes • Proceed immediately to the next step
6.2 Oxidation	• Turn switch from Anneal to Oxidation • Turn on bubbler and heater • Hold for 30 minutes • Turn off bubbler and heater • Turn off the furnace main switch • Cool for 200 °C or less to remove • Oxide thickness: ~ 250 nm
STEP 7.0: n^+ Phosphorus Doping of Contact Vias	
7.1 Lithography	7.1.1 HMDS Prime: • Standard HMDS prime recipe (program 1) 7.1.2 Photo Resist Coat: • Photoresist: HPR 504 • Spread: 500 rpm for 10 seconds • Spin: 4000 rpm for 40 seconds • Soft-bake: 115 °C for 90 seconds on hotplate • Rehydration: 15 minutes 7.1.3 Expose Photo Resist: • Mask layer: 13 • UV light (365 nm + 405 nm) • Dose: ~140 mJ/cm^2 7.1.4 Develop Photo Resist: • Developer: 354 • Time: ~18-20 seconds (visual endpoint) • DI H_2O rinse
7.2 Oxide Etch	• Open group a windows • Tool: Trion RIE • Condition Recipe: O_2 Clean • Condition Time: 20 minutes • Etch Recipe: Oxide Etch

	• Etch Time: 7 minutes (~250 nm oxide etch) • Over Etch: 30% of etch time
7.3 Photo Resist Strip	• Tool: Branson 3000 Barrel Etcher • time: 20 minutes
7.4 Phosphorus Doping	• Tool: Diffusion Furnace • Doping Source: PhosPlus® TP-250 • Doping Temperature: 875 °C • Wafer Insertion Temperature: 700 °C • Time: 1 hour (start timer at 873 °C) • Nitrogen Flow Rate: 40 Liter/minute
STEP 8.0: Silicon Nitride Deposition (Stressing layer)	
8.1 Oxide and PSG Etch	• Wet Etch using BOE • Etch rate: 44 nm/min • Etch Time: 7 minutes and 30 Seconds • Dump rinse • Spin-rinse-dry • Over Etch 30% to totally remove the oxide layer
8.2 Nitride Deposition	• Tool: PECVD Trion • Select Nitride conditioning for 10 mins • Deposition rate: 50 nm/min • Target thickness: 400 nm
STEP 9.0: Aluminum Sputtering	
9.1 Lithography	9.1.1 HMDS Prime: • Standard HMDS prime recipe (program 1) 9.1.2 Photo Resist Coat: • Photoresist: HPR 504 • Spread: 500 rpm for 10 seconds • Spin: 4000 rpm for 40 seconds • Soft-bake: 115 °C for 90 seconds on hotplate • Rehydration: 15 minutes 9.1.3 Expose Photo Resist: • Mask layer: 13 • UV light (365 nm + 405 nm) • Dose: ~140 mJ/cm^2 9.1.4 Develop Photo Resist: • Developer: 354 • Time: ~18-20 seconds (visual endpoint) • DI H_2O rinse

9.2 Nitride Etch	• Define contact vias • Tool: Trion RIE • Condition Recipe: O_2 Clean • Condition Time: 20 minutes • Etch Recipe: Nitride Etch • Etch rate: 350 nm/min (~400 nm Nitride etch) • Over Etch: 15% of etch time •
9.3 Photo Resist Strip	• Tool: Branson 3000 Barrel Etcher • time: 20 minutes • Proceed immediately to the next step
9.4 Aluminum Deposition	• Tool: Floyd Magnetron sputtering • Burn-in time: 120 seconds • Deposition Time: 3135 seconds
STEP 10.0: Patterning Aluminum Traces and Pads	
10.1 Lithography	10.1.1 HMDS Prime: • Standard HMDS prime recipe (program 1) 10.1.2 Photo Resist Coat: • Photoresist: HPR 504 • Spread: 500 rpm for 10 seconds • Spin: 4000 rpm for 40 seconds • Soft-bake: 115 °C for 90 seconds on hotplate • Rehydration: 15 minutes 10.1.3 Expose Photo Resist: • Mask layer: 14 • UV light (365 nm + 405 nm) • Dose: ~140 mJ/cm^2 10.1.4 Develop Photo Resist: • Developer: 354 • Time: ~18-20 seconds (visual endpoint) • DI H_2O rinse
10.2 Aluminum Etch	• Wet Etch using commercial Al Etchant • Etch Rate: 35 nm/min • Etching Time: 20 minutes • Over Etch: 20% of etch time
10.3 Photo Resist Strip	• Acetone Bath • time: 5 minutes • Dump rinse • Spin-rinse-dry

10.4 Annealing	• Tool: Diffusion Furnace • Wafer insertion at room temperature • Nitrogen Flow Rate: 40 Liter/ minute • Set Temperature: 450 °C • Ramp up to 453 °C then start timer • Time: 15 minutes